NASA Contractor Report **187495**

Personnel Launch System Autoland Development Study

J. A. Bossi
M. A. Langehough
J. C. Tollefson

(NASA-CR-187495) PERSONNEL LAUNCH SYSTEM AUTOLAND DEVELOPMENT STUDY Final Report (Boeing Co.) 168 p CSCL 01C
N91-18116
Unclas
G3/08 0330165

Boeing Aerospace & Electronics
20403 68th Ave South
18-26 Bldg Kent, WA 98032

Contract NAS1-18762
JANUARY 1991

National Aeronautics and
Space Administration

Langley Research Center
Hampton, Virginia 23665-5225

TABLE OF CONTENTS

TABLE OF CONTENTS

LIST OF FIGURES

LIST OF FIGURES

LIST OF TABLES

SYMBOLS AND ACRONYMS

Acronym	**Description**
6-DOF	Six Degree of Freedom
[A]	Plant matrix
[B]	Input matrix
[C]	Fin mixer matrix
[C]	Transmission output matrix
[Ruu]	Input weighting matrix
[Rxx]	State weighting matrix
[U]	Input vector
[X]	State variable vector
α	Angle of attack
α trim	Estimated trim angle of attack
A/L	Approach and Landing (autoland phase)
α_c	Angle of attack command
$\alpha_{command}$	Angle of attack command
ACRC	Assured Crew Return Capability
alpha	Angle of attack
ALTCMD	Altitude command
A_{ref}	Reference area
ax	Axial acceleration , body axis
ay	Lateral acceleration , body axis
az	Normal acceleration , body axis
β	Sideslip angle
β_c	Sideslip angle command
CERV	Crew Emergency Rescue Vehicle
C_L	Lift coefficient
$C_{l\beta}$	Roll moment coefficient derivative with respect to sideslip angle
δ_1	Left, upper body flap deflection
δ_{1c}	Left upper body flap command
δ_2	Left, lower body flap deflection
δ_{2c}	Left lower body flap command
δ_3	Right, upper body flap deflection

δ_{3c}	Right upper body flap command
δ_4	Right, lower body flap deflection
δ_{4c}	Right lower body flap command
δ_5	Rudder flap deflection
δ_{5c}	Rudder flap command
δ_6	Left wing flap deflection
δ_{6c}	Left wing flap command
δ_7	Right wing flap deflection
δ_{7c}	Right wing flap command
δ_{ac}	Aileron command
δ_{ail}	Aileron command
δ_{bfLL}	Left, lower body flap deflection
δ_{bfLR}	Right, lower body flap deflection
δ_{bfUL}	Left, upper body flap deflection
δ_{bfUR}	Right, upper body flap deflection
δ_{ec}	Elevator command
DELH	Altitude change
DELS	Ground track range travel
Δny	Lateral acceleration
Δnz	Normal acceleration
δ_r	Rudder flap deflection
δ_{rc}	Rudder command
δ_{rud}	Rudder command
δ_s	Speedbrake command
δsb	Speedbrake deflection
δ_{sbc}	Speedbrake command
δ_{wfL}	Left wing flap deflection
δ_{wfR}	Right wing flap deflection
ΔY	Lateral error, cross track error
$\Delta\psi$	HAC heading angle change
$\Delta Yerr$	Lateral error, cross track error
dYerr	Cross track rate error
ϕ_c	Roll angle command
ϕe	Unlimited roll angle error
ϕ_{HAC}	HAC steady state bank angle command
γ	Flight path angle (glideslope), pitch axis

g	Gravitational constant (32.2 ft/sec**2)
G&C	Guidance and Control
GAM0	A/L initial flight path angle (pitch)
GAM1	Glideslope value for the shallow glideslope phase
γ_{HAC}	Constant HAC flight path angle (glideslope), pitch axis
γ_{HAC}	HAC flight path angle (glideslope), pitch axis
GPS	Global Positioning System
GRAM	Global Reference Atmospheric Model
H	Altitude
η cmd	Yaw flight path angle command
η crab	Crab angle
η err	Velocity heading error
H0	A/L initial altitude
H1C	Altitude command at start of pre-flare phase (A/L)
H2	Initial altitude for shallow glideslope phase
H2C	Altitude command at start of transient phase (A/L)
H3	Initial altitude for final flare phase
H3C	Altitude command at start of final flare (A/L)
HAC	Heading Alignment Cone
h_C	Altitude command
h_C	Altitude rate command
HERR	Altitude error
HHAC	Instantaneous altitude during HAC
HNEP	Altitude at nominal entry point (NEP)
HTDC	Command touchdown altitude
HW1	TAEM altitude at W1 (1st way point)
Hz	Hertz, cycles per second
I-LQR	Integral Linear Quadratic Regulator
Integral-LQR	Integral Linear Quadratic Regulator
I_{XX}	Roll axis moment of inertia
I_{YY}	Pitch axis moment of inertia
I_{ZZ}	Yaw axis moment of inertia
J	Cost function
K	Airspeed error gain
$K\alpha$	Angle of attack feedback gain
K_{AC}	Longitudinal guidance gain

$K_{\beta a}$	Yaw/roll autopilot gain, sideslip to aileron command
$K_{\beta r}$	Yaw/roll autopilot gain, sideslip to rudder command
Kc	Speedbrake forward loop gain
$K_{\delta aa}$	Yaw/roll autopilot gain, aileron command feedback to aileron
$K_{\delta ar}$	Yaw/roll autopilot gain, aileron command feedback to rudder
$K\delta ec$	Elevator command feedback gain
$K_{\delta ra}$	Yaw/roll autopilot gain, rudder command feedback to aileron
$K_{\delta rr}$	Yaw/roll autopilot gain, rudder command feedback to rudder
KEAS	Equivalent airspeed in knots
K_{ϕ}	Lateral guidance forward loop gain
$K_{\phi a}$	Yaw/roll autopilot gain, roll angle error to aileron command
$K_{\phi r}$	Yaw/roll autopilot gain, roll angle error to rudder command
K_h	Altitude error gain
K_{pa}	Yaw/roll autopilot gain, roll rate error to aileron command
K_{phi}	Lateral guidance forward loop gain
K_{pr}	Yaw/roll autopilot gain, roll rate error to rudder command
Kq	Pitch rate gain
K_{ra}	Yaw/roll autopilot gain, yaw rate error to aileron command
K_{rr}	Yaw/roll autopilot gain, yaw rate error to rudder command
K_{SI}	Speedbrake integral gain
K_Y	Cross track error gain
L/D	Lift divided by drag
L_{ref}	Reference length
L_X	X axis wind turbulence model integral scale length
L_Y	Y axis wind turbulence model integral scale length
L_Z	Z axis wind turbulence model integral scale length
M	Mach number
MATRIXx	Trademark for Integrated Systems Incorporated product
MEP	Minimum Entry Point
MIMO	Multi-input, multi-output control system
MLS	Microwave Landing System
NEP	Nominal entry point for A/L (end of HAC)
OTT	Option TAEM Target
p	Roll rate, body axis
PLS	Personnel Launch System
Q	Dynamic pressure

q	Pitch rate, body axis
Qatm	Dynamic pressure
Qatmos	Dynamic pressure
Qmax	Maximum dynamic pressure
Qpres	Dynamic pressure
ρ	Weighting coefficient
r	Yaw rate, body axis
R1	Turn radius spiral equation linear coefficient
R2	Turn radius spiral equation squared coefficient
RF	Final turn radius on HAC
RT	Instantaneous turn radius during HAC
RVEC	Cross range vector
RW1	Initial HAC turn radius (at W1)
S	Ground track range
S	Reference area
S	S- Laplace Transform
S1	Ground track distance at start of pre-flare phase (A/L)
S1	Ground track distance at start of transient phase (A/L)
S3	Ground track distance at start of final flare (A/L)
S4	Ground track distance where shallow glideslope intercepts the ground
Span	Reference span
Std	Ground track distance at touchdown
σ_X	X axis wind turbulence model gaussian distribution
σ_Y	Y axis wind turbulence model gaussian distribution
σ_Z	Z axis wind turbulence model gaussian distribution
t	Time
TAEM	Terminal Area Energy Management
TSRV	Transportation System Research Vehicle
U	Airspeed
Uw	X axis wind component in body axis
V	Airspeed
V1	Velocity command at initiation of pullup maneuver
Vc	Velocity command
VELHAC	Instantaneous airspeed during HAC
VELNEP	Airspeed at nominal entry point (NEP)
VELW1	TAEM velocity at W1 (1st way point)

V_{EQ}	Equivalent airspeed in fps
Vhoriz	Velocity in horizontal plan
V_{KEAS}	Equivalent airspeed in knots
VT0	Initial velocity (A/L phase)
Vw	Y axis wind component in body axis
W	Vehicle weight
W1	TAEM 1st way point (entry into HAC)
WFLAR1	1st flare break frequency
WFLAR2	2nd flare break frequency
X	X axis velocity component in launch tangent axis
X	X position in launch tangent coordinates
X_{cg}	X axis center of gravity measured from vehicle nose
X_{HAC}	X displacement in HAC coordinates
X_{LT}	X position in launch tangent coordinates
Y	Y axis velocity component in launch tangent axis
Y	Y position in launch tangent coordinates
ψ	HAC heading angle
ψ_0	InitialHAC heading angle
Y_C	Cross track error
Y_{CTerr}	Lateral error, cross track error
Y_{err}	Lateral error, cross track error
Y_{HAC}	Y displacement in HAC coordinates
ψ_{HAC}	Heading angle change during HAC
Y_{LT}	Y position in launch tangent coordinates
Z	Z axis velocity component in launch tangent axis
Z	Z position in launch tangent coordinates
Z	Z- transform
Zd	Sink rate
Zdot	Sink rate
Z_{LT}	Z position in launch tangent coordinates
$\int \alpha$	Integral alpha

1.0 Introduction

The Personnel Launch System (PLS) Autoland Development study has been performed as Task Assignment 8 under NASA contract No. NAS1-18762, "Aircraft and Spacecraft Guidance and Control Technology". This work was a follow-on effort to that reported in reference 7.

1.1 Background

A recent NASA effort to provide an Assured Crew Return Capability (ACRC) for the Space Station Freedom has resulted in the proposal of several concepts, one of which is the Personnel Launch System (PLS) vehicle designed by NASA Langley Research Center.

The PLS vehicle is to be used to carry up to 10 astronauts to and from the Space Station. A requirement for such a vehicle is the capability to perform the entire flight automatically, from deorbit burn through reentry to landing. This will provide increased reliability and allow for safe return of crews that are either pilotless or in which the pilot-qualified crew members are incapacitated. In addition, the vehicle must be a fully or partially reusable, and it must provide for emergency crew escape from the Space Station and return to Earth and land on a prescribed runway without subjecting the passengers to detrimental accelerations.

The purpose of this task is to develop a practical autoland guidance and control system for the PLS vehicle. The autoland system is to be capable of both automatic and manual control. This task focuses on the automatic control system and covers two major automatic flight phases: the Terminal Area Energy Management (TAEM) phase, and the Approach and Landing (A/L) or autoland phase.

The purpose of the TAEM phase is to transit the vehicle from the high energy state at the end of the atmospheric re-entry phase, to the initiation of the approach and landing phase with sufficient total energy for a safe landing. The A/L phase initiates at the beginning of the turn onto the runway centerline and ends at touchdown.

The aerodynamic data and vehicle mass properties for the 10 man PLS vehicle were provided by NASA Langley Research Center. The aerodynamic data was obtained at Mach

0.08 and 0.6, at various angles of attack, sideslip angles and different control surface positions.

The mission requirements and limits are summarized in Table 1-1. These requirements are not fixed "hard" requirements, but are intended to serve as a general guideline during this preliminary development of the PLS autoland system. For example, the requirement that the sink rate be less than 2 feet per second at touchdown is severe and may be relaxed, given that the landing gear used on the Shuttle allow sink rates in excess of 4 fps.

The purpose of this study was to develop a control system with the capability of meeting requirements, especially tracking the trajectory in the presence of wind turbulence and wind shear with both head and side wind conditions. The study also specified that the autoland design be verified using a non-linear 6-DOF flight simulation.

1.2 Technical Approach

The PLS vehicle was geometrically scaled up in size from CERV (Crew Emergency Rescue Vehicle). As a result, the work performed in developing the CERV autoland system (as reported in reference 7), was used as a starting point in the design of the PLS autoland system.

The PLS autoland development study focused on developing the guidance and control system for performing an automatic landing at a prescribed runway. The study consisted of the following five prescribed tasks:

1) Develop TAEM and A/L trajectory profile and algorithms;
2) Design a multi-input, multi-output (MIMO) system control law;
3) Develop a non-linear simulation;
4) Determine autoland guidance and control system feasibility ;
5) Perform parameter sensitivity studies to evaluate the effect of varying mission parameters on vehicle flight performance.

General Mission Requirements	
Requirement	**Definition/Comment**
$\Delta nz \leq 0.6$ g	normal acceleration limit
$\Delta ny \leq 0.1$ g	lateral acceleration limit
$Qmax \leq 450$ psf	maximum dynamic pressure
δsb-bias=20º	speedbrake bias setting during steep glideslope

Touchdown Requirements	
Requirement	**Definition/Comment**
$\alpha \leq 15.0$º	angle-of-attack limit (18º hard limit w/ wind)
η crab ≤ 5.0º	runway heading alignment for decrab maneuver
$KEAS \geq 200$ knots	velocity - knots of equivalent airspeed
nominal Zdot= 2.0 fps with 1σ = 1fps	sink rate
$\Delta Y = \pm 25$ ft	allowable lateral error at touchdown
aimpoint=2000 ft	delta-X aimpoint from the end of the runway

Table 1-1 PLS General Mission Requirements/Guideline

Our technical approach consisted of developing a MIMO autoland system including pitch, yaw, and roll autopilots, lateral steering, altitude and speed controller. The autopilots were designed using the integral-LQR control technique. The integral-LQR technique consists of using state weighting for transmission zero placement which allows direct design in the frequency domain. The resulting design, by using high gain on the integral control offers excellent low frequency characteristics with robustness to parameter biases. The control weighting is based on decoupling the control surface effectors. The design process uses a discrete LQR design technique with computational delay compensation. Details of the design synthesis are contained in section 3.0 .

The resulting MIMO autoland system was verified using a non-linear 6 DOF simulation. A block diagram for the simulation is shown in figure 1-1. The CERV 6- DOF simulation developed under the previous NASA task (reference 7) was used as a basis for developing the PLS 6 DOF simulation. PLS vehicle characteristics, aerodynamic model and the digital control system were incorporated into this simulation.

The stability, control, and performance of the PLS vehicle was verified using this 6 DOF simulation. In addition, mission performance was verified for various wind conditions including wind shear, wind gusts, and wind turbulence. The 6 DOF simulation was also used for parameter sensitivity studies, varying glideslope angles, initial velocity, guidance parameters, final flare altitude and speedbrake settings. Details of the simulation analysis are described in section 4.0 and 6.0.

The A/L and TAEM autoland phases were developed separately, and therefore are presented separately in sections 3.0 and 5.0 respectively. Section 2.0 describes the overall mission, vehicle characteristics and the control techniques.. The A/L system is presented first, followed by the TAEM system.

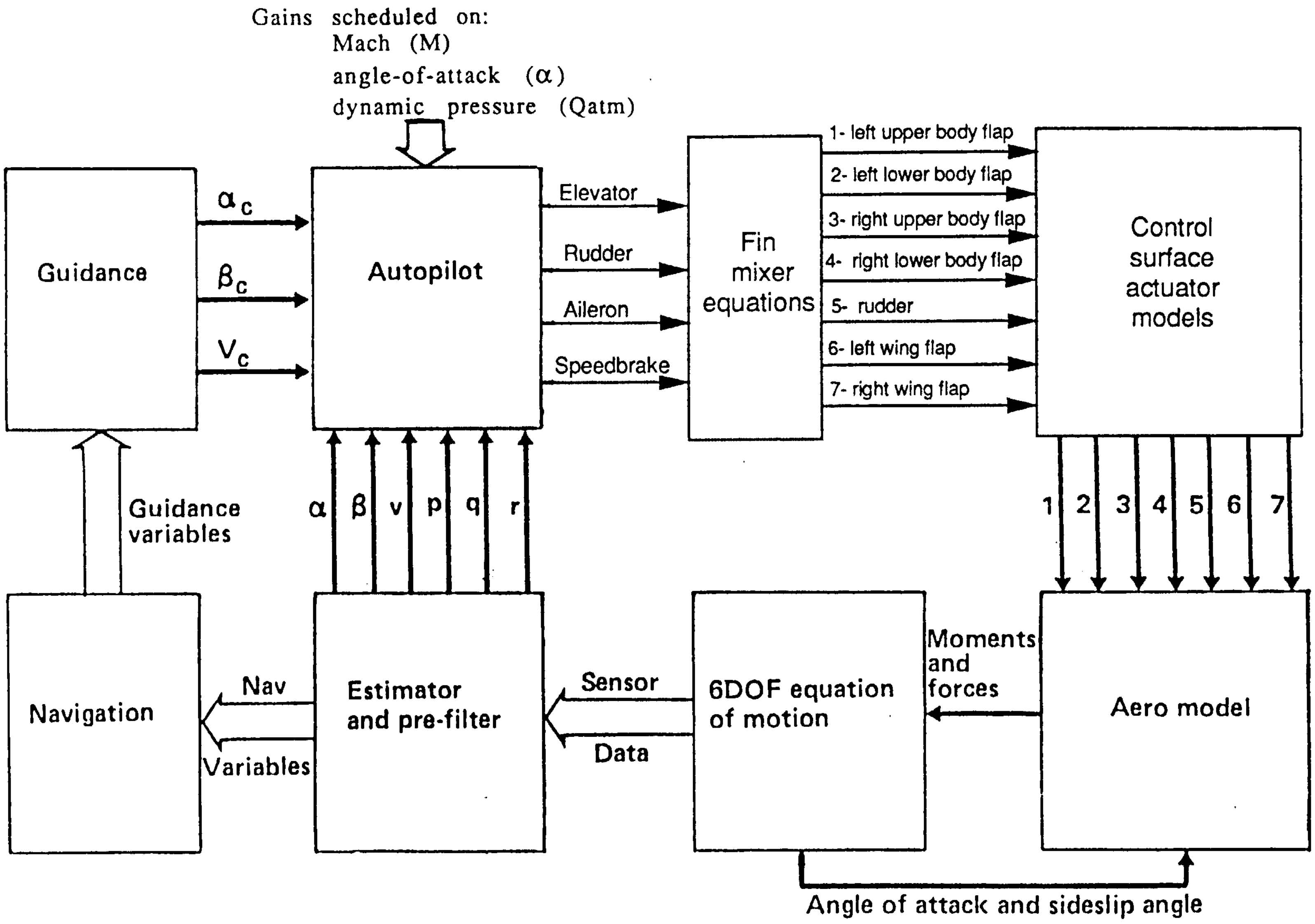

Figure 1-1 Simulation Block Diagram

1.3 Summary of Results

An autoland system for the PLS vehicle has been developed for the approach and landing (A/L) phase, and the Terminal Area Energy Management (TAEM) phase. The feasibility of the design of the autoland system has been demonstrated through simulation.

The baseline control consists of using the Integral-LQR autopilot design with classical guidance laws. An overall block diagram is shown in figure 1.-2. Landing reference information for the guidance and control is received either from a microwave landing system, the global-positioning system (GPS), or both, supplemented with inertial reference data. The guidance, navigation and control will use a common set of strap-down sensors. The guidance forms angle-of-attack and bank angle commands for the autopilot. The modern control autopilot together with fin mixer equations, form the control surface actuator commands. The design is an all digital design; sample times and computational delays selected are shown in figure 1-2. Details of the autoland system are described in section 2.0 .

A straight-in trajectory profile was developed for the approach and landing phase. The trajectory is shown in figure 1-3 and consists of a "double flare" landing profile similar to the Shuttle's landing profile. A unique feature of the profile is the pre-flare maneuver which is used to decrease the sink rate, modulate the airspeed and reduce the flight path angle from a steep glideslope to a shallow glideslope. The double flare landing profile is preferred by astronauts/pilots because it presents a less threatening ground approach when compared to the single parabolic profile. Starting at the end of the steep glideslope, there is approximately 15 seconds to touchdown during which the vehicle descends from 300 feet along a flight path angle of -2.5º. The excellent touchdown performance obtained using the double flare profile is graphically summarized in figure 1-4. The sink rate, altitude profile and flight path angle and angle-of-attack during the final approach and final flare are plotted in figure 1-4 . This data was obtained from a 6-DOF simulation of a nominal A/L mission without wind. The sink rate quickly dissipates during the final flare, without commanding large angle-of-attack.

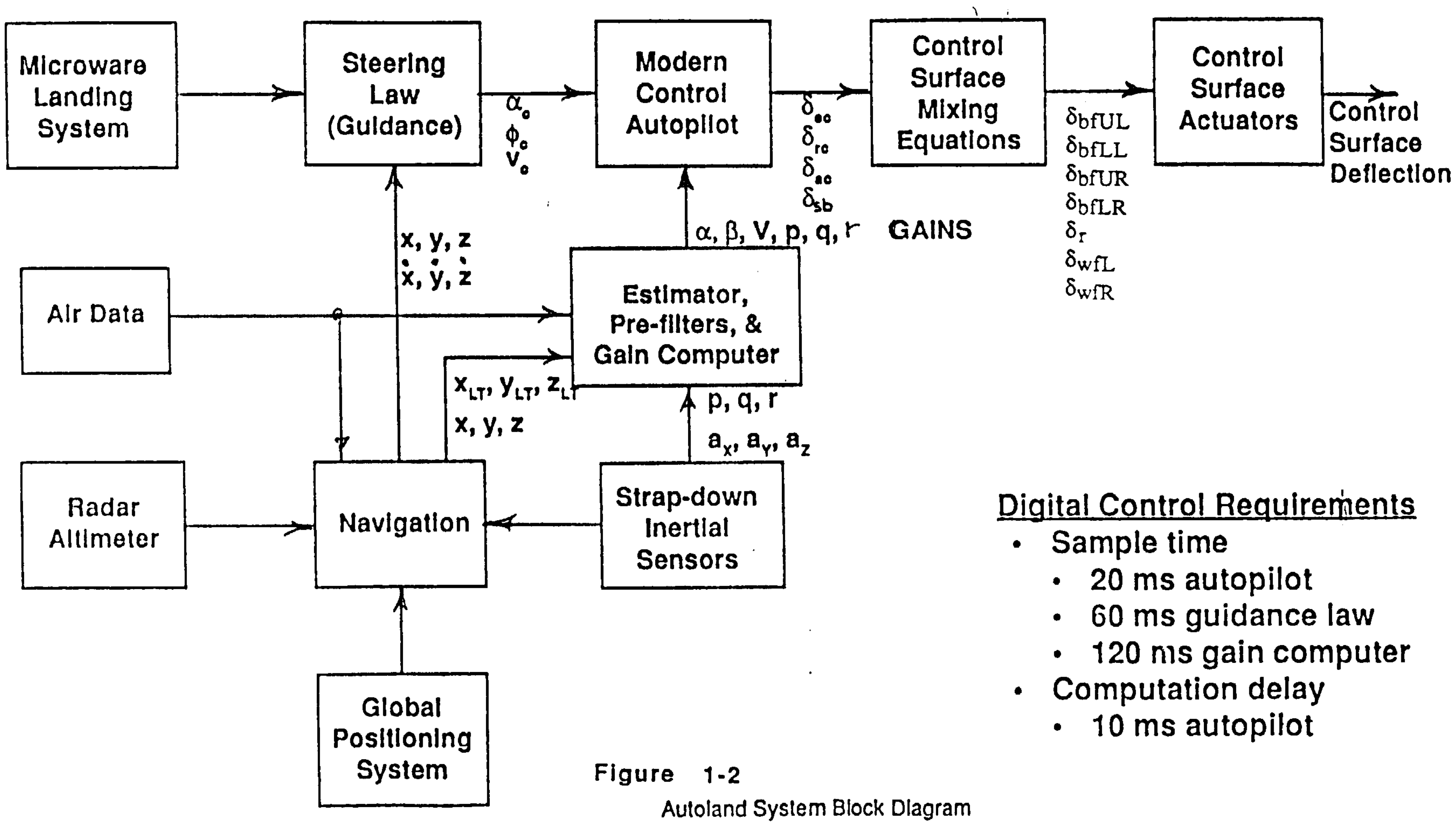

Figure 1-2
Autoland System Block Diagram

Digital Control Requirements

- Sample time
    - 20 ms autopilot
    - 60 ms guidance law
    - 120 ms gain computer
- Computation delay
    - 10 ms autopilot

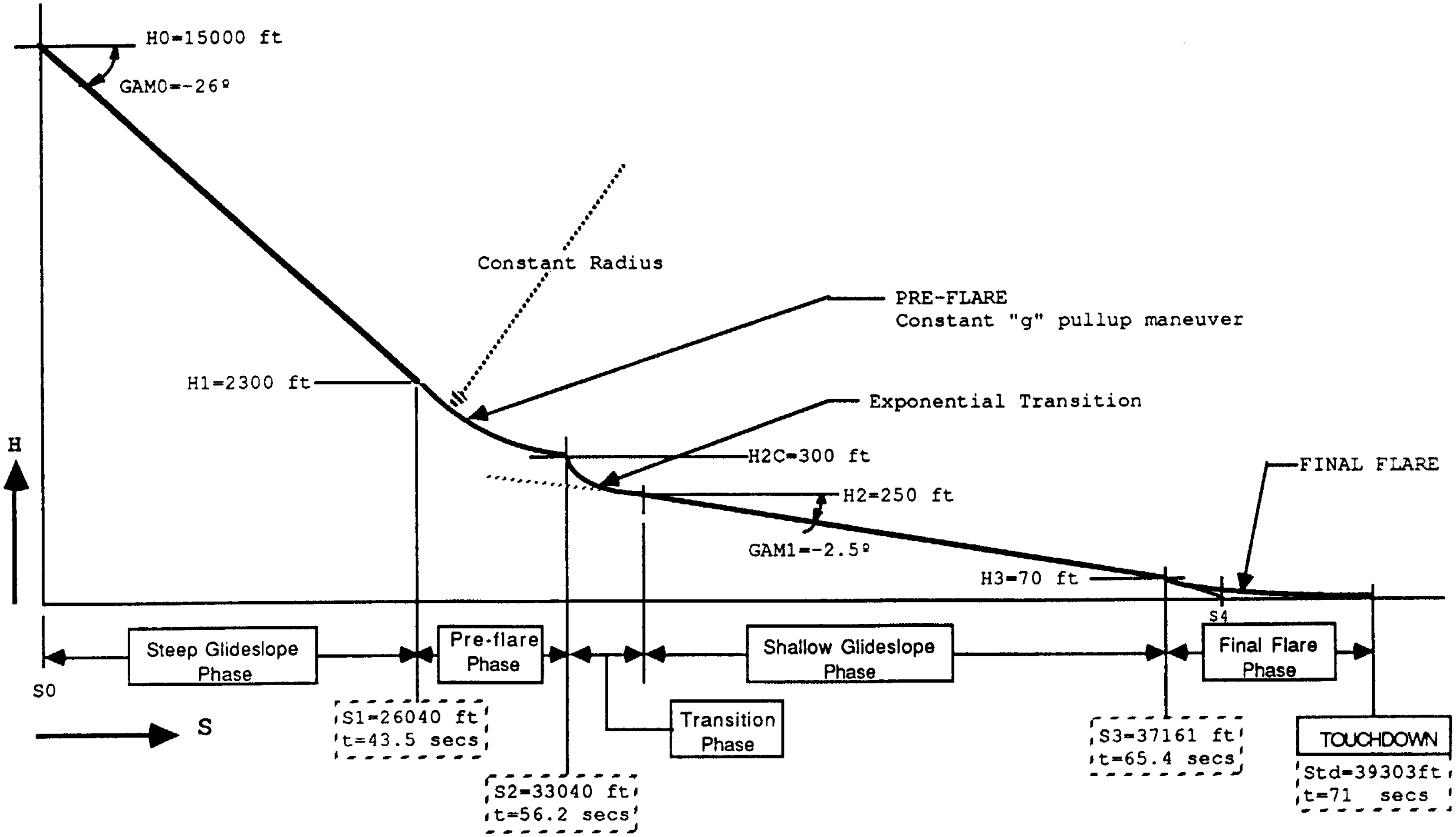

Figure 1-3 Summary of PLS Straight-In Trajectory Profile

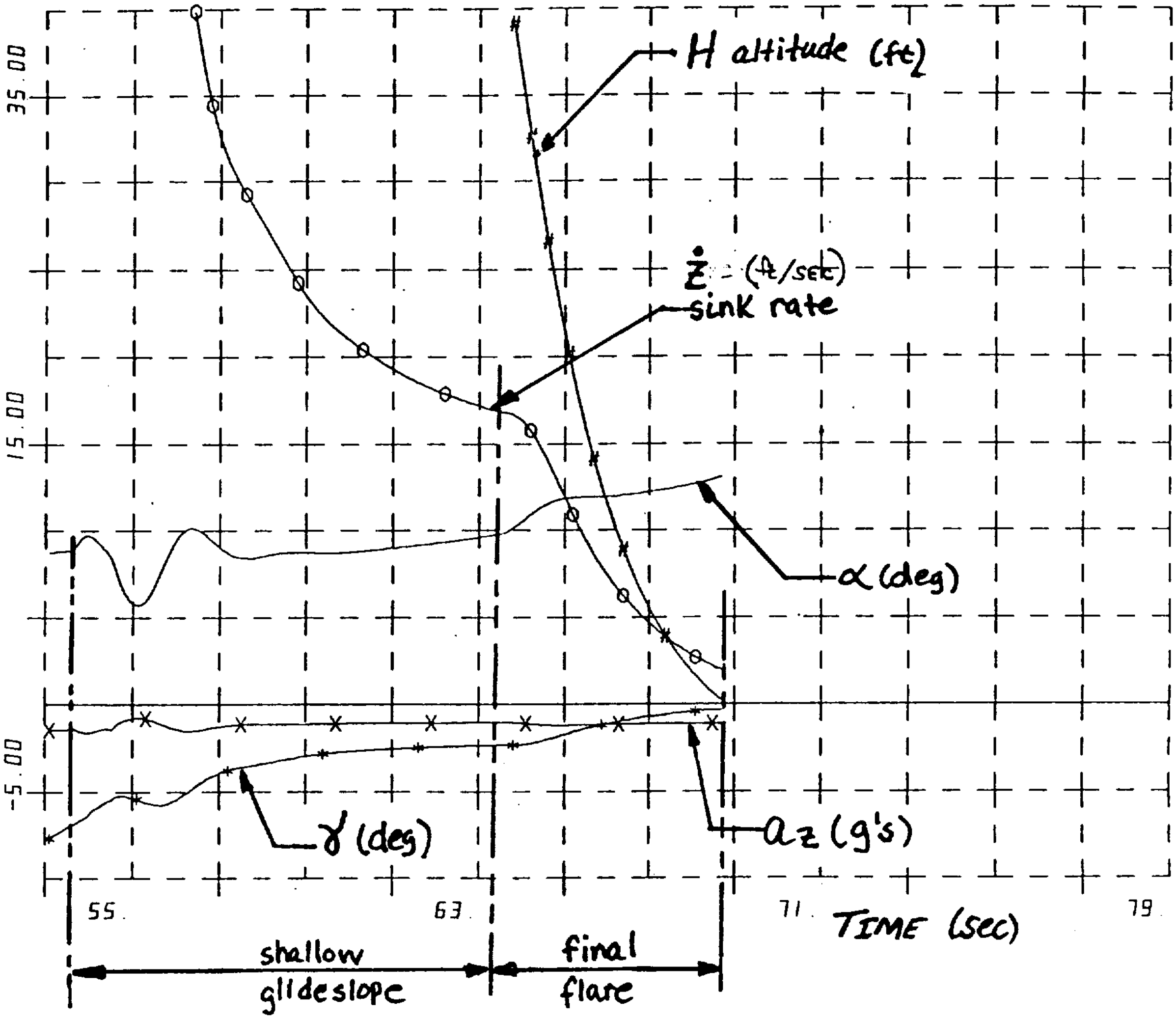

Figure 1-4 **Summary of A/L Nominal Touchdown Profile**

The PLS vehicle control configuration and autoland system meets the accuracy requirements and desired stability in the presence of wind disturbance. A summary of the results in shown in figure 1-5. The touchdown performance with wind turbulence was evaluated at five different wind conditions; the results are excellent with all requirements being met.

A TAEM trajectory was developed using a Heading Alignment Cone (HAC) spiral profile similar to the Shuttle's TAEM system. The TAEM guidance and control system was adapted from the A/L system. This was done to maintain a consistent set of guidance and control algorithms and hardware, and to improve transition from the TAEM phase to the A/L phase.

The TAEM trajectory profile developed for this study is shown in figure 1-6. The study focused on using a Heading Alignment Cone (HAC). The TAEM spiral HAC trajectory algorithms were generated to follow a constantly decreasing turn radius and velocity while maintaining a constant bank angle. A 6-DOF simulation was developed to evaluate the TAEM performance. The TAEM simulation results with wind turbulence are summarized in figure 1-7. These results indicated acceptable TAEM performance.

	Sink Rate (fps)	KEAS (knots)	Qatmos (psf)	alpha (deg)	crab angle (deg)	ΔX (feet)	ΔY (feet)
Design Goal/ Requirement	≤2.0	≥200	- -	≤18	- -	- -	+ - 25
Nominal A/L No wind	1.98	208	147	13.5	≈ 0	≈ 0	≈ 0
Wind Turbulence 1-sigma=5 knots	1.80	180	117	17.0	≈ 0	116	≈ 0
Decreasing Head Wind Shear (head wind=30 knots)	1.90	180	110	18.0	≈ 0	206	≈0
Side Wind Shear Cross wind=22 knots	2.0	211	152	13.0	6.2*	5.0	8.0

* decrab maneuver not performed

Figure 1-5 Summary of PLS Touchdown Accuracy

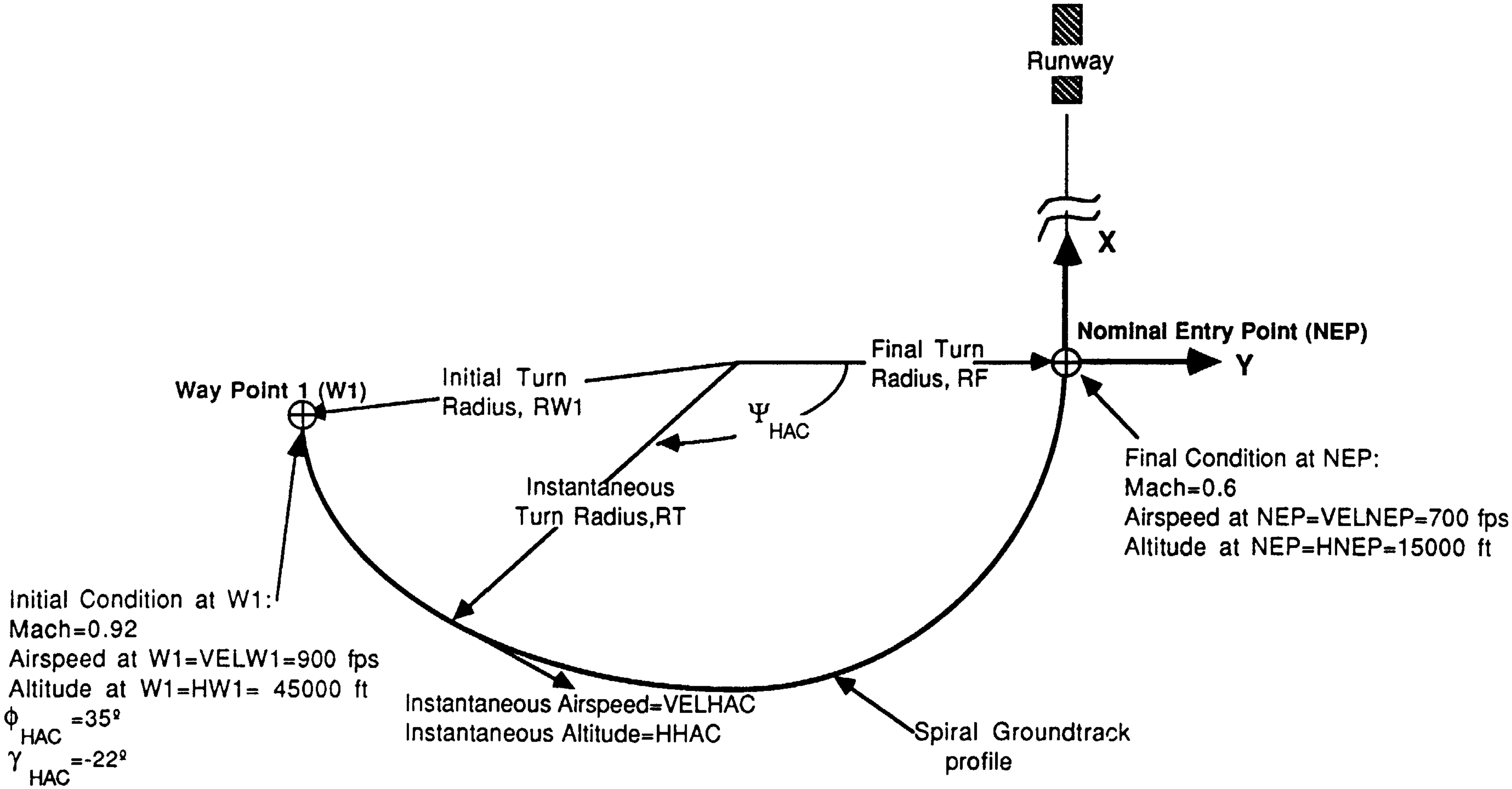

Figure 1-6 Summary of TAEM Trajectory Profile

TAEM Wind Input	Value	Description
$\sigma_X = \sigma_Y = \sigma_Z$	17.3 ft/sec	wind stnd deviation
$L_X = L_Y = L_Z$	1753 ft	integral scale factor

TAEM End Condition	Nominal	Wind Turbulence	Description
ΔX err	33 ft	66 ft	along track error
ΔY err	-26 ft	-25 ft	cross track error
H	14620 ft	14612 ft	altitude
η	$\approx 0.^\circ$	$\approx 0.^\circ$	heading angle

Figure 1-7 Summary of TAEM End Conditions With Wind Turbulence

2.0 PLS System Description

The following section describes the PLS autoland mission and the control configuration and techniques used for the PLS autoland operation.

2.1 PLS TAEM and Autoland Mission

The PLS mission is to return astronauts from low Earth orbit to Earth, landing at a prescribed runway. The mission consists of de-orbit, re-entry, terminal area energy management (TAEM), and finally approach and landing (A/L) on the runway. Only the TAEM and the A/L phases of the PLS mission are considered in this study.

The TAEM trajectory was developed specifically for the PLS vehicle, based on the Shuttle's TAEM system. The TAEM flight phases are shown in figure 2-1 . The TAEM mission initiates TAEM acquisition after re-entry at approximately 82000 feet and Mach 2.5. This phase is performed to acquire a heading which is tangent to the heading alignment cone. The heading alignment phase is initiated at approximately 45000 feet and Mach 0.95 and performs a constant bank angle maneuver to fly the vehicle around an imaginary inverted cone called the Heading Alignment Cone (HAC), until the vehicle is aligned with the runway centerline at approximately 15000 ft and Mach 0.6 . At this point the A/L trajectory is captured.

The A/L trajectory was developed for the PLS vehicle, based on the Shuttle's A/L trajectory. The A/L flight profile is shown in figure 2-2. The A/L trajectory starts at an altitude of approximately 15000 feet and Mach 0.6, with an initial steep glideslope. A constant "g" pullup maneuver is performed at an altitude of approximately 2300 feet to decrease the sink rate and to capture the final shallow glideslope. The constant "g" pullup maneuver is a preflare maneuver that results in a less threatening ground approach compared with the standard single parabolic flare maneuver. At approximately 70 foot altitude, a final flare maneuver is performed to bring the vehicle down to a nominal touchdown at 200 knots of equivalent airspeed and a sink rate less than 2 fps.

- **Terminal Area Energy Management (TAEM) Phases:**
  1) **Acquisition**
  2) **Heading alignment**
  3) **Pre-final approach and trajectory capture (TAEM-A/L switching)**

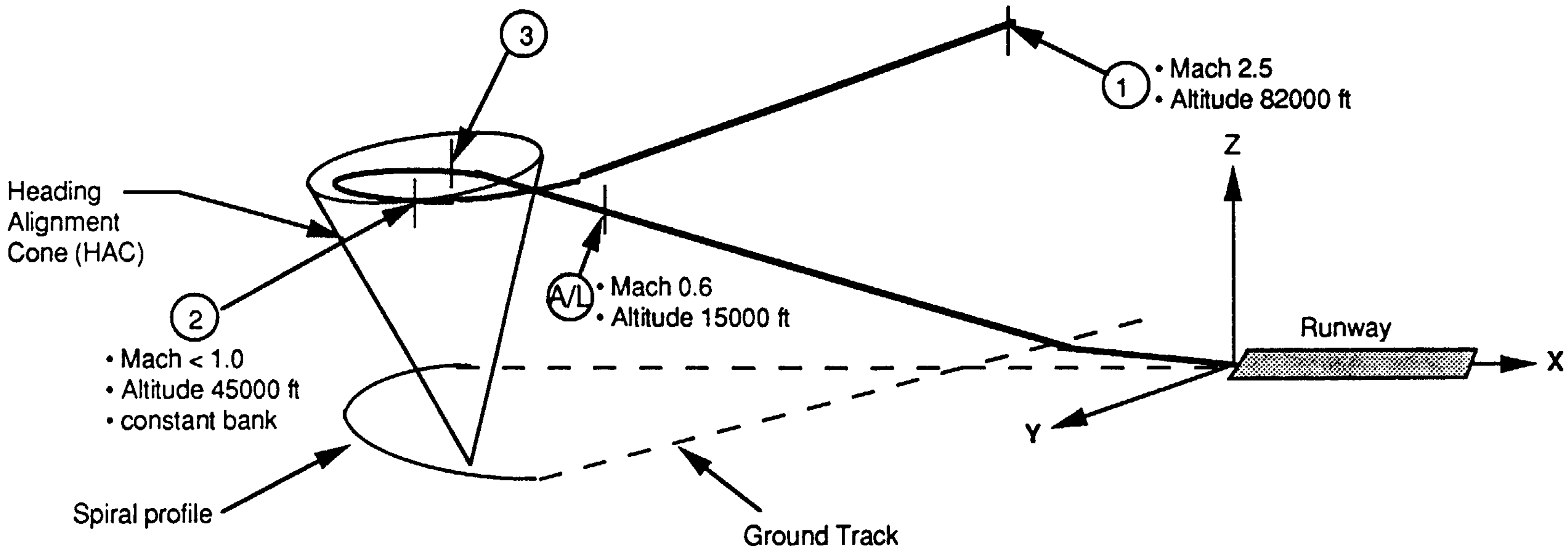

Figure 2-1 TAEM Guidance Phases

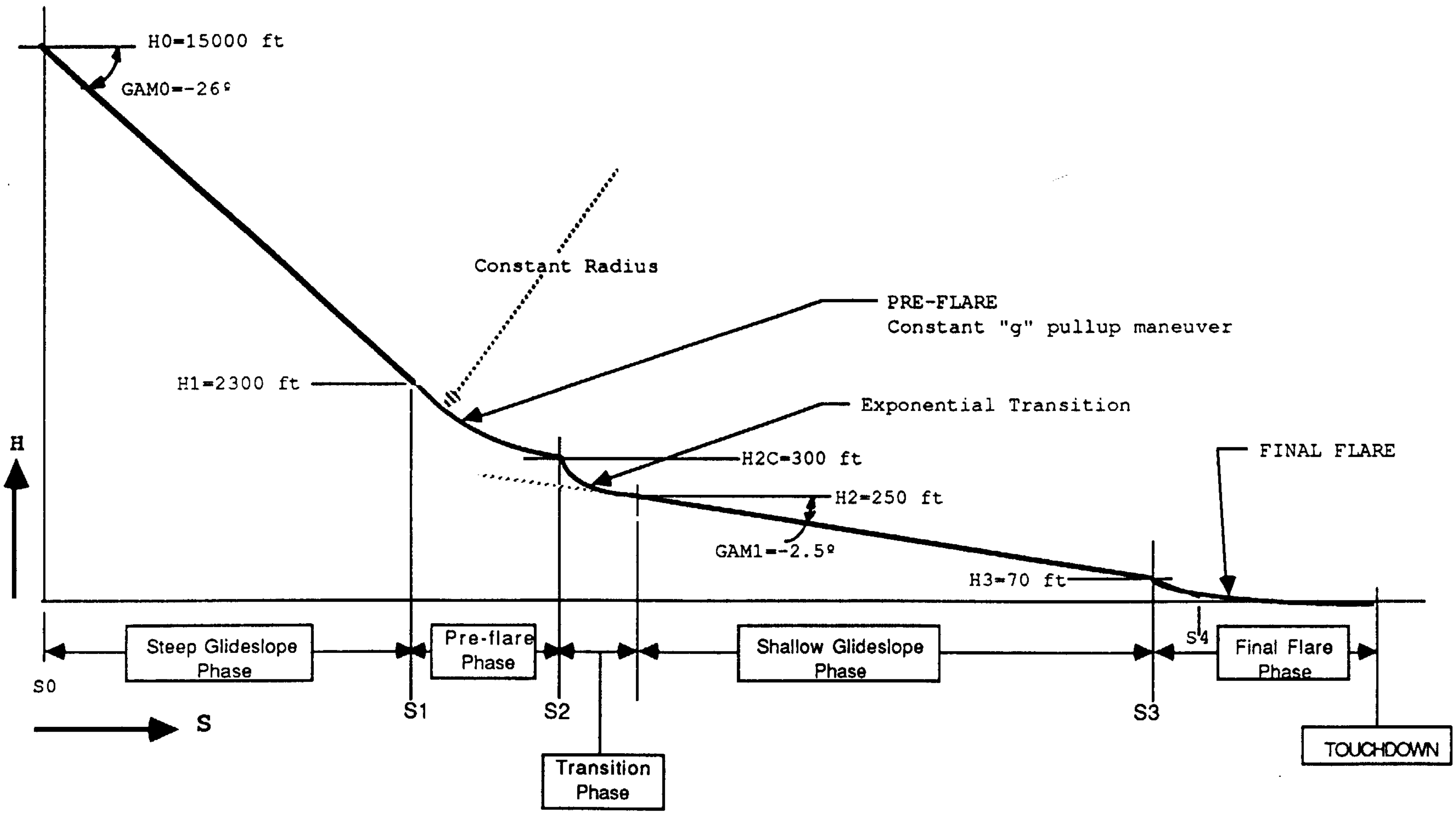

Figure 2-2 PLS Approach and Landing Trajectory Phases

2.2 PLS Vehicle Configuration

The PLS configuration is a relatively low lift-to-drag (max L/D is 3.2 with gear up) lifting body configured to perform autoland on one of several commercial landing facilities. Figure 2.-3 shows a drawing of the configuration. This configuration is similar to the CERV vehicle (see reference 7), but reflects a 15% geometric scaling up of the CERV vehicle for increased payload and more passengers. Included in figure 2-3 is a summary of the vehicle mass properties, comparing PLS mass properties to CERV mass properties.

For control, the vehicle has seven control surfaces as shown in figure 2-4, including 4 body flaps, 2 wing elevons, and an all-moveable tail for rudder control. The surface mixer equations are included in this figure, showing the usage of control surfaces for vehicle control. Pitch control can be achieved using either the body flaps or wing elevons. Our baseline approach is to use the wing elevons for pitch control and reserve the body flaps for roll control and drag modulation. Yaw control is achieved using the rudder. Roll control can be achieved using differential body flaps and/or differential wing flaps. However, the usage of differential wing flaps for roll control causes large yawing moments due to the large wing dihedral. This in turn requires a larger rudder to trim the induced yawing moments. This configuration also results in additional drag. Therefore, differential body flaps were chosen to control roll.

2.3 Functional Description of Control System

The proposed autoland system is an all digital control system consisting of sensors, flight processor, interfaces and control surface actuators. The algorithms associated with navigation, guidance, and control are contained within the flight processor. A functional block diagram for the system is shown in figure 2-5. Navigation uses velocity and altitude information from strap-down inertial sensors augmented with altitude information from a radar altimeter and inertial measurement updates based on Global Positioning System (GPS) data. Vehicle information with respect to the runway is received from the Microwave Landing System (MLS). An alternate would be to use GPS data instead of MLS data, with a data load for runway altitude and location.

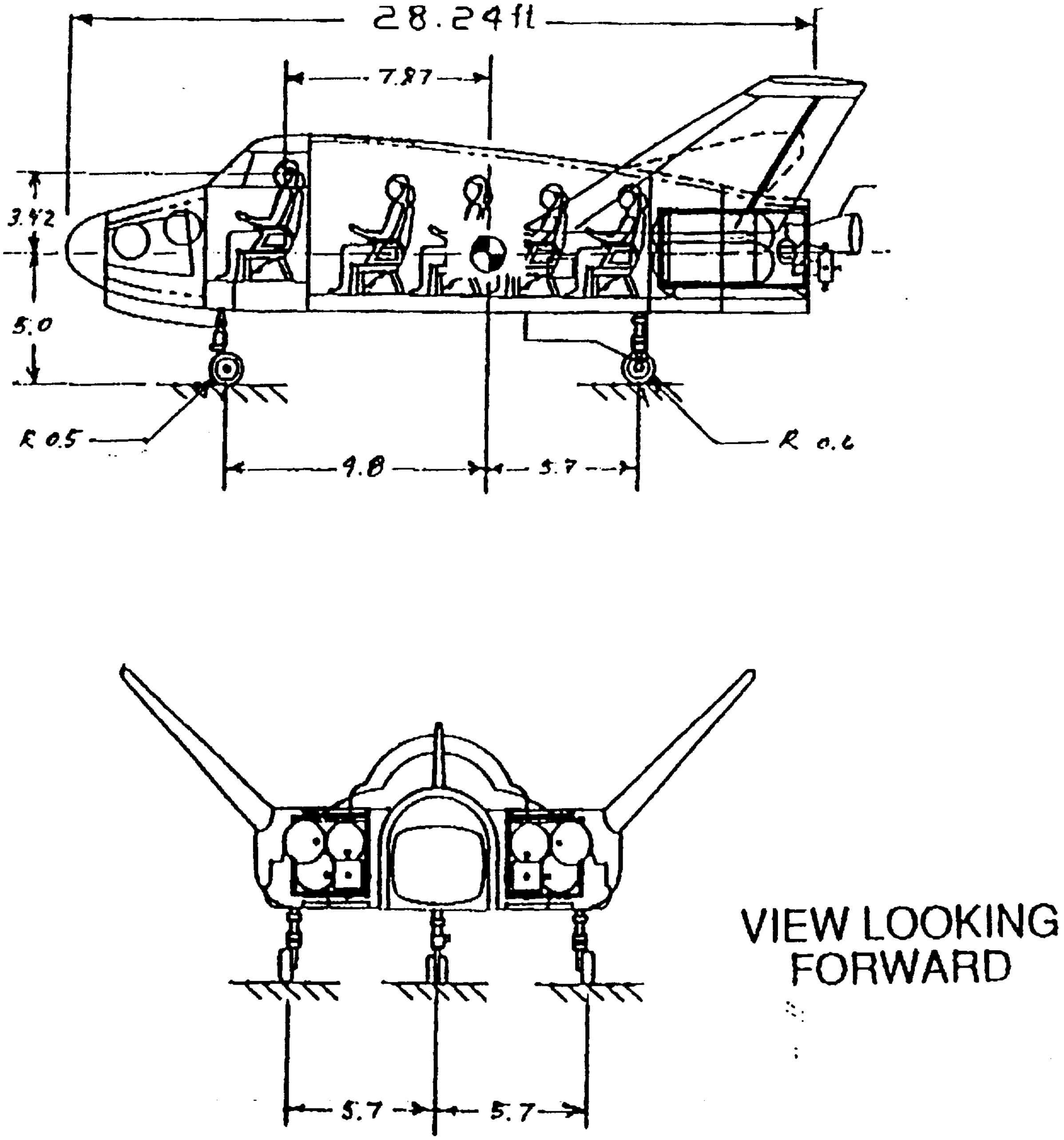

MASS PROPERTIES:

	PLS	CERV
Crew Size	10	8
Weight (lbs)	19,100	11,193
Xcg (%)	55.5%	54%
Ixx (slug-ft2)	7512	6345
Iyy (slug-ft2)	33594	13994
Izz (slug-ft2)	35644	17123
Lref (ft)	28.24	24.583
Aref(ft2)	286.45	215.61
Span (ft)	13.89	12.132

Figure 2-3 PLS Vehicle Configuration and Mass Properties

PLS Vehicle Control Surface Sign Conventions

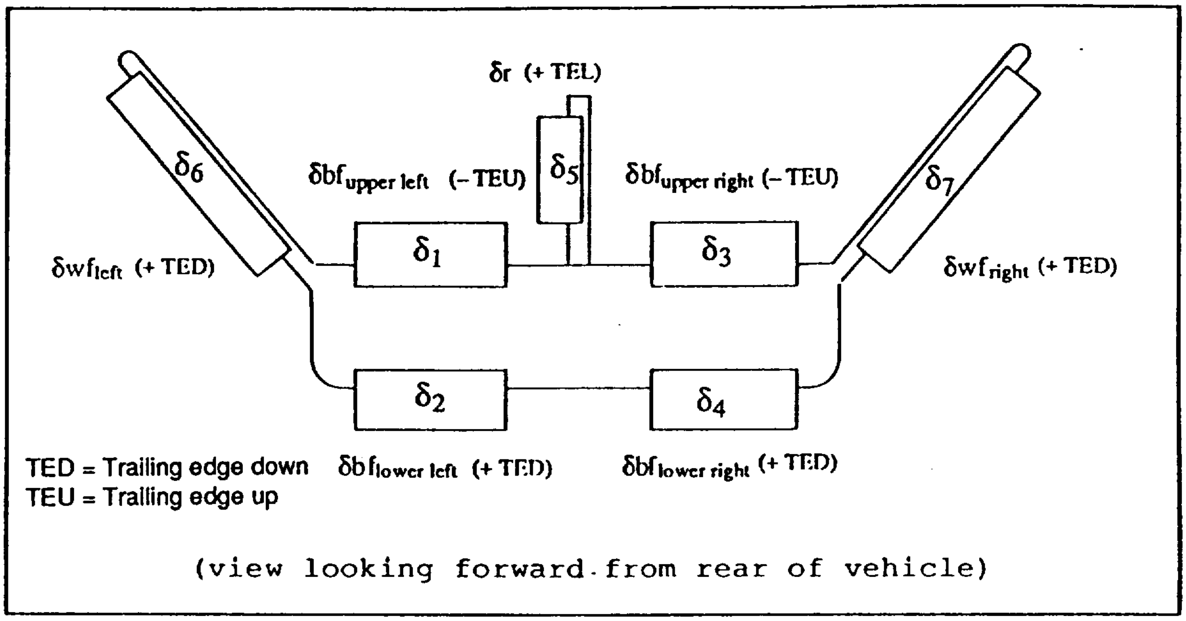

(view looking forward from rear of vehicle)

Control Surface Input Mixing Equations

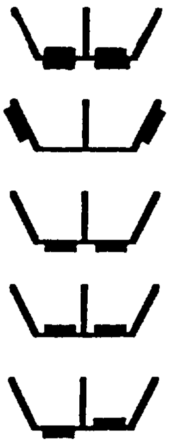

$$\delta_{sb} = \delta_{f+} + \delta_{f-} = \frac{\delta_2 + \delta_4 + \delta_1 + \delta_3}{2}$$

$$\delta_e = \frac{\delta wf_{\text{left}} + \delta wf_{\text{right}}}{2} = \frac{\delta_6 + \delta_7}{2}$$

$$\delta f^+ = \frac{\delta bf_{\text{lower left}} + \delta bf_{\text{lower right}}}{2} = \frac{\delta_2 + \delta_4}{2}$$

$$\delta f^- = \frac{\delta bf_{\text{upper left}} + \delta bf_{\text{upper right}}}{2} = \frac{\delta_1 + \delta_3}{2}$$

$$\delta_a = \frac{\delta bf_{\text{upper left}} + \delta bf_{\text{lower left}} - \delta bf_{\text{upper right}} - \delta bf_{\text{lower right}}}{2}$$

$$= \frac{\delta_1 + \delta_2 - \delta_3 - \delta_4}{2}$$

Figure 2-4 **PLS Vehicle Control Surface and Mixing Equations**

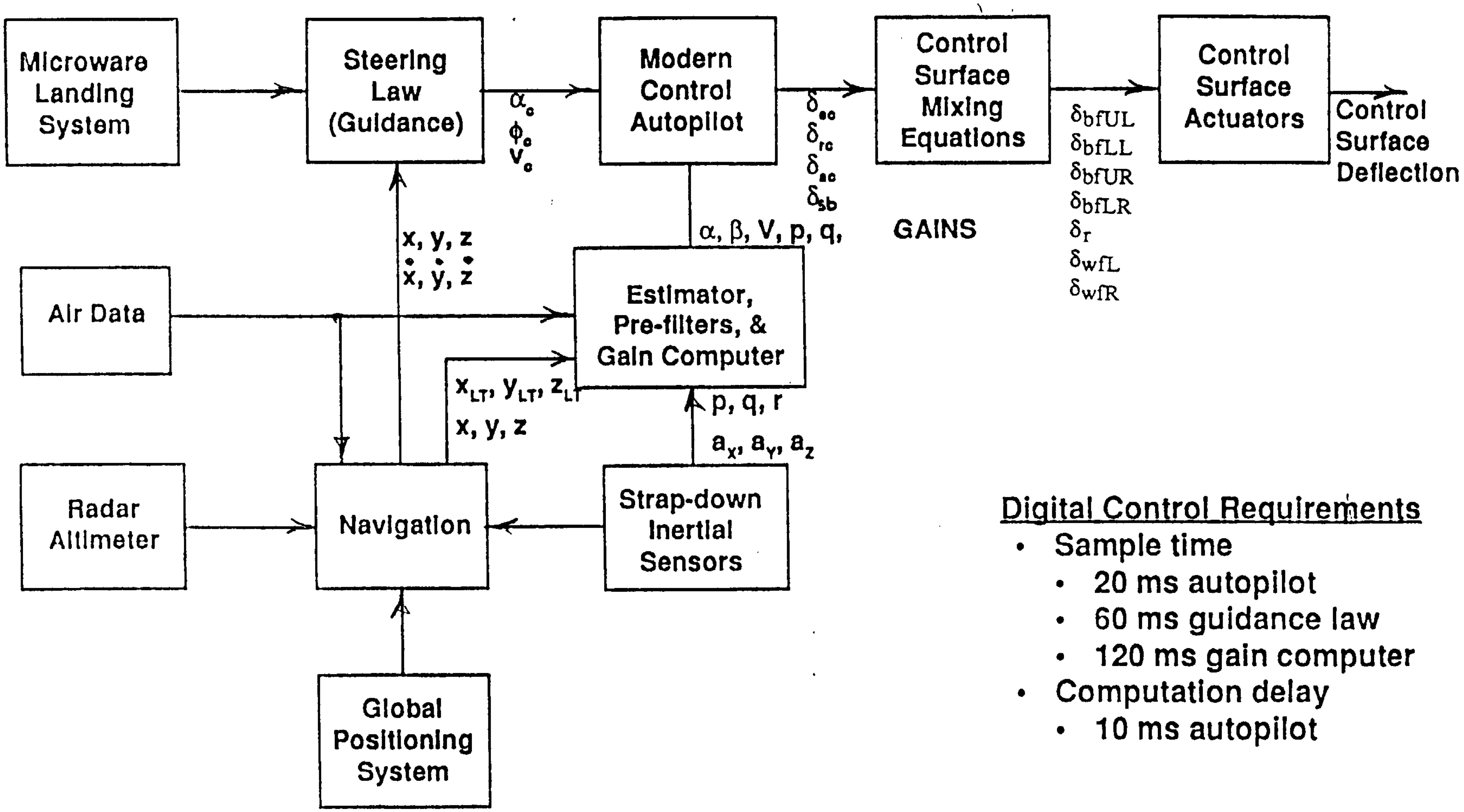

Digital Control Requirements
- Sample time
  - 20 ms autopilot
  - 60 ms guidance law
  - 120 ms gain computer
- Computation delay
  - 10 ms autopilot

Figure 2-5 Autoland System Block Diagram

A block diagram for the guidance law is shown in figure 2-6. The longitudinal guidance is an altitude/altitude-rate system using feedback information from the Microwave Landing System and augmented with navigation information. Output of the longitudinal guidance is angle-of-attack command for the pitch autopilot. An angle-of-attack command limit is included along with an angle-of-attack trim function based on level flight.

The lateral guidance is a cross track/cross track rate system using information derived from the Microwave Landing System. The output of the lateral guidance is bank angle command.

An integral-plus-proportional inertial velocity control loop is also included. Inertial velocity feedback information is derived from the navigation system. The speed loop commands all four body flaps, splitting them to produce a drag force with a small resulting pitching moment depending on the vehicle angle of attack. The pitching moment is trimmed by wing elevons. The nominal setting selected was 20º during the steep descent to account for head winds.

A block diagram of the autopilots is shown in figure 2-7. The design was developed using the integral-LQR technique. The pitch autopilot is an angle-of-attack autopilot with integral control and pitch rate damping. Elevator command feedback (δEC) is used to compensate for the computer computational delay. The yaw/roll autopilot is a coupled design controlling bank angle. Other feedback variables are sideslip angle, yaw rate, bank angle, and roll rate. Rudder command feedback (δRC) and aileron command feedback (δAC) are also used to compensate for the computer computational delays. A control surface mixer is included to change the elevator, speedbrake, and aileron commands to individual surface commands. Elevator, speedbrake, rudder, and aileron command limiters are also included. A block diagram of the control surface mixer is shown in figure 2-8

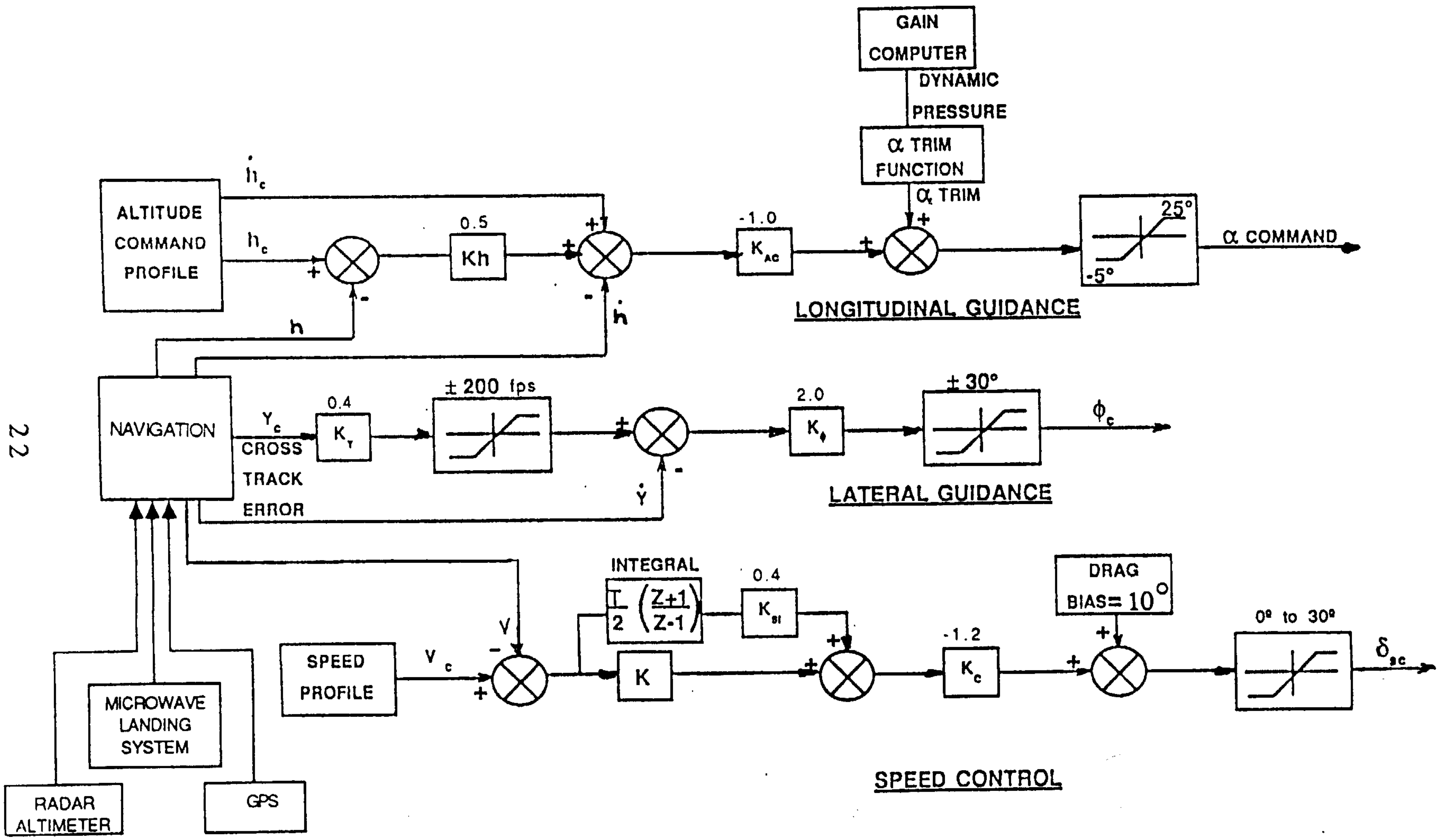

Figure 2-6 Autoland Guidance (Steering Laws)

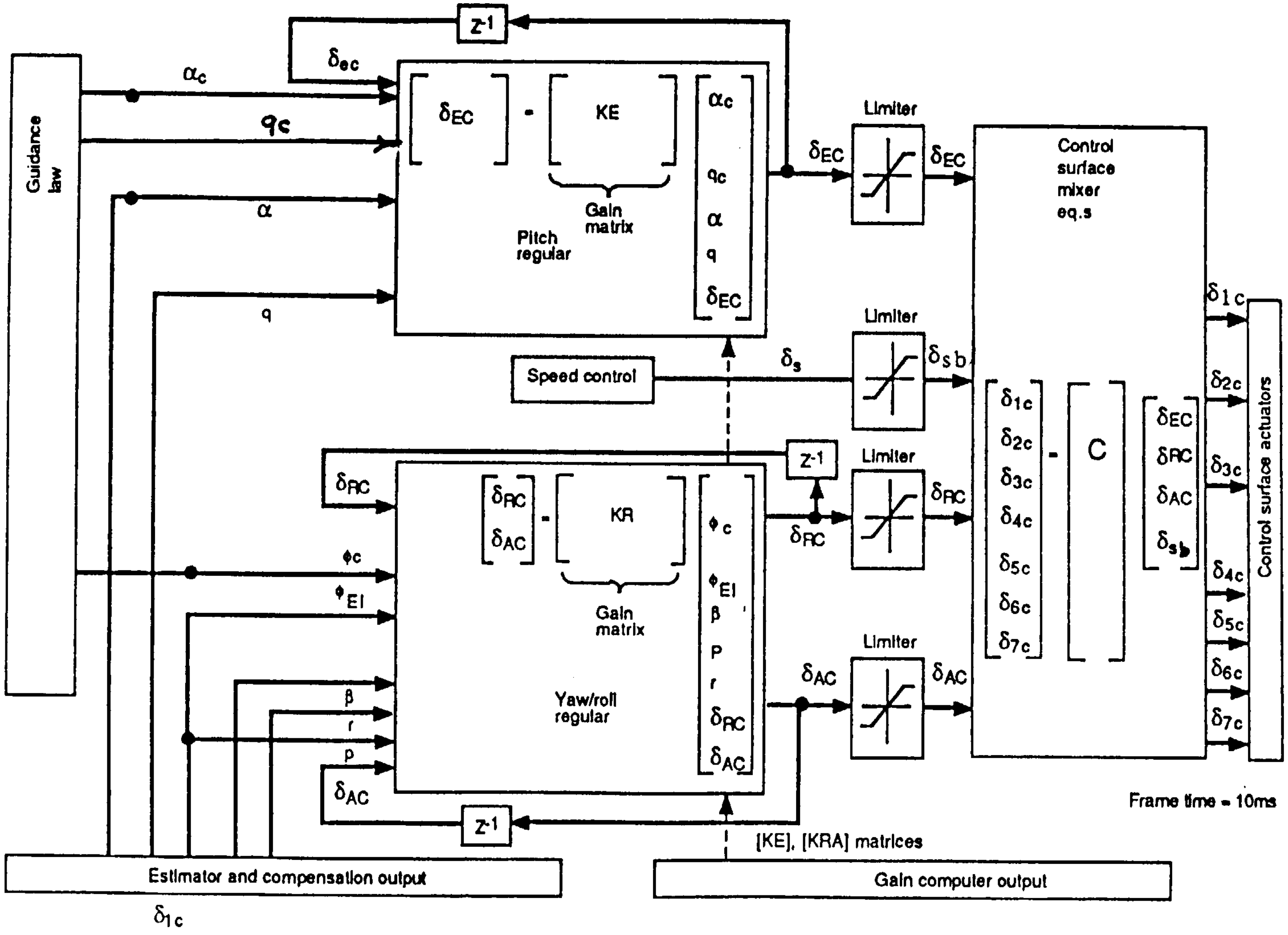

Figure 2-7 Block Diagram of Pitch and Yaw/Roll Autopilots

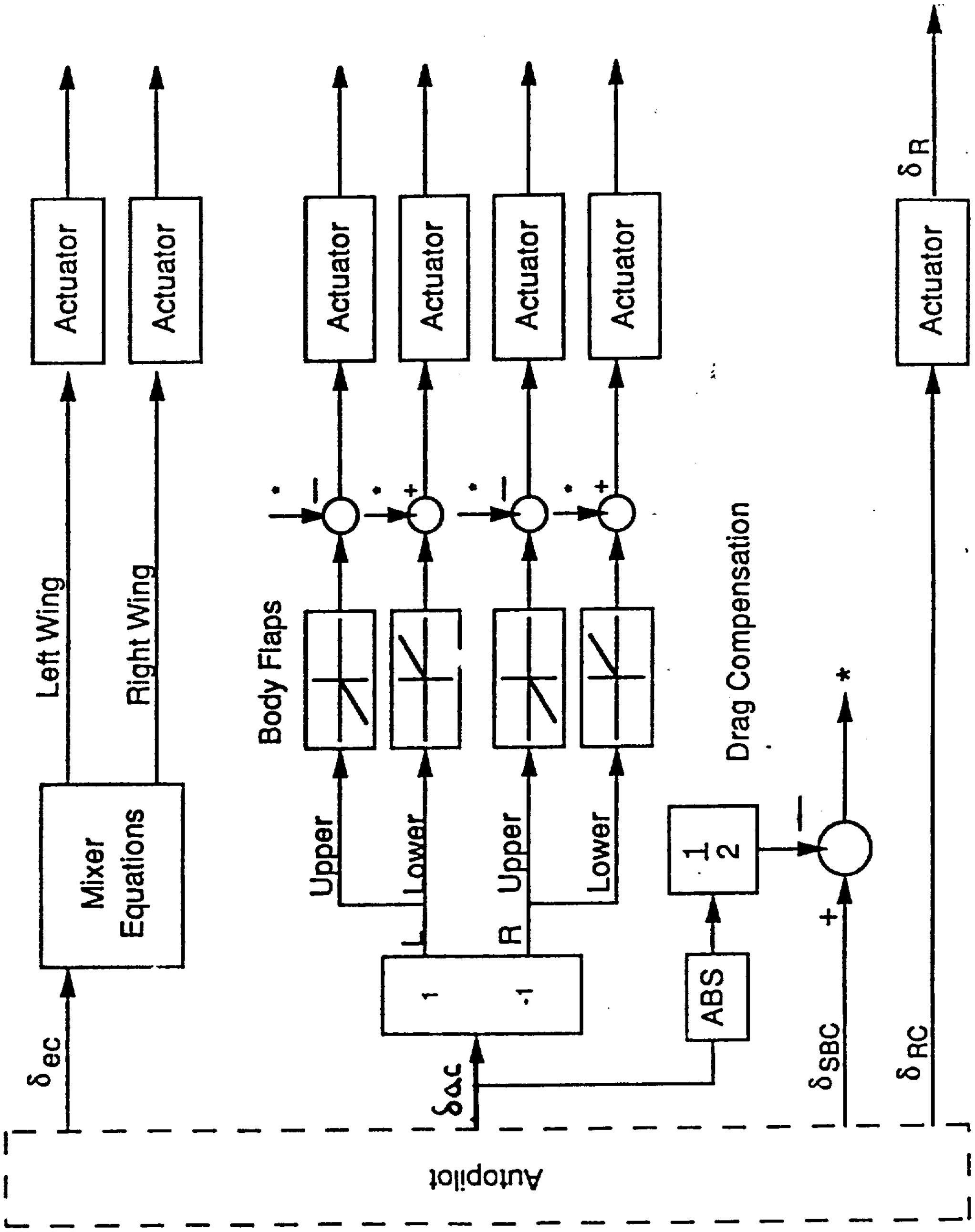

Figure 2-8 Control Surface Mixer Equations

3.0 Approach and Landing Design Synthesis

This section discusses the design synthesis for the A/L autopilot, guidance and speed controller. The designs are not optimum, but are adequate to conduct studies and to assess the PLS autoland system.

3.1 Autopilot Design

Linear models were constructed from the aerodynamic derivative data at various trim conditions. During approach and landing, the dynamic pressure (Qpres) varies from approximately 300 psf at 15,000 feet and Mach 0.6, to nominally 135 psf at sea level (200 knots). The design points were chosen at two phases of the flight: first, with speedbrake setting at 20º during high speed steep glideslope descent, and second, with speedbrake setting at 0º during lower speed descent. The autopilot gains were designed at the following four trim conditions:

Condition 1: Q=300 psf, Mach 0.6 $\alpha = 8^{\circ}$; Speedbrake=20º
Condition 2: Q=270 psf, Mach 0.47 $\alpha = 5^{\circ}$; Speedbrake=20º
Condition 3: Q=220 psf, Mach 0.41 $\alpha = 12^{\circ}$; Speedbrake=0º
Condition 4: Q=140 psf, Mach 0.32 $\alpha = 16^{\circ}$; Speedbrake=0º

The autopilot was synthesized using a modern Integral-Linear Quadratic Regulator (I-LQR) design technique. The pitch and yaw/roll autopilots were designed separately, since there is little aerodynamic cross coupling between these axes. The following sections present a short description of the design methodology, the structure and resulting gains of the autopilots.

3.1.1 Pitch Autopilot

A derivative and trim program was first used to obtain pitch trim at the four design conditions. The derivatives are calculated around a trim condition, using the body or wing flaps for trim. The vehicle was trimmed in pitch using the wing flaps; this configuration was shown to be desirable, allowing the body flaps to be used for roll control and speed control.

State Space Equation: $dX/dt=[A]\,X + [B]\,U$

State Vector: $X=[\ \alpha, q, \int \alpha\, dt]'$

Control Vector: $U=[\ \delta \text{ elev}]$ {wing flap}

	PLANT MATRIX [A]	INPUT MATRIX [B]	Eigen- values
Qpress=300 psf alpha =8°, Mach 0.6 speedbrake=20°	-.5480 : 1.0 : 0 -8.3636 : -.2150 : 0 1.0 : 0 : 0	-.0661 -7.6572 0	0 -.3815 ±i 2.8872
Qpress=270 psf alpha =5°, Mach 0.47 speedbrake=20°	-.6235 : 1.0 : 0 -7.4992 : -.2446 : 0 1.0 : 0 : 0	-.0752 -6.8659 0	0 -.4340 ±i 2.7319
Qpress=220psf alpha=12°, Mach 0.41 speedbrake=0°	-.5699 : 1.0 : 0 -5.1877 : -.3033 : 0 1.0 : 0 : 0	-.0652 -5.048 0	0 -.4366 ±i2.2737
Qpress=140psf alpha=16°, Mach 0.32 speedbrake=0°	-.4230 : 1.0 : 0 -2.1558 : -.2456 : 0 1.0 : 0 : 0	-.0458 -2.6754 0	0 -..3343 ±1.4656

Table 3-1 Pitch Linear Models

Using the derivative data generated from the trim program, a continuous linear pitch model for each condition was developed as shown in table 3-1. The state vector includes angle of attack (α), pitch rate (q) and integral of angle of attack ($\int\alpha$) which is included to improve on command following and robustness to parameter variation. A block diagram of the pitch control loop is shown in figure 3-1.

The autopilot was synthesized on the MATRIXx program using the Integral-Linear Quadratic Regulator (I-LQR) design technique. This technique helps the designer to form a desired state weighting matrix methodically, instead of by trial-and-error as is done with the LQR technique. The I-LQR method involves selecting outputs for weighting, which produce transmission zeroes of the LQ regulator to control the position to which the closed loop poles will migrate. The primary condition imposed by the I-LQR method is that the number of output variables must equal the number of input variables to allow the specification of the transmission zeroes. For the pitch autopilot, there is one input, so one output equation is used for output weighting.

The equations and development of the I-LQR gains are given in figure 3.-2; the example is obtained from the development of the pitch gains for condition 1. First, the transmission output matrix [C] is developed from a given set of transmission zeroes. Given the cost function J, the state weighting matrix [Rxx] is developed using the transmission output matrix [C]. The input weighting matrix [Ruu] is given a nominal value of one, and [Rxx] is multiplied by coefficient ρ, to apply a relative weight between [Rxx] and [Ruu]. MATRIXx was used to compute the LQR optimal state-feedback gains and the resulting eigenvalues. The coefficient ρ is varied until desired closed loop eigenvalues are obtained.

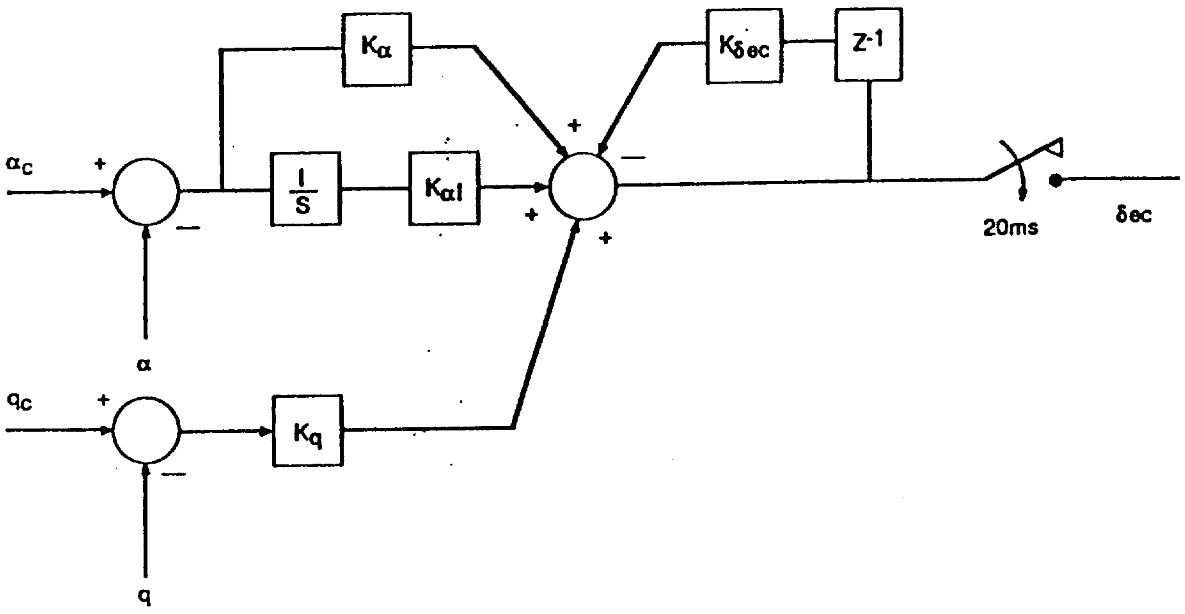

Figure 3-1 Pitch Autopilot Block Diagram

Using this methodology, the complete continuous gain schedule was developed for each condition as summarized in table 3-2.

Q (psf)	K_α	Kq	K_{α_I}	Closed Loop Poles (continuous)
300	-3.890	-1.188	-8.174	-2.717 -3.701±i3.063
270	-3.412	-1.127	-7.311	-2.539 -3.162± i 3.134
220	-4.590	-1.467	-8.954	-2.620 -2.980± i 2.905
140	-6.171	-2.297	-9.708	-2.633 -2.232± i 2.220

Table 3-2 Pitch Continuous Autopilot Gains

The major advantage of using the I-LQR design method over the classical design is that the I-LQR design results in larger integral gains, while maintaining larger gain and phase margins. This is evident in the integral alpha gains ($K\alpha_I$) obtained using the I-LQR design, as summarized in table 3-2 .

The discrete pitch autopilot was synthesized using the I-LQR technique. The discrete design was aided by using the same LQ weighting matrix developed for the continuous case. A 20 msec autopilot sampling rate was used with a 10 msec computational delay as shown in the block diagram of figure 3-1. The resulting regulator gains for the discrete autopilot are given in table 3-3.

Discrete gains were also computed for a NASA cockpit simulation study. NASA's simulation study for evaluation of the PLS vehicle utilizes the Transportation Systems Research Vehicle (TSRV) simulation cockpit and real time simulation facility. This simulation facility runs on a 30 msec sampling interval and the computational delay can be approximated at 30 msec. As a result of the 30 msec requirement, the discrete pitch gains were recalculated at the larger sampling

- **STATE EQUATION:** [dX/dt]= [A]* [X] + [B] * [U]

$$\begin{bmatrix} d\alpha/dt \\ dq/dt \\ d\alpha_i/dt \end{bmatrix} = \begin{bmatrix} -0.548 & 1.0 & 0. \\ -8.364 & -0.215 & 0. \\ 1.0 & 0.0 & 0. \end{bmatrix} \begin{bmatrix} \alpha \\ q \\ \alpha_i \end{bmatrix} + \begin{bmatrix} -0.066 \\ -7.657 \\ 0. \end{bmatrix} [\delta ev]$$

- **OUTPUT EQUATIONS TO PLACE TRANSIMISSION ZEROES**

$$Y(s)= \frac{(s^2 + 2\omega\zeta\, s + \omega^2)}{s}\, \alpha(s) \qquad \text{let} \quad \omega=3.40 \text{ rps}; \ \zeta=0.95$$

$$a=2\omega\zeta=6.46; \ b=\omega^2=11.56$$

or, $Y=(d\alpha/dt) + a\alpha + b\alpha_i$; where: $d\alpha/dt= A(1,1)\cdot\alpha + A(1,2)\cdot q + A(1,3)\cdot\alpha_i$

$Y= (A(1,1)+ a)\cdot\alpha + A(1,2)\cdot q + b\cdot\alpha_i$

Thus, for condition #1 :

$[Y]= [C] * [X]$ where: $[C]= [A(1,1)+ a \quad A(1,2) \quad b]$

$[Y]= [5.912 \quad 1. \quad 11.56] * [\alpha \ q \ \alpha_i]^T$

- **COST FUNCTION:** $J= \int_0^\infty (X^T Rxx\, X + U^T Ruu\, U + U^T Rxu\, X)\, dt$

- **WEIGHTING MATRIX**

$$\begin{bmatrix} Rxx & Rxu^T \\ Rxu & Ruu \end{bmatrix} \qquad \text{where;} \quad Rxx= \rho\, [C^T C] \qquad Ruu=[1]$$

$Rxu= [0 \ 0 \ 0]$

$$Rxx= \rho [C^T C] = \rho \begin{bmatrix} 34.95 & 5.91 & 68.34 \\ 5.91 & 1.0 & 11.56 \\ 68.34 & 11.56 & 133.63 \end{bmatrix}$$

- **RESULTING LQR GAINS:**

for $\rho= 0.5$ **Kr**= [-3.89 -1.19 -8.17]

Eigenvalues= -2.72; -3.70 ± i 3.06

FIGURE 3-2 Example of Integral-LQR Design

interval of 30 msec with a computational delay of 30 msec. These gains are also summarized in table 3-3.

Q (psf)	T-samp/ T-comp	K_α	Kq	K_{α_I}	$K_{\delta_{ec}}$
300	20ms/10ms	-3.471	-1.150	-7.456	.089
	30ms/30ms	-3.201	-1.173	-7.105	.266
270	20ms/10ms	-3.088	-1.099	-6.757	.077
	30ms/30ms	-2.875	-1.123	-6.486	.230
220	20ms/10ms	-4.226	-1.437	-8.297	.074
	30ms/30ms	-4.019	-1.473	-7.978	.223
140	20ms/10ms	-5.828	-2.261	-9.109	.062
	30ms/30ms	-5.680	-2.318	-8.816	.188

Table 3-3 Pitch Discrete Autopilot Gains

A second order, 10 Hz actuator model with 0.5 damping ratio was added to the pitch autopilot design model. Nichols plots for the 4 conditions with the loop open at the actuator are shown in figure 3-3. Plotted are the results from the continuous pitch gains, and two discrete conditions:

-discrete condition 1= 20 msec sampling /10 msec computational delay
-discrete condition 2= 30 msec sampling /30 msec computational delay

A region of typical stability margin requirements is also shown in the Nichols plots. The frequency response results show that there is sufficient gain and phase margin to guarantee stability and robustness. However, as expected, the stability margin of the discrete case decreases compared to the continuous case, and the stability margin further decrease using the larger sampling interval and computational delay.

In addition, system response to an a step command is plotted for α,q, d/dt(δe) and δe in figures 3-4 for all four flight conditions. The results show a quick time response with the actuator elevator rate $\leq$ 50 deg/sec .

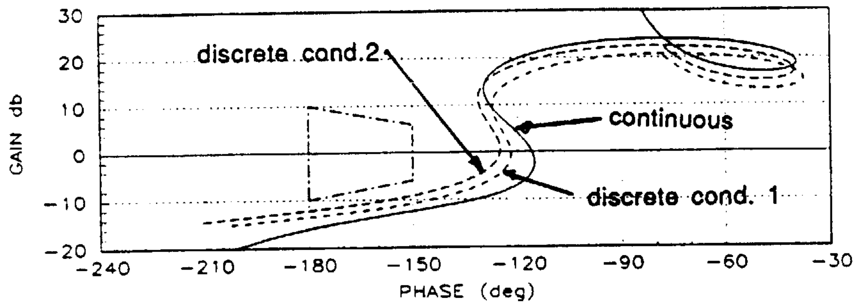

PITCH NICHOLS PLOT FOR CONDITION 1

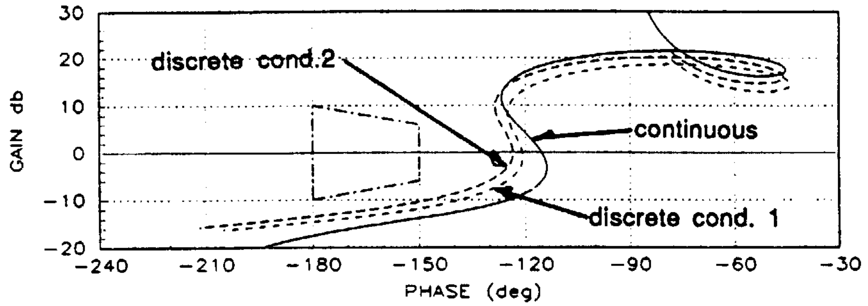

PITCH NICHOLS PLOT FOR CONDITION 2

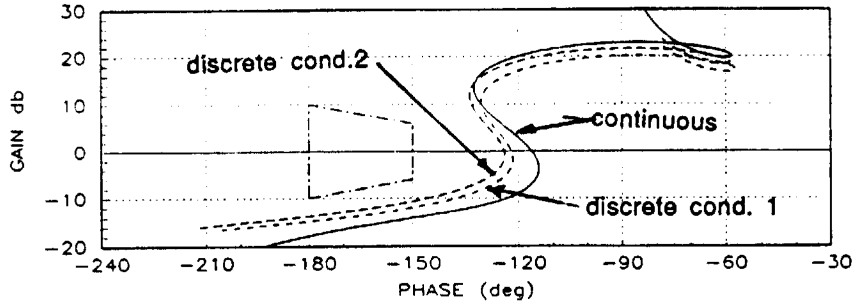

PITCH NICHOLS PLOT FOR CONDITION 3

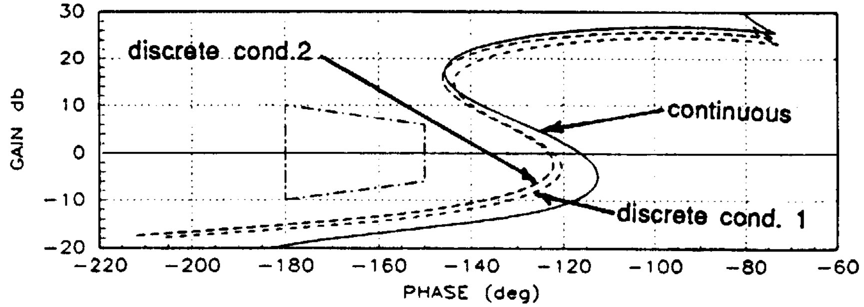

PITCH NICHOLS PLOT FOR CONDITION 4

Figure 3-3 Continuous and Discrete Pitch Nichols Plots

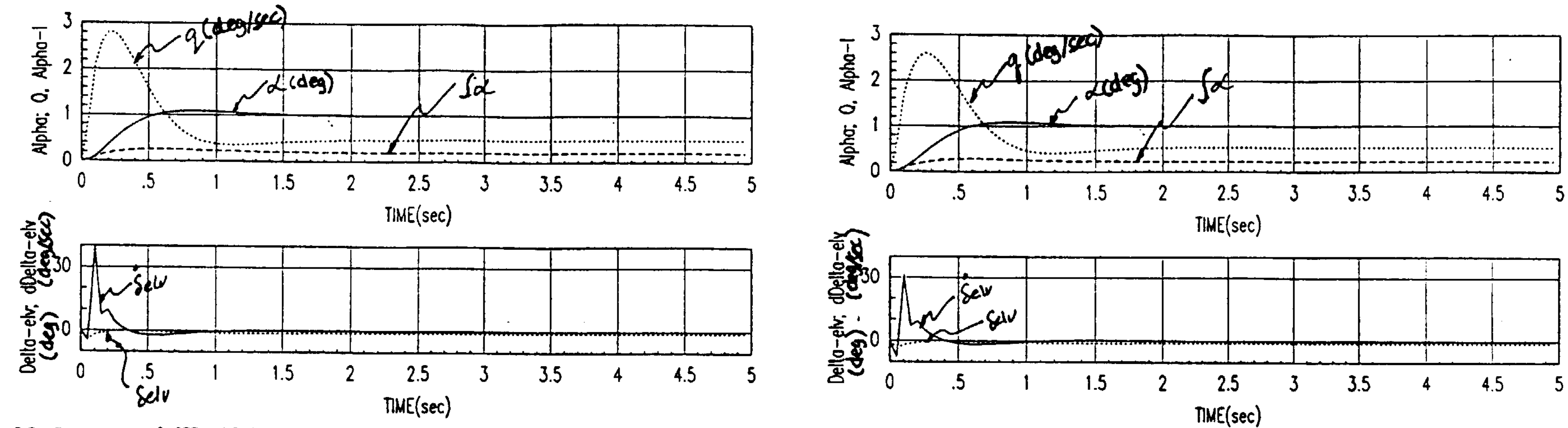

CONDITION #1 SYSTEM RESPONSE TO ALPHA STEP CMD

CONDITION #2 SYSTEM RESPONSE TO ALPHA STEP CMD

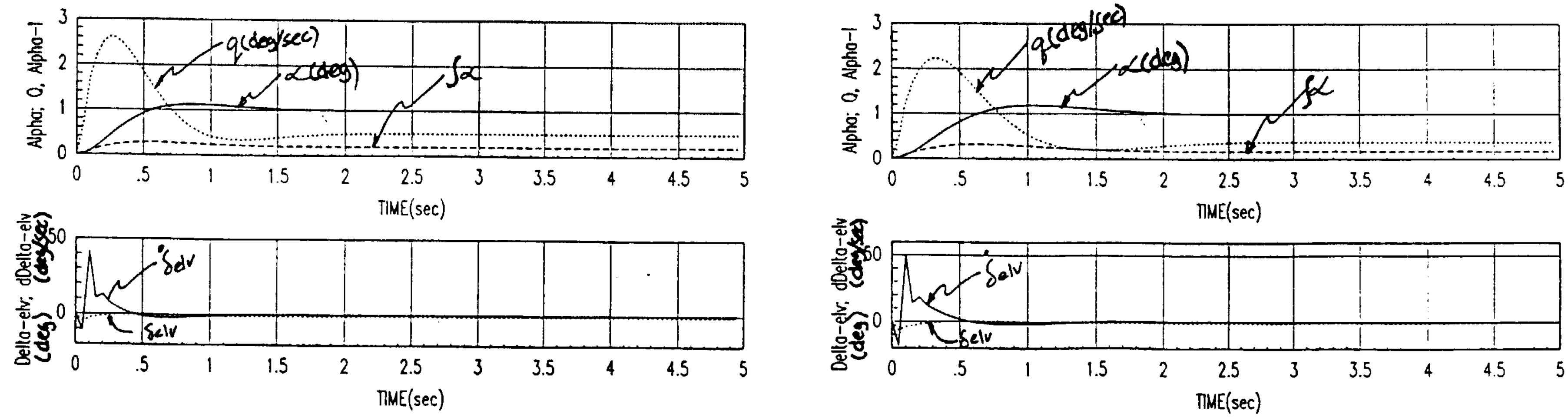

CONDITION #3 SYSTEM RESPONSE TO ALPHA STEP CMD

CONDITION #4 SYSTEM RESPONSE TO ALPHA STEP CMD

Figure 3-4 System Response to Alpha Step Command

3.1.2 Yaw/Roll Autopilot

A derivative and trim program was used to obtain yaw/roll stability derivatives at four flight conditions listed in section 3.1 . The vehicle was trimmed using only the body flaps for roll control, and the smaller of two possible all-moveable tail sizes as a rudder for yaw control.

The yaw/roll continuous linear model data for each of the four flight conditions is given in table 3-4. The state vector $X=[\ \beta\ \ r\ \ p\ \ \phi\ ]$ and the input vector $U=[\ \delta\ \text{rud}\ \ \delta\ \text{ail}\ ]$.

For the PLS design, only the body flaps are used for roll control, and the small all-moveable tail as a rudder for yaw control. Previous studies on the CERV vehicle (reference 7) showed that using the body flap alone lacked sufficient roll control authority to decrab the vehicle with a side wind greater than 15 knots. However, the configuration was acceptable for PLS because the requirements for decrab were relaxed somewhat by specifying that the heading alignment at touchdown be $\leq 5^{\circ}$ as opposed to complete alignment for CERV. Decrab design and analysis was not performed for PLS because NASA postponed this for a later study when new data becomes available for landing gear and ground effect.

The yaw/roll autopilot design is based on the CERV design. A block diagram of the resulting yaw/roll autopilot is shown in figure 3.-5. The yaw-roll Integral-LQR design was done for a state vector that includes sideslip angle, yaw rate, roll rate and roll angle. As was done with the pitch autopilot, a continuous autopilot was first designed. The resulting gain schedule and eigenvalues are given in table 3-5.

The same LQ weighting developed in the continuous synthesis was used to obtain a corresponding discrete design with computational delay compensation included. Two sets of discrete gains were obtained for different sampling rates and computational delay:

- discrete condition 1: T-sample= 20 msec; T-computational delay= 10 msec
- discrete condition 2: T-sample= 30 msec; T-computational delay= 30 msec

The corresponding discrete gain schedule is given in table 3-6.

***** CONDITION 1 *****

V=635 ft/sec; QPRES=300 psf; MACH=0.6; Alpha=5 deg

$$A=\begin{bmatrix} -0.1624 & -1.0000 & 0.0873 & 0.0000 \\ 5.5647 & -0.3082 & 0.1254 & 0.0000 \\ -71.8552 & 1.0638 & -0.9901 & 0.0000 \\ 0.0000 & 0.0000 & 1.0000 & 0.0000 \end{bmatrix} \qquad B=\begin{bmatrix} 0.0267 & -0.0020 \\ -2.5041 & 0.0038 \\ 2.4037 & 6.0456 \\ 0.0000 & 0.0000 \end{bmatrix}$$

Eigenvalues= 0.; .1648; -.8127-3.487i; -.8127+3.487i

***** CONDITION 2 *****

V=500 ft/sec; QPRES=270 psf; MACH=0.47; Alpha=5 deg

$$A=\begin{bmatrix} -0.1856 & -1.0000 & 0.0873 & 0.0000 \\ 5.0082 & -0.3523 & 0.1433 & 0.0000 \\ -64.6697 & 1.2159 & -1.1316 & 0.0000 \\ 0.0000 & 0.0000 & 1.0000 & 0.0000 \end{bmatrix} \qquad B=\begin{bmatrix} 0.0306 & -0.0023 \\ -2.2537 & 0.0035 \\ 2.1633 & 5.4410 \\ 0.0000 & 0.0000 \end{bmatrix}$$

Eigenvalues= 0.; .1831; -0.9263 - 3.2607i; -0.9263 + 3.2607i

***** CONDITION 3 *****

V=435 ft/sec; QPRES=220 psf; MACH=0.41; Alpha=10 deg

$$A=\begin{bmatrix} -0.1738 & -1.0000 & 0.1745 & 0.0000 \\ 5.6286 & -0.3612 & 0.0859 & 0.0000 \\ -52.6938 & 1.5630 & -0.7406 & 0.0000 \\ 0.0000 & 0.0000 & 1.0000 & 0.0000 \end{bmatrix} \qquad B=\begin{bmatrix} 0.0335 & -0.0042 \\ -1.9911 & 0.0619 \\ 2.5305 & 4.1664 \\ 0.0000 & 0.0000 \end{bmatrix}$$

Eigenvalues= 0.; -.0967; -0.5895 + 3.8325i; -0.5895 - 3.8325i

***** CONDITION 4 *****

V=340 ft/sec; QPRES=140 psf; MACH=0.32; Alpha=16 deg

$$A=\begin{bmatrix} -0.1415 & -1.0000 & 0.2792 & 0.0000 \\ 2.7759 & -0.2944 & 0.0533 & 0.0000 \\ -33.5324 & 0.8666 & -0.7560 & 0.0000 \\ 0.0000 & 0.0000 & 1.0000 & 0.0000 \end{bmatrix} \qquad B=\begin{bmatrix} 0.0326 & -0.0048 \\ -1.3665 & 0.0609 \\ 2.0437 & 2.7873 \\ 0.0000 & 0.0000 \end{bmatrix}$$

Eigenvalues =-3.9417 - 1.3138i; -3.9417 + 1.3138i
-3.8689 + 3.7090i; -3.8689 - 3.7090i

$\dot{X} = [A]X + [B]U$ where: $X = [\beta(deg), r(deg/sec), p(deg/sec), \phi(deg)]^T$
$U = [\delta rud(deg), \delta ail(deg)]^T$

TABLE 3-4 YAW/ROLL LINEAR MODEL DATA

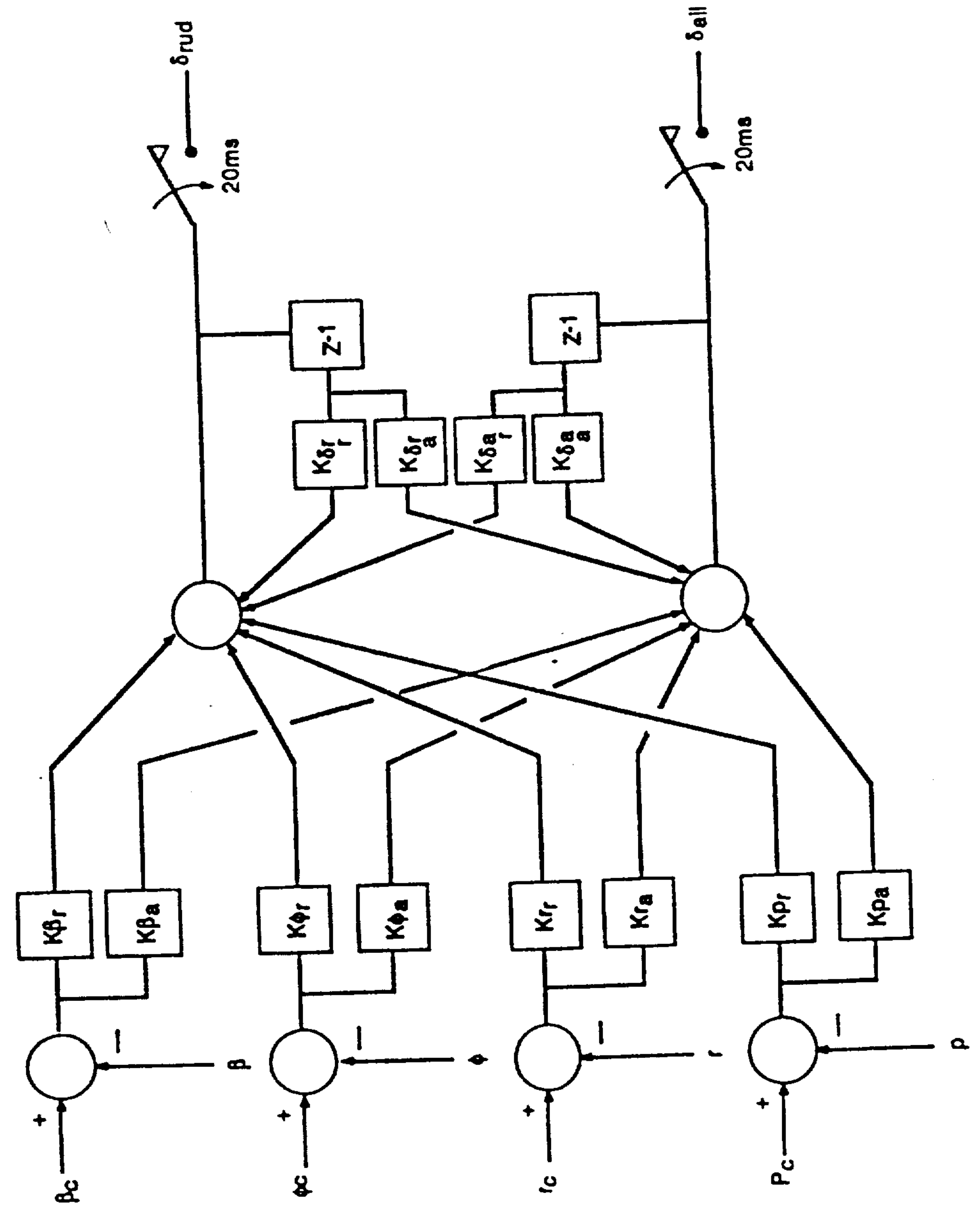

Figure 3-5 PLS Yaw/Roll Autopilot Block Diagram

K- RUDDER CONTINUOUS GAINS

Condition #	K-beta	K-r	K-p	K-phi
1	11.5602	-3.1173	-0.2505	-0.8380
2	11.6715	-3.2571	-0.2791	-0.9199
3	10.9234	-3.4077	-0.2393	-1.2800
4	12.5104	-4.3575	-0.0294	-1.9237

K- AILERON CONTINUOUS GAINS

Condition #	K-beta	K-r	K-p	K-phi
1	-14.2882	1.7535	1.8251	5.9263
2	-14.1947	1.8542	1.9171	6.2254
3	-15.5621	2.5746	2.2310	6.6544
4	-16.3209	3.3596	2.8141	8.8851

TABLE 3-5 YAW/ROLL CONTINUOUS GAIN SCHEDULE

K-RUDDER DISCRETE GAINS (Tsamp=20 msec; Tcomp=10 msec)

Condition #	K-beta	K-r	K-p	K-phi	K-dar	K-drr
1	9.9224	-3.0850	-0.1863	-0.6318	0.1462	-0.0232
2	10.1188	-3.2275	-0.2137	-0.7026	0.1383	-0.0239
3	9.3022	-3.3565	-0.1649	-1.0523	0.1281	-0.0189
4	10.5550	-4.2032	0.0104	-1.6707	0.1192	-0.0061

K-AILERON DISCRETE GAINS (Tsamp=20 msec; Tcomp=10 msec)

Condition #	K-beta	K-r	K-p	K-phi	K-daa	K-dra
1	-15.7416	2.0054	1.6420	5.0488	-0.0224	0.1964
2	-15.5594	2.1061	1.7343	5.3467	-0.0225	0.1869
3	-16.6148	2.8430	2.0109	5.7949	-0.0156	0.1707
4	-16.8250	3.5638	2.4574	7.5560	-0.0032	0.1419

K-RUDDER DISCRETE GAINS (Tsamp=30 msec; Tcomp=30 msec)

Condition #	K-beta	K-r	K-p	K-phi	K-dar	K-drr
1	9.8524	-3.1732	-0.1882	-0.6400	0.2224	-0.0351
2	10.0612	-3.3167	-0.2162	-0.7104	0.2102	-0.0362
3	9.1642	-3.4356	-0.1633	-1.0595	0.1943	-0.0285
4	10.4016	-4.2920	0.0184	-1.6763	0.1808	-0.0089

K-AILERON DISCRETE GAINS (Tsamp=30 msec; Tcomp=30 msec)

Condition #	K-beta	K-r	K-p	K-phi	K-daa	K-dra
1	-16.7603	2.1770	1.6568	5.0204	-0.0398	0.2954
2	-16.5259	2.2780	1.7498	5.3198	-0.0394	0.2812
3	-17.4681	3.0330	2.0202	5.7737	-0.0292	0.2566
4	-17.5199	3.7460	2.4628	7.5383	-0.0087	0.2132

TABLE 3-6 YAW/ROLL DISCRETE GAIN SCHEDULE

To evaluate the stability margins, Nichols plots with the control loops opened at each actuator were generated for the 4 flight conditions, and are plotted in figures 3-6 through 3.-9. These plots include the actuator dynamics as described for the pitch autopilot analysis. Each figure contains the open yaw loop Nichols plot with the roll loop closed, and the open roll loop Nichols plot with the yaw loop closed. Plotted are the results from the continuous yaw/roll gain, and for the two discrete conditions. As expected, the stability margins of the discrete case decrease compared to the continuous case, and the margins decrease further using the larger sampling time and larger computational delay. However, all stability margins are sufficient and do not violate the design margins shown on the plots.

In addition to the frequency analysis of the yaw/roll autopilot, a time response study was performed. The system response to a roll step input was evaluated at each of the four flight conditions. The results are plotted in figure 3.-10. Only 1.5 seconds is needed for the roll response to equal the roll command.

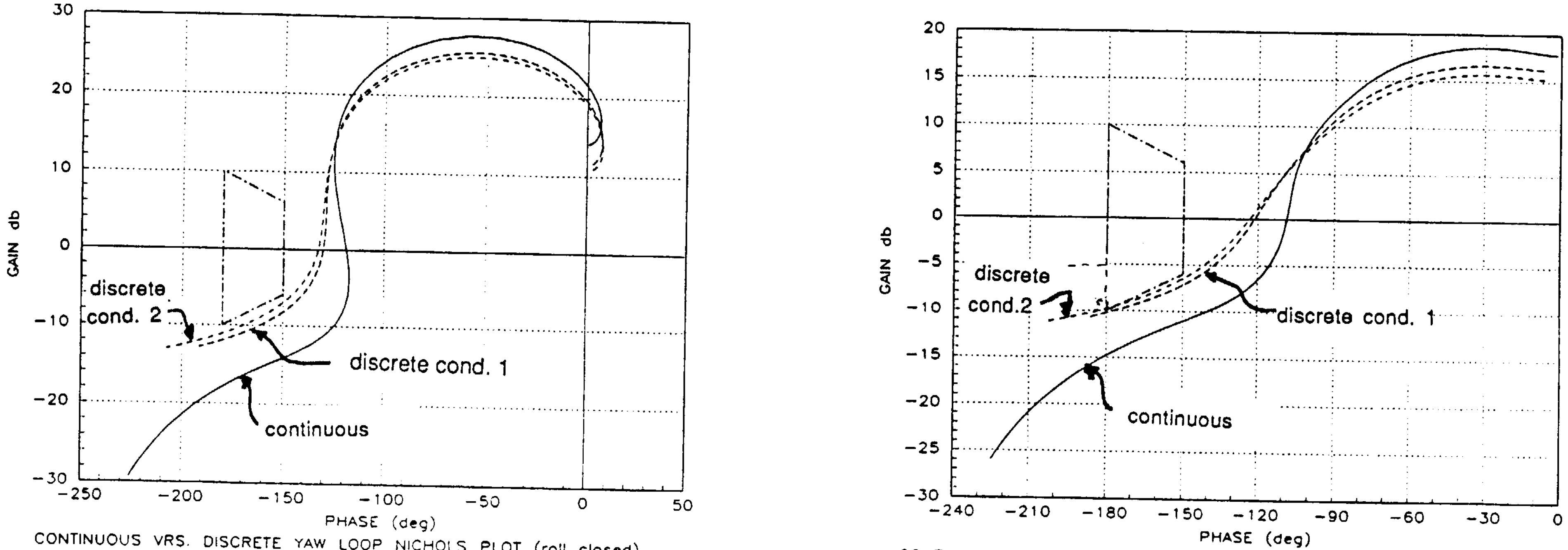

CONTINUOUS VRS. DISCRETE YAW LOOP NICHOLS PLOT (roll closed)

CONTINUOUS VRS. DISCRETE ROLL LOOP NICHOLS PLOT (yaw closed)

Figure 3-6 Yaw/Roll Nichols Plot for Flight Condition #1

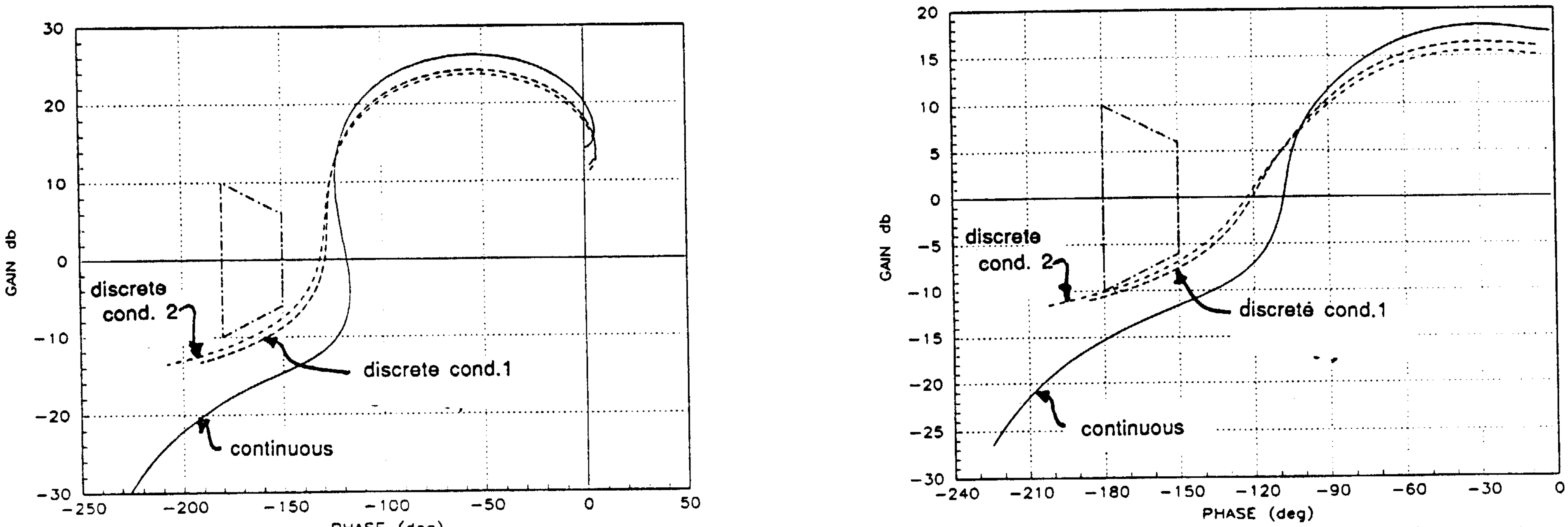

CONTINUOUS VRS. DISCRETE YAW LOOP NICHOLS PLOT (roll closed)

CONTINUOUS VRS. DISCRETE ROLL LOOP NICHOLS PLOT (yaw closed)

Figure 3-7 Yaw/Roll Nichols Plot for Flight Condition #2

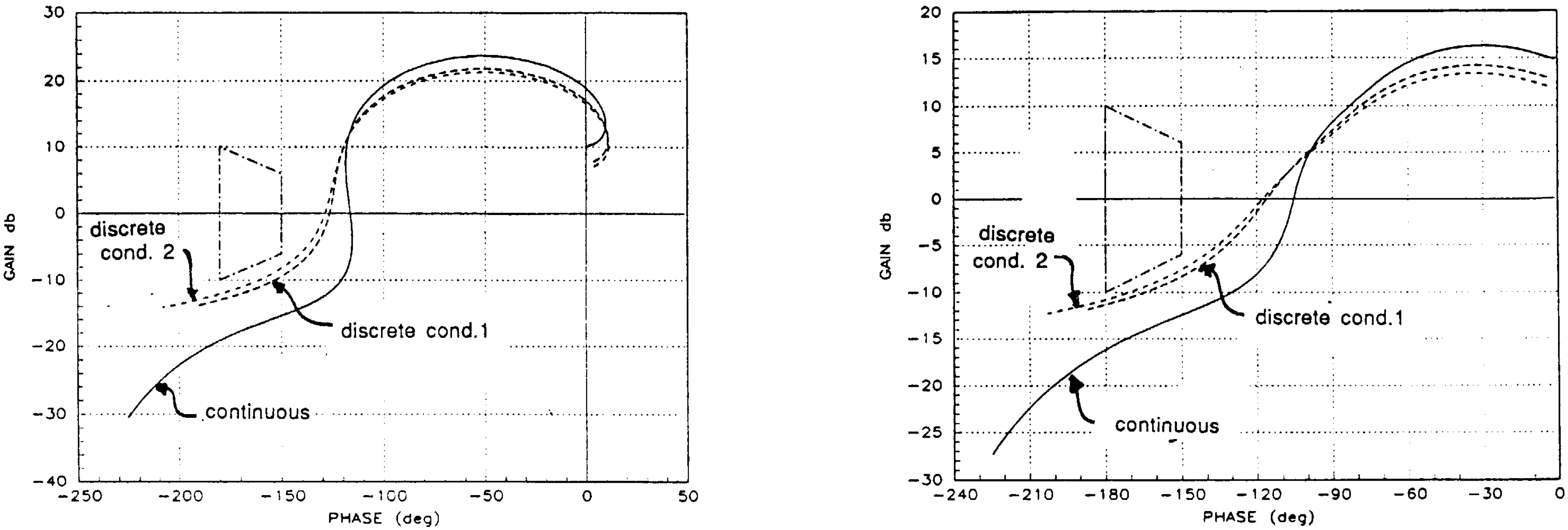

CONTINUOUS VRS. DISCRETE YAW LOOP NICHOLS PLOT (roll closed)

CONTINUOUS VRS. DISCRETE ROLL LOOP NICHOLS PLOT (yaw closed)

Figure 3-8 Yaw/Roll Nichols Plot for Flight Condition #3

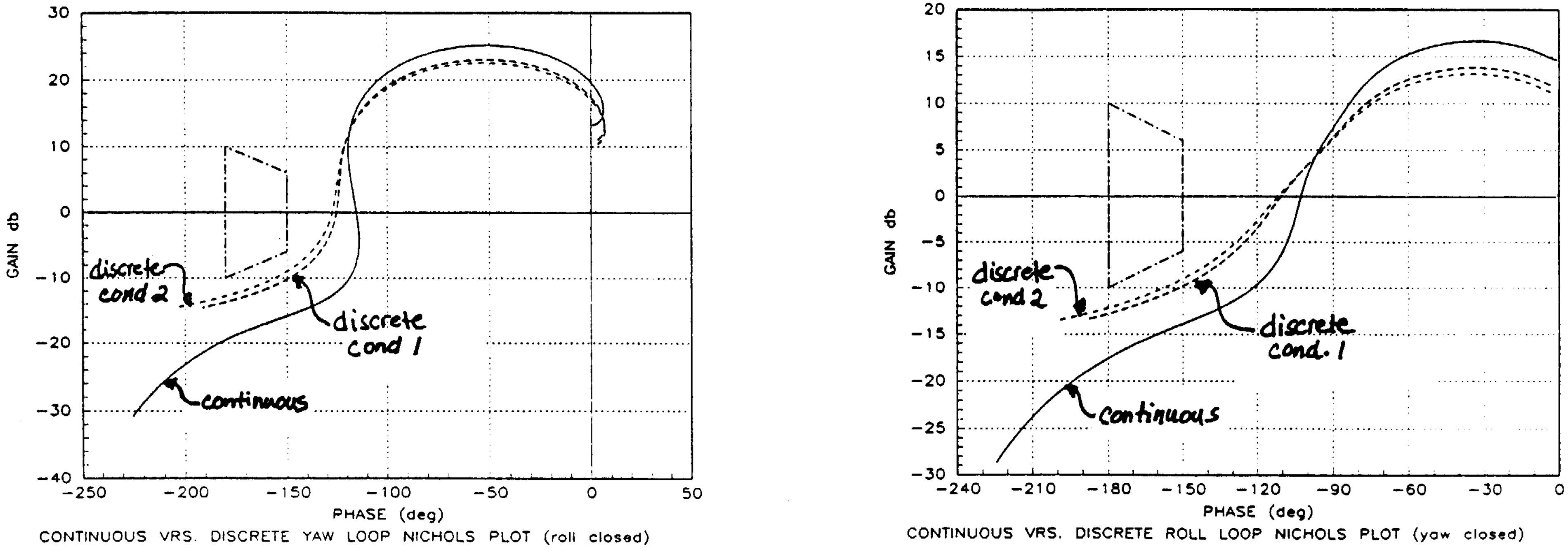

CONTINUOUS VRS. DISCRETE YAW LOOP NICHOLS PLOT (roll closed)

CONTINUOUS VRS. DISCRETE ROLL LOOP NICHOLS PLOT (yaw closed)

Figure 3-9 Yaw/Roll Nichols Plot for Flight Condition #4

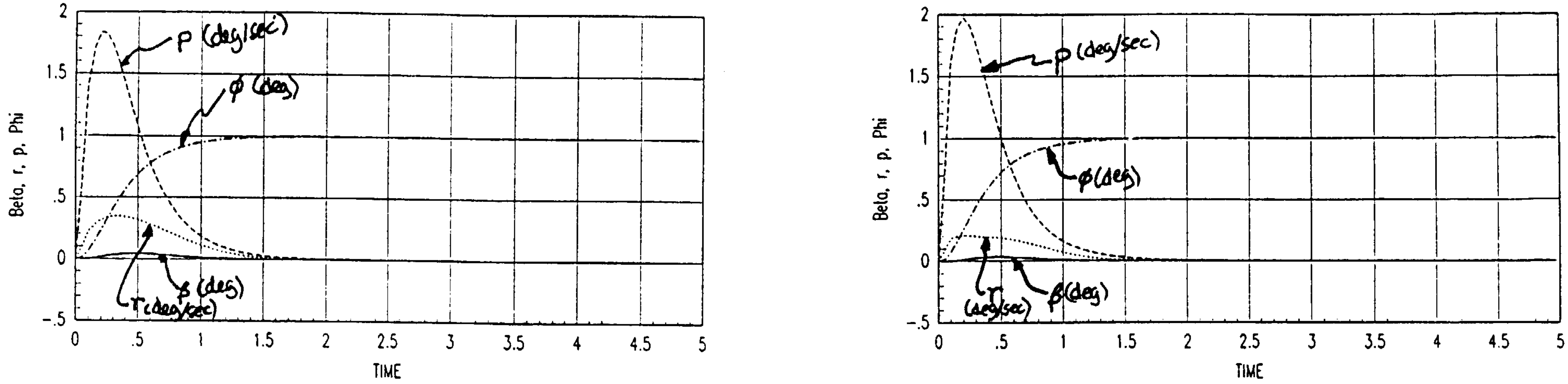

SYSTEM RESPONSE TO ROLL STEP INPUT - **Condition 1**

SYSTEM RESPONSE TO ROLL STEP INPUT - **Condition 2**

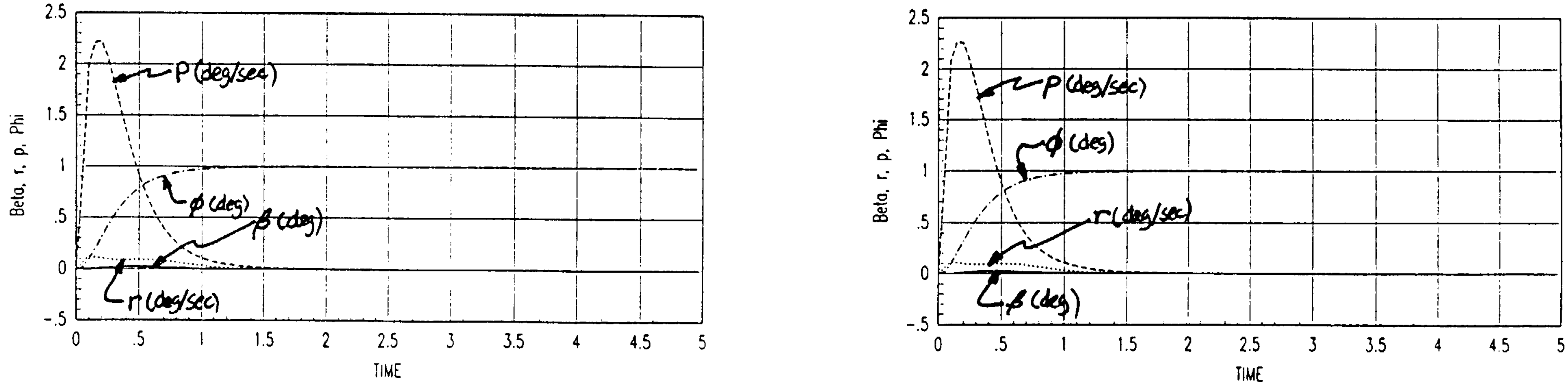

SYSTEM RESPONSE TO ROLL STEP INPUT - **Condition 3**

SYSTEM RESPONSE TO ROLL STEP INPUT - **Condition 4**

Figure 3-10 System Response to a Roll Step Input

3.2 A/L Longitudinal Guidance and Control System

The A/L longitudinal guidance and control system is made up of the trajectory (or flight profile) generator, the altitude control module and the speed control module, as shown in the signal flow diagram of figure 2-6. The trajectory generator determines the desired altitude and descent rate from the vehicle current position relative to the runway. Trajectory algorithms were developed to calculate the PLS flight profile. The guidance system operates in a 60 msec time frame.

The along track error is indirectly controlled by the altitude control module and the speed controller. The altitude controller translates altitude and sink rate commands from the trajectory generator into angle-of-attack commands. The speed controller is covered in section 3.4.

3.2.1 A/L Trajectory Generator

The A/L trajectory generator generates straight-in trajectory commands. The PLS straight-in trajectory uses a Shuttle-like landing profile. The trajectory and algorithm variables are defined in figure 3-11. The trajectory profile can be divided into 5 sections:

1- steep glideslope (H0 to H1, glide slope=-26º);
2- pull-up (or pre-flare) maneuver (constant g circle;H1 to H2C);
3- exponential transition (shallow glideslope capture , H2C to H2)
4- shallow glideslope (H2 to H3, glide slope=-2.5º)
5- final flare and decrab (H3 to touchdown).

The trajectory algorithms calculating the trajectory variables is given in appendix G. Figure 3-11 also defines preliminary trajectory parameters. These parameters define a nominal PLS mission. They were determined after repeated 6-DOF simulations were performed, varying the input parameters until satisfactory landing performance was obtained (see section 4.1.1). The resulting mission initial conditions that define the nominal PLS A/L straight-in trajectory are summarized in Table 3-6.

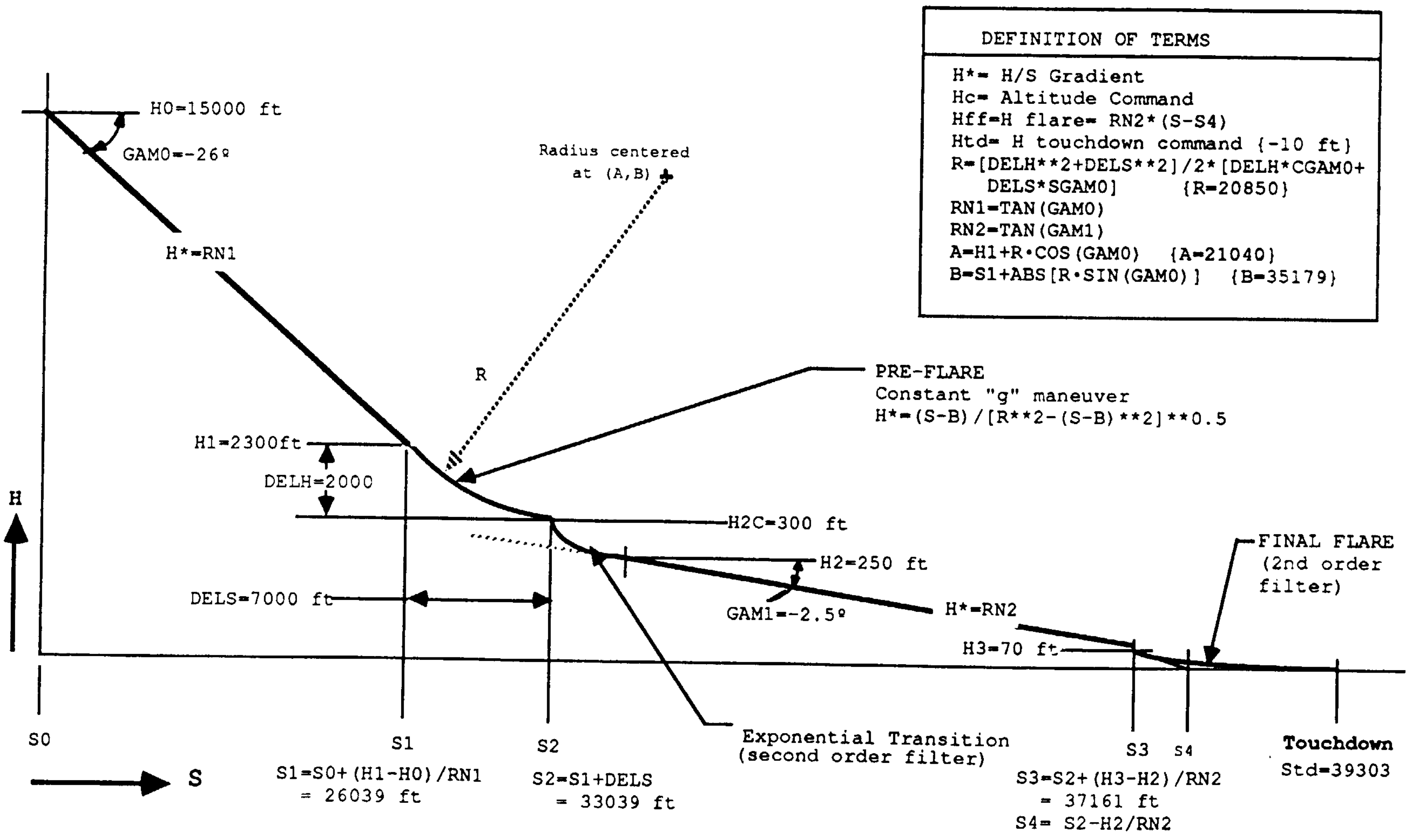

Figure 3-11 PLS Straight-In Trajectory Profile

Input Parameter	Value	Description
GAM0	-26°	steep glideslope angle
GAM1	-2.5°	shallow glideslope angle
WFLAR1	0.220	1st flare rate (rps)
WFLAR2	0.280	2nd flare rate (rps)
ZFLARE	1.0	flare damping ratio zeta
DELS	7000	1st flare (constant g pullup) delta range
DELH	2000	1st flare (constant g pullup) delta range
H1	2300	start of 1st flare altitude
H2C	300	end of 1st flare altitude
H2	250	shallow glideslope capture altitude
H3	70	start of 2nd (final) flare altitude
HTDC	-10	commanded touchdown altitude
ACIR	0.5	g pullup during 1st flare

Table 3.-6 Mission Input Parameters For A/L Nominal Trajectory

Each of the 5 trajectory profile sections will be explained in greater detail. The first A/L phase starts with a steep glideslope which is strongly dependent on the lift-to-drag (L/D) characteristics of the vehicle. Due to the low L/D ratio of the PLS vehicle, a glide path angle of 24° or higher is necessary to maintain enough total energy to carry the vehicle through to touchdown. For the final nominal trajectory, a 26° glide path angle was chosen. This allows for a nominal speedbrake deflection of 20° during the steep glideslope descent phase necessary to control speed in the presence of wind.

The second A/L phase is the preflare (or pullup) maneuver consisting of a constant "g" pullup maneuver. This maneuver is performed to decrease the sink rate and to capture the final shallow glideslope. This preflare maneuver is prefered by astronauts/pilots because it results in a less threatening ground approach compared with the standard single parabolic flare maneuver. The trajectory generator commands a constant "g" circular profile defined by a constant radius. The radius length results in a "g" load factor, and is determined from the desired circular delta altitude (DELH) and delta range (DELS) as shown in figure 3-11 . A 0.5 "g" load was chosen for the PLS pullup.

The third phase of the trajectory is the exponential transition phase. A second order exponential decay filter is used to generate an exponential transition profile to capture the shallow glideslope angle. The algorithm calculates an altitude acceleration command. The acceleration command decays to zero as the commanded altitude rate and position reaches the desired final value.

Kinetic energy is quickly lost as the vehicle remains in the preflare (constant g pullup) maneuver. To minimize the loss of energy during this maneuver, simulation results showed that the final glideslope angle at the end of the preflare should be as large as feasible. However, it is also desirable for the final glideslope angle at the end of the preflare be equal to the shallow glideslope angle; this minimizes the transients that occur during the exponential transition . As a result, it was established that the final flight path angle at the end of the preflare should be slightly greater than the shallow glideslope angle. By varying the DELH and DELS parameters, the flight path angle at the end of the preflare can be controlled. As a result, DELH and DELS were adjusted to obtain a glideslope angle of approximately 5º, which is slightly larger than the shallow glideslope of 2.5º .

The shallow glideslope phase is the final low altitude approach to the runway. To maintain sufficient kinetic energy, a flight path angle of -2.5º is required.

The final flare profile is similar to the exponential transition flare, and is used to reduce the sink rate at touchdown to an acceptable level. The most sensitive parameters affecting the touchdown conditions are the final flare rate (WFLAR2), the altitude at which to start the final flare (H3) and the commanded touchdown altitude (HTDC). The final flare should start at approximately 70 feet to allow the autoland system to decrease the sink rate prior to touchdown. A lower H3 altitude results in a higher landing speed but at the expense of a larger sink rate. On the other hand, a higher H3 results in lowering the sink rate but at the expense of an unacceptably low landing speed.

3.2.2 A/L Altitude Control Module

The function of the altitude control module is to translate the altitude and sink rate commands from the trajectory generator into appropriate angle-of-attack signals for the flight control. A block diagram of the longitudinal guidance loop is shown in figure 3-12. The guidance loop is designed classically, and consists of an altitude and altitude rate feedback. The gain KH associated with the altitude error forms a zero in the root locus plot. Gain KAC is the guidance loop gain. An altitude step response analysis was performed using the 6-DOF simulation to evaluate the altitude gains. The nominal value for KAC is 0.3; the KH gain is a function of altitude as shown in figure 3-12.

Trimmed angle-of-attack generated from the lift curve as a function of dynamic pressure is summed with the altitude steering command to form a total angle-of-attack command. Feed forward loops are used instead of an integrator in the altitude loop, and as a result, an altitude error bias is observed when the calculated trimmed angle-of-attack is not exactly matched with the real trim angle. However, this error bias is small and does not affect the landing performance. An altitude error integrator can reduce this bias, but it may pose stability problems in the steering loop due to the presence of an additional pole at the origin.

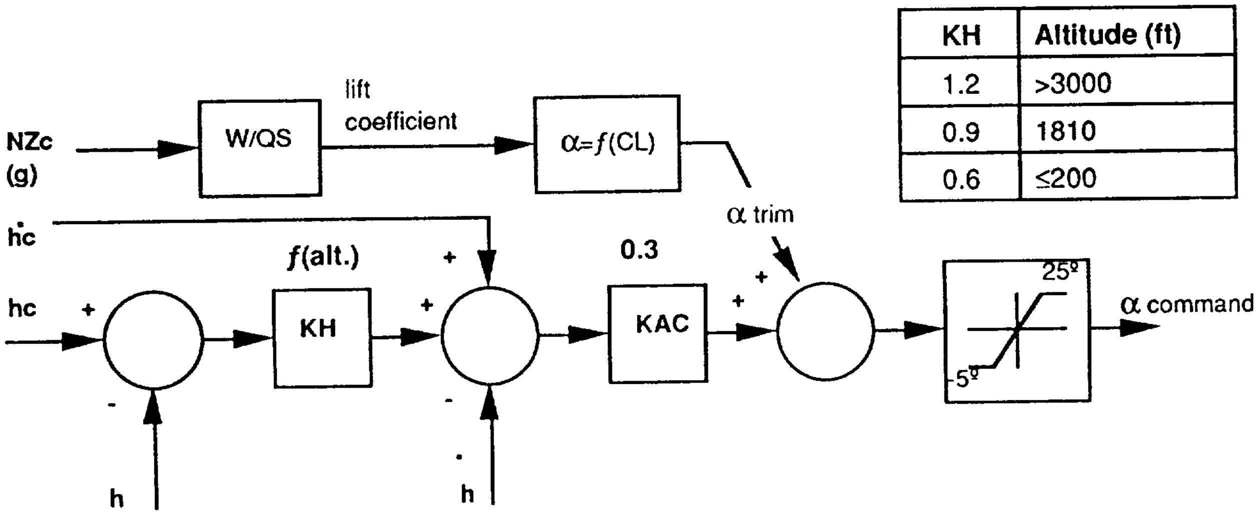

KH	Altitude (ft)
1.2	>3000
0.9	1810
0.6	≤200

Figure 3-12 Longitudinal Guidance Design

3.3 A/L Lateral Guidance and Control System

The approach and landing lateral guidance system tracks the runway centerline during the descent. The system uses a roll-to-steer method by generating bank angle commands to null the cross track error and cross track rate with respect to the runway centerline. A block diagram of the lateral guidance loop is shown in figure 3-13. The feedback signals are the lateral displacement (Y) from the centerline and the lateral velocity normal to the fixed center line. The KY and KPHI gains were varied to evaluate the response to a lateral step input. As a result of this study, the best results were obtained with KY=0.4 and KPHI=2.0 .

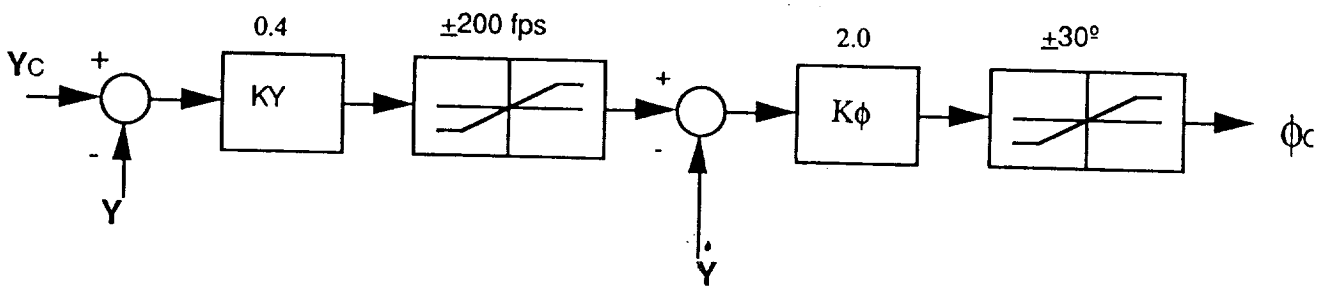

Figure 3-13 A/L Lateral Guidance Block Diagram

3.4 A/L Speed Control

PLS uses a speed controller method similar to the Space Shuttle's. The vehicle is controlled to follow a predetermined speed profile. The purpose of the speed controller during the A/L phase is to deliver the vehicle to a proper inertial speed at the start of the first flare. The desired nominal speed at the initiation of the first flare is approximately 350 knots of equivalent airspeed (KEAS).

The speed controller is most effective during the steep glideslope descent phase. During this phase, the speedbrake nominal setting is 20°. This setting allows for speedbrake deflections of ±20° to account for head and tail winds. The speedbrake retracts to a zero bias setting at the initiation of the first flare which occurs at an altitude of 2300 feet.

This results in a minimum drag configuration which is needed as the total energy quickly dissipates during the remainder of the flight.

A block diagram of the speed controller is shown in figure 3.-14 . The integral gain (K_{SI}) is used to reduce the regulator error (velocity error). The integrator stops integrating when the speedbrake position is limited. The upper limit is set by defining the input parameter SPBRUL (=30º nominal). The lower limit defaults to zero. The speedbrake bias ($\delta_{sb\text{-}bias}$) is set for the steep glideslope descent phase at 20º, and for the remainder of the flight the bias is set to 0º.

The 6-DOF simulation was used to evaluate the regulator gains and the integral gain values. The best results were obtained with the following gains:

- $K_S = -1.2$
- $K_{SI} = 0.4$

Wind conditions will affect the speedbrake performance. The wind uncertainty is corrected by the speed controller primarily during the steep glideslope descent . With a head wind, the speed controller retracts the speedbrake to reduce drag and maintain a constant KEAS. The speed controller performance in the presence of a maximum expected head wind of 22 knots was evaluated. A plot of the wind, speedbrake command and the velocity error is shown in figure 3-15 . These data were obtained during the steep glideslope descent phase. The results show the velocity error is well regulated, despite the speedbrake being limited at zero deflection during the last few seconds. The speed brake performance is covered in greater detail in section 4.5 .

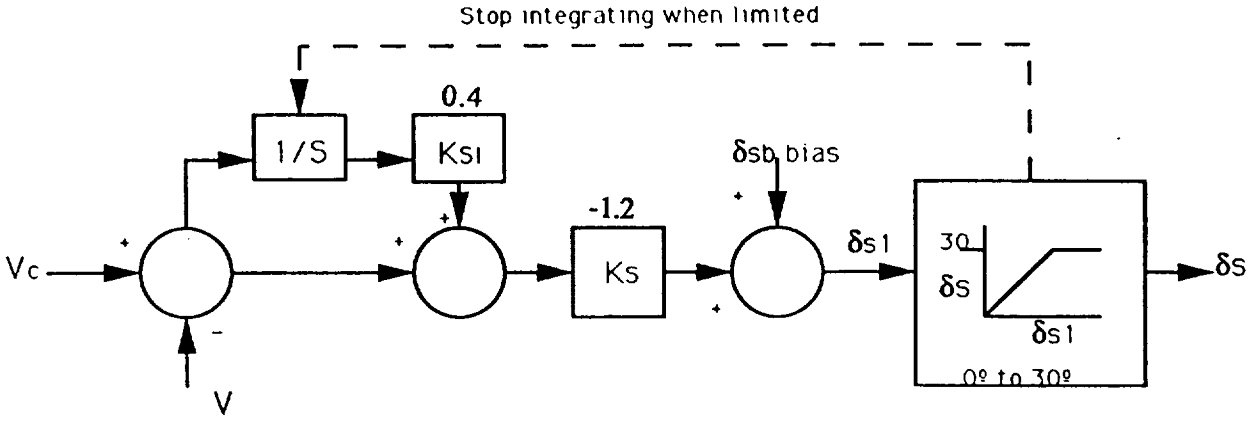

Figure 3-14 Block Diagram of A/L Speed Controller

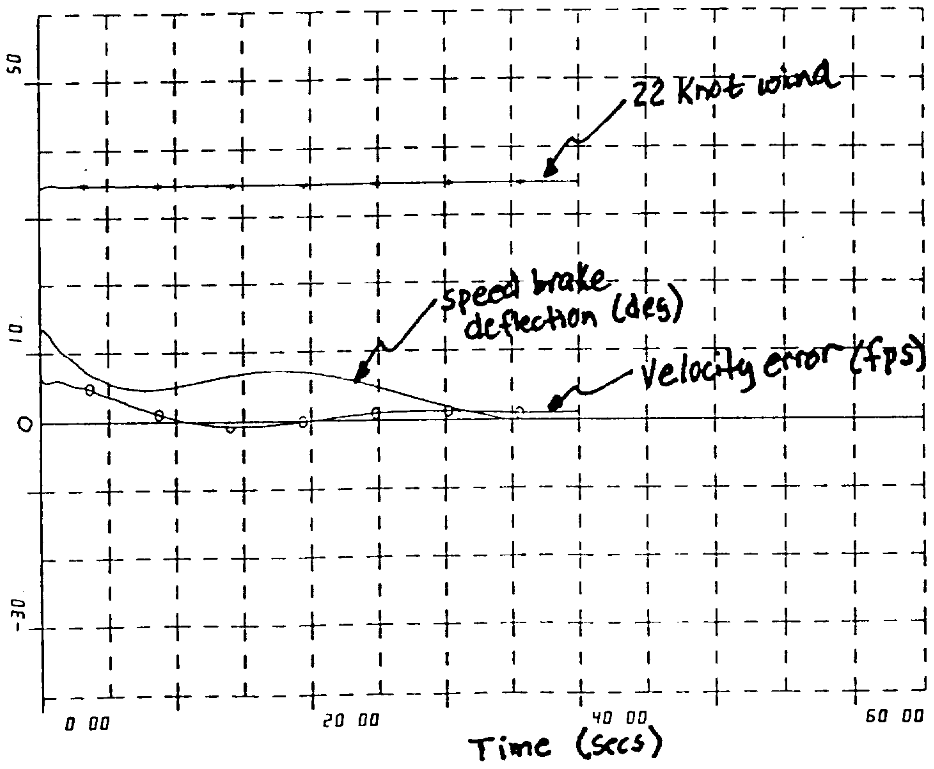

Figure 3-15 Speed Controller Performance (w/22 knot head wind)

4.0 Approach and Landing 6 DOF Simulation Analysis

The 6-DOF simulation was used to evaluate the performance of the A/L design. First, a parameter sensitivity study was performed to evaluate the effect of mission input parameters on vehicle touchdown performance. Then, different wind conditions were added to the simulation to evaluate the effect of wind on vehicle performance. Finally, the speed controller performance was analyzed.

4.1 Parameter Sensitivity Study

The 6-DOF simulation was used to evaluate the effect of mission input parameters on final touchdown performance. The purpose of this study is to determine what factors have the most influence on landing performance, that is, what is the sensitivity of a given parameter to landing performance. The results aid in determining nominal A/L mission input conditions and also give general trends that can be used in designing a mission. For example, increasing the shallow glideslope angle results in an increase of the touchdown velocity and sink rate, and decreases angle-of-attack. Therefore, if a higher vehicle velocity is desired to provide a larger energy margin in the presence of wind uncertainty near touchdown, and larger sink rates are acceptable, the shallow glideslope angle may be increased.

A test matrix was developed to perform repeated 6-DOF simulations without wind, varying the following A/L mission input parameters:

- GAM0= steep glideslope angle
- GAM1= shallow glideslope angle
- VT0= initial true airspeed
- V1= velocity at start of pullup maneuver
- H2= shallow glideslope capture altitude
- H3= start of 2nd (final) flare altitude
- HTDC= commanded touchdown altitude
- WFLAR2= 2nd flare command filter frequency (rps)

The following states are used to evaluate touchdown performance:

- Zdot= Sink rate (fps)
- α = angle-of-attack (deg)
- KEAS= velocity in knots of equivalent airspeed
- Qatm= Q-atmosphere, or dynamic pressure (psf)

The results are plotted in figures 4-1 through 4-9. These simulations were run without wind. Each plot contains the resulting touchdown conditions for a given mission input parameter. The mission general guidelines/requirements at touchdown given in table 1-1 serve as a tool in evaluating the landing performance. These mission guidelines, applied to landing in the absence of wind, results in the following design criteria :

- Zdot $\leq$ 2 ft/sec
- $\alpha \leq$ 15 degrees
- KEAS $\geq$ 200 knots

The effect of the steep glideslope angle (GAM0) on touchdown performance is shown in figure 4-1. In general, the increase in the glideslope angle results in better landing performance. Note that GAM0-22º yields an unacceptably high sink rate of 16.6 fps. The results of this test show that GAM0$\leq$-24º, the optimum being GAM0=-26º.

The effect of the shallow glideslope angle (GAM1) on touchdown performance is shown in figure 4-2. The touchdown performance is very sensitive to this parameter. Too small an angle (GAM1=-1.5º) results in the vehicle running out of speed and dynamic pressure causing a large angle-of-attack and an unacceptably high sink rate at touchdown. Essentially, the aircraft loses lift and "falls out of the sky". At the other end of the spectrum, (GAM1 = -3.0º), a higher glideslope angle results in sufficient speed and dynamic pressure, but also yields a large sink rate (Zdot=3.60 fps). The best landing performance meeting all of the design criteria is obtained with GAM1=-2.5º .

The touchdown performance is not very sensitive to the change in altitude at initiation of the shallow glideslope (H2) as can be seen in figure 4-3. It is desirable to initiate this at an altitude high enough to reduce the sinkrate to an acceptable value prior to the final flare. On the other hand, too high an altitude may cause unacceptable energy loss and stall before touchdown. As a result, a nominal value of H2=250 feet is chosen.

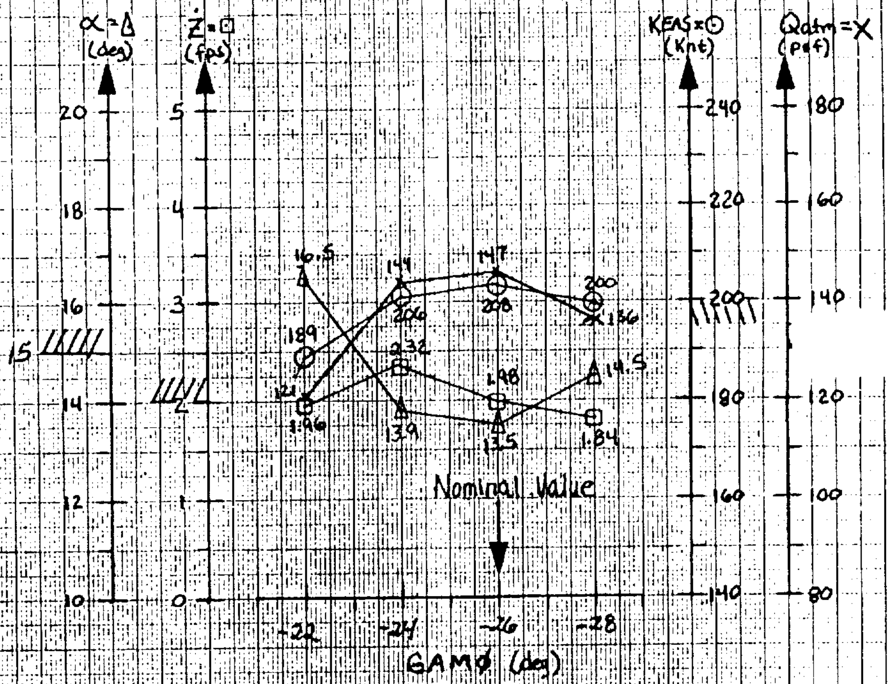

Figure 4-1 Touchdown Conditions as a Function of Steep Glideslope Angle

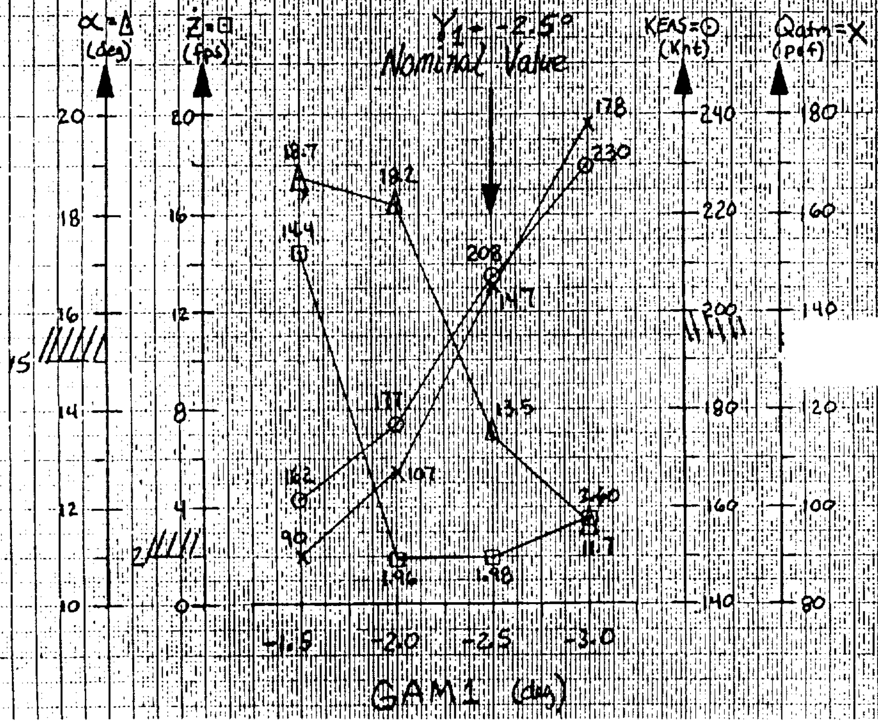

Figure 4-2 Touchdown Conditions as a Function of Shallow Glideslope Angle

ORIGINAL PAGE IS OF POOR QUALITY

The sink rate at touchdown is very sensitive to the change in altitude at initiation of the final flare (H3) as shown in figure 4-4. In order to maintain a low sink rate at touchdown, H3 was chosen to be greater or equal to 70 feet; this allows for a sufficient altitude for the autoland system to decrease the sink rate. However, increasing H3 has the negative effect of lowering the landing speed. Therefore, the nominal value of H3 is set to 70 feet.

Figures 4-5 and 4-6 shows the effect of additional touchdown parameters on landing performance. The commanded touchdown altitude (HTDC) has a dramatic affect on the touchdown performance, especially on the sink rate. Only one of the four specific conditions investigated satisfies all the design criteria, at HTDC=-10 feet. HTDC=-5 feet yields better sink rate performance but at the expense of a lower KEAS. The final flare rate (WFLAR2) also affects the touchdown performance as shown in figure 4-6 . The best choice is for WFLAR2=0.28 rad/sec.

The next two plots show an interesting contrast between using the speed controller versus not using the controller, as a function of initial velocity (VT0). As could be expected, with the speed controller turned off, the touchdown end conditions are a linear function of the initial velocity as shown in figure 4-7. A 50 ft/sec increase in initial velocity yields a corresponding 6 ft/sec increase in final touchdown velocity, a linear increase in sink rate, and a linear decrease in angle-of-attack. However, with the speed controller turned on, the touchdown conditions remain fairly constant despite a change in initial velocity as shown in figure 4-8 . This result shows the effectiveness of the speed controller in taking out velocity deviations.

The results of the speed controller comparison test indicate that in order to affect the touchdown conditions, the speed controller setting must be changed. The speed controller is most effective during the steep glideslope descent phase, during which a constant KEAS velocity (V1) is commanded up to the initiation of the pullup maneuver. A test was performed varying V1 from 310 to 370 KEAS and the results are plotted in figure 4-9 . The results show that for an acceptable touchdown, V1≥330 KEAS should be used. It is desirable to maintain a V1 low enough to avoid reaching the maximum allowable dynamic pressure when wind turbulence or gusts occur. This criteria yields the selection of V1=330 KEAS. However, wind disturbance may decrease the touchdown speed and require a higher V1. As a result of wind conditions tests, V1 is chosen to be V1=350 KEAS. This case is presented in section 4.3.3 and 4.3.4.

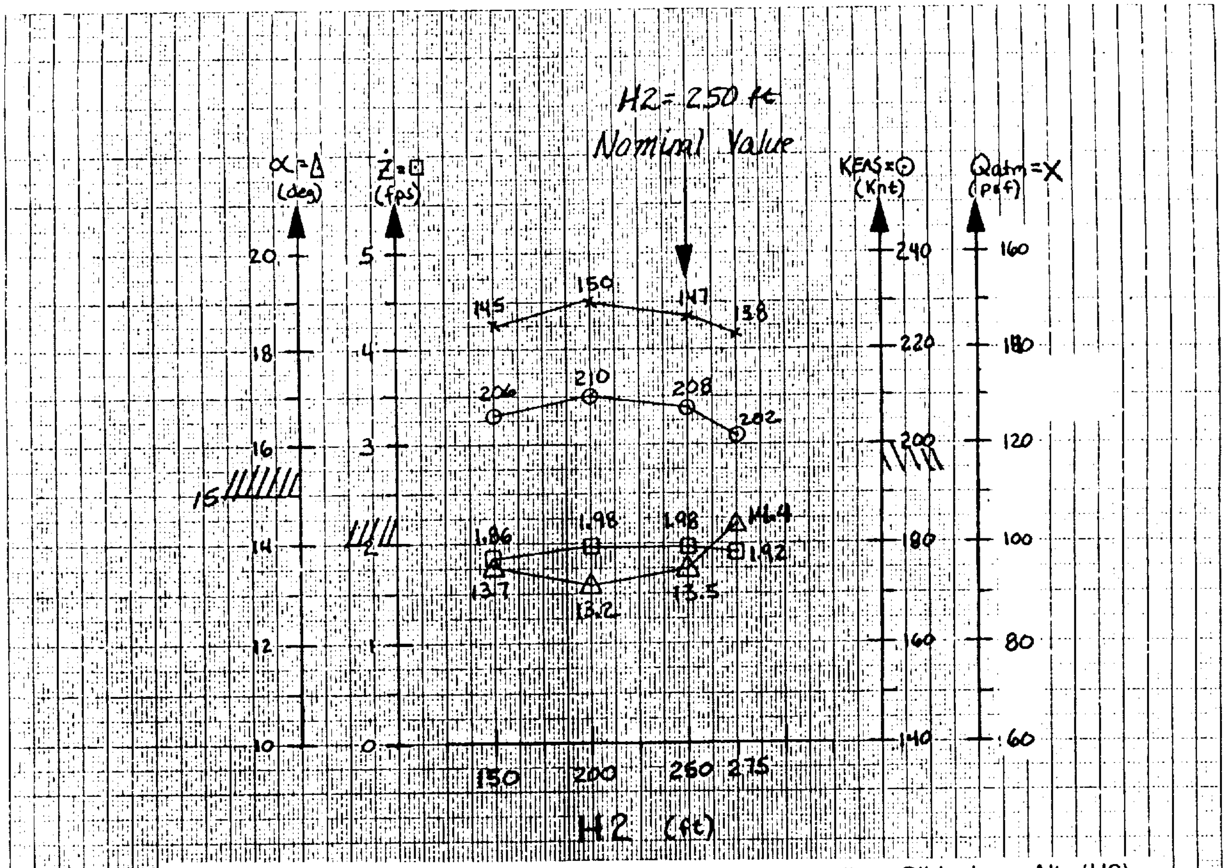

Figure 4-3 Touchdown Conditions as a Function of Shallow Glideslope Alt. (H2)

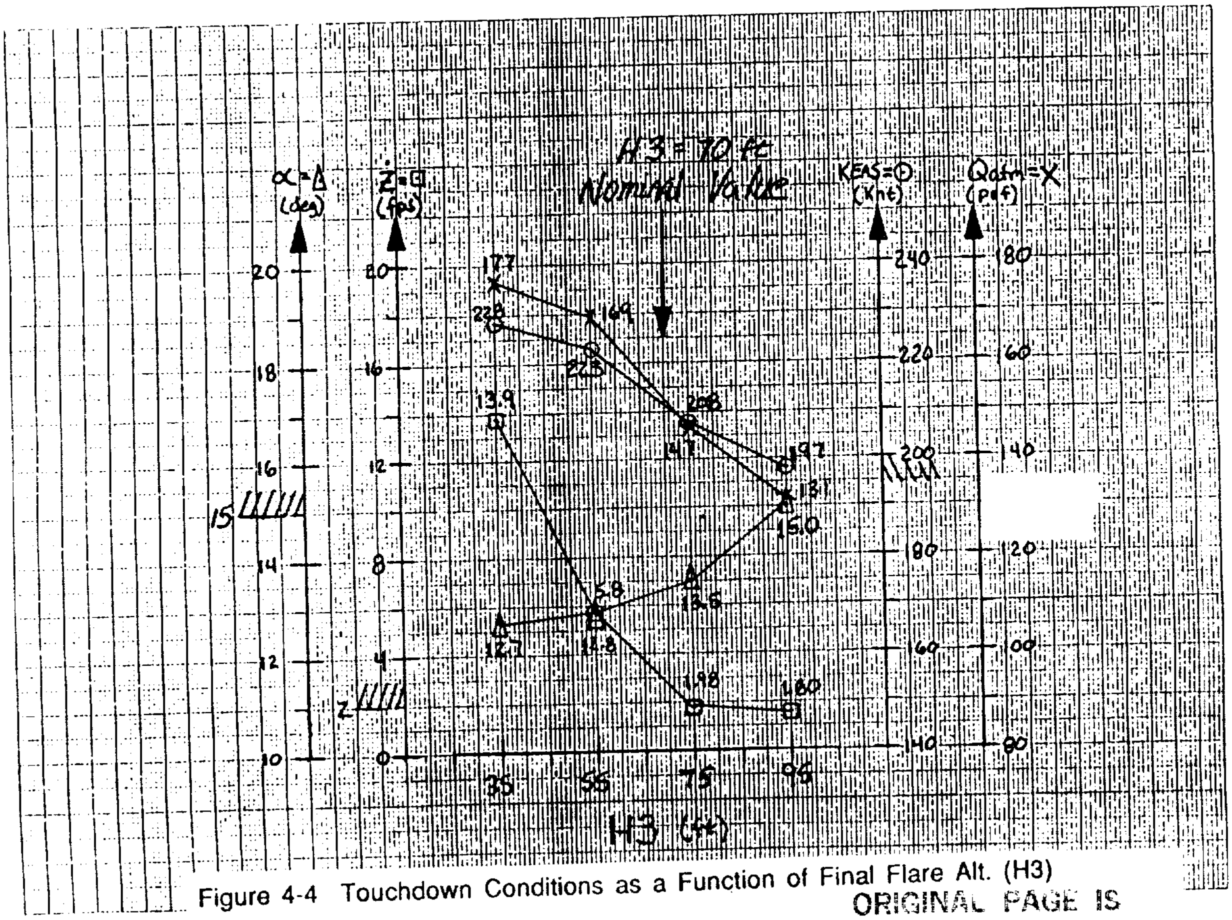

Figure 4-4 Touchdown Conditions as a Function of Final Flare Alt. (H3)

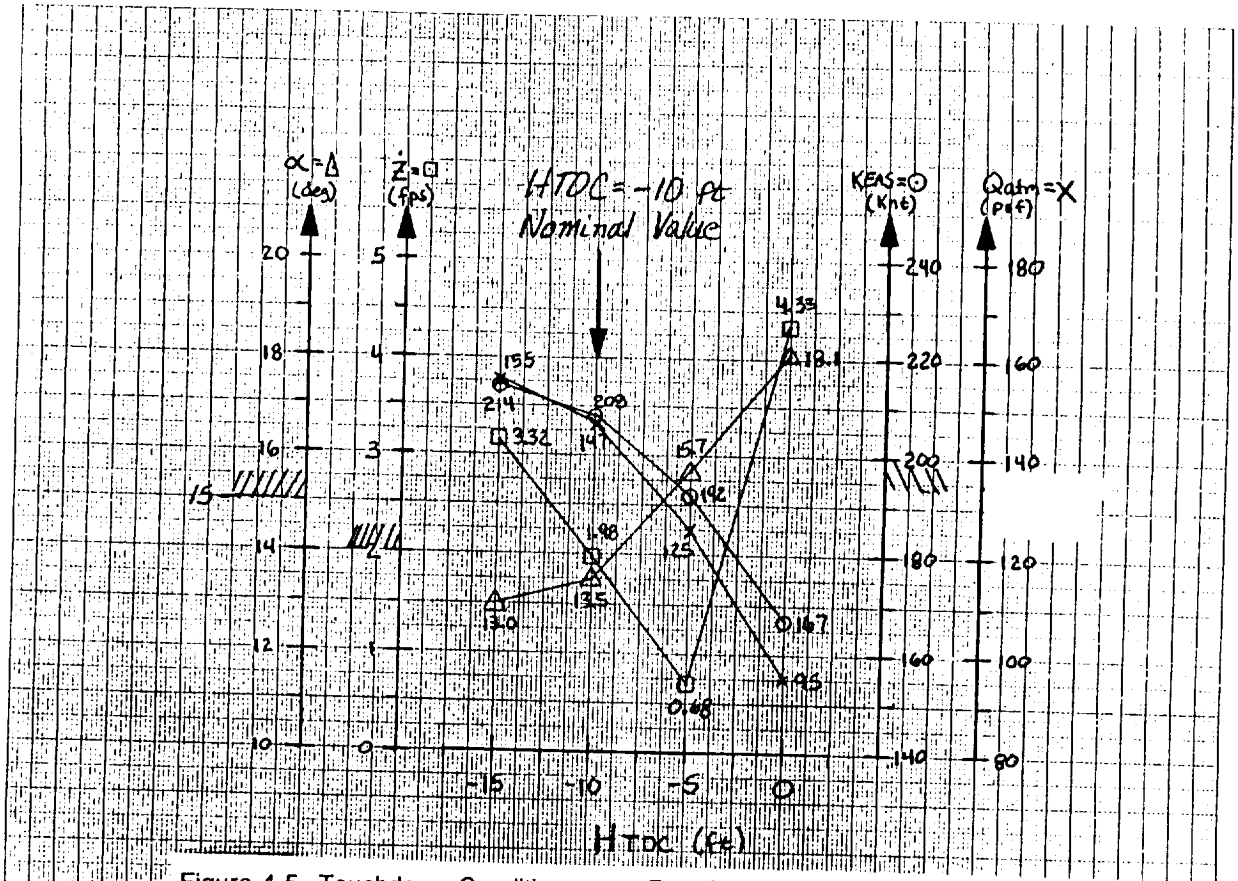

Figure 4-5 Touchdown Conditions as a Function of T.D. Command Alt (HTDC)

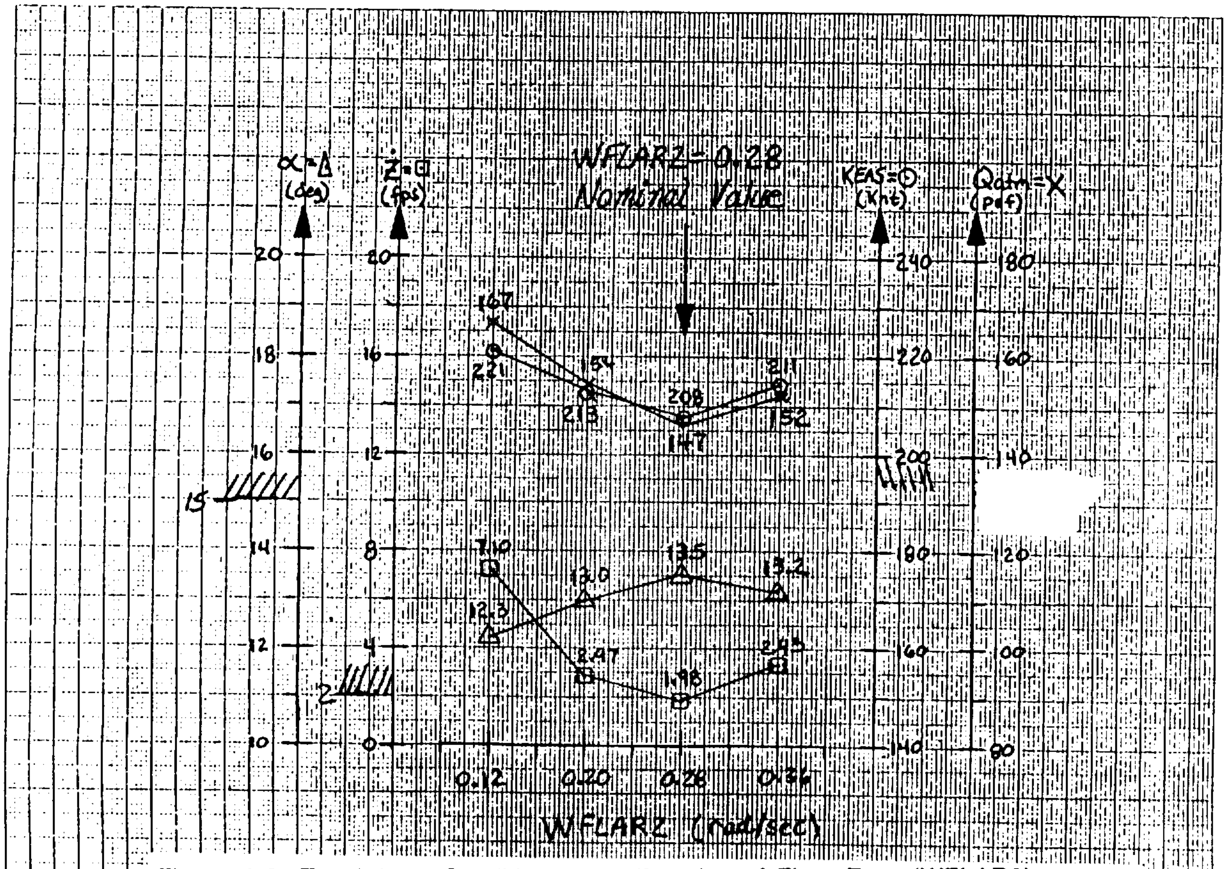

Figure 4-6 Touchdown Conditions as a Function of Flare Rate (WFLAR2)

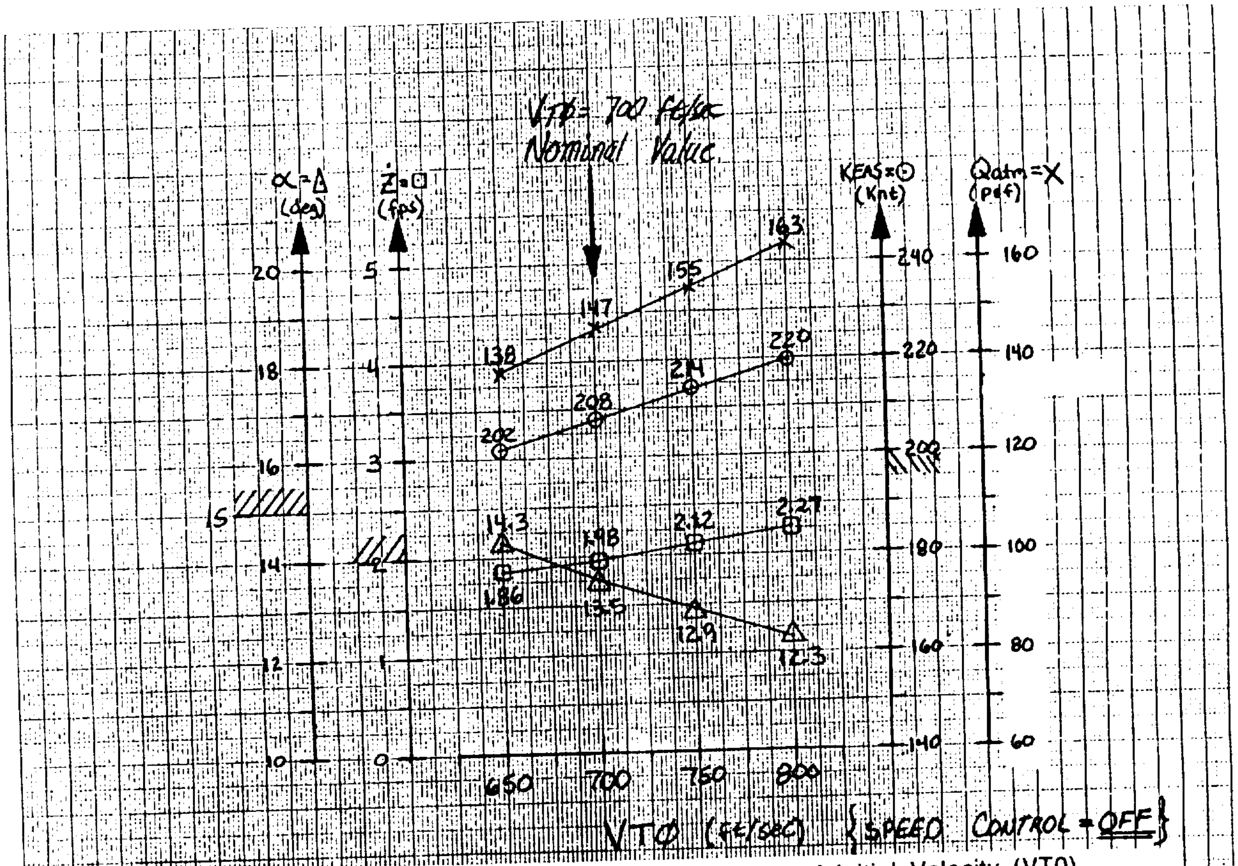

Figure 4-7 Touchdown Conditions as a Function of Initial Velocity (VT0) With Speed Controller **OFF**

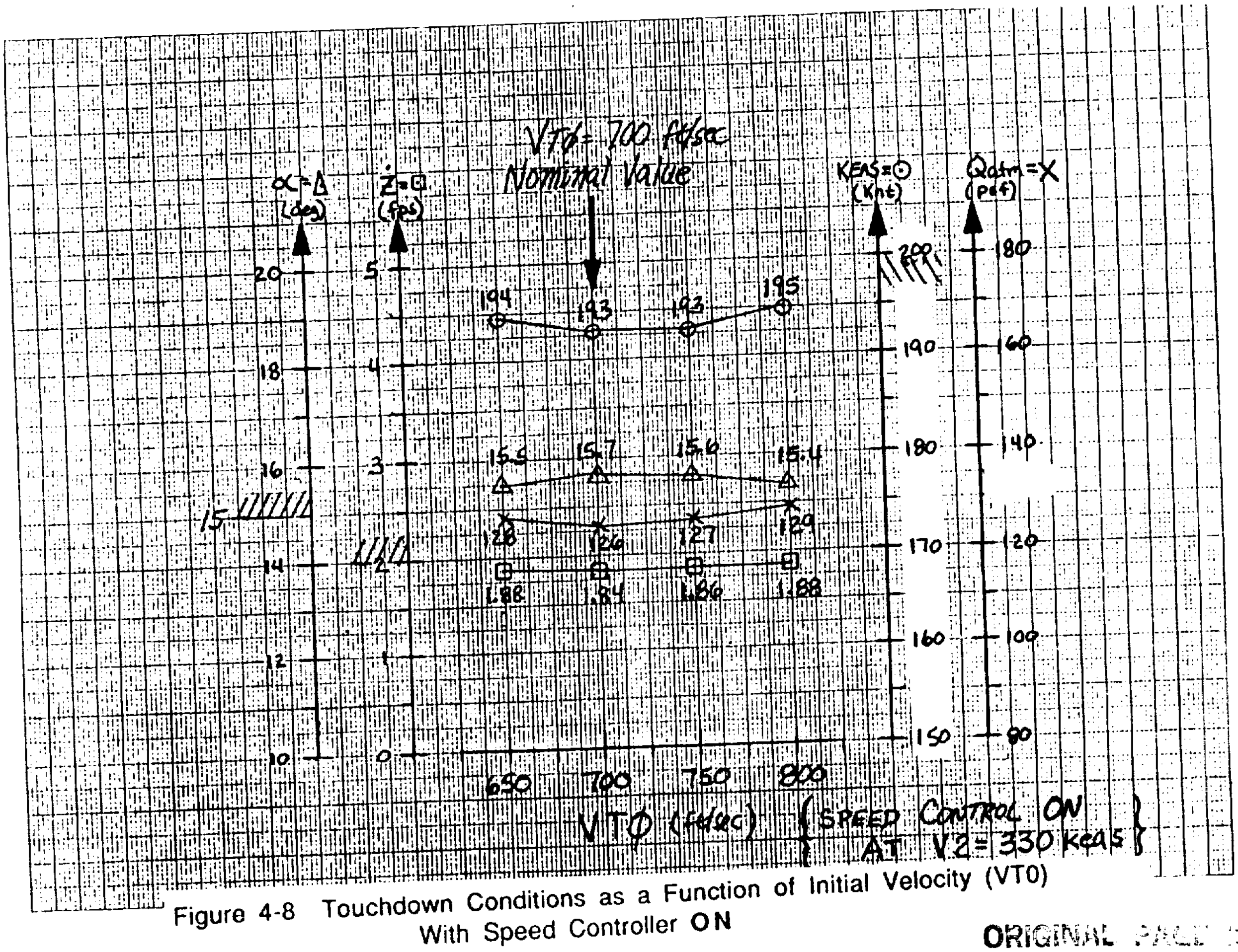

Figure 4-8 Touchdown Conditions as a Function of Initial Velocity (VT0) With Speed Controller **ON**

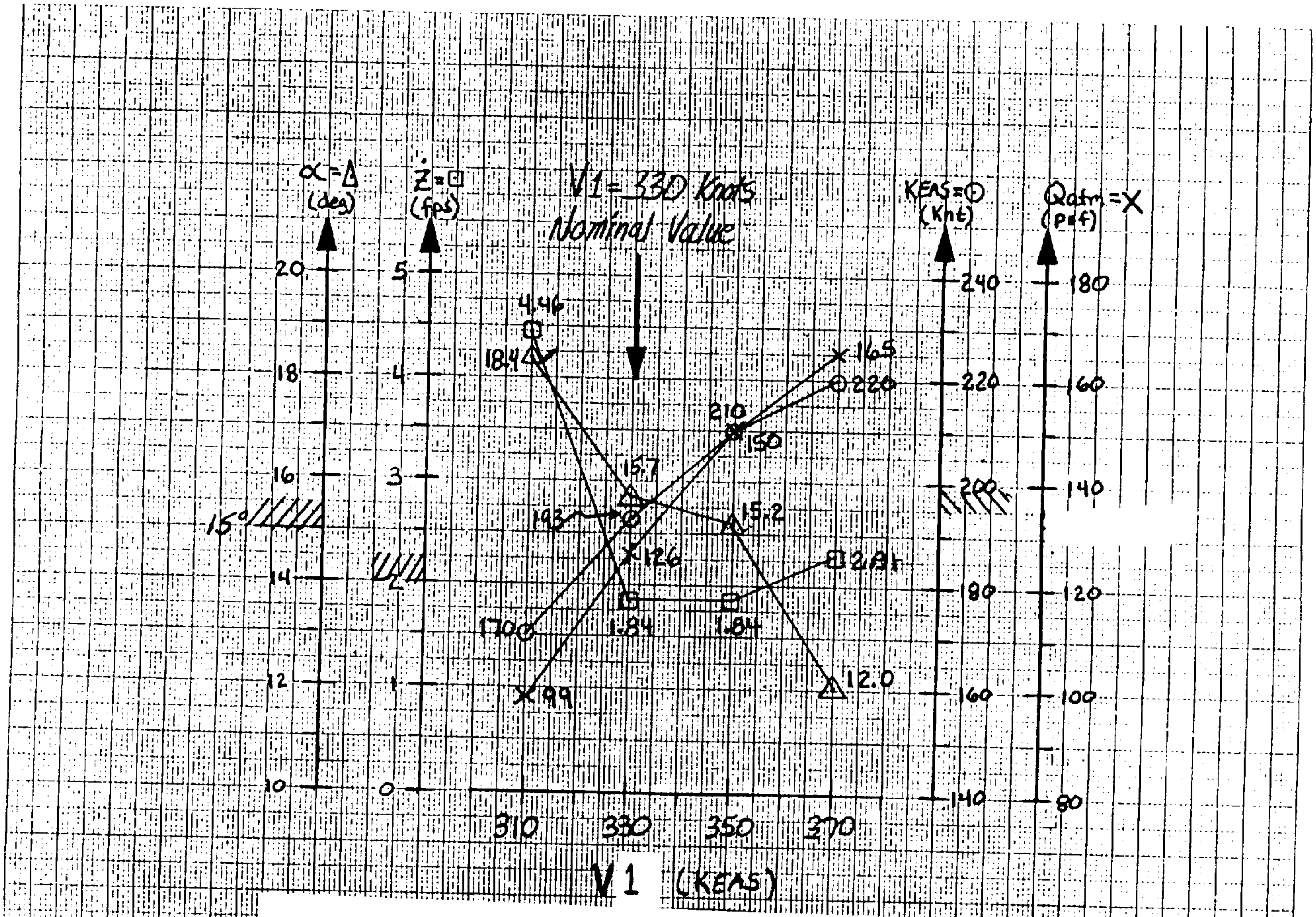

Figure 4-9 Touchdown Conditions as a Function of Steep Glideslope Controlled Velocity (V1)

4.2 Landing Performance Without Wind

As a result of the parameter sensitivity study, the mission input parameters that result in an acceptable touchdown were determined for the case without wind. These parameters, summarized below in table 4-1, form a database that defines the nominal PLS autoland mission parameters . These parameters were tested using the 6-DOF simulation to evaluate the touchdown performance with the no wind condition. The results of the final touchdown conditions are summarized in table 4-1.

The complete simulation results are given in appendix D. However, a few plots are given in figures 4-10 through 4-12 to show general autoland landing performance. Figure 4-10 shows the velocity and dynamic pressure dynamics as a function of range (s). The constant KEAS velocity of 330 knots is clearly seen during the steep glideslope descent phase. The altitude profile versus range is shown in figure 4-11.

Figure 4-12 contains the altitude, sink rate, angle-of-attack, flight path angle and normal acceleration dynamics as a function of time, during the final approach and flare phases. The results show an excellent sink rate (Zdot) performance. The final flare initiates with Zdot=16 fps at approximately 60 foot altitude, and decays such that at an altitude of 20 feet, the sink rate is 10 ft/sec. In addition, the angle-of-attack profile during the entire approach and landing is benign, requiring approximately 14º at touchdown.

The simulation without wind established the nominal autoland performance of the PLS vehicle. The addition of wind turbulence and discrete wind gust is the final test of the autoland performance. This is covered in the next sections.

Input Parameter	Value	Description
GAM0	-26°	steep glideslope angle
GAM1	-2.5°	shallow glideslope angle
VT0	700.	initial velocity (fps)
V1	330.	steep descent speed control setting (KEAS)
WFLAR1	0.220	1st flare rate (rps)
WFLAR2	0.280	2nd flare rate (rps)
ZFLARE	1.0	flare damping ratio zeta
DELS	7000	1st flare (constant g pullup) delta range
DELH	2000	1st flare (constant g pullup) delta range
H1	2300	start of 1st flare altitude
H2C	300	end of 1st flare altitude
H2	250	shallow glideslope capture altitude
H3	70	start of 2nd (final) flare altitude
HTDC	-10	commanded touchdown altitude
ACIR	0.5	g pullup during 1st flare

Touchdown Condition	Value	Description
Zdot	1.98	sink rate (fps)
KEAS	208.	knots of equivalent airspeed
Vtot	352.	total velocity (fps)
Qatmos	147.	dynamic pressure (psf)
alpha	13.5	angle-of-attack (deg)
ΔY	≈ 0.	cross-track error (feet)

Table 4-1 Touchdown Performance For A/L Nominal Trajectory Without Wind

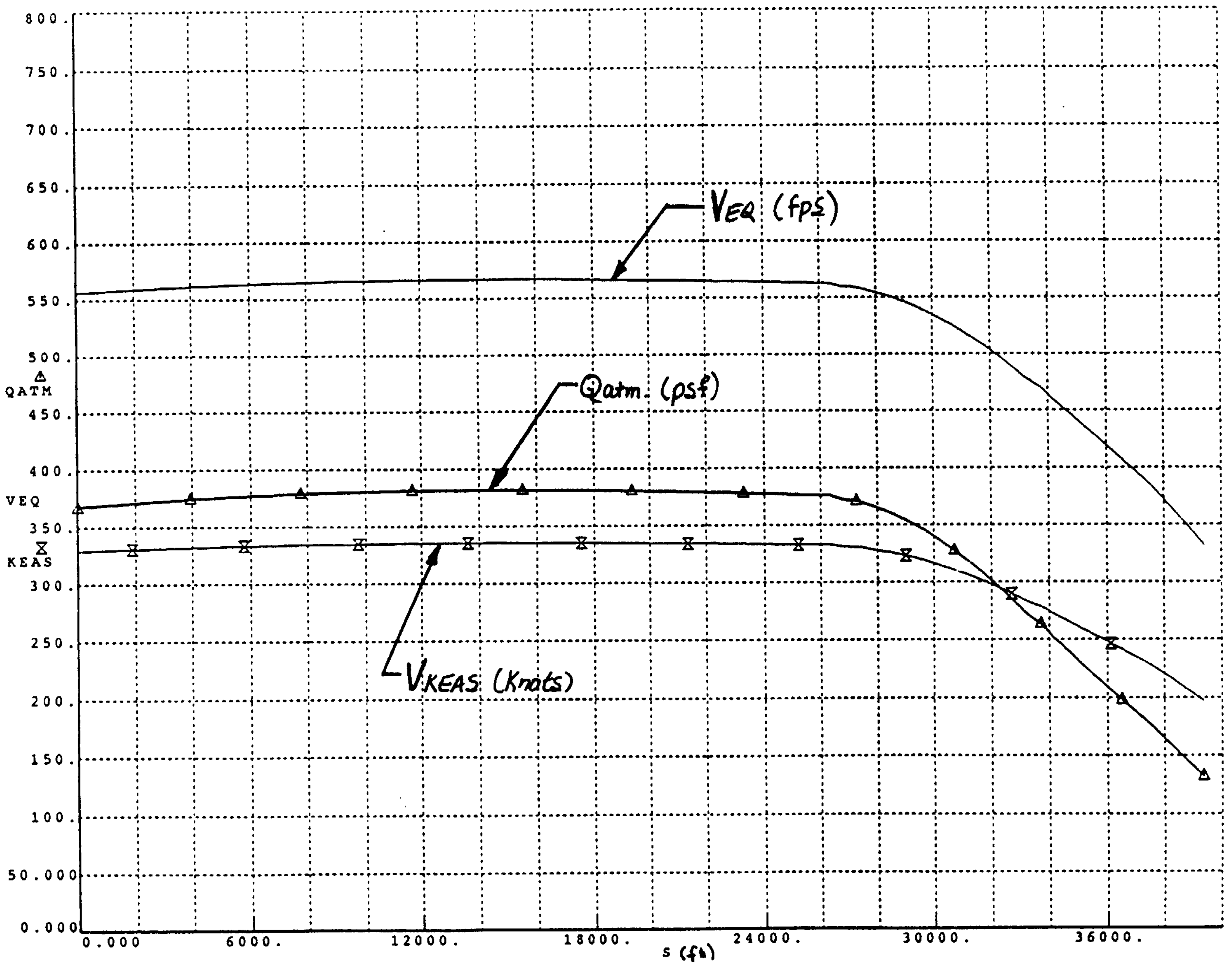

Figure 4-10 Velocity and Dynamic Pressure Results From Nominal A/L Simulation - NO Winds

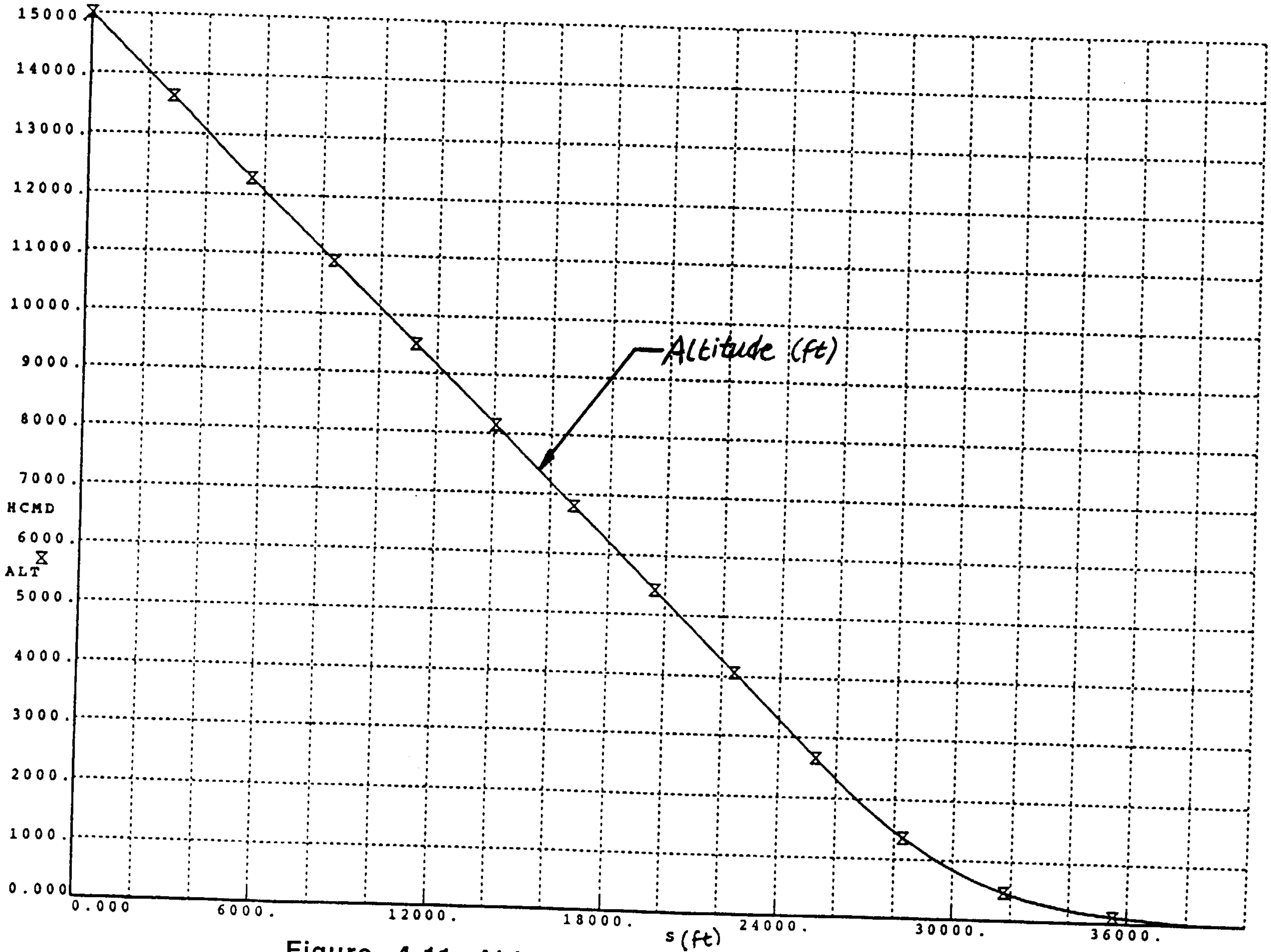

Figure 4-11 Altitude Performance Results From Nominal A/L Simulation - NO Wind

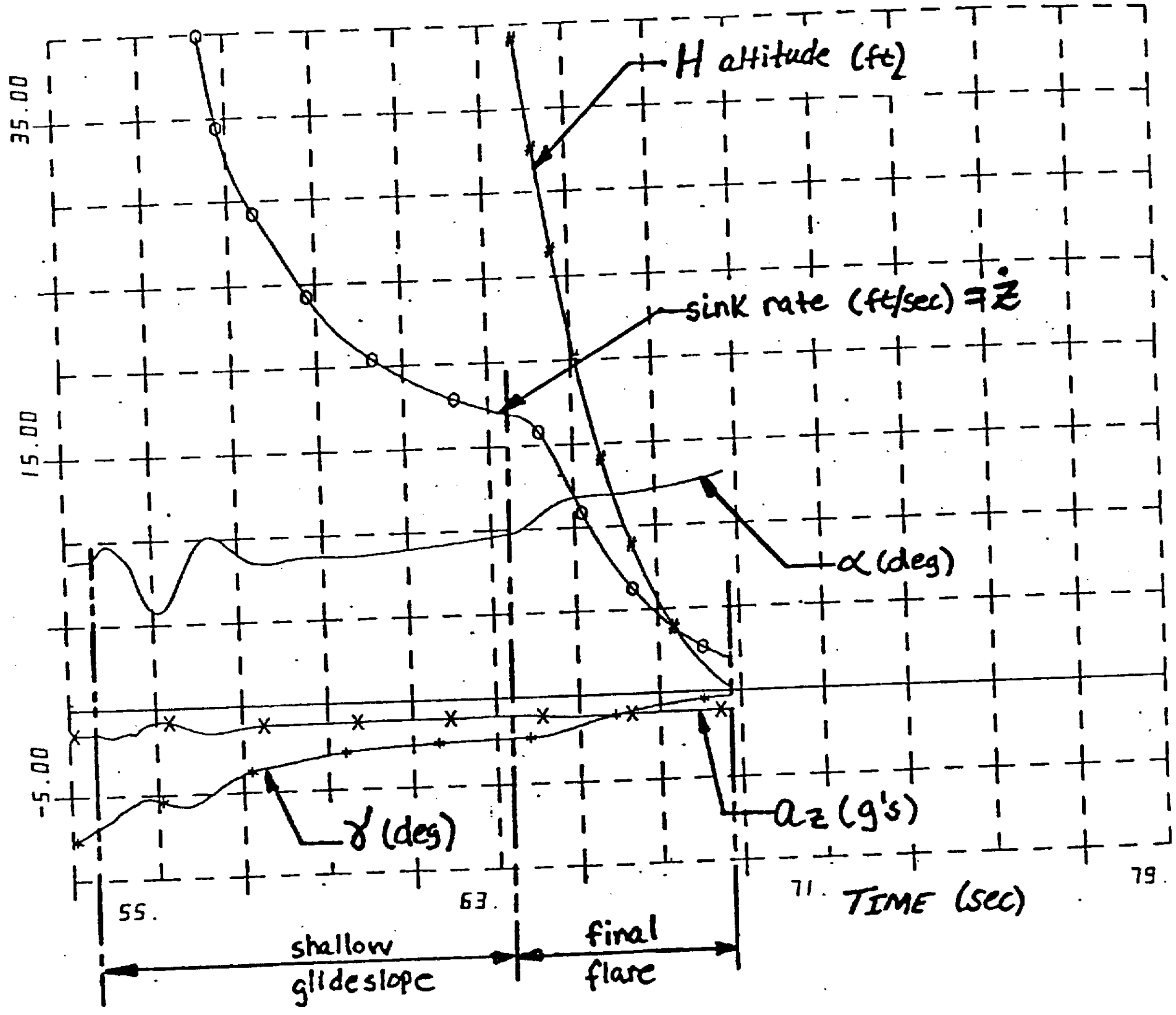

Figure 4-12 Touchdown Time History for Nominal A/L Simulation - NO Winds

4.3 Landing performance in wind turbulence

The wind turbulence model is extracted from the work of Holley and Bryson (reference 4), in the article "Wind Modelling and Lateral Aircraft Control for Automatic Landing", January 1975, Standford University Department of Aeronautics and Astronautics Report (SUDDAR) No. 489. The model approximates the major characteristics of the Dryden and Von Karman wind models. A description of the wind model is included in Appendix C.

The 6-DOF simulation contains the GRAM atmospheric database with 16 different atmospheres. This model was used to generate a steady wind profile. One of the 16 atmospheres was chosen as the nominal wind profile to be used for evaluating the PLS performance with wind. This profile was chosen because it simulated a strong longitudinal wind useful for evaluating longitudinal performance. The PLS nominal A/L flight trajectory was flown through this steady wind profile and was augmented with the wind turbulence data. The final wind profile is shown in figure 4.-13. The wind turbulence has a Gaussian distribution of 1σ equal to 5 knots for the x and y axes, and 3 knots for the z axis. The integral scale length is Lu=69 ft, Lv=36 ft, and Lw=16 ft.

The effect of the wind turbulence on landing performance is summarized in table 4-3. The results show acceptable landing performance with all requirements being met. The sink rate of 1.80 ft/sec is excellent. The ΔX and ΔY values represent the deviation from the nominal runway touchdown without wind, and falls within the required landing "footprint". Time history plots are given in Appendix E .

Touchdown Condition	Value	Description
Zdot	1.80	sink rate (fps)
KEAS	180.	knots of equivalent airspeed
Vtot	304.	ground velocity (fps)
Qatmos	117	dynamic pressure (psf)
α	17.0	angle-of-attack (deg)
ηcrab	= 0.	crab angle(deg)
ΔY	= 0.	cross-track error (feet)
ΔX	-116.	along-track error (feet)

Table 4-3 Touchdown Performance With Wind Turbulence

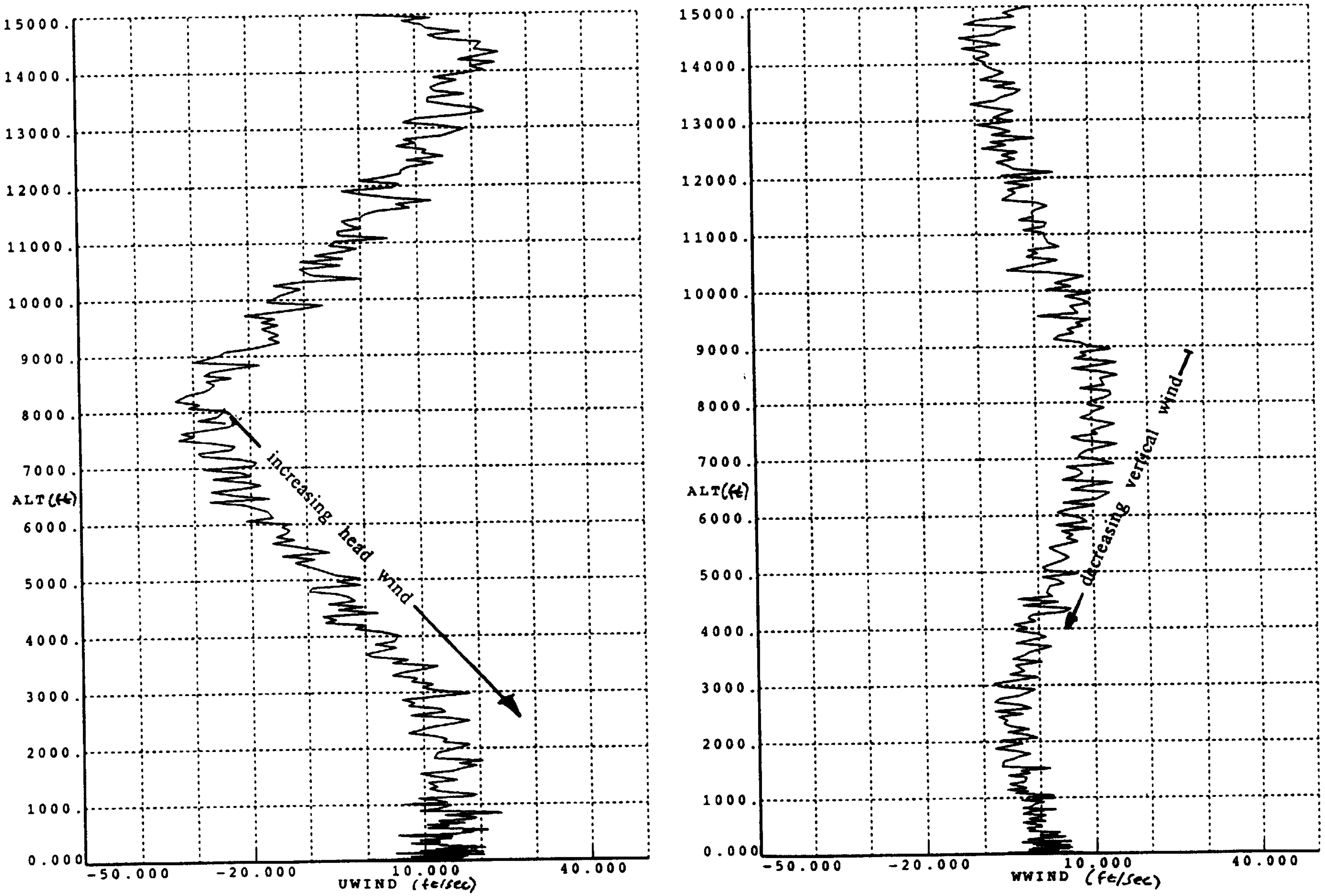

Figure 4-13 Approach and Landing Turbulent Wind Profile

4.4 Landing Performance in Wind Shear

A wind shear of magnitude 8 knots/100 ft altitude was added to the wind to obtain a wind shear profile at landing. The wind shear was added first as head wind, and then as a cross wind.

Three wind conditions were evaluated. Two head wind profiles were developed as shown in figure 4-14. The first profile contains a constant 30 knot head wind profile at landing, and second profile contains a 30 knot head wind with a decreasing final shear. With both cases, the head wind increases from 0 at an altitude of 4925 feet to 30 knots at an altitude 2300 feet, the altitude at which the pullup maneuver begins. The increasing headwind at this part of the flight presents a worst case scenario in terms of speed control because once the pullup maneuver begins, the speed profile is dominated by high deceleration and changing wind conditions. However, this wind would increase the airspeed which is not necessarily worst case in terms of maintaining sufficient airspeed for the landing. The second wind condition is a worst case condition in terms of landing because of the decreasing headwind starting at 375 feet. This will cause a decreasing airspeed which could result in unacceptably low touchdown airspeed. The third wind shear condition is a cross wind profile. This profile contains an increasing cross wind shear of 8 knots/100 ft altitude to a maximum of 22 knots at landing, as shown in figure 4-14.

A summary of the touchdown conditions is given in table 4-3 for all three wind shear conditions.

As expected, excellent landing performance was obtained with the constant 30 knot head wind (condition 1). The addition of the final shear greatly affected the angle-of-attack. This wind shear is similar to having a sudden tail wind. The sudden decrease in total velocity due to the wind shear, causes a decrease in lift. As a result, a high angle-of-attack is commanded. Despite this, the touchdown requirements were still met.

	Touchdown Results			
Parameter	Cond. 1	Cond. 2	Cond. 3	Description
Zdot	1.84	1.90	2.0	sink rate (fps)
KEAS	205.	180	211	knots of equiv.airspeed
Vtot	346.	110	359	ground velocity (fps)
Qatmos	142	304	152	dynamic pressure (psf)
α	13.9	18.0	13.0	angle-of-attack (deg)
ηcrab	= 0.	= 0.	6.0	crab angle(deg)
ΔY	= 0.	= 0.	8.0	cross-track error (ft)
ΔX	215.	206	5.0	along-track error (ft)

Table 4-3 Touchdown Performance With Wind Shear

A decrab maneuver was not performed at touchdown. Despite this, the cross wind shear of 22 knots resulted in a crab angle of only 6 degrees.

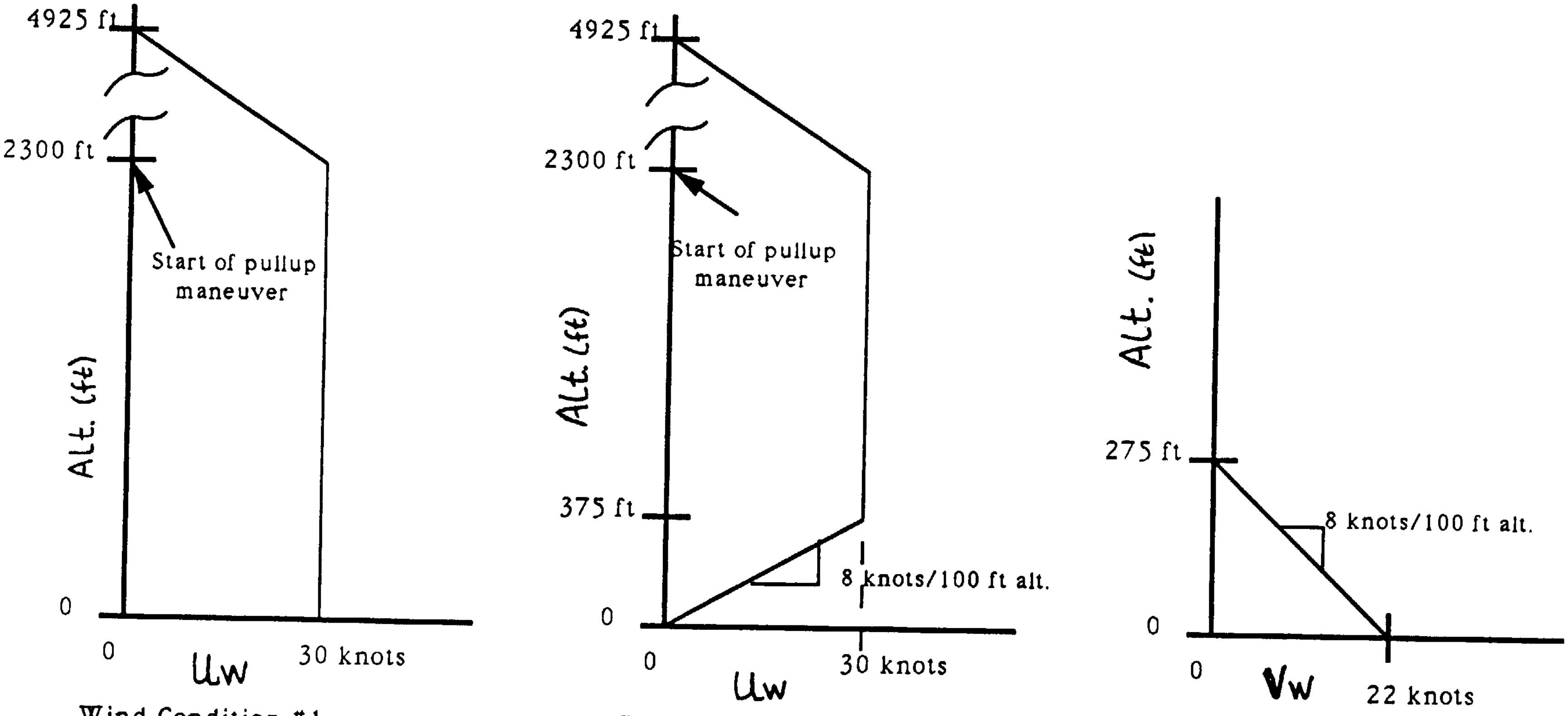

Wind Condition #1
Head Wind Profile

Wind Condition #2
Head Wind W/ Final
Shear Profile

Wind Condition #3
Cross Wind Shear
Profile

Figure 4-14 Wind Shear Profile

4.5 Speed Control Performance

To evaluate the speed control performance in the presence of head winds, simulation runs were executed with the speed controller OFF and ON . The results are shown in figure 4.-15. The resulting velocity error is plotted for two conditions of speed controller off and on. The vehicle inertial velocity is controlled to within 2 fps of the velocity command. The wind profile is superimposed on the plot. Note the additional discrete gust profile which occurs at the end of the mission when the speed controller is disabled. The resulting speedbrake command is shown in figure 4-16 with the wind profile included.

The speed control performance is further proven in the summary of the touchdown condition given in table 4-4. The nominal simulation without wind is used as a measure of speed controller performance. With head winds shown in figure 4-15, the speed controller was turned OFF and then ON. With the speed controller OFF, the touchdown speed (KEAS) is unacceptably lowered by 11 knots, and the touchdown footprint (ΔX) is dispersed 54 feet from the nominal. However, with the speed controller ON, the touchdown sink rate (ZD) and the velocity (KEAS) are identical with the nominal no wind case; the touchdown footprint is only dispersed by 4 feet.

Simulation Case	Speed Control	Wind	Zdot fps	KEAS knots	Alpha deg	ΔX-touchdown feet
Nominal Case	ON	OFF	1.87	196	15.4	N.A.
ControllerOFF	OFF	ON	1.85	185	17.1	-54.
Controller ON	ON	ON	1.87	196	15.2	-4.

Table 4-4 Summary of Touchdown Conditions With Speed Controller OFF Versus ON

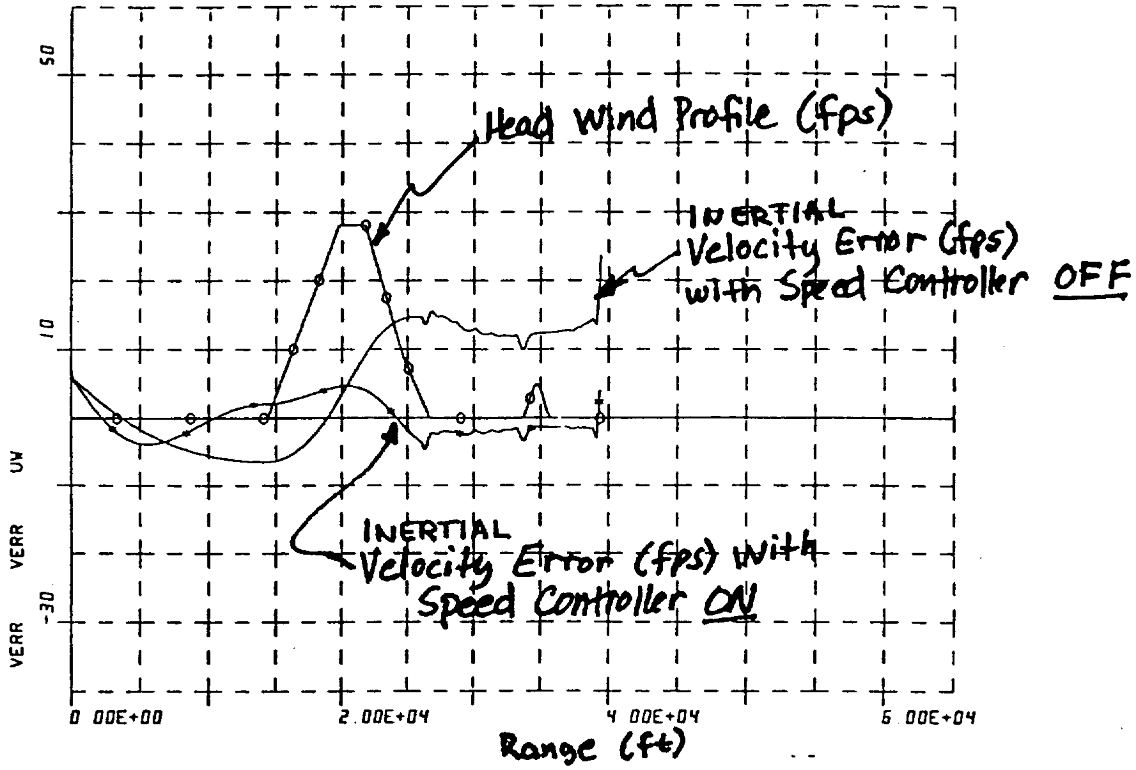

Figure 4-15 Velocity Error With Speed Controller ON Versus OFF

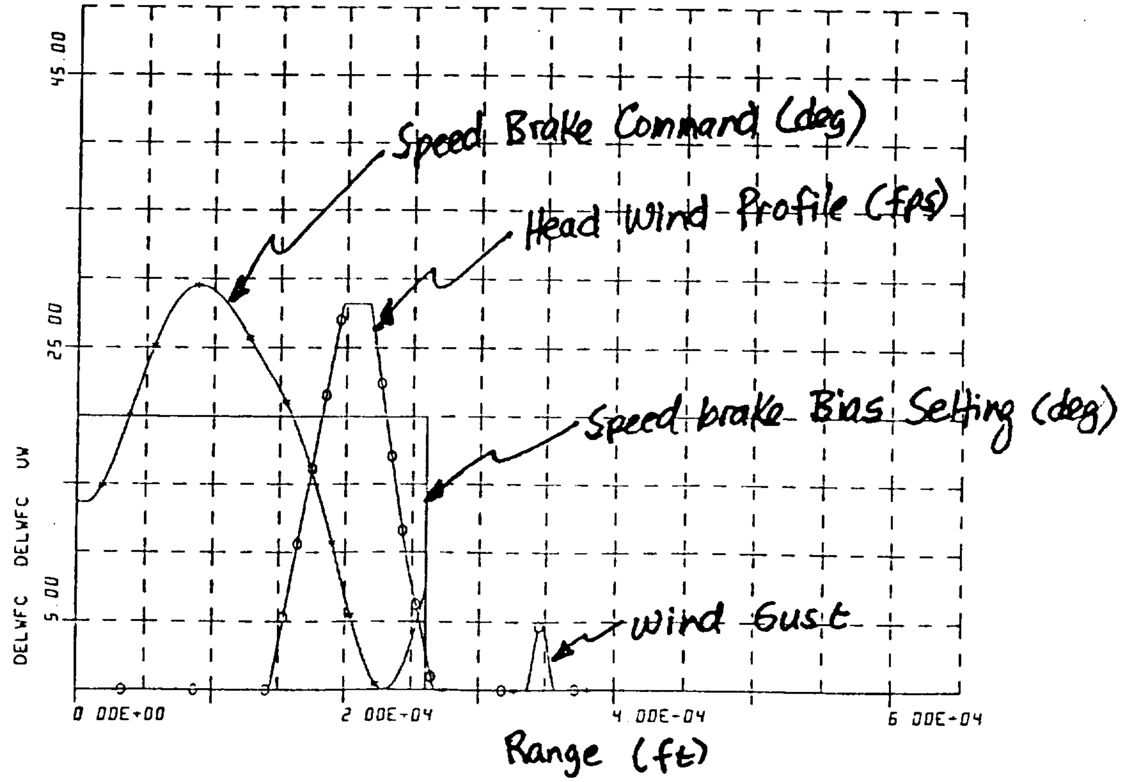

Figure 4-16 Speed Brake Command Profile In Presence of Wind

5.0 TAEM Design Synthesis

Our approach for the Terminal Area Energy Management (TAEM) design synthesis is to integrate the TAEM mission together with the guidance and control laws used on the approach and landing phase. The guidance gains have been developed consistent with the TAEM flight conditions and maneuver requirements. Minor changes are incorporated in the autopilot gains to assure stability at the TAEM flight conditions. An overview block diagram for the integrated TAEM mission generator and guidance law is shown in figure 5-1. The TAEM trajectory generator forms commands for the longitudinal guidance, speed controller, and the lateral guidance.

5.1 TAEM Guidance and Control

The TAEM longitudinal guidance system is made up of the trajectory generator and altitude controller. The trajectory generator generates a spiral trajectory command. The altitude controller translates altitude and sink rate commands from the trajectory generator into angle-of-attack commands.

The following section describes the trajectory generator and longitudinal guidance and control.

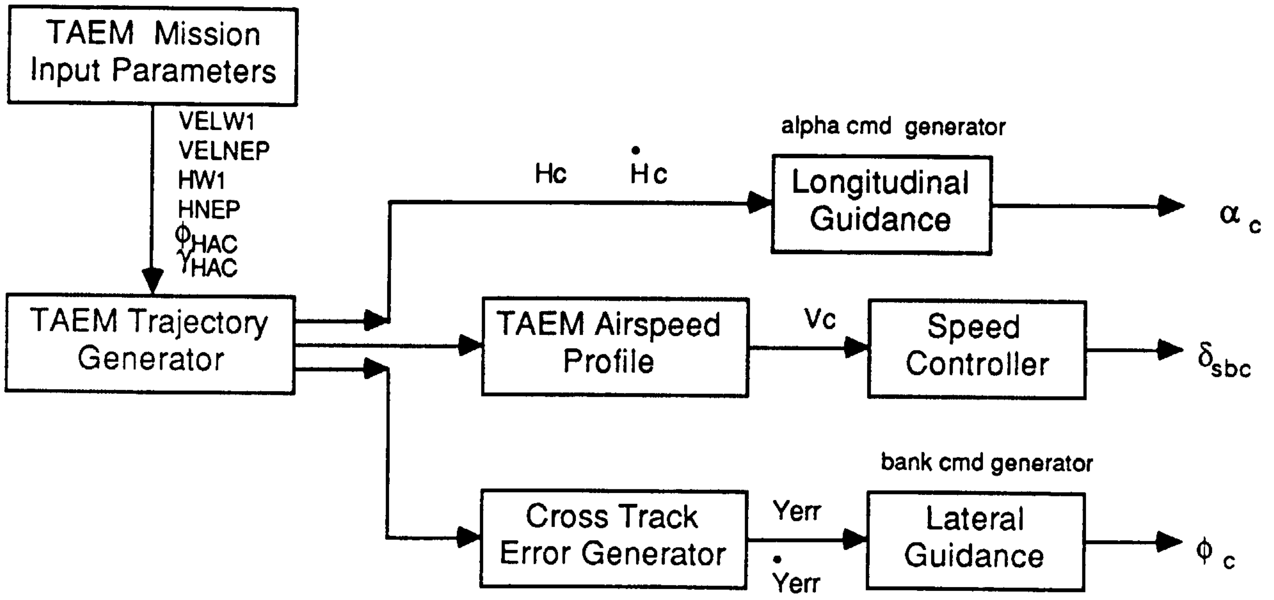

Figure 5-1 Simplied Block Diagram of TAEM Guidance and Control System

5.1.1 TAEM Trajectory Generator

Our approach in the PLS trajectory generator is to adapt the Shuttle's TAEM system. The Shuttle's TAEM consists of the following 4 guidance phases :

- Phase 0: S-Turn Phase is an optional phase for excess energy condition. Vehicle turns away from the nominal approach to increase ground track range.
- Phase 1: Acquisition Phase is performed to acquire a heading which is tangent to the heading alignment cone (HAC).
- Phase 2: Heading Alignment Phase rolls the vehicle to follow a spiral trajectory along the heading alignment cone.
- Phase 3: Prefinal Phase converges trajectory to the final approach plane until A/L phase is captured within a set criteria.

Guidance phases one through three are graphically illustrated in figure 5-2 . TAEM acquisition phase initiates at Mach 2.5 and 82000 ft altitude. The heading alignment phase initiates at Mach<1.0 at a nominal altitude of 35,000 feet and terminates at the acquisition of the A/L phase at Mach 0.6 and 15,000 ft altitude.

In this report, the design analysis is included for phases 2 and 3 (heading alignment and prefinal phases). The two initial TAEM phases are left to future analysis.

- **Terminal Area Energy Management (TAEM) Phases:**

  1) Acquisition
  2) Heading alignment
  3) Pre-final approach and trajectory capture (TAEM-A/L switching)

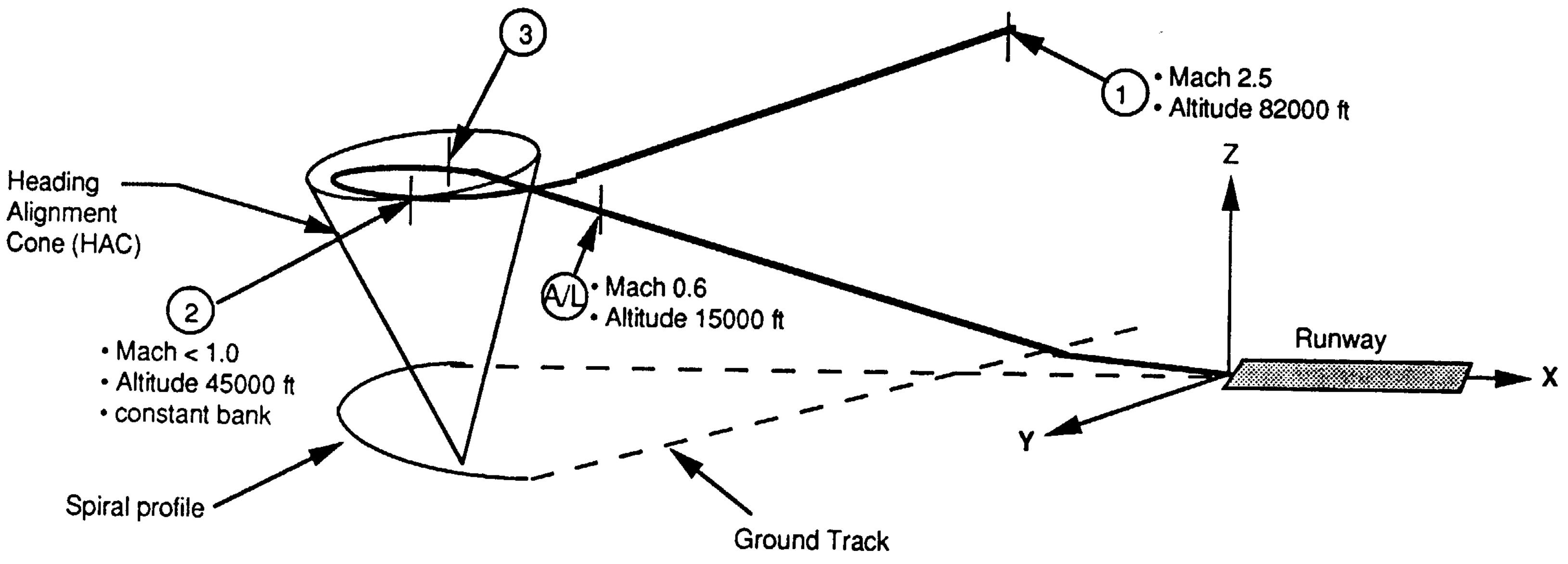

Figure 5-2 TAEM Guidance Phases

Figure 5-3 shows the HAC configuration in greater detail. The heading alignment phase maneuvers the vehicle onto final approach by flying around the HAC. The HAC is an imaginary inverted cone tangent to the runway centerline at approximately 15000 ft altitude and 45000 ft from the runway. Way Point 1 (WP1) is the target entry point to the HAC; this is the desired vehicle location to initiate the HAC turn. The A/L nominal entry point (NEP) is the target entry point to the runway centerline; this initiates the A/L capture.

The prefinal phase simply provides a smooth transition from TAEM to A/L . In prefinal, the guidance turns the vehicle heading towards WP2 (Way Point 2) and activates the A/L guidance once all capture criteria are met.

For the Shuttle vehicle, there are 4 optional TAEM targeting (OTT) profiles; each OTT results in a different HAC position based on the entry point and on vehicle location. Briefly, the option is based on either a straight-in (nearest HAC) or overhead (far HAC) approach, and on selecting a nominal or a minimum entry point, as shown in Figure 5-4. The minimum entry point (MEP) HAC is selected when a low energy condition exists. In addition, the spiral radius during the HAC maneuver can also be shrunk to reduce the range-to-go thereby alleviating the low energy condition. The selection of a required OTT is a function of the amount of total energy at the start of the TAEM.

The development of the TAEM trajectory for this report will cover only the nominal overhead entry point. The algorithms for the other approaches would be an extension of the basic nominal overhead algorithm, but adjusted based on the available energy. As a result, the trajectory equations will concentrate on the heading alignment cone trajectory profile.

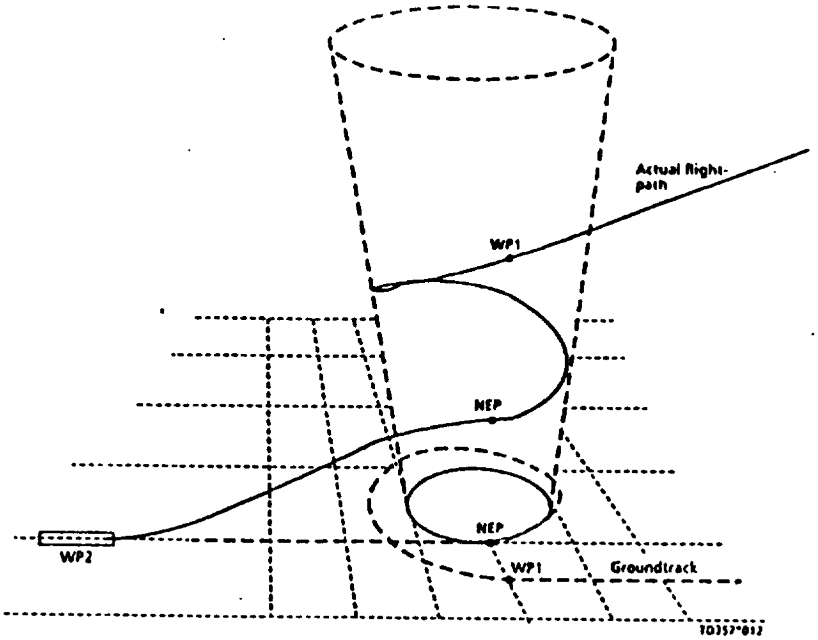

Figure 5-3 ·HAC Configuration

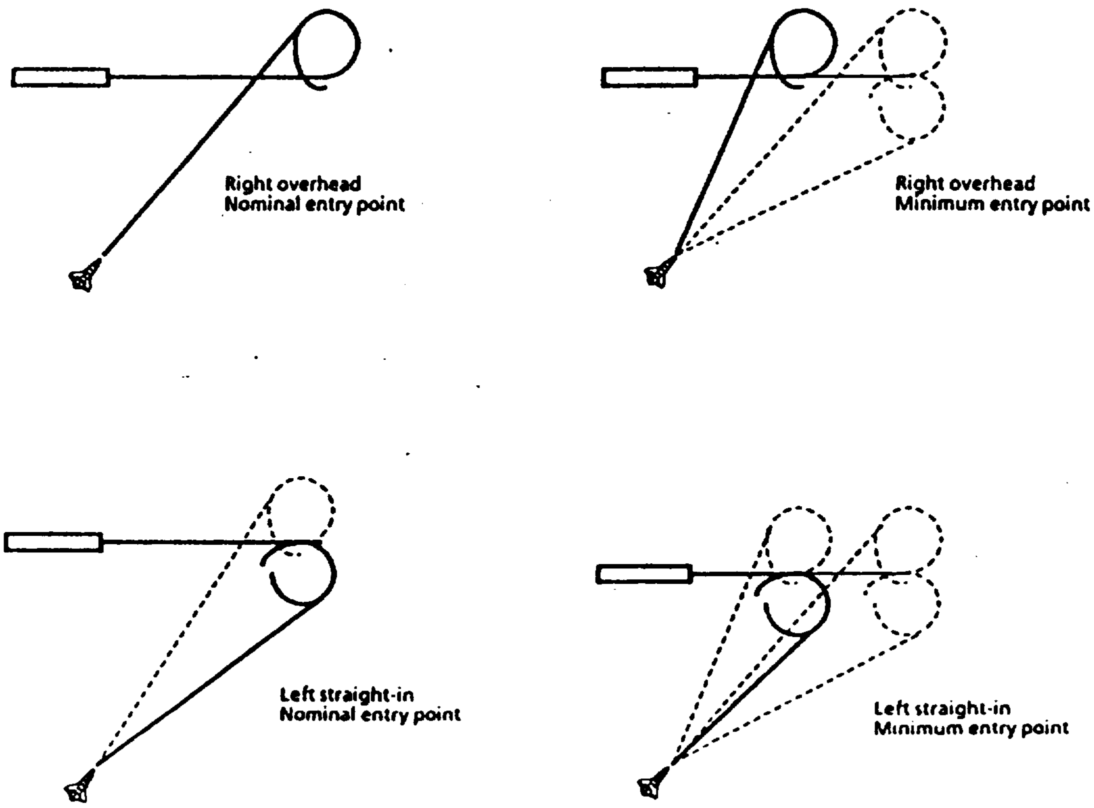

Figure 5-4 Optional TAEM HAC Trajectories

Figure 5-5 shows a graphical representation of the HAC trajectory parameters and variables. It is assumed the following initial HAC conditions and final conditions are known:

- VELW1= Initial HAC velocity at WP1 (ft/sec)
- HW1= Initial HAC altitude (ft)
- VELNEP= Final HAC velocity at NEP (ft/sec)
- HNEP= Final HAC altitude at NEP(ft)
- γ_{HAC}= Constant HAC flight path angle
- ϕ_{HAC}= Constant HAC bank angle

Given the desired initial and final HAC conditions, the final fixed radius RF and initial radius at W1 can be calculated as follows:

(1) $RF=(VHNEP**2)/(g*\tan(\phi_{HAC}))$ where: VHNEP= horizontal velocity at NEP

(2) $RW1=RF * (VHW1/VHNEP)**2$ VHW1= horizontal velocity at W1

The basic polar equation describing the spiral turn radius is :

(3) $RT= RF + R1*\Psi + R2*\Psi**2$ where:

RT=turn radius, for given Ψ
RF= final turn radius ($\Psi=0$)
Ψ =HAC heading angle (deg)
R1, R2= spiral coefficients

From equation (3), the spiral coefficients R1, and R2 need to be determined to define the spiral turn radius RT. The primary purpose of the spiral is to enable a constant bank angle to be maintained during the HAC turn while modulating the velocity as given in equation (4).

(4) $V_{horiz}=SQRT[\ RT*g*\tan(\phi_{HAC})]$

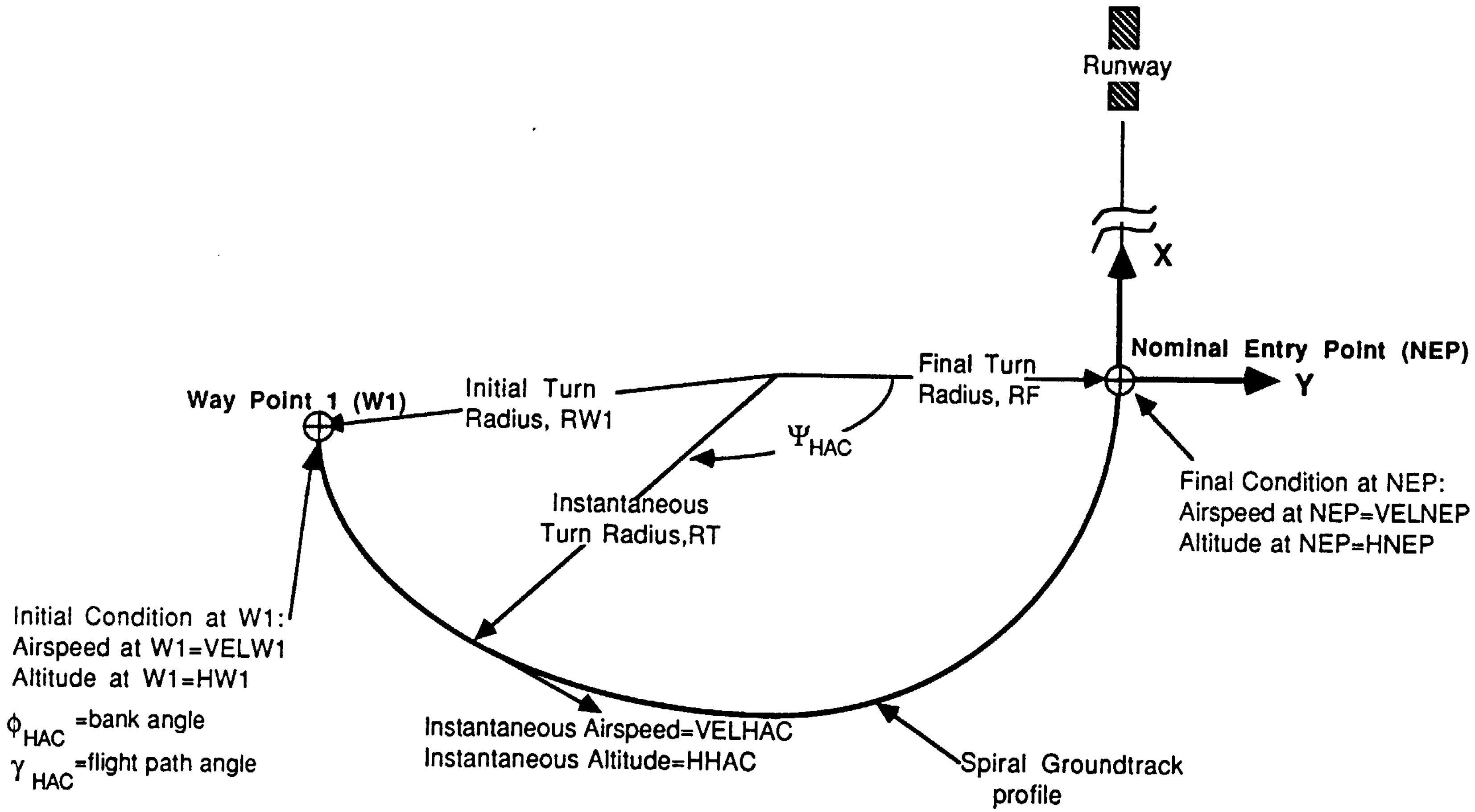

Figure 5-5 Definition of HAC Spiral Profile

If the velocity were held constant during the HAC maneuver, the radius would be held constant generating a circular profile, resulting in a cylindrical shaped trajectory. However, PLS requires that the velocity decrease during the HAC maneuver while holding the bank angle constant; this requires a changing turn radius (RT). As the velocity decreases, the turn radius must also decrease resulting in a spiral profile. The spiral coefficients are used to shape the spiral to a desired profile as a function of the required velocity.

The velocity constraints imposed by equations (1) and (2) may be used to solve for the spiral coefficients. In addition, there are altitude constraints imposed on the spiral trajectory. This constraint is imposed as result of the desired range during the HAC maneuver, as a function of flight path angle γ_{HAC}:

(5) $RG_{HAC} = (HW1\text{-}HNEP)/\tan(\gamma_{HAC})$ where: RG_{HAC}=desired HAC range

The resulting spiral range equation (RG'=predicted range) can be obtained by integrating the spiral equation (3) from 0 to the HAC heading angle Ψ(deg) :

(6) $RG' = {}_0\!\int^{\Psi} RT\,(d\Psi\ {*}DTR) = [RF + R1{*}\Psi\ /2 + (R2{*}\Psi{**}2)/3]{*}\Psi\ {*}DTR$

where $DTR = 1/57.3$ (RAD/DEG)

By setting the desired range RG_{HAC} equal to the predicted range RG', a solution for the required initial heading angle Ψ_0 may be obtained. However, there is one equation with three unknowns. Experimentation showed that setting R1=0 and only using R2 yielded satisfactory trajectories. By setting R1=0, there are 2 unknowns, R2 and Ψ_0 , and one equation. A quick iteration yields a solution determining both the spiral coefficient R2 and the required initial heading angle Ψ_0 that will yield a spiral profile within given altitude and velocity constraints. Section 6.1 gives a solution to the required initial heading angle Ψ_0 and the spiral coefficient R2 for a sample TAEM trajectory.

Having established the spiral coefficients, the desired trajectory profile command can be generated by equation (3), and the velocity command is defined by equation (4).

5.1.2 TAEM Altitude Control Module

The TAEM altitude control module is identical to the A/L altitude control module. The altitude gains were developed for the A/L phase as a function of dynamic pressure. The TAEM dynamic pressure range is within the A/L range, therefore the gain schedules are sufficient for both phases.

5.2 TAEM Lateral Guidance and Control System

Lateral guidance is used during the TAEM heading alignment phase to track a nominal HAC (Heading Alignment Cone) spiral ground track profile. Ideally, if the vehicle maintains a constant bank angle in the absence of winds or external disturbance, the desired spiral ground track should be followed with minimum error. However, an external disturbance or deviation from the nominal velocity profile results in a change to the turn radius, and therefore ground track error. The lateral guidance system generates a roll command to eliminate the cross track error. The cross track error is the vehicle lateral ΔY error. The longitudinal ΔX error is controlled by the altitude and speed controller, and is covered in section 5.1.2 and 5.3.

Our approach in the lateral guidance is to use the same cross track error and cross track rate law used in the A/L phase. The lateral guidance system used during the A/L phase as reported in section 3.3 consists of controlling the lateral displacement from the runway centerline, and the lateral velocity normal to the fixed centerline. The A/L control laws are easily adapted to the TAEM phase by using cross track error in place of the lateral displacement error and cross track rate error in place of the lateral velocity error. A block diagram of the lateral controller is given in figure 5-6. The bank angle generator is used to generate the proper HAC bank angle command as a function of the turn radius and the vehicle velocity. This relationship is defined by:

$$(7) \quad \phi_{HAC} = \tan^{-1} (V_{horiz}^2/(g^*RT)$$

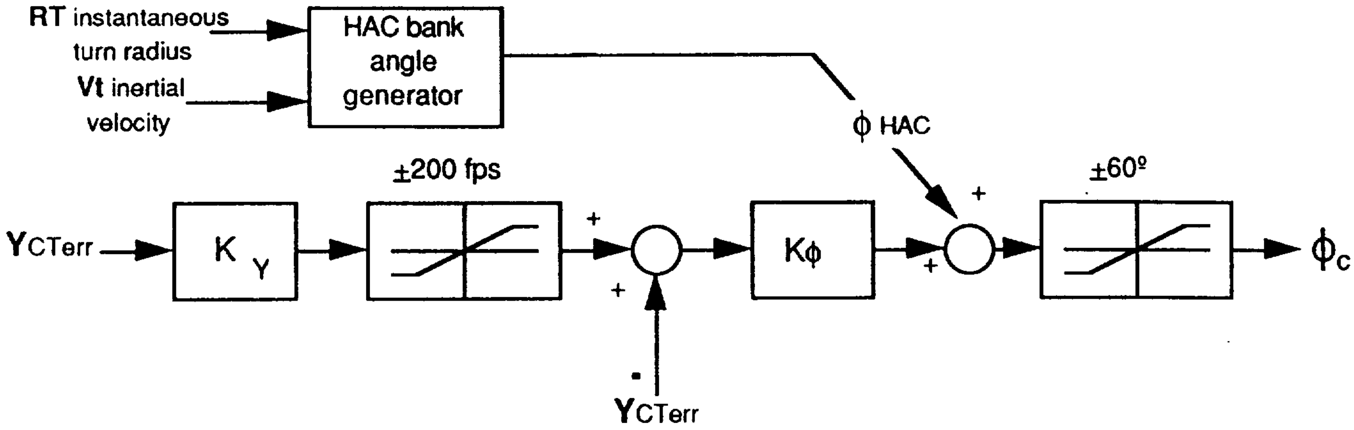

Figure 5-6 TAEM Lateral Control Law Block Diagram

A simplified block diagram of the method used to calculated the cross track errors is given in figure 5-7. The detailed definition of each block shown in figure 5-7 is given in appendix H, which contains the full set of algorithms. A brief description of the cross track error and cross track rate error is presented below.

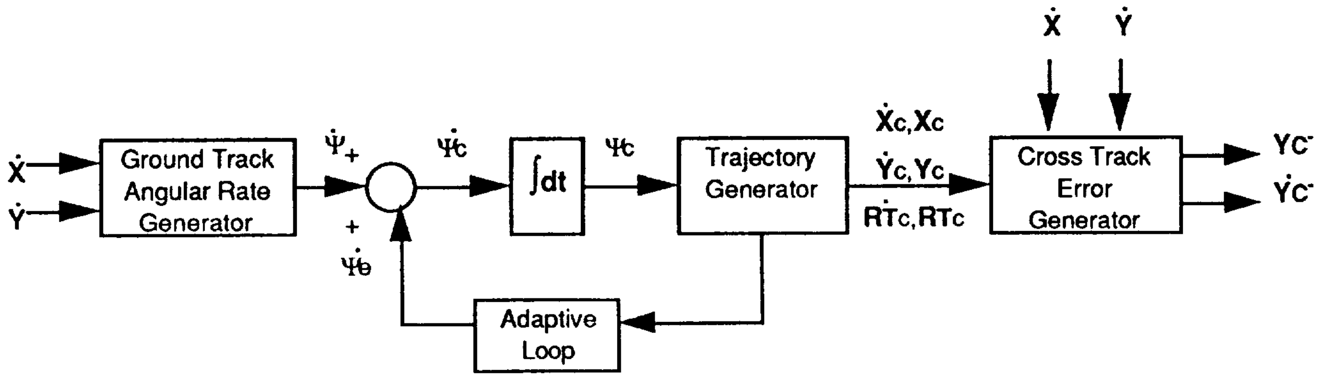

Figure 5-7 Block Diagram of Lateral Controller Cross Track Error Generator

A diagram showing the variables used to calculate the cross track error terms is given in figure 5-8. The commanded ground track spiral profile and the actual ground track profile is shown. The vehicle desired position is defined by the turn radius (RT), the commanded HAC ground track angle (Ψc) defined in equation (3), and the commanded velocity (Vc) defined by equation (4). The resulting commanded radius vector is $\dot{R}c$.

The actual vehicle position is defined by the radius vector R, and the velocity vector V. The commanded ground track angle (Ψc) is adjusted by the adaptive loop such that for a corrected Ψc,

(8) dot product $(Re \cdot Vc)=0$;

that is, Ψc is adjusted to maintain Re perpendicular to Vc. Re is defined by:

(9) $Re=(X-Xc)i + (Y-Yc)j$;

and the commanded velocity is defined by:

(10) $Vc= Xc\, i + Yc\, j$.

Substituting the above equations into the dot product equation (8),

(11) dot product $(Re \cdot Vc)=0 = Xc(X-Xc) + Yc(Y-Yc)$.

Equation (11) is used in the adaptive loop (see appendix H) to create the Ψe error signal. As Ψe approaches zero, $\Psi=\Psi c$.

The cross track error becomes:

(12) $YCTerr=|\ Re\ |{}^*sign(R-Rc)=SQRT[\ (X-Xc)^2 + (Y-Yc)^2\ ]{}^*sign(R-Rc)$;

and the cross track rate error becomes:

(13) $\dot{Y}CTerr=|(V \times Vc)|/|Vc| = (X^*Yc - Y^*Xc)/SQRT(Xc^2 + Yc^2)$

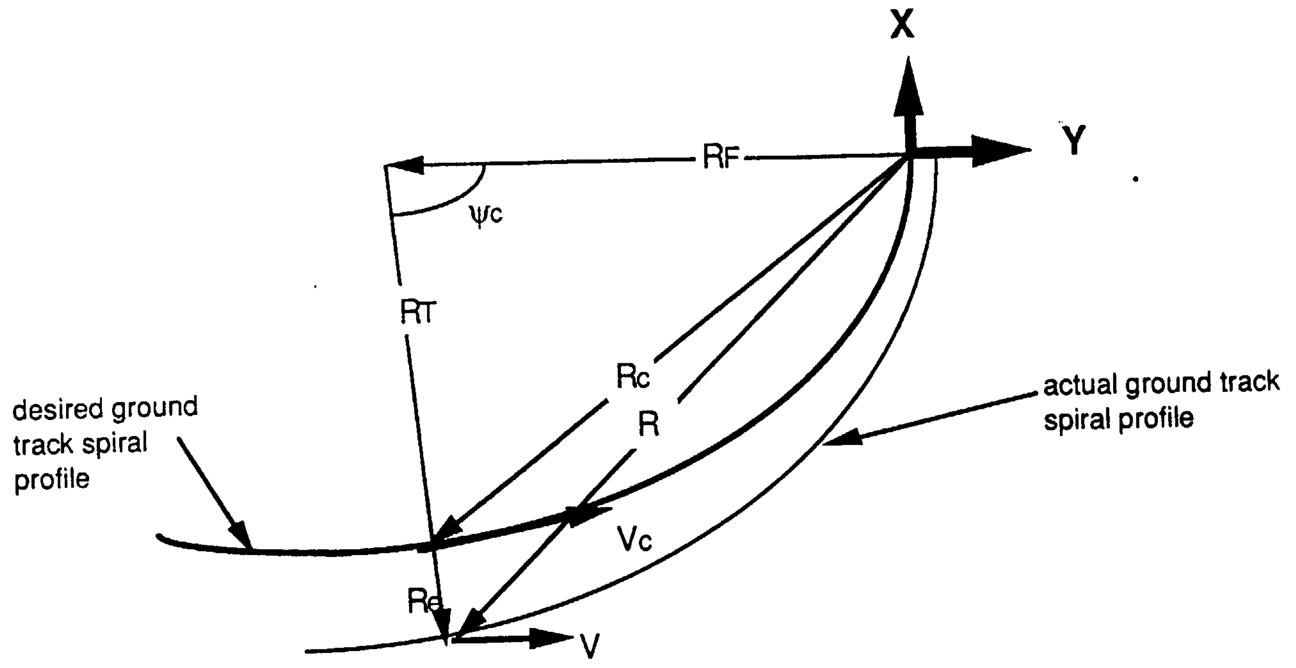

Figure 5-8 TAEM Cross Track Error Diagram

The gains for the lateral steering were developed through nonlinear simulation analysis. Figure 5-9 shows the cross track error and bank angle command time histories as the vehicle captures the HAC spiral profile. The response is shown for combinations of cross track error gains and bank command gains. Nominal gain values selected were Ky=0.2 and Kϕ=0.5. Using constant values for these gains, the PLS vehicle follows the desired HAC spiral profile within 50 feet throughout the heading alignment phase as shown in figure 5-10. The nominal error at the end of the phase is 33 feet in the X direction and 26 feet in the Y direction.

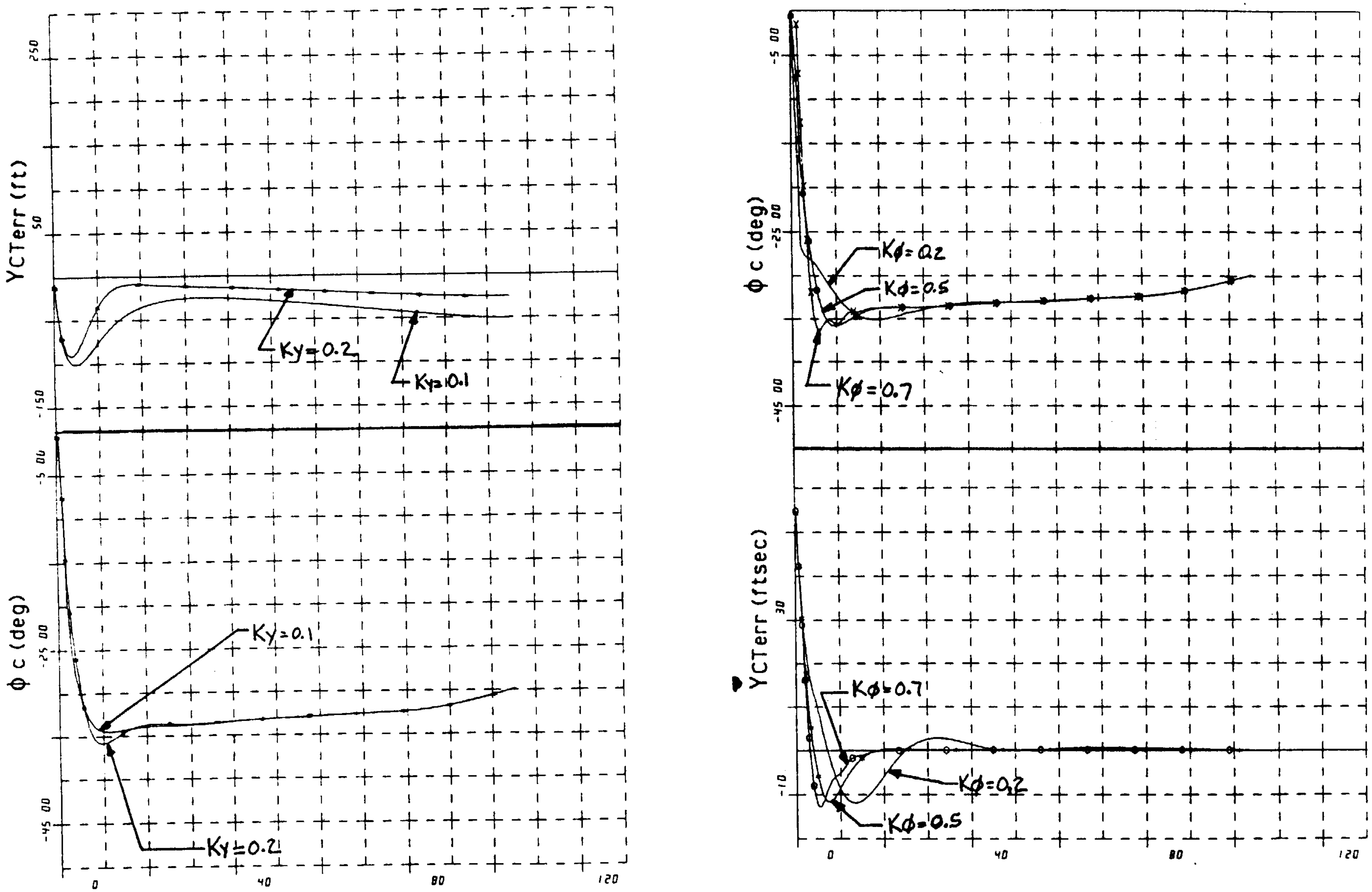

Figure 5-9 TAEM Lateral Control Performance For Different Lateral Gains

C-2

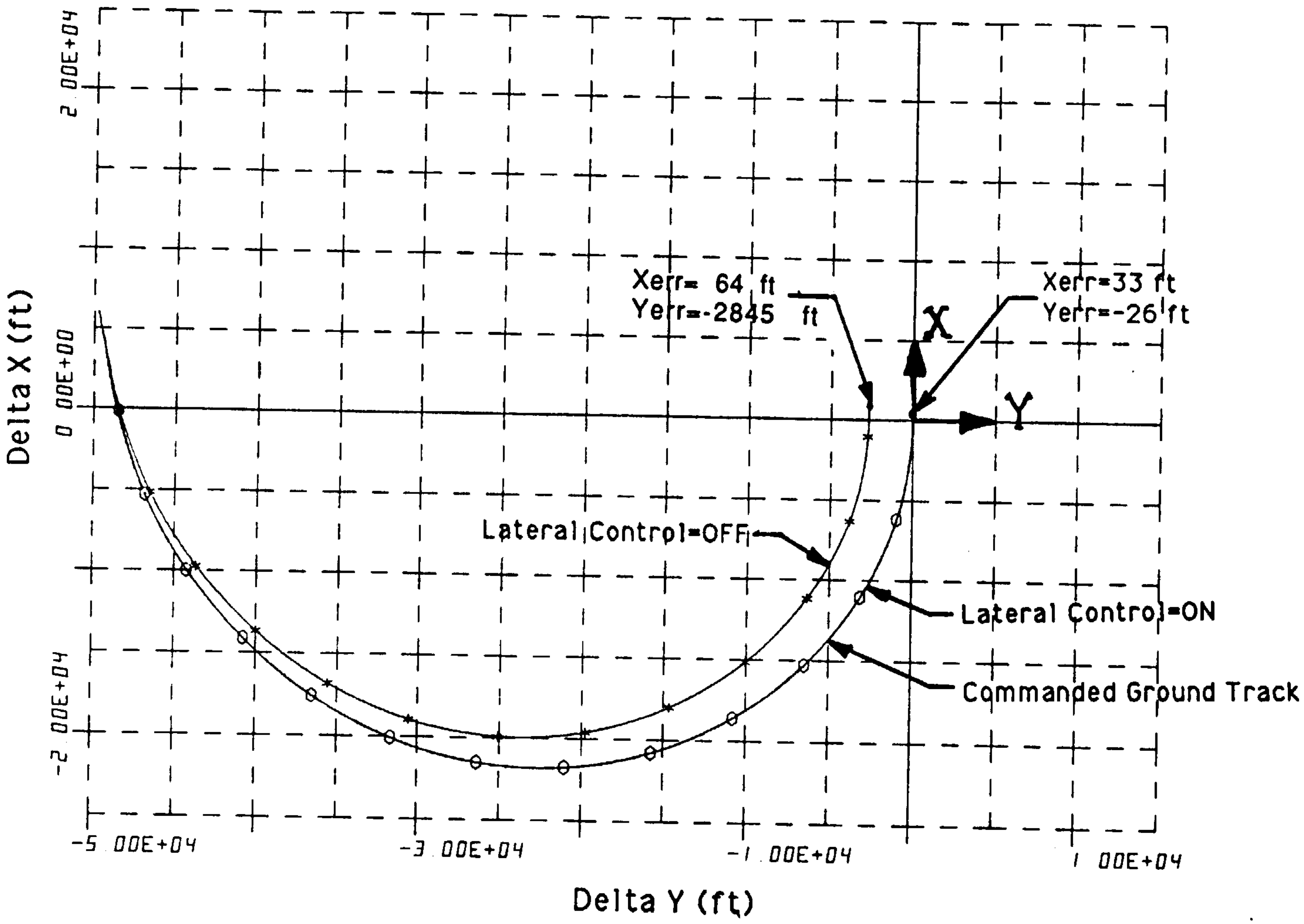

Figure 5-10 TAEM Performance with Lateral Controller On Versus Off

5.3 TAEM Speed Control

The purpose of the PLS speed controller during the TAEM guidance phase is to control the vehicle to follow a predetermined speed profile. Speedbrake deflection is used to control the vehicle velocity.

The A/L speed controller was adapted for use during the TAEM phase. The control law is identical (see figure 3-14), using an integral gain (K_{SI}) to reduce the regulator (velocity) steady state error, and gain K_S to reduce the velocity error. The speedbrake limit during TAEM is increased to 60º .

The velocity command (Vcmd) is based on the desired turn radius (equation 3) and the steady state bank angle command profile (ϕ_{HAC}, equation 7), resulting in equation (13):

$$(13) \quad V_{cmd} = \text{SQRT}[\, R_{turn} * g * \tan(\phi_{HAC})]$$

The 6-DOF simulation was used to evaluate the speed controller gains. The study showed that the gains used for the A/L phase result in sufficient speed control performance, and will therefore be used for the TAEM phase.

6.0 TAEM Six DOF Simulation Analysis

In this section, the 6 DOF simulation is used in the mission design and evaluation of the TAEM performance. A TAEM parameter sensitivity study was conducted to define the nominal mission. The resulting mission design was verified through wind turbulence simulation.

6.1 TAEM Parameter Sensitivity Study

The 6-DOF simulation was used to evaluate the sensitivity of mission input parameters on the heading alignment phase final conditions. The results of these were used to select the nominal mission. The mission constraint is that an overhead approach to the runway be used to allow the pilot to view the runway before the landing. As a result, the heading angle changes during the heading alignment phase must be larger than 180º.

The mission parameters analyzed, includes:

- γ = HAC initial glideslope angle
- ϕ = steady state bank angle command
- VELW1= velocity at way point 1 (start of HAC)
- VELNEP= velocity at nominal entry point (end of HAC)
- ΔH = altitude change during HAC

Figure 6.1 shows heading angle change ($\Delta\Psi$) sensitivity to the mission parameters. The sensitivity were run around the base point shown. The domain parameter is the steady state bank angle command with insufficient effect due to initial glideslope angle.

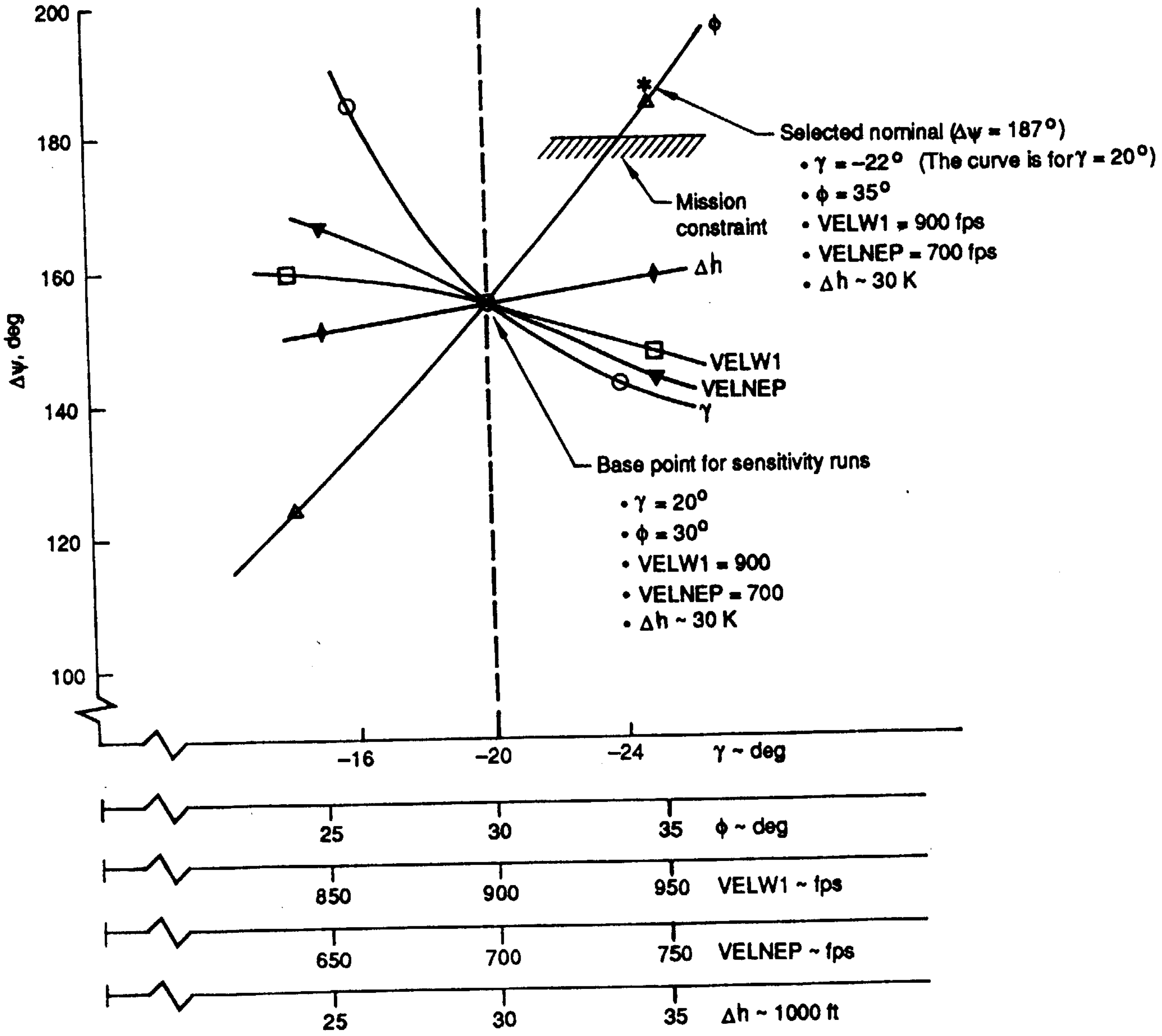

Figure 6-1. TAEW Heading Angle Sensitivity

As a result of this study, the following mission input parameters will define the default TAEM mission:

- $\gamma = -22^{\circ}$
- $\phi = -35^{\circ}$
- VELW1= 900 ft/sec
- VELNEP= 700 ft/sec
- $\Delta H =$ 30000 ft (from 45000 to 15000 ft)

With the above mission parameters, the HAC change in heading and spiral coefficient is:

- $\Delta\Psi \approx 187^{\circ}$.
- R2=0.3505

The guidance and control performance for the nominal mission are shown in figures 6-2 through 6-5. Figure 6-2 contains 2 plots. Figure 6-2 shows the HAC commanded ground track (ΔY versus ΔX) and the resulting ground track profile; time histories for the ground track X and Y error are also shown. The position error and the end of the HAC flight is 33 feet in X and 26 feet in Y.

The cross track error and rate error time histories for the lateral guidance system is plotted in figure 6-3 . Figure 6-4 shows the roll angle that results from the lateral error. The simulation starts with straight and level flight and proceeds to bank at the start of the HAC maneuver. As a result, there is an initial bank angle ramp to approximately 33 degrees. The vehicle bank angle response to the commanded bank angle shows well damped roll control performance.

The flight path angle and angle of attack time histories are shown in figure 6-4 with altitude control time histories in figure 6-5 . The altitude error remains small and the error is only a couple feet at the end of the HAC phase. The altitude error is defined as the difference between the commanded and the actual altitude. Note, the commanded altitude at the end of the HAC flight is approximately 14620 feet, which is less than the targeted 15000 feet. This is due to the algorithm used to terminate the HAC flight phase. The algorithm uses the heading alignment angle as a test to terminate the HAC simulation; when the angle reaches zero, the simulation is terminated. This occurs at an altitude of 14620 feet.

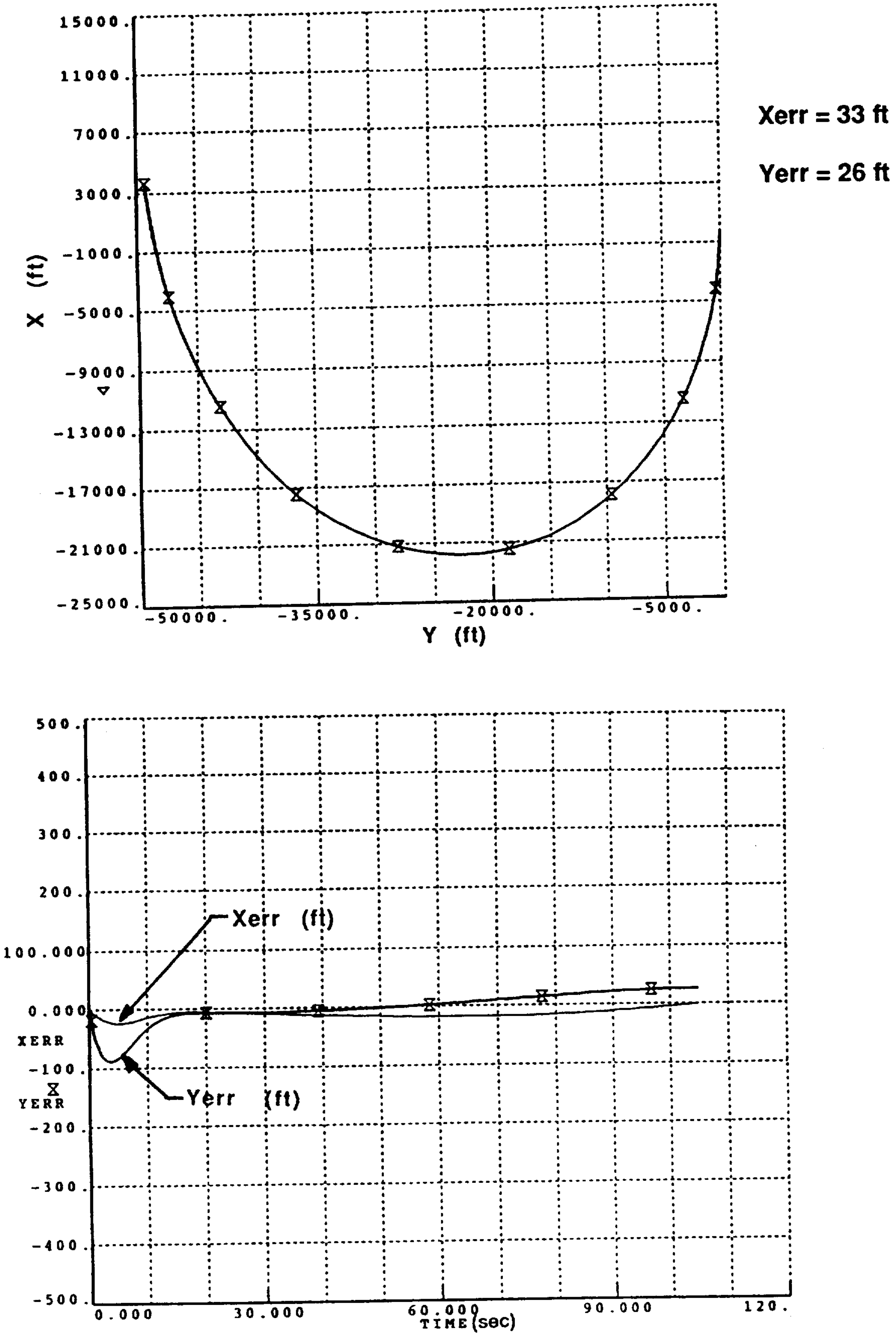

Figure 6-2 TAEM Simulation Ground Track Performance Results

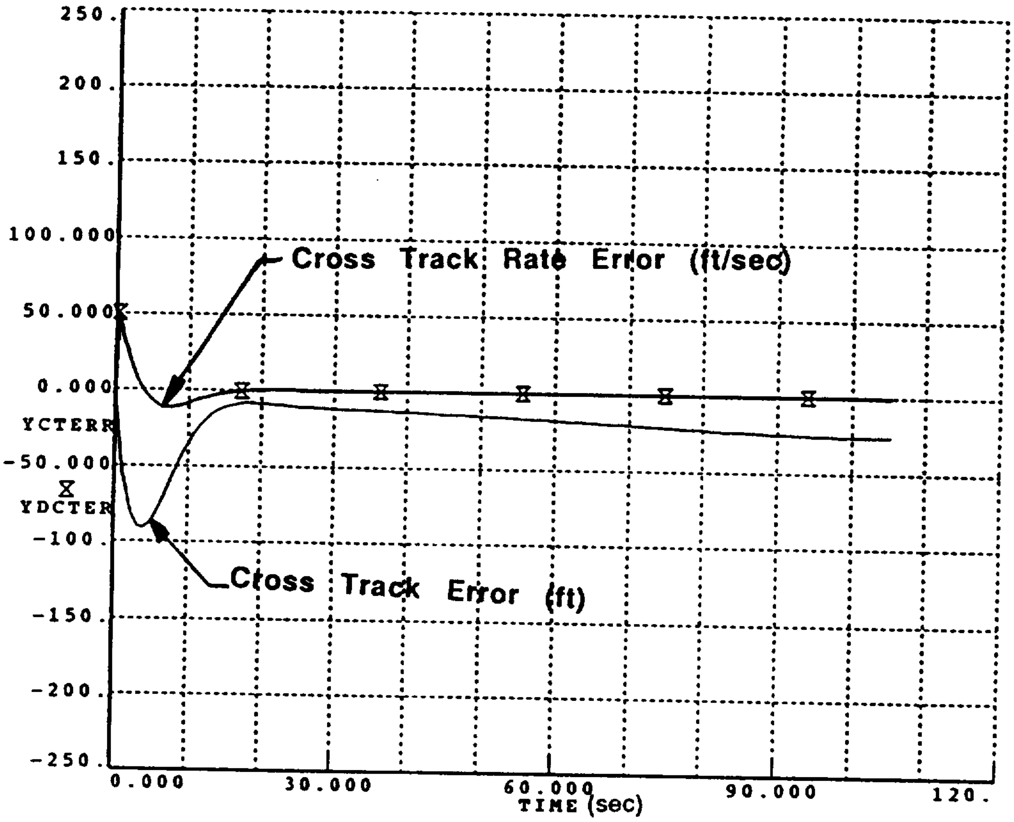

Figure 6-3 TAEM Simulation Cross Track Error Results

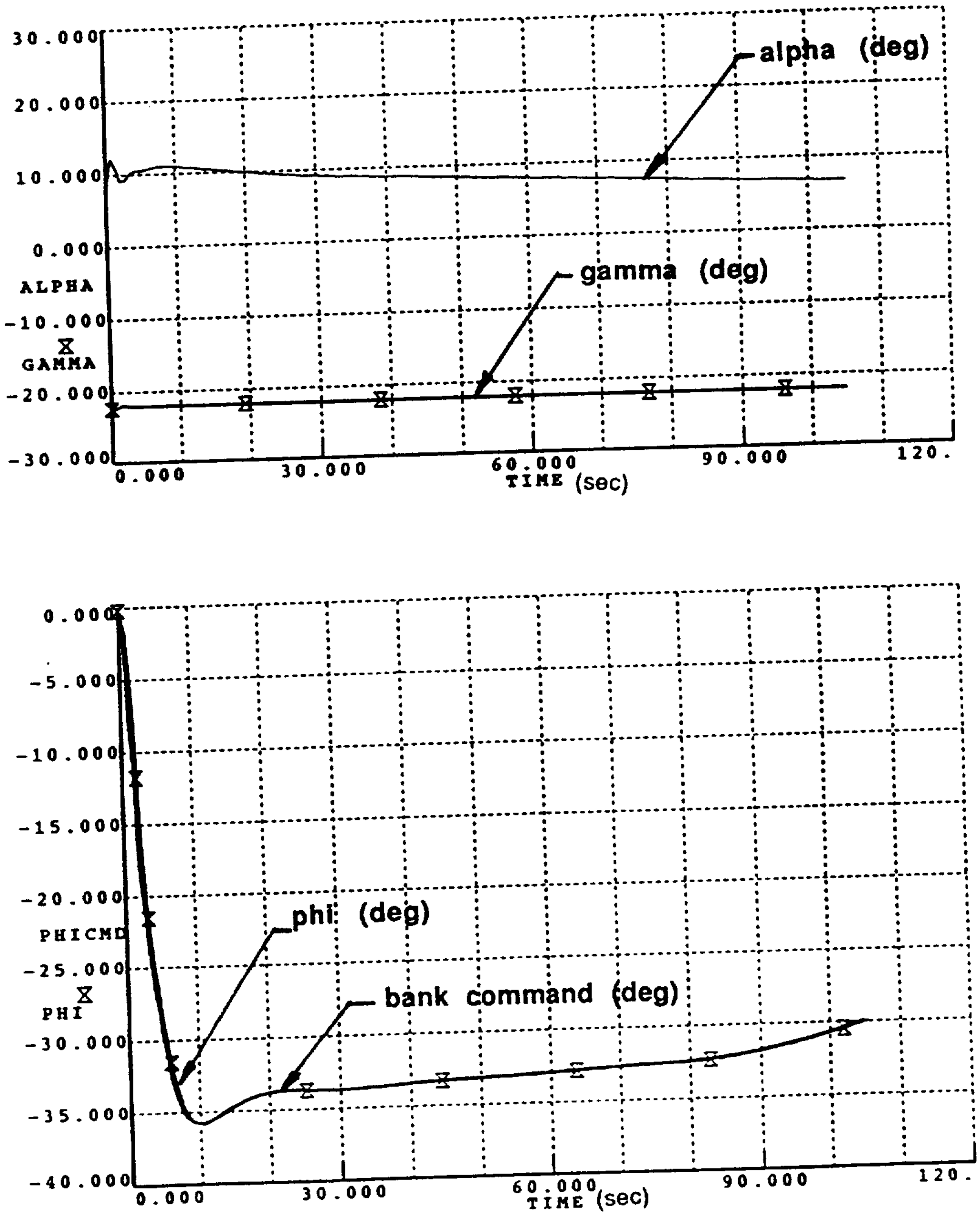

Figure 6-4 TAEM Simulation Phi, Alpha, and Gamma Results

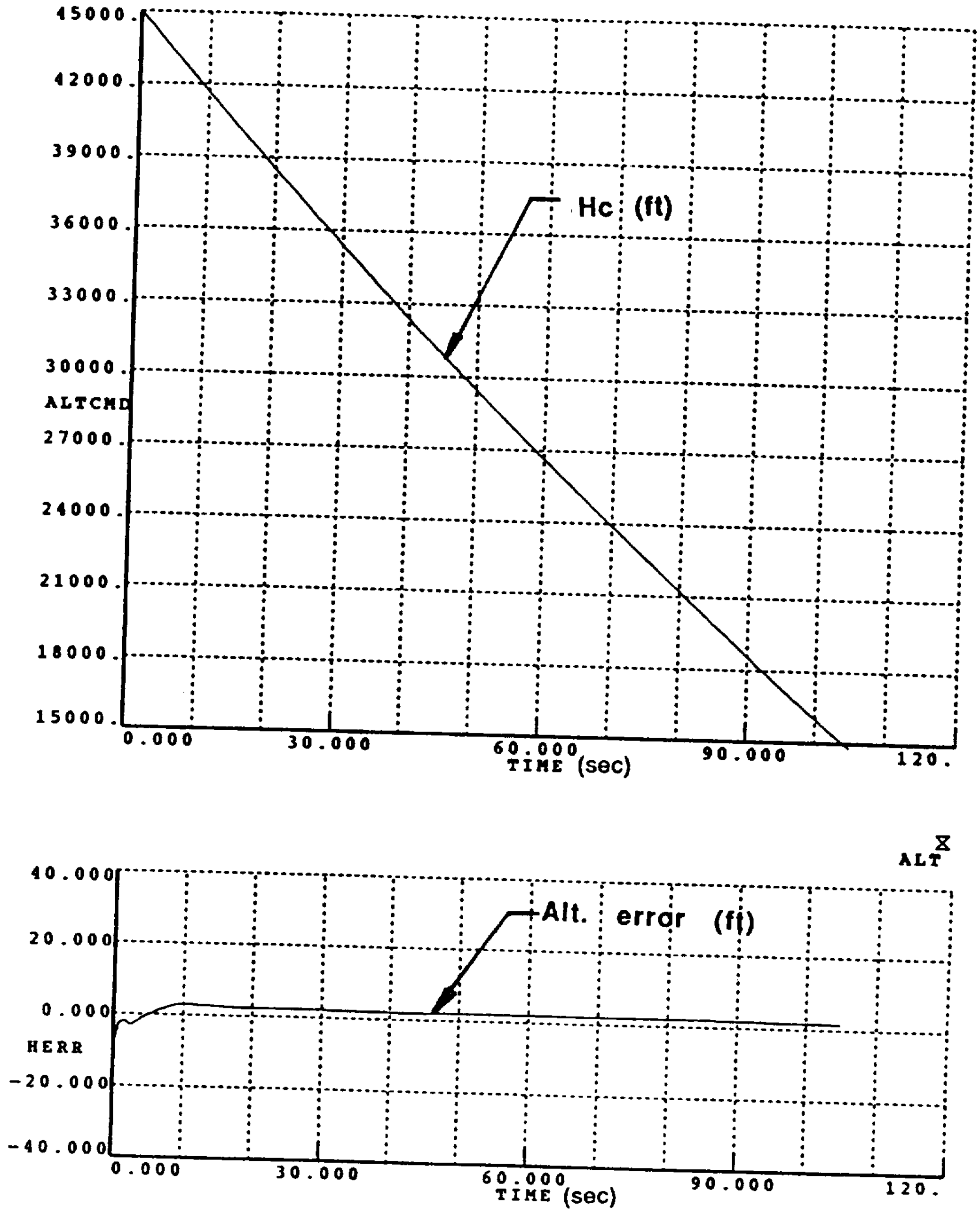

Figure 6-5 TAEM Simulation Altitude Performance Results

6.2 TAEM Performance With Wind Disturbance

Simulation runs were also conducted using the wind turbulence model used for the A/L analysis (see section 4.3). The turbulence 1σ gaussian distribution and integral scale length is set according to the data in Appendix C, at an altitude of 9000 meters. These parameters are set at:

- $\sigma_X = \sigma_Y = \sigma_Z =$ 17.3 ft/sec
- $L_X = L_Y = L_Z =$ 1753 ft.

Time history results for the HAC mission with wind turbulence, are presented in Appendix F A comparison of the final conditions with and without winds are shown in table 6-1. The wind turbulence has a very small effect on the final conditions.

TAEM End Condition	Nominal	Wind Turbulence	Description
ΔX err	33 ft	66 ft	along track error
ΔY err	-26 ft	-25 ft	cross track error
H	14620 ft	14612 ft	altitude
η	≈ 0. º	≈ 0. º	heading angle

Table 6-1 TAEM End Conditions

6.3 TAEM Speed Control Performance

Speed controller results from a nominal TAEM mission without wind is given in figure 6-6. The initial velocity error oscillation is due to the initial speedbrake setting being 30º. Despite this, the speed controller performed well up to 75 seconds. At this point, the vehicle velocity falls below the commanded velocity, and the speedbrake becomes fully retracted.

The speed control performance can be easily improved through the re-sizing of the turn radius constants used in the velocity command profile and bank command profile. This would have the effect of selecting an HAC spiral flight more consistent with the PLS drag characteristics. The speedbrake would operate between the full deflection and full retracted condition.

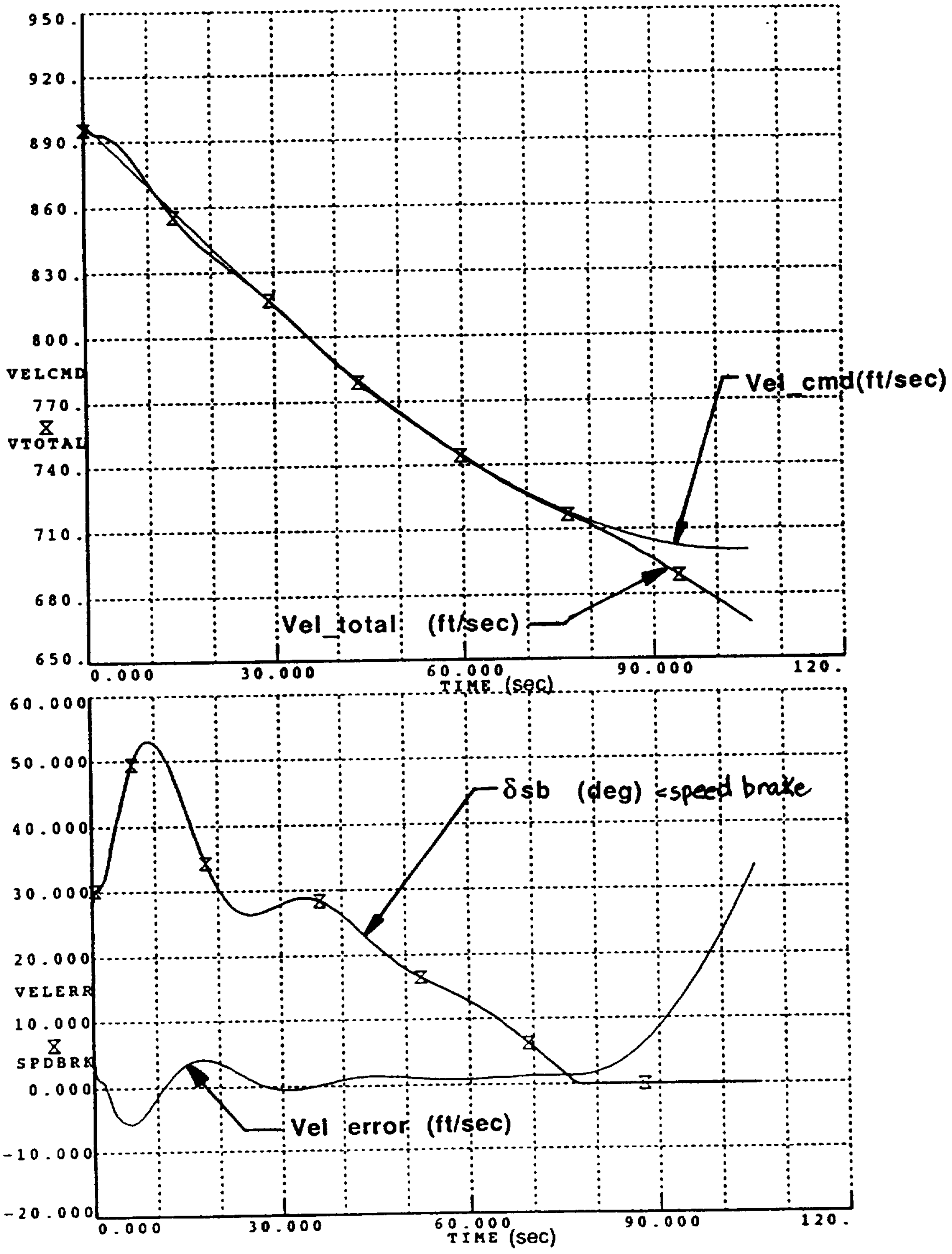

Figure 6-6 TAEM Simulation Speed Controller Results

Note: this page is intentionally left black.

7.0 Conclusion

The NASA Langley 10 man PLS configuration is a very flyable configuration for performing a complete autoland mission similar to the previously studied 8 man CERV configuration. Acceptable landing performance can be achieved. If a manual backup or complete manual flight is required, the configuration is marginal and a higher L/D configuration is desired to ease the landing operation. The configuration has an L/D of 3.2 and should be increased for manual flight.

The autoland system performance was demonstrated using a non-linear 6-DOF simulation. The feasibility of using a double flare autoland profile was demonstrated with improved landing characteristics compared to the parabolic flare. The touchdown accuracy on sink rate and speed were within requirements. Adequate stability and control was demonstrated for wind turbulence and wind shear.

Initial studies have been conducted on a portion of the TAEM system, including the heading alignment phase and prefinal phase. The feasibility of using a Shuttle type TAEM system for PLS was verified using a 6-DOF simulation; acceptable performance was demonstrated. Further studies will be required to complete the TAEM design including the design of the S-turn phase and acquisition phase. The purpose of these phases will be to transit from midcourse position and velocity uncertainties to the desired approach and landing initial conditions.

8.0 Recommendations

Design studies have been conducted for the PLS Autoland system and simulation results demonstrate acceptable performance. To increase confidence in the approach, a number of configuration iterations and tailoring, along with control refinements and extension of the design could be pursued. Following are our suggestions for resolving some of the issues.

The present PLS configuration has sufficient L/D for a pure autoland system, but for manual backup or manual flight, the L/D needs to be increased. One configuration suggestion would be to reduce the wing dihedral and increase the wing area to give additional lift required in the pitch plane. This would also reduce the C_{l_β}, which could help the trim during the decrab maneuver. However, because configuration change could adversely effect the high Mach number trim characteristic and yaw/roll stability, both high and low Mach regions would need to be studied.

Landing in a cross wind has always been a problem with autolanding a lifting body. Vehicles with large C_{l_β} are difficult to trim at large sideslip angles. The decrab autopilot design in the CERV study (reference 7) was a complex design using an estimate of the trim state as feedforward command. Additional autopilot studies for the design of the decrab autopilot are needed. Relaxation of the decrab performance to only 3 º of the runway centerline can be considered in the re-design.

Areas where additional wind tunnel data is needed include:

1) body flap deflection from zero to 40º to cover their use as speed brake and roll control;
2) control surface hinge moment data is needed for actuator sizing;
3) landing gear and ground effect for the final flare.

Initial studies have been conducted on the last two segments of the TAEM system. An extension of this study is recommended to include the S-turn phase and acquisition phases of the TAEM system. A feasible study is needed to assure the PLS configuration can eliminate the re-entry guidance errors. This may be critical since the flight angle-of-attack capability of PLS is very low in this Mach region.

Also suggested is a feasibility study for the re-entry flight phase (440K ft to 60K ft altitude) to assure the stability and control characteristics, and to demonstrate re-entry phase accuracy. Initial 6-DOF simulations studies should be conducted using an integrated guidance and control design.

9.0 References

1. Blight, J., Coleman, E., Thompson, C., "Integral LQG Controller Design for a Fighter Aircraft", AIAA-87-2452-CP, Proc. of 1987 Guidance, Navigation, and Control Conference, Monterey, California, Aug. 1987.

2. Tsikalas, G., Dyer, D., "Shuttle Automatic Landing System", AAS-82-017, Proc. of 1982 Annual Rocky Mountain Guidance and Control Conference, Keystone, Colorado, Jan. 1982

3. Barr, N. M., Gangsaas, D., and Schaeffer, D. R., "Wind Models for Flight Simulator Certification of Landing and Approach Guidance and Control System", FAA-RD-74-206, Dec. 1974.

4. Holley, W. E., and Bryson, A. E., "Wind Modeling and Lateral Aircraft Control for Automatic Landing", Stanford University Department of Aeronautics and Astronautics Report No. 489, Jan. 1975.

5. Chalk, C. R., Neal, T. P., Harris, F. E., and Pritchard, F. E., "Background Information and User Guide for MIL-F-8785B (ASG), Military Specification - Flying Qualities of Piloted Airplanes", AFFDL-TR-69-72, Aug. 1967.

6. Tatom, F. B., and Smith, S. R., "Advanced Space Shuttle Simulation Model", NASA CR-3541, 1982.

7. Bossi, J., Langehough, M., Lee, K. L., "Crew Emergency Return Vehicle Autoland Feasibility Study", NASA Contractor Report 181940, December, 1989.

Appendix A

AERODYNAMIC MODEL

An aerodynamic model for the PLS vehicle was generated from the wind tunnel data provided. This data was obtained from NASA Langley Research Center. Force and moment equations of the model as a function of alpha and beta is given in figure A-1. Note, that this data is not a function of the control surface deflection. A simplification was used when generating this data, calculating the force and moment coefficient as a linear function of the control surface deflections.

The nomenclature for the aerodynamic data is given in figure A-2; the definition of the control surface angles is given in figure 2-4.

A trim program and derivative program were also developed. The derivatives are calculated around the trim conditions listed in section 3.1 . Sample derivatives at these trim conditions are given in figure A-3 . These derivatives were used to form the linear model for the autopilot point design analysis.

The aerodynamic tabular data obtained from NASA is summarized as one large table . Figure A-4 shows the aerodynamic table format used to define the table.

<u>Aerodynamic</u> <u>Coefficient</u> <u>Buildup</u> <u>equations</u>

$$C_X = C_{X_0}(\alpha,\beta) + \Delta C_{X_{\delta e}}(\alpha)\,\delta e + \Delta C_{X_{|\delta a|}}(\alpha)\,|\delta a| + \Delta C_{X_{\delta f^+}}(\alpha)\,\delta f^+ + \Delta C_{X_{\delta f^-}}(\alpha)\,\delta f^-$$
$$+ \Delta C_{X_{|\delta\Delta f|}}(\alpha)\,|\delta\Delta f| + \Delta C_{X_{|\delta r|}}(\alpha)\,|\delta r| + \cancel{\Delta C_{X_{\delta lg}}(\alpha, \delta lg)} \rightarrow 0 + \cancel{\Delta C_{X_{ge}}(\alpha, \tfrac{h}{b})} \rightarrow 0$$

$$C_Y = C_{Y_\beta}\beta + \Delta C_{Y_{\delta a}}(\alpha)\,\delta a + \Delta C_{Y_{\delta\Delta f}}(\alpha)\,\delta\Delta f + \Delta C_{Y_{\delta r}}(\alpha)\,\delta r + \cancel{\Delta C_{Y_{\delta lg}}(\beta, \delta lg)} \rightarrow 0$$

$$C_Z = C_{Z_0}(\alpha,\beta) + \Delta C_{Z_{\delta e}}(\alpha)\,\delta e + \Delta C_{Z_{\delta f^+}}(\alpha)\,\delta f^+ + \Delta C_{Z_{\delta f^-}}(\alpha)\,\delta f^-$$
$$\cancel{+ \Delta C_{Z_{\delta lg}}(\alpha, \delta lg)} \rightarrow 0 + \cancel{\Delta C_{Z_{ge}}(\alpha, \tfrac{h}{b})} \rightarrow 0$$

$$C_l = C_{l_\beta}\beta + \Delta C_{l_{\delta a}}(\alpha)\,\delta a + \Delta C_{l_{\delta\Delta f}}(\alpha)\,\delta\Delta f + \Delta C_{l_{\delta r}}(\alpha)\,\delta r + \Delta C_{l_p}(\alpha)\,\frac{pb}{2V}$$
$$+ \Delta C_{l_r}(\alpha)\,\frac{rb}{2V} + \cancel{\Delta C_{l_{\delta lg}}(\beta, \delta lg)} \rightarrow 0 + \cancel{\Delta C_{l_{ge}}(\beta, \tfrac{h}{b})} \rightarrow 0$$

$$C_m = C_{m_0}(\alpha,\beta) + \Delta C_{m_{\delta e}}(\alpha)\,\delta e + \Delta C_{m_{|\delta a|}}(\alpha)\,|\delta a| + \Delta C_{m_{\delta f^+}}(\alpha)\,\delta f^+ + \Delta C_{m_{\delta f^-}}(\alpha)\,\delta f^-$$
$$+ \Delta C_{m_{|\delta a|}}(\alpha)\,|\delta a| + \Delta C_{m_q}(\alpha)\,\frac{qc}{2V} + \cancel{\Delta C_{m_{\delta lg}}(\alpha, \delta lg)} \rightarrow 0 + \cancel{\Delta C_{m_{ge}}(\alpha, \tfrac{h}{b})} \rightarrow 0$$

$$C_n = C_{n_0}(\alpha,\beta) + \Delta C_{n_{\delta a}}(\alpha)\,\delta a + \Delta C_{n_{\delta\Delta f}}(\alpha)\,\delta\Delta f + \Delta C_{n_{\delta r}}(\alpha)\,\delta r + \Delta C_{n_p}(\alpha)\,\frac{pb}{2V}$$
$$+ \Delta C_{n_r}(\alpha)\,\frac{rb}{2V} + \cancel{\Delta C_{n_{\delta lg}}(\beta, \delta lg)} \rightarrow 0 + \cancel{\Delta C_{n_{ge}}(\beta, \tfrac{h}{b})} \rightarrow 0$$

Figure A-1 PLS Aerodynamic Model

Aerodynamic Table Cross Reference

$C_{X_0}(\alpha,\beta)$	CX0	$\Delta C_{l_{\delta\Delta f}}(\alpha)$	CLLDDBF
$C_{Z_0}(\alpha,\beta)$	CZ0	$\Delta C_{n_{\delta\Delta f}}(\alpha)$	CLNDDBF
$C_{m_0}(\alpha,\beta)$	CM0	$\Delta C_{X_{\lvert\delta_r\rvert}}(\alpha)$	CXDR
C_{Y_β}	CYB	$\Delta C_{Y_{\delta_r}}(\alpha)$	CYDR
C_{l_β}	CLLB	$\Delta C_{l_{\delta_r}}(\alpha)$	CLLDR
$C_{n_0}(\alpha,\beta)$	CLN0	$\Delta C_{n_{\delta_r}}(\alpha)$	CLNDR
$\Delta C_{X_{\delta_e}}(\alpha)$	CXDE	$\Delta C_{m_q}(\alpha)$	CMQ
$\Delta C_{Z_{\delta_e}}(\alpha)$	CZDE	$\Delta C_{l_p}(\alpha)$	CLP
$\Delta C_{m_{\delta_e}}(\alpha)$	CMDE	$\Delta C_{l_r}(\alpha)$	CLR
$\Delta C_{X_{\lvert\delta_a\rvert}}(\alpha)$	CXDDE -	$\Delta C_{n_p}(\alpha)$	CNP
$\Delta C_{m_{\lvert\delta_a\rvert}}(\alpha)$	CMDDE -	$\Delta C_{n_r}(\alpha)$	CNR
$\Delta C_{Y_{\delta_a}}(\alpha)$	CYDDE	$\Delta C_{X_{\delta lg}}(\alpha, \delta_{lg})$	CXLG
$\Delta C_{l_{\delta_a}}(\alpha)$	CLLDDE	$\Delta C_{Y_{\delta lg}}(\beta, \delta_{lg})$	CYLG
$\Delta C_{n_{\delta_a}}(\alpha)$	CLNDDE	$\Delta C_{Z_{\delta lg}}(\alpha, \delta_{lg})$	CZLG
$\Delta C_{X_{\delta f+}}(\alpha)$	CXDBFP	$\Delta C_{l_{\delta lg}}(\beta, \delta_{lg})$	CRLG
$\Delta C_{Z_{\delta f+}}(\alpha)$	CZDBFP	$\Delta C_{m_{\delta lg}}(\alpha, \delta_{lg})$	CMLG
$\Delta C_{m_{\delta f+}}(\alpha)$	CMDBFP	$\Delta C_{n_{\delta lg}}(\beta, \delta_{lg})$	CNLG
$\Delta C_{X_{\delta f-}}(\alpha)$	CXDBFN	$\Delta C_{X_{ge}}(\alpha, \frac{b}{h})$	CXGE
$\Delta C_{Z_{\delta f-}}(\alpha)$	CZDBFN	$\Delta C_{Z_{ge}}(\alpha, \frac{b}{h})$	CZGE
$\Delta C_{m_{\delta f-}}(\alpha)$	CMDBFN	$\Delta C_{l_{ge}}(\beta, \frac{b}{h})$	CRGE
$\Delta C_{X_{\lvert\delta\Delta f\rvert}}(\alpha)$	CXDDBF	$\Delta C_{m_{ge}}(\alpha, \frac{b}{h})$	CMGE
$\Delta C_{Y_{\delta\Delta f}}(\alpha)$	CYDDBF	$\Delta C_{n_{ge}}(\beta, \frac{b}{h})$	CNGE

Figure A-2 Aerodynamic Table Cross Reference

```
ALPHA=   8.00          PITCHING MOMENT TRIM
COEFF       DEL=  20.00       DEU= -20.00       DWFE=         6.63
CX= -0.070579          CD=   0.108981
CY=  0.000000
CZ= -0.280860          CL=   0.268304
CL=  0.000000                             CLR=    0.74333       CLP=    -0.4789
CM= -0.004217                             CMQ=   -0.1332
CN=  0.000000          CMA                CNR=   -0.88774       CNP=     0.2726
                                                CMDE
                          /A            /B            /DE             /DA           /DR            /BFP           /BFN          /E
CL         0.000000    0.000000     -0.007892      0.000000       0.002474      0.000332       0.000000       0.000000      0.0006
CM        -0.004217   -0.002013      0.000002     -0.001843       0.000206      0.000000      -0.000989      -0.000981      0.0000
CN         0.000000    0.000000      0.003400      0.000000      -0.002549     -0.001567       0.000000       0.000000      0.0000
CX        -0.070579    0.002951     -0.000206      0.000151      -0.000518     -0.000651      -0.000225       0.000504     -0.0007
CY         0.000000    0.000000     -0.012421      0.000000       0.002641      0.002241       0.000000       0.000000     -0.0002
CZ        -0.280860   -0.041729      0.000755     -0.005025       0.000000      0.000000      -0.003734      -0.003382      0.0000
                        CZA                        CZDE
```

```
ALPHA=  12.00          PITCHING MOMENT TRIM
COEFF       DEL=   0.00       DEU=   0.00       DWFE=         3.79
CX= -0.039602          CD=   0.126934
CY=  0.000000
CZ= -0.424206          CL=   0.406702
CL=  0.000000                             CLR=    0.80612       CLP=    -0.5791
CM= -0.006369                             CMQ=   -0.1764
CN=  0.000000                             CNR=   -0.92234       CNP=     0.2440

                          /A            /B            /DE             /DA           /DR            /BFP           /BFN          /E
CL         0.000000    0.000000     -0.007892      0.000000       0.002294      0.000421       0.000000       0.000000      0.0006
CM        -0.006369   -0.001709      0.000244     -0.001663       0.000179      0.000000      -0.000988      -0.000977      0.0000
CN         0.000000    0.000000      0.003600      0.000000      -0.002393     -0.001460       0.000000       0.000000      0.0000
CX        -0.039602    0.004615     -0.000724      0.000080      -0.000342     -0.000736      -0.000324       0.000557     -0.0007
CY         0.000000    0.000000     -0.012421      0.000000       0.002774      0.002556       0.000000       0.000000     -0.0003
CZ        -0.424206   -0.040726      0.002708     -0.004658       0.000000      0.000000      -0.003681      -0.003289      0.0000
```

```
ALPHA=  16.00          PITCHING MOMENT TRIM
COEFF       DEL=   0.00       DEU=   0.00       DWFE=         1.21
CX= -0.019569          CD=   0.176289
CY=  0.000000
CZ= -0.571324          CL=   0.543798
CL=  0.000000                             CLR=    0.57213       CLP=    -0.4991
CM= -0.008578                             CMQ=   -0.1754
CN=  0.000000                             CNR=   -0.92234       CNP=     0.1670

                          /A            /B            /DE             /DA           /DR            /BFP           /BFN          /E
CL         0.000000    0.000000     -0.007892      0.000000       0.002031      0.000481       0.000000       0.000000      0.0006
CM        -0.008578   -0.001116      0.000486     -0.001385       0.000206      0.000000      -0.000986      -0.001014      0.0000
CN         0.000000    0.000000      0.003100      0.000000      -0.002106     -0.001526       0.000000       0.000000      0.0000
CX        -0.019569    0.005213     -0.001241     -0.000043      -0.000308     -0.000860      -0.000430       0.000626     -0.0008
CY         0.000000    0.000000     -0.012421      0.000000       0.002456      0.002859       0.000000       0.000000     -0.0004
CZ        -0.571324   -0.037127      0.004664     -0.004016       0.000000      0.000000      -0.003608      -0.003292      0.0000
```

Figure A-3 Sample of Derivative Data

ORIGINAL PAGE IS
OF POOR QUALITY

Aerodynamic Table Format

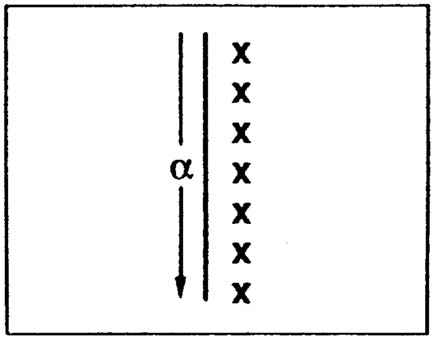

One Dimensional Table

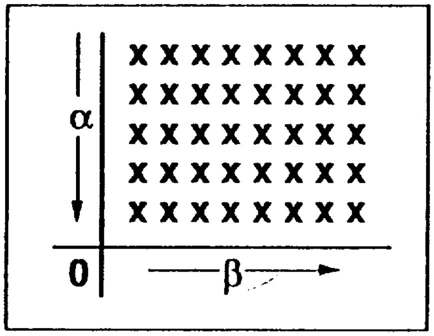

Two Dimensional Tables

Note: α and β are shown as representative independent variables; refer to the cross reference table above to determine actual independent variables.

Figure A-4 Aerodynamic Table Format

```
CX0         =

  Columns    | 1 thru      6
 -1.0000D+01 | -3.8089D-02  -4.2403D-02  -4.5911D-02  -4.9690D-02  -5.3195D-02
 -6.5021D+00 | -5.0061D-02  -5.3242D-02  -5.5828D-02  -5.8872D-02  -6.1798D-02
 -3.0324D+00 | -5.9863D-02  -6.1921D-02  -6.3593D-02  -6.5907D-02  -6.8258D-02
  3.8120D-01 | -6.5318D-02  -6.6271D-02  -6.7043D-02  -6.8639D-02  -7.0426D-02
  3.7112D+00 | -6.5707D-02  -6.5582D-02  -6.5476D-02  -6.6372D-02  -6.7608D-02
  6.9309D+00 | -6.1423D-02  -6.0256D-02  -5.9301D-02  -5.9520D-02  -6.0223D-02
  1.0014D+01 | -5.3571D-02  -5.1406D-02  -4.9638D-02  -4.9208D-02  -4.9401D-02
  1.2936D+01 | -4.3580D-02  -4.0469D-02  -3.7932D-02  -3.6887D-02  -3.6597D-02
  1.5674D+01 | -3.2884D-02  -2.8887D-02  -2.5628D-02  -2.4008D-02  -2.3264D-02
  1.8205D+01 | -2.2690D-02  -1.7873D-02  -1.3947D-02  -1.1795D-02  -1.0632D-02
  2.0508D+01 | -1.3850D-02  -8.2879D-03  -3.7544D-03  -1.1177D-03   4.2600D-04
  2.2566D+01 | -6.8265D-03  -5.9827D-04   4.4778D-03   7.5473D-03   9.4315D-03
  2.4362D+01 | -1.7240D-03   5.0855D-03   1.0635D-02   1.4082D-02   1.6263D-02
  2.5881D+01 |  1.6300D-03   8.9312D-03   1.4881D-02   1.8648D-02   2.1081D-02
  2.7112D+01 |  3.5833D-03   1.1283D-02   1.7557D-02   2.1582D-02   2.4219D-02
  2.8043D+01 |  4.5551D-03   1.2556D-02   1.9076D-02   2.3297D-02   2.6088D-02
  2.8668D+01 |  4.9439D-03   1.3147D-02   1.9832D-02   2.4185D-02   2.7079D-02
  2.8982D+01 |  5.0557D-03   1.3361D-02   2.0128D-02   2.4547D-02   2.7493D-02
  2.9061D+01 |  5.0748D-03   1.3405D-02   2.0193D-02   2.4628D-02   2.7587D-02
  2.9375D+01 |  5.1148D-03   1.3547D-02   2.0418D-02   2.4919D-02   2.7930D-02
  3.0000D+01 |  5.0188D-03   1.3653D-02   2.0689D-02   2.5321D-02   2.8436D-02
 ------------------------------------------------------------------------------
  0.0000D+00 | -1.0000D+01  -7.5001D+00  -5.4643D+00  -3.8402D+00  -2.5622D+00

  Columns      7 thru     12
 -5.6026D-02  -5.8150D-02  -5.9701D-02  -5.8150D-02  -5.6026D-02  -5.3195D-02
 -6.4172D-02  -6.5923D-02  -6.7143D-02  -6.5923D-02  -6.4172D-02  -6.1798D-02
 -7.0180D-02  -7.1561D-02  -7.2453D-02  -7.1561D-02  -7.0180D-02  -6.8258D-02
 -7.1901D-02  -7.2918D-02  -7.3488D-02  -7.2918D-02  -7.1901D-02  -7.0426D-02
 -6.8648D-02  -6.9310D-02  -6.9565D-02  -6.9310D-02  -6.8648D-02  -6.7608D-02
 -6.0843D-02  -6.1161D-02  -6.1112D-02  -6.1161D-02  -6.0843D-02  -6.0223D-02
 -4.9619D-02  -4.9608D-02  -4.9267D-02  -4.9608D-02  -4.9619D-02  -4.9401D-02
 -3.6433D-02  -3.6110D-02  -3.5493D-02  -3.6110D-02  -3.6433D-02  -3.6597D-02
 -2.2743D-02  -2.2128D-02  -2.1253D-02  -2.2128D-02  -2.2743D-02  -2.3264D-02
 -9.7806D-03  -8.8964D-03  -7.7812D-03  -8.8964D-03  -9.7806D-03  -1.0632D-02
  1.5786D-03   2.7086D-03   4.0415D-03   2.7086D-03   1.5786D-03   4.2600D-04
  1.0853D-02   1.2202D-02   1.3730D-02   1.2202D-02   1.0853D-02   9.4315D-03
```

```
  1.7919D-02 |  1.9460D-02   2.1158D-02   1.9460D-02   1.7919D-02   1.6263D-02
  2.2935D-02 |  2.4638D-02   2.6479D-02   2.4638D-02   2.2935D-02   2.1081D-02
  2.6234D-02 |  2.8068D-02   3.0025D-02   2.8068D-02   2.6234D-02   2.4219D-02
  2.8224D-02    3.0158D-02   3.2203D-02   3.0158D-02   2.8224D-02   2.6088D-02
  2.9297D-02    3.1297D-02   3.3401D-02   3.1297D-02   2.9297D-02   2.7079D-02
  2.9752D-02 |  3.1786D-02   3.3919D-02   3.1786D-02   2.9752D-02   2.7493D-02
  2.9857D-02 |  3.1899D-02   3.4040D-02   3.1899D-02   2.9857D-02   2.7587D-02
  3.0240D-02 |  3.2316D-02   3.4487D-02   3.2316D-02   3.0240D-02   2.7930D-02
  3.0828D-02 |  3.2970D-02   3.5200D-02   3.2970D-02   3.0828D-02   2.8436D-02
 ------------------------------------------------------------------------------
 -1.5538D+00 | -7.3001D-01   0.0000D+00   7.3001D-01   1.5538D+00   2.5622D+00
      7      |      8            9           10           11           12
  Columns      13 thru     16
 -4.9690D-02  -4.5911D-02  -4.2403D-02  -3.8089D-02
 -5.8872D-02  -5.5828D-02  -5.3242D-02  -5.0061D-02
 -6.5907D-02  -6.3593D-02  -6.1921D-02  -5.9863D-02
 -6.8639D-02  -6.7043D-02  -6.6271D-02  -6.5318D-02
 -6.6372D-02  -6.5476D-02  -6.5582D-02  -6.5707D-02
 -5.9520D-02  -5.9301D-02  -6.0256D-02  -6.1423D-02
 -4.9208D-02  -4.9638D-02  -5.1406D-02  -5.3571D-02
 -3.6887D-02  -3.7932D-02  -4.0469D-02  -4.3580D-02
 -2.4008D-02  -2.5628D-02  -2.8887D-02  -3.2884D-02
 -1.1795D-02  -1.3947D-02  -1.7873D-02  -2.2690D-02
 -1.1177D-03  -3.7544D-03  -8.2879D-03  -1.3850D-02
  7.5473D-03   4.4778D-03  -5.9827D-04  -6.8265D-03
  1.4082D-02   1.0635D-02   5.0855D-03  -1.7240D-03
  1.8648D-02   1.4881D-02   8.9312D-03   1.6300D-03
  2.1582D-02   1.7557D-02   1.1283D-02   3.5833D-03
  2.3297D-02   1.9076D-02   1.2556D-02   4.5551D-03
  2.4185D-02   1.9832D-02   1.3147D-02   4.9439D-03
  2.4547D-02   2.0128D-02   1.3361D-02   5.0557D-03
  2.4628D-02   2.0193D-02   1.3405D-02   5.0748D-03
  2.4919D-02   2.0418D-02   1.3547D-02   5.1148D-03
  2.5321D-02   2.0689D-02   1.3653D-02   5.0188D-03
 ----------------------------------------------------
  3.8402D+00   5.4643D+00   7.5001D+00   1.0000D+01
```

Table A-1 PLS Aerodynamic Model Function Table

```
CZ0      =

  Columns      1 thru     6
 -1.0000D+01   4.4846D-01   4.6077D-01   4.7619D-01   4.9109D-01   5.0353D-01
 -6.5021D+00   2.9980D-01   3.0785D-01   3.1981D-01   3.3195D-01   3.4222D-01
 -3.0324D+00   1.6994D-01   1.7378D-01   1.8230D-01   1.9170D-01   1.9982D-01
  3.8120D-01   4.7314D-02   4.7002D-02   5.2148D-02   5.8852D-02   6.4844D-02
  3.7112D+00  -7.3011D-02  -7.7371D-02  -7.5520D-02  -7.1446D-02  -6.7523D-02
  6.9309D+00  -1.9131D-01  -1.9959D-01  -2.0092D-01  -1.9939D-01  -1.9747D-01
  1.0014D+01  -3.0524D-01  -3.1726D-01  -3.2165D-01  -3.2255D-01  -3.2254D-01
  1.2936D+01  -4.1153D-01  -4.2710D-01  -4.3438D-01  -4.3759D-01  -4.3940D-01
  1.5674D+01  -5.0723D-01  -5.2613D-01  -5.3612D-01  -5.4149D-01  -5.4500D-01
  1.8205D+01  -5.9036D-01  -6.1234D-01  -6.2483D-01  -6.3220D-01  -6.3728D-01
  2.0508D+01  -6.6017D-01  -6.8494D-01  -6.9971D-01  -7.0890D-01  -7.1541D-01
  2.2566D+01  -7.1695D-01  -7.4423D-01  -7.6104D-01  -7.7185D-01  -7.7964D-01
  2.4362D+01  -7.6179D-01  -7.9125D-01  -8.0984D-01  -8.2207D-01  -8.3098D-01
  2.5881D+01  -7.9615D-01  -8.2746D-01  -8.4755D-01  -8.6098D-01  -8.7083D-01
  2.7112D+01  -8.2156D-01  -8.5436D-01  -8.7567D-01  -8.9007D-01  -9.0069D-01
  2.8043D+01  -8.3938D-01  -8.7331D-01  -8.9554D-01  -9.1068D-01  -9.2187D-01
  2.8668D+01  -8.5067D-01  -8.8536D-01  -9.0821D-01  -9.2384D-01  -9 3542D-01
  2.8982D+01  -8.5614D-01  -8.9121D-01  -9.1437D-01  -9.3025D-01  -9.4203D-01
  2.9061D+01  -8.5749D-01  -8.9265D-01  -9.1589D-01  -9.3183D-01  -9.4366D-01
  2.9375D+01  -8.6279D-01  -8.9834D-01  -9.2189D-01  -9.3808D-01  -9.5010D-01
  3.0000D+01  -8.7299D-01  -9.0930D-01  -9.3346D-01  -9.5015D-01  -9.6256D-01
  0.0000D+00  -1.0000D+01  -7.5001D+00  -5.4643D+00  -3.8402D+00  -2.5622D+00

  Columns      7 thru    12
  5.1316D-01   5.2051D-01   5.2634D-01   5.2051D-01   5.1316D-01   5.0353D-01
  3.5014D-01   3.5608D-01   3.6067D-01   3.5608D-01   3.5014D-01   3.4222D-01
  2.0603D-01   2.1059D-01   2.1395D-01   2.1059D-01   2.0603D-01   1.9982D-01
  6.9389D-02   7.2578D-02   7.4724D-02   7.2578D-02   6.9389D-02   6.4844D-02
 -6.4611D-02  -6.2755D-02  -6.1791D-02  -6.2755D-02  -6.4611D-02  -6.7523D-02
 -1.9613D-01  -1.9557D-01  -1.9574D-01  -1.9557D-01  -1.9613D-01  -1.9747D-01
 -3.2272D-01  -3.2339D-01  -3.2466D-01  -3.2339D-01  -3.2272D-01  -3.2254D-01
 -4.4101D-01  -4.4285D-01  -4.4516D-01  -4.4285D-01  -4.4101D-01  -4.3940D-01
 -5.4795D-01  -5.5088D-01  -5.5417D-01  -5.5088D-01  -5.4795D-01  -5.4500D-01
 -6.4147D-01  -6.4542D-01  -6.4960D-01  -6.4542D-01  -6.4147D-01  -6.3728D-01
 -7.2074D-01  -7.2561D-01  -7.3061D-01  -7.2561D-01  -7.2074D-01  -7.1541D-01
 -7.8597D-01  -7.9167D-01  -7.9740D-01  -7.9167D-01  -7.8597D-01  -7.7964D-01
```

```
 -8.3819D-01  -8.4460D-01  -8.5097D-01  -8.4460D-01  -8.3819D-01  -8.3098D-01
 -8.7879D-01  -8.8581D-01  -8.9271D-01  -8.8581D-01  -8.7879D-01  -8.7083D-01
 -9.0925D-01  -9.1676D-01  -9.2410D-01  -9.1676D-01  -9.0925D-01  -9.0069D-01
 -9.3089D-01  -9.3878D-01  -9.4645D-01  -9.3878D-01  -9.3089D-01  -9.2187D-01
 -9.4475D-01  -9.5289D-01  -9.6078D-01  -9.5289D-01  -9.4475D-01  -9.3542D-01
 -9.5150D-01  -9.5977D-01  -9.6777D-01  -9.5977D-01  -9.5150D-01  -9.4203D-01
 -9.5318D-01  -9.6147D-01  -9.6951D-01  -9.6147D-01  -9.5318D-01  -9.4366D-01
 -9.5977D-01  -9.6819D-01  -9.7634D-01  -9.6819D-01  -9.5977D-01  -9.5010D-01
 -9.7253D-01  -9.8121D-01  -9.8957D-01  -9.8121D-01  -9.7253D-01  -9.6256D-01
 -1.5538D+00  -7.3001D-01   0.0000D+00   7.3001D-01   1.5538D+00   2.5622D+00

  Columns     13 thru    16
  4.9109D-01   4.7619D-01   4.6077D-01   4.4846D-01
  3.3195D-01   3.1981D-01   3.0785D-01   2.9980D-01
  1.9170D-01   1.8230D-01   1.7378D-01   1.6994D-01
  5.8852D-02   5.2148D-02   4.7002D-02   4.7314D-02
 -7.1446D-02  -7.5520D-02  -7.7371D-02  -7.3011D-02
 -1.9939D-01  -2.0092D-01  -1.9959D-01  -1.9131D-01
 -3.2255D-01  -3.2165D-01  -3.1726D-01  -3.0524D-01
 -4.3759D-01  -4.3438D-01  -4.2710D-01  -4.1153D-01
 -5.4149D-01  -5.3612D-01  -5.2613D-01  -5.0723D-01
 -6.3220D-01  -6.2483D-01  -6.1234D-01  -5.9036D-01
 -7.0890D-01  -6.9971D-01  -6.8494D-01  -6.6017D-01
 -7.7185D-01  -7.6104D-01  -7.4423D-01  -7.1695D-01
 -8.2207D-01  -8.0984D-01  -7.9125D-01  -7.6179D-01
 -8.6098D-01  -8.4755D-01  -8.2746D-01  -7.9615D-01
 -8.9007D-01  -8.7567D-01  -8.5436D-01  -8.2156D-01
 -9.1068D-01  -8.9554D-01  -8.7331D-01  -8.3938D-01
 -9.2384D-01  -9.0821D-01  -8.8536D-01  -8.5067D-01
 -9.3025D-01  -9.1437D-01  -8.9121D-01  -8.5614D-01
 -9.3183D-01  -9.1589D-01  -8.9265D-01  -8.5749D-01
 -9.3808D-01  -9.2189D-01  -8.9834D-01  -8.6279D-01
 -9.5015D-01  -9.3346D-01  -9.0930D-01  -8.7299D-01
  3.8402D+00   5.4643D+00   7.5001D+00   1.0000D+01
```

Table A-1 PLS Aerodynamic Model Function Table (continued)

```
CM0        =

  Columns      1 thru      6
 -1.0000D+01  3.8066D-02  4.0272D-02  4.2887D-02  4.4914D-02  4.6361D-02
 -6.5021D+00  3.1390D-02  3.3066D-02  3.5250D-02  3.6932D-02  3.8108D-02
 -3.0324D+00  2.6100D-02  2.7250D-02  2.9006D-02  3.0346D-02  3.1254D-02
  3.8120D-01  2.0739D-02  2.1372D-02  2.2706D-02  2.3711D-02  2.4354D-02
  3.7112D+00  1.5152D-02  1.5280D-02  1.6204D-02  1.6881D-02  1.7266D-02
  6.9309D+00  9.7267D-03  9.3678D-03  9.8937D-03  1.0254D-02  1.0389D-02
  1.0014D+01  4.9106D-03  4.0845D-03  4.2300D-03  4.2865D-03  4.1833D-03
  1.2936D+01  9.9185D-04 -2.7702D-04 -4.9204D-04 -7.2313D-04 -1.0527D-03
  1.5674D+01 -1.9203D-03 -3.6039D-03 -4.1567D-03 -4.6572D-03 -5.1989D-03
  1.8205D+01 -3.8242D-03 -5.8913D-03 -6.7563D-03 -7.5060D-03 -8.2436D-03
  2.0508D+01 -4.7507D-03 -7.1668D-03 -8.3161D-03 -9.2925D-03 -1.0209D-02
  2.2566D+01 -4.7350D-03 -7.4630D-03 -8.8662D-03 -1.0045D-02 -1.1121D-02
  2.4362D+01 -3.8442D-03 -6.8442D-03 -8.4690D-03 -9.8248D-03 -1.1039D-02
  2.5881D+01 -2.2300D-03 -5.4602D-03 -7.2724D-03 -8.7777D-03 -1.0110D-02
  2.7112D+01 -1.6746D-04 -3.5841D-03 -5.5481D-03 -7.1745D-03 -8.6021D-03
  2.8043D+01  1.9542D-03 -1.6035D-03 -3.6825D-03 -5.4006D-03 -6.9003D-03
  2.8668D+01  3.6979D-03  4.5395D-05 -2.1107D-03 -3.8903D-03 -5.4385D-03
  2.8982D+01  4.6813D-03  9.8128D-04 -1.2135D-03 -3.0241D-03 -4.5965D-03
  2.9061D+01  4.9396D-03  1.2276D-03 -9.7689D-04 -2.7952D-03 -4.3737D-03
  2.9375D+01  6.0210D-03  2.2615D-03  1.8229D-05 -1.8309D-03 -3.4338D-03
  3.0000D+01  8.4281D-03  4.5739D-03  2.2535D-03  3.4283D-04 -1.3084D-03
  0.0000D+00 -1.0000D+01 -7.5001D+00 -5.4643D+00 -3.8402D+00 -2.5622D+00

  Columns      7 thru     12
  4.7428D-02  4.8290D-02  4.9085D-02  4.8290D-02  4.7428D-02  4.6361D-02
  3.8961D-02  3.9649D-02  4.0290D-02  3.9649D-02  3.8961D-02  3.8108D-02
  3.1895D-02  3.2409D-02  3.2897D-02  3.2409D-02  3.1895D-02  3.1254D-02
  2.4787D-02  2.5130D-02  2.5467D-02  2.5130D-02  2.4787D-02  2.4354D-02
  1.7495D-02  1.7672D-02  1.7861D-02  1.7672D-02  1.7495D-02  1.7266D-02
  1.0422D-02  1.0439D-02  1.0485D-02  1.0439D-02  1.0422D-02  1.0389D-02
  4.0274D-03  3.8902D-03  3.8003D-03  3.8902D-03  4.0274D-03  4.1833D-03
 -1.3872D-03 -1.6703D-03 -1.8895D-03 -1.6703D-03 -1.3872D-03 -1.0527D-03
 -5.7006D-03 -6.1204D-03 -6.4607D-03 -6.1204D-03 -5.7006D-03 -5.1989D-03
 -8.9001D-03 -9.4462D-03 -9.8985D-03 -9.4462D-03 -8.9001D-03 -8.2436D-03
 -1.1006D-02 -1.1667D-02 -1.2221D-02 -1.1667D-02 -1.1006D-02 -1.0209D-02
 -1.2044D-02 -1.2808D-02 -1.3453D-02 -1.2808D-02 -1.2044D-02 -1.1121D-02
```

```
 -1.2072D-02 -1.2926D-02 -1.3650D-02 -1.2926D-02 -1.2072D-02 -1.1039D-02
 -1.1236D-02 -1.2165D-02 -1.2957D-02 -1.2165D-02 -1.1236D-02 -1.0110D-02
 -9.8029D-03 -1.0794D-02 -1.1640D-02 -1.0794D-02 -9.8029D-03 -8.6021D-03
 -8.1580D-03 -9.1953D-03 -1.0083D-02 -9.1953D-03 -8.1580D-03 -6.9003D-03
 -6.7344D-03 -7.8029D-03 -8.7182D-03 -7.8029D-03 -6.7344D-03 -5.4385D-03
 -5.9116D-03 -6.9958D-03 -7.9250D-03 -6.9958D-03 -5.9116D-03 -4.5965D-03
 -5.6936D-03 -6.7817D-03 -7.7144D-03 -6.7817D-03 -5.6936D-03 -4.3737D-03
 -4.7729D-03 -5.8767D-03 -6.8232D-03 -5.8767D-03 -4.7729D-03 -3.4338D-03
 -2.6857D-03 -3.8208D-03 -4.7949D-03 -3.8208D-03 -2.6857D-03 -1.3084D-03
 -1.5538D+00 -7.3001D-01  0.0000D+00  7.3001D-01  1.5538D+00  2.5622D+00

  Columns     13 thru     16
  4.4914D-02  4.2887D-02  4.0272D-02  3.8066D-02
  3.6932D-02  3.5250D-02  3.3066D-02  3.1390D-02
  3.0346D-02  2.9006D-02  2.7250D-02  2.6100D-02
  2.3711D-02  2.2706D-02  2.1372D-02  2.0739D-02
  1.6881D-02  1.6204D-02  1.5280D-02  1.5152D-02
  1.0254D-02  9.8937D-03  9.3678D-03  9.7267D-03
  4.2865D-03  4.2300D-03  4.0845D-03  4.9106D-03
 -7.2313D-04 -4.9204D-04 -2.7702D-04  9.9185D-04
 -4.6572D-03 -4.1567D-03 -3.6039D-03 -1.9203D-03
 -7.5060D-03 -6.7563D-03 -5.8913D-03 -3.8242D-03
 -9.2925D-03 -8.3161D-03 -7.1668D-03 -4.7507D-03
 -1.0045D-02 -8.8662D-03 -7.4630D-03 -4.7350D-03
 -9.8248D-03 -8.4690D-03 -6.8442D-03 -3.8442D-03
 -8.7777D-03 -7.2724D-03 -5.4602D-03 -2.2300D-03
 -7.1745D-03 -5.5481D-03 -3.5841D-03 -1.6746D-04
 -5.4006D-03 -3.6825D-03 -1.6035D-03  1.9542D-03
 -3.8903D-03 -2.1107D-03  4.5395D-05  3.6979D-03
 -3.0241D-03 -1.2135D-03  9.8128D-04  4.6813D-03
 -2.7952D-03 -9.7689D-04  1.2276D-03  4.9396D-03
 -1.8309D-03  1.8229D-05  2.2615D-03  6.0210D-03
  3.4283D-04  2.2535D-03  4.5739D-03  8.4281D-03
  3.8402D+00  5.4643D+00  7.5001D+00  1.0000D+01
```

Table A-1 PLS Aerodynamic Model Function Table (continued)

```
AGCB PLS/CERV Subsonic Aerodynamic Model Function Tables          February 15, 1990

 CYB       =                                  CLLB      =

  -1.2421D-02                                  -7.8919D-03

 CLNO      =

   Columns    1 thru     6
  -1.0000D+01  -2.3000D-02  -1.1500D-02  -4.6000D-03   0.0000D+00   4.6000D-03
  -5.0000D+00  -2.8000D-02  -1.4000D-02  -5.6000D-03   0.0000D+00   5.6000D-03
   0.0000D+00  -4.0000D-02  -2.0000D-02  -1.0000D-02   0.0000D+00   1.0000D-02
   5.0000D+00  -3.0000D-02  -1.4000D-02  -5.0000D-03   0.0000D+00   5.0000D-03
   1.0000D+01  -3.0000D-02  -1.8000D-02  -8.0000D-03   0.0000D+00   8.0000D-03
   1.5000D+01  -3.0000D-02  -1.5000D-02  -6.0000D-03   0.0000D+00   6.0000D-03
   2.0000D+01  -1.2000D-02  -1.0000D-02  -7.0000D-03   0.0000D+00   7.0000D-03
   2.5000D+01  -9.9000D-03  -5.3000D-03  -1.7000D-03   0.0000D+00   1.7000D-03
   3.0000D+01  -2.0000D-04   2.4000D-03   2.9000D-03   0.0000D+00  -2.9000D-03
   0.0000D+00  -1.0000D+01  -5.0000D+00  -2.0000D+00   0.0000D+00   2.0000D+00

   Columns    7 thru     8
   1.1500D-02   2.3000D-02
   1.4000D-02   2.8000D-02
   2.0000D-02   4.0000D-02
   1.4000D-02   3.0000D-02
   1.8000D-02   3.0000D-02
   1.5000D-02   3.0000D-02
   1.0000D-02   1.2000D-02
   5.3000D-03   9.9000D-03
  -2.4000D-03   2.0000D-04
   5.0000D+00   1.0000D+01
```

```
AGCB PLS/CERV Subsonic Aerodynamic Model Function Tables          February 15, 1990

 CXDE      =                                  CZDE      =

  -1.0000D+01   4.4325D-04                     -1.0000D+01  -4.1348D-03
  -6.2900D+00   2.6802D-04                     -6.2900D+00  -4.6625D-03
  -3.1200D+00   2.0531D-04                     -3.1200D+00  -4.9652D-03
  -4.3000D-01   1.8677D-04                     -4.3000D-01  -5.1227D-03
   1.8400D+00   1.8177D-04                      1.8400D+00  -5.1868D-03
   3.7500D+00   1.7817D-04                      3.7500D+00  -5.1918D-03
   5.3600D+00   1.7216D-04                      5.3600D+00  -5.1605D-03
   6.7300D+00   1.6325D-04                      6.7300D+00  -5.1074D-03
   7.9200D+00   1.5182D-04                      7.9200D+00  -5.0410D-03
   8.9900D+00   1.3816D-04                      8.9900D+00  -4.9644D-03
   1.0000D+01   1.2206D-04                      1.0000D+01  -4.8770D-03
   1.1010D+01   1.0266D-04                      1.1010D+01  -4.7743D-03
   1.2080D+01   7.8401D-05                      1.2080D+01  -4.6481D-03
   1.3270D+01   4.6908D-05                      1.3270D+01  -4.4859D-03
   1.4640D+01   4.8688D-06                      1.4640D+01  -4.2690D-03
   1.6250D+01  -5.1989D-05                      1.6250D+01  -3.9700D-03
   1.8160D+01  -1.2859D-04                      1.8160D+01  -3.5487D-03
   2.0430D+01  -2.2926D-04                      2.0430D+01  -2.9448D-03
   2.3120D+01  -3.5455D-04                      2.3120D+01  -2.0667D-03
   2.6290D+01  -4.9384D-04                      2.6290D+01  -7.7336D-04
   3.0000D+01  -6.1043D-04                      3.0000D+01   1.1547D-03
```

Table A-1 PLS Aerodynamic Model Function Table (continued)

CMDE =

-1.0000D+01	-1.5496D-03
-6.2900D+00	-1.7144D-03
-3.1200D+00	-1.8292D-03
-4.3000D-01	-1.8953D-03
1.8400D+00	-1.9228D-03
3.7500D+00	-1.9233D-03
5.3600D+00	-1.9065D-03
6.7300D+00	-1.8793D-03
7.9200D+00	-1.8460D-03
8.9900D+00	-1.8083D-03
1.0000D+01	-1.7660D-03
1.1010D+01	-1.7172D-03
1.2080D+01	-1.6585D-03
1.3270D+01	-1.5852D-03
1.4640D+01	-1.4905D-03
1.6250D+01	-1.3659D-03
1.8160D+01	-1.2014D-03
2.0430D+01	-9.8538D-04
2.3120D+01	-7.0766D-04
2.6290D+01	-3.6398D-04
3.0000D+01	3.3662D-05

CXDDE =

-1.0000D+01	-9.0377D-04
-6.2900D+00	-9.0377D-04
-3.1200D+00	-9.0377D-04
-4.3000D-01	-9.0377D-04
1.8400D+00	-9.0377D-04
3.7500D+00	-7.9201D-04
5.3600D+00	-6.8599D-04
6.7300D+00	-5.9604D-04
7.9200D+00	-5.2271D-04
8.9900D+00	-4.6317D-04
1.0000D+01	-4.1415D-04
1.1010D+01	-3.7324D-04
1.2080D+01	-3.3965D-04
1.3270D+01	-3.1471D-04
1.4640D+01	-3.0240D-04
1.6250D+01	-3.0932D-04
1.8160D+01	-3.4327D-04
2.0430D+01	-4.0784D-04
2.3120D+01	-4.8833D-04
2.6290D+01	-5.1985D-04
3.0000D+01	-3.2150D-04

CMDDE =

-1.0000D+01	2.0797D-04
-6.2900D+00	2.0797D-04
-3.1200D+00	2.0797D-04
-4.3000D-01	2.0797D-04
1.8400D+00	2.0797D-04
3.7500D+00	2.2992D-04
5.3600D+00	2.2772D-04
6.7300D+00	2.1762D-04
7.9200D+00	2.0628D-04
8.9900D+00	1.9612D-04
1.0000D+01	1.8790D-04
1.1010D+01	1.8199D-04
1.2080D+01	1.7910D-04
1.3270D+01	1.8070D-04
1.4640D+01	1.8936D-04
1.6250D+01	2.0881D-04
1.8160D+01	2.4305D-04
2.0430D+01	2.9302D-04
2.3120D+01	3.4765D-04
2.6290D+01	3.6331D-04
3.0000D+01	2.2101D-04

Table A-1 PLS Aerodynamic Model Function Table (continued)

```
AGCB PLS/CERV Subsonic Aerodynamic Model Function Tables          February 15, 1990

CYDDE     =

 -1.0000D+01   3.3156D-03
 -6.2900D+00   3.3156D-03
 -3.1200D+00   3.3156D-03
 -4.3000D-01   3.3156D-03
  1.8400D+00   3.3156D-03
  3.7500D+00   3.2514D-03
  5.3600D+00   3.1819D-03
  6.7300D+00   3.1128D-03
  7.9200D+00   3.0458D-03
  8.9900D+00   2.9806D-03
  1.0000D+01   2.9148D-03
  1.1010D+01   2.8454D-03
  1.2080D+01   2.7681D-03
  1.3270D+01   2.6779D-03
  1.4640D+01   2.5691D-03
  1.6250D+01   2.4352D-03
  1.8160D+01   2.2689D-03
  2.0430D+01   2.0627D-03
  2.3120D+01   1.8090D-03
  2.6290D+01   1.5010D-03
  3.0000D+01   1.1336D-03

CLLDDE    =

 -1.0000D+01   2.5618D-03
 -6.2900D+00   2.5618D-03
 -3.1200D+00   2.5618D-03
 -4.3000D-01   2.5618D-03
  1.8400D+00   2.5618D-03
  3.7500D+00   2.5611D-03
  5.3600D+00   2.5416D-03
  6.7300D+00   2.5119D-03
  7.9200D+00   2.4767D-03
  8.9900D+00   2.4380D-03
  1.0000D+01   2.3955D-03
  1.1010D+01   2.3473D-03
  1.2080D+01   2.2902D-03
  1.3270D+01   2.2198D-03
  1.4640D+01   2.1299D-03
  1.6250D+01   2.0129D-03
  1.8160D+01   1.8587D-03
  2.0430D+01   1.6552D-03
  2.3120D+01   1.3874D-03
  2.6290D+01   1.0378D-03
  3.0000D+01   5.8611D-04
```

```
AGCB PLS/CERV Subsonic Aerodynamic Model Function Tables          February 15, 1990

CLNDDE    =

 -1.0000D+01  -2.8178D-03
 -6.2900D+00  -2.8178D-03
 -3.1200D+00  -2.8178D-03
 -4.3000D-01  -2.8178D-03
  1.8400D+00  -2.8178D-03
  3.7500D+00  -2.8112D-03
  5.3600D+00  -2.7696D-03
  6.7300D+00  -2.7139D-03
  7.9200D+00  -2.6535D-03
  8.9900D+00  -2.5918D-03
  1.0000D+01  -2.5284D-03
  1.1010D+01  -2.4613D-03
  1.2080D+01  -2.3872D-03
  1.3270D+01  -2.3026D-03
  1.4640D+01  -2.2037D-03
  1.6250D+01  -2.0876D-03
  1.8160D+01  -1.9524D-03
  2.0430D+01  -1.7973D-03
  2.3120D+01  -1.6213D-03
  2.6290D+01  -1.4173D-03
  3.0000D+01  -1.1579D-03
```

Table A-1 PLS Aerodynamic Model Function Table (continued)

AGCB PLS/CERV Subsonic Aerodynamic Model Function Tables

February 15, 1990

CXDBFP =

-1.0000D+01	-2.7210D-04
-6.2900D+00	-1.9054D-04
-3.1200D+00	-1.4613D-04
-4.3000D-01	-1.3133D-04
1.8400D+00	-1.3632D-04
3.7500D+00	-1.5274D-04
5.3600D+00	-1.7473D-04
6.7300D+00	-1.9875D-04
7.9200D+00	-2.2313D-04
8.9900D+00	-2.4744D-04
1.0000D+01	-2.7210D-04
1.1010D+01	-2.9807D-04
1.2080D+01	-3.2655D-04
1.3270D+01	-3.5878D-04
1.4640D+01	-3.9559D-04
1.6250D+01	-4.3673D-04
1.8160D+01	-4.7941D-04
2.0430D+01	-5.1557D-04
2.3120D+01	-5.2697D-04
2.6290D+01	-4.7610D-04
3.0000D+01	-2.9061D-04

CZDBFP =

-1.0000D+01	-3.7100D-03
-6.2900D+00	-3.7512D-03
-3.1200D+00	-3.7720D-03
-4.3000D-01	-3.7787D-03
1.8400D+00	-3.7764D-03
3.7500D+00	-3.7689D-03
5.3600D+00	-3.7587D-03
6.7300D+00	-3.7473D-03
7.9200D+00	-3.7353D-03
8.9900D+00	-3.7230D-03
1.0000D+01	-3.7100D-03
1.1010D+01	-3.6958D-03
1.2080D+01	-3.6794D-03
1.3270D+01	-3.6596D-03
1.4640D+01	-3.6348D-03
1.6250D+01	-3.6033D-03
1.8160D+01	-3.5626D-03
2.0430D+01	-3.5103D-03
2.3120D+01	-3.4437D-03
2.6290D+01	-3.3607D-03
3.0000D+01	-3.2607D-03

AGCB PLS/CERV Subsonic Aerodynamic Model Function Tables

February 15, 1990

CMDBFP =

-1.0000D+01	-9.8909D-04
-6.2900D+00	-9.8953D-04
-3.1200D+00	-9.8958D-04
-4.3000D-01	-9.8957D-04
1.8400D+00	-9.8957D-04
3.7500D+00	-9.8958D-04
5.3600D+00	-9.8956D-04
6.7300D+00	-9.8951D-04
7.9200D+00	-9.8941D-04
8.9900D+00	-9.8928D-04
1.0000D+01	-9.8909D-04
1.1010D+01	-9.8882D-04
1.2080D+01	-9.8844D-04
1.3270D+01	-9.8788D-04
1.4640D+01	-9.8699D-04
1.6250D+01	-9.8557D-04
1.8160D+01	-9.8320D-04
2.0430D+01	-9.7921D-04
2.3120D+01	-9.7236D-04
2.6290D+01	-9.6049D-04
3.0000D+01	-9.3986D-04

Table A-1 PLS Aerodynamic Model Function Table (continued)

```
AGCB PLS/CERV Subsonic Aerodynamic Model Function Tables          February 15, 1990

CXDBFN    -

 -1.0000D+01   4.2241D-04
 -6.2900D+00   5.5211D-04
 -3.1200D+00   4.7540D-04
 -4.3000D-01   3.4820D-04
  1.8400D+00   2.3184D-04
  3.7500D+00   1.4402D-04
  5.3600D+00   8.4652D-05
  6.7300D+00   4.8043D-05
  7.9200D+00   2.8093D-05
  8.9900D+00   2.0184D-05
  1.0000D+01   2.1651D-05
  1.1010D+01   3.1762D-05
  1.2080D+01   5.1630D-05
  1.3270D+01   8.4116D-05
  1.4640D+01   1.3359D-04
  1.6250D+01   2.0504D-04
  1.8160D+01   3.0146D-04
  2.0430D+01   4.1752D-04
  2.3120D+01   5.2544D-04
  2.6290D+01   5.4634D-04
  3.0000D+01   2.9495D-04
```

```
CZDBFN    -

 -1.0000D+01  -3.4461D-03
 -6.2900D+00  -3.7456D-03
 -3.1200D+00  -3.7862D-03
 -4.3000D-01  -3.7261D-03
  1.8400D+00  -3.6387D-03
  3.7500D+00  -3.5547D-03
  5.3600D+00  -3.4841D-03
  6.7300D+00  -3.4282D-03
  7.9200D+00  -3.3848D-03
  8.9900D+00  -3.3510D-03
  1.0000D+01  -3.3243D-03
  1.1010D+01  -3.3033D-03
  1.2080D+01  -3.2876D-03
  1.3270D+01  -3.2785D-03
  1.4640D+01  -3.2789D-03
  1.6250D+01  -3.2939D-03
  1.8160D+01  -3.3305D-03
  2.0430D+01  -3.3952D-03
  2.3120D+01  -3.4893D-03
  2.6290D+01  -3.5947D-03
  3.0000D+01  -3.6471D-03
```

```
AGCB PLS/CERV Subsonic Aerodynamic Model Function Tables          February 15, 1990

CMDBFN    -

 -1.0000D+01  -1.0612D-03
 -6.2900D+00  -1.1362D-03
 -3.1200D+00  -1.1276D-03
 -4.3000D-01  -1.0931D-03
  1.8400D+00  -1.0568D-03
  3.7500D+00  -1.0271D-03
  5.3600D+00  -1.0054D-03
  6.7300D+00  -9.9077D-04
  7.9200D+00  -9.8142D-04
  8.9900D+00  -9.7603D-04
  1.0000D+01  -9.7369D-04
  1.1010D+01  -9.7410D-04
  1.2080D+01  -9.7751D-04
  1.3270D+01  -9.8480D-04
  1.4640D+01  -9.9742D-04
  1.6250D+01  -1.0172D-03
  1.8160D+01  -1.0459D-03
  2.0430D+01  -1.0830D-03
  2.3120D+01  -1.1222D-03
  2.6290D+01  -1.1427D-03
  3.0000D+01  -1.0927D-03
```

Table A-1 PLS Aerodynamic Model Function Table (continued)

```
 CXDDBF     =                                      CYDDBF     =

  -1.0000D+01  -2.7645D-04                          -1.0000D+01   4.3519D-04
  -6.2900D+00  -4.4161D-04                          -6.2900D+00   2.8177D-04
  -3.1200D+00  -5.3697D-04                          -3.1200D+00   1.5067D-04
  -4.3000D-01  -5.9619D-04                          -4.3000D-01   4.3358D-05
   1.8400D+00  -6.3611D-04                           1.8400D+00  -4.2446D-05
   3.7500D+00  -6.6506D-04                           3.7500D+00  -1.1033D-04
   5.3600D+00  -6.8730D-04                           5.3600D+00  -1.6404D-04
   6.7300D+00  -7.0515D-04                           6.7300D+00  -2.0701D-04
   7.9200D+00  -7.2006D-04                           7.9200D+00  -2.4217D-04
   8.9900D+00  -7.3307D-04                           8.9900D+00  -2.7204D-04
   1.0000D+01  -7.4502D-04                           1.0000D+01  -2.9866D-04
   1.1010D+01  -7.5665D-04                           1.1010D+01  -3.2376D-04
   1.2080D+01  -7.6853D-04                           1.2080D+01  -3.4868D-04
   1.3270D+01  -7.8111D-04                           1.3270D+01  -3.7438D-04
   1.4640D+01  -7.9449D-04                           1.4640D+01  -4.0138D-04
   1.6250D+01  -8.0814D-04                           1.6250D+01  -4.2967D-04
   1.8160D+01  -8.2024D-04                           1.8160D+01  -4.5867D-04
   2.0430D+01  -8.2632D-04                           2.0430D+01  -4.8726D-04
   2.3120D+01  -8.1656D-04                           2.3120D+01  -5.1417D-04
   2.6290D+01  -7.7070D-04                           2.6290D+01  -5.3891D-04
   3.0000D+01  -6.4848D-04                           3.0000D+01  -5.6388D-04
```

```
AGCB PLS/CERV Subsonic Aerodynamic Model Function Tables                February 15, 1990

 CLLDDBF    =                                      CLNDDBF    =

  -1.0000D+01   7.8721D-04                          -1.0000D+01  -1.4644D-04
  -6.2900D+00   8.2521D-04                          -6.2900D+00  -1.1726D-04
  -3.1200D+00   7.9730D-04                          -3.1200D+00  -8.5288D-05
  -4.3000D-01   7.5307D-04                          -4.3000D-01  -5.5830D-05
   1.8400D+00   7.1215D-04                           1.8400D+00  -3.0833D-05
   3.7500D+00   6.8035D-04                           3.7500D+00  -1.0538D-05
   5.3600D+00   6.5775D-04                           5.3600D+00   5.5843D-06
   6.7300D+00   6.4260D-04                           6.7300D+00   1.8334D-05
   7.9200D+00   6.3294D-04                           7.9200D+00   2.8532D-05
   8.9900D+00   6.2721D-04                           8.9900D+00   3.6903D-05
   1.0000D+01   6.2446D-04                           1.0000D+01   4.4040D-05
   1.1010D+01   6.2425D-04                           1.1010D+01   5.0367D-05
   1.2080D+01   6.2673D-04                           1.2080D+01   5.6124D-05
   1.3270D+01   6.3253D-04                           1.3270D+01   6.1301D-05
   1.4640D+01   6.4269D-04                           1.4640D+01   6.5560D-05
   1.6250D+01   6.5838D-04                           1.6250D+01   6.8085D-05
   1.8160D+01   6.8003D-04                           1.8160D+01   6.7385D-05
   2.0430D+01   7.0528D-04                           2.0430D+01   6.1023D-05
   2.3120D+01   7.2446D-04                           2.3120D+01   4.5296D-05
   2.6290D+01   7.1152D-04                           2.6290D+01   1.4897D-05
   3.0000D+01   6.0641D-04                           3.0000D+01  -3.7330D-05
```

Table A-1 PLS Aerodynamic Model Function Table (continued)

```
AGCB PLS/CERV Subsonic Aerodynamic Model Function Tables                February 15, 1990

 CXDR        =                                   CYDR        =

  -1.0000D+01  -6.0020D-04                        -1.0000D+01   1.8950D-03
  -6.2900D+00  -6.0020D-04                        -6.2900D+00   1.8950D-03
  -3.1200D+00  -6.0020D-04                        -3.1200D+00   1.8950D-03
  -4.3000D-01  -6.0020D-04                        -4.3000D-01   1.8950D-03
   1.8400D+00  -6.0020D-04                         1.8400D+00   1.8950D-03
   3.7500D+00  -6.1220D-04                         3.7500D+00   1.9730D-03
   5.3600D+00  -6.2276D-04                         5.3600D+00   2.0622D-03
   6.7300D+00  -6.3528D-04                         6.7300D+00   2.1513D-03
   7.9200D+00  -6.5020D-04                         7.9200D+00   2.2363D-03
   8.9900D+00  -6.6744D-04                         8.9900D+00   2.3173D-03
   1.0000D+01  -6.8723D-04                         1.0000D+01   2.3964D-03
   1.1010D+01  -7.1042D-04                         1.1010D+01   2.4770D-03
   1.2080D+01  -7.3843D-04                         1.2080D+01   2.5628D-03
   1.3270D+01  -7.7309D-04                         1.3270D+01   2.6571D-03
   1.4640D+01  -8.1616D-04                         1.4640D+01   2.7620D-03
   1.6250D+01  -8.6803D-04                         1.6250D+01   2.8766D-03
   1.8160D+01  -9.2463D-04                         1.8160D+01   2.9947D-03
   2.0430D+01  -9.7056D-04                         2.0430D+01   3.1000D-03
   2.3120D+01  -9.6462D-04                         2.3120D+01   3.1591D-03
   2.6290D+01  -8.1120D-04                         2.6290D+01   3.1104D-03
   3.0000D+01  -3.0594D-04                         3.0000D+01   2.8473D-03
```

```
AGCB PLS/CERV Subsonic Aerodynamic Model Function Tables                February 15, 1990

 CLLDR       =                                   CLNDR       =

  -1.0000D+01   2.1894D-04                        -1.0000D+01  -1.2684D-03
  -6.2900D+00   2.1894D-04                        -6.2900D+00  -1.2684D-03
  -3.1200D+00   2.1894D-04                        -3.1200D+00  -1.2684D-03
  -4.3000D-01   2.1894D-04                        -4.3000D-01  -1.2684D-03
   1.8400D+00   2.1894D-04                         1.8400D+00  -1.2684D-03
   3.7500D+00   2.3902D-04                         3.7500D+00  -1.2832D-03
   5.3600D+00   2.6954D-04                         5.3600D+00  -1.3093D-03
   6.7300D+00   3.0082D-04                         6.7300D+00  -1.3377D-03
   7.9200D+00   3.2961D-04                         7.9200D+00  -1.3652D-03
   8.9900D+00   3.5546D-04                         8.9900D+00  -1.3908D-03
   1.0000D+01   3.7899D-04                         1.0000D+01  -1.4150D-03
   1.1010D+01   4.0110D-04                         1.1010D+01  -1.4384D-03
   1.2080D+01   4.2251D-04                         1.2080D+01  -1.4618D-03
   1.3270D+01   4.4355D-04                         1.3270D+01  -1.4854D-03
   1.4640D+01   4.6404D-04                         1.4640D+01  -1.5086D-03
   1.6250D+01   4.8353D-04                         1.6250D+01  -1.5295D-03
   1.8160D+01   5.0232D-04                         1.8160D+01  -1.5446D-03
   2.0430D+01   5.2464D-04                         2.0430D+01  -1.5487D-03
   2.3120D+01   5.6622D-04                         2.3120D+01  -1.5368D-03
   2.6290D+01   6.7108D-04                         2.6290D+01  -1.5087D-03
   3.0000D+01   9.4552D-04                         3.0000D+01  -1.4815D-03
```

Table A-1 PLS Aerodynamic Model Function Table (continued)

CMQ =

0.0000D+00	-2.0336D-01
5.0000D+00	-1.5836D-01
1.0000D+01	-1.1635D-01
1.2000D+01	-1.7636D-01
1.4000D+01	-1.7636D-01
1.6000D+01	-1.7536D-01
1.8000D+01	-1.7436D-01
2.0000D+01	-2.5237D-01
2.2000D+01	-2.9937D-01
2.5000D+01	-5.7136D-01
3.0000D+01	-8.0036D-01

CLP =

0.0000D+00	-4.9811D-01
5.0000D+00	-6.0011D-01
1.0000D+01	-3.9811D-01
1.2000D+01	-5.7911D-01
1.4000D+01	-4.2511D-01
1.6000D+01	-4.9911D-01
1.8000D+01	-6.4911D-01
2.0000D+01	-6.1911D-01
2.2000D+01	-8.1011D-01
2.5000D+01	-8.7211D-01
3.0000D+01	-2.4101D+00

CLR =

0.0000D+00	4.9613D-01
5.0000D+00	5.9813D-01
1.0000D+01	8.4013D-01
1.2000D+01	8.0613D-01
1.4000D+01	6.8613D-01
1.6000D+01	5.7213D-01
1.8000D+01	6.0313D-01
2.0000D+01	8.9913D-01
2.2000D+01	9.5713D-01
2.5000D+01	1.3571D+00
3.0000D+01	4.4901D+00

CNP =

0.0000D+00	3.8097D-01
5.0000D+00	3.5297D-01
1.0000D+01	2.1897D-01
1.2000D+01	2.4397D-01
1.4000D+01	1.7897D-01
1.6000D+01	1.6697D-01
1.8000D+01	2.0097D-01
2.0000D+01	2.2197D-01
2.2000D+01	3.0697D-01
2.5000D+01	3.7897D-01
3.0000D+01	8.4997D-01

CNR =

0.0000D+00	-7.9434D-01
5.0000D+00	-8.3734D-01
1.0000D+01	-9.2134D-01
1.2000D+01	-9.2234D-01
1.4000D+01	-8.6734D-01
1.6000D+01	-9.2234D-01
1.8000D+01	-9.4634D-01
2.0000D+01	-1.0073D+00
2.2000D+01	-1.0903D+00
2.5000D+01	-1.2863D+00
3.0000D+01	-2.0413D+00

Table A-1 PLS Aerodynamic Model Function Table (continued)

Appendix B

6DOF NON-LINEAR SIMULATION

The computer resources used in the 6DOF simulation are shown in figure B-1. The non-linear equations of motion are hosted on the AD100. The autopilot and other slower processes are hosted on the Harris 1000. The PLS simulation runs three times real time. Figure B-2 shows the PLS simulation functional block diagram. The major blocks consist of the autopilot, guidance, 6DOF equations of motion, actuator models, rate gyro models, and the gain computer. The autopilot operates at a 20 ms cycle, with a 10 ms computational delay. Autopilot gains are updated from the gain computer every 120 ms. Perfect knowledge of α, β, and ϕ is assumed and used as feedback signals. Autopilot fin commands are fed to a mixer set equations to obtain the proper command to the actuators. The actual fin positions are then un-mixed before going to the aerodynamic model. The actuators are modeled as a second order filter with a 10 hz bandwidth and 0.5 damping, and a rate limit of 200 degrees/sec.

The guidance operates at a 60 ms cycle. Perfect knowledge of the spacecraft position and inertial velocities is assumed and used as feedback signals to the guidance. Longitudinal and lateral guidance designs are described in more detail in sections 3.1. Rate gyro sensors are modeled as second order filters with a bandwidth of 60 hz and 0.4 damping. The turbulence wind model is described in more detail in Appendix C.

ENGINEERING
TECHNOLOGY

Boeing Aerospace

6 DOF Simulation Resources

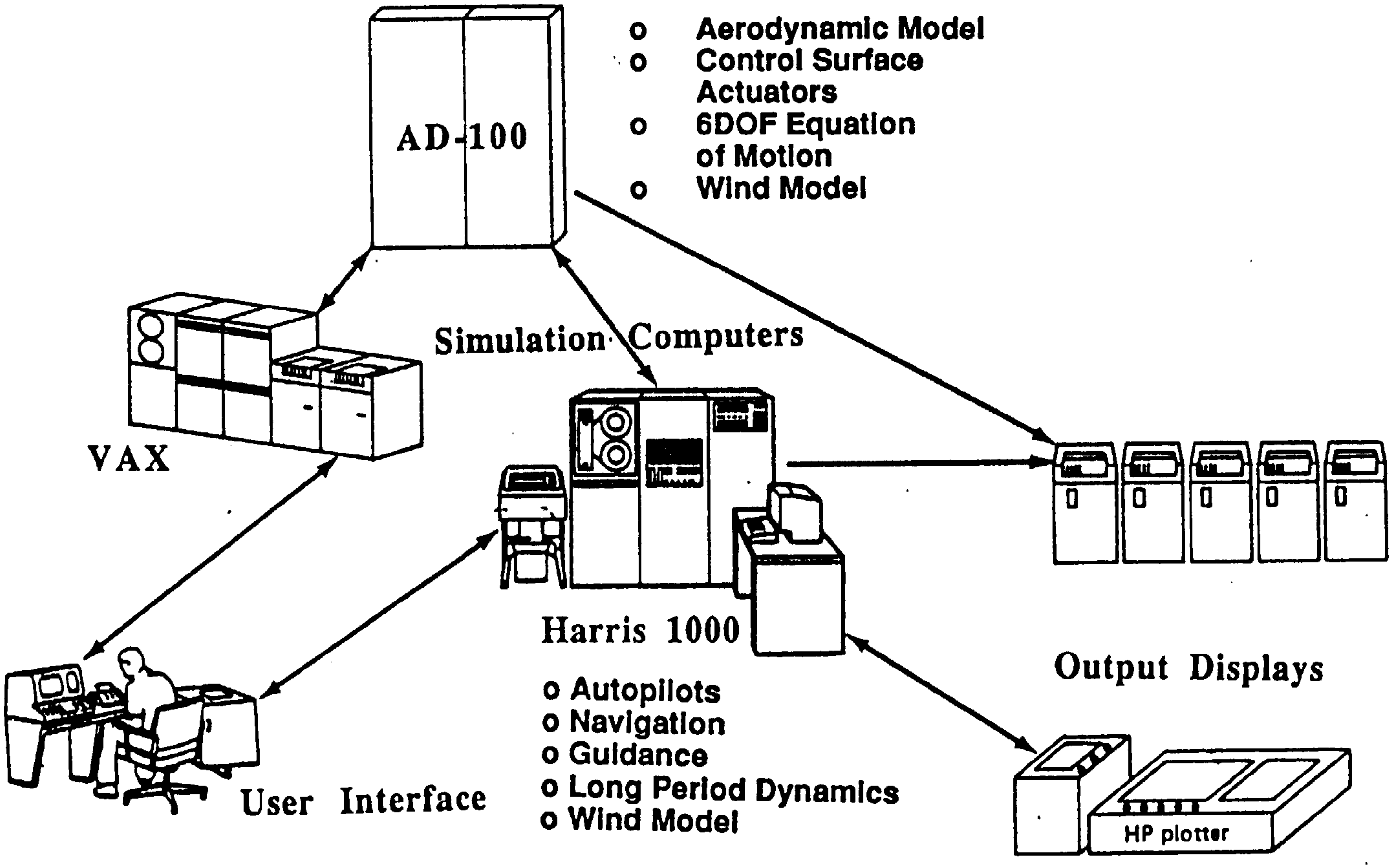

AD-100

- o Aerodynamic Model
- o Control Surface Actuators
- o 6DOF Equation of Motion
- o Wind Model

VAX

Simulation Computers

Harris 1000

- o Autopilots
- o Navigation
- o Guidance
- o Long Period Dynamics
- o Wind Model

User Interface

Output Displays

FLT 3634
NK;3 May 1989;ARA Rvw. 6
ML DISK 1989 PG18

Figure B-1 6 DOF Simulation Resources

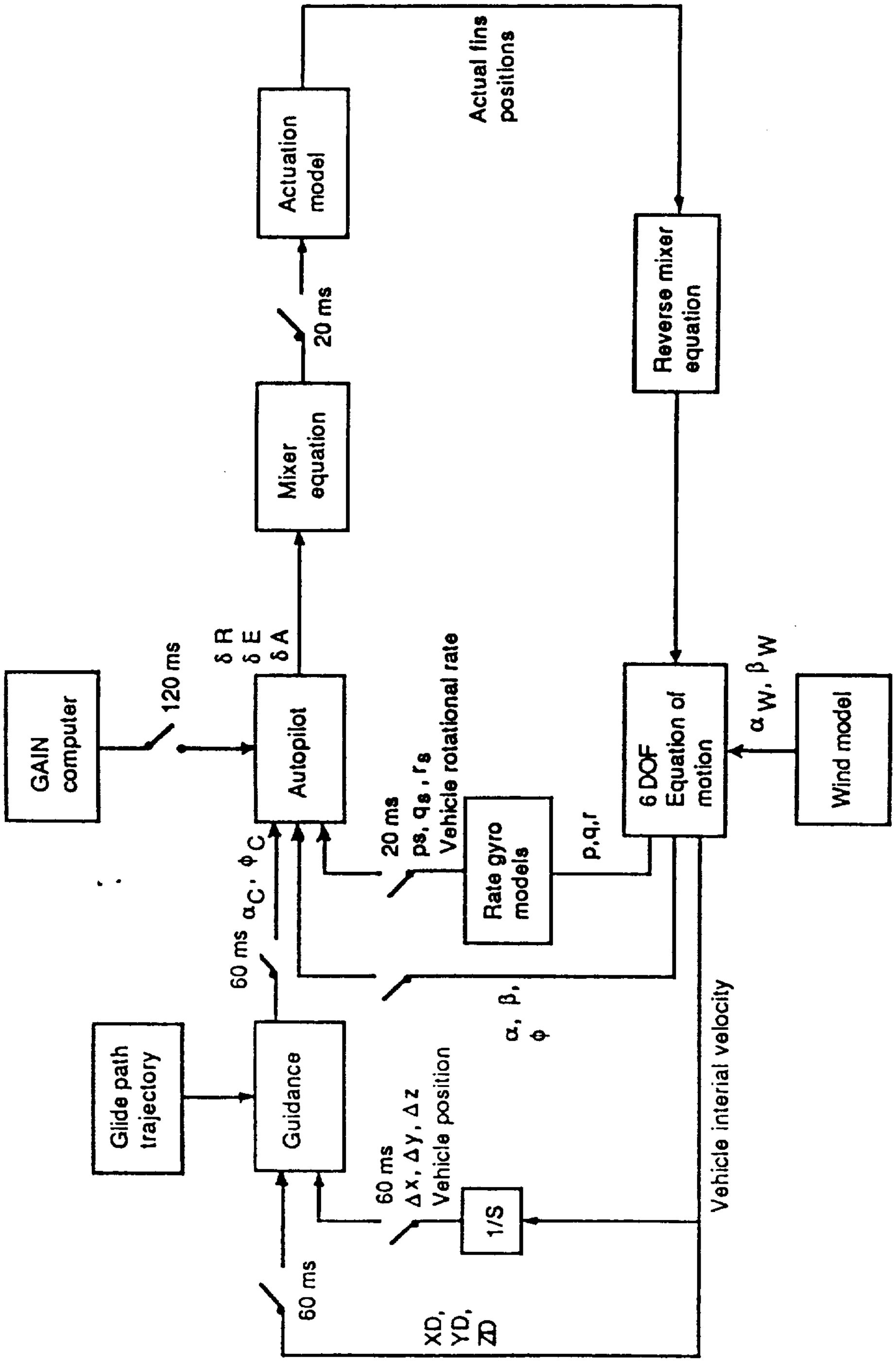

Figure B-2 PLS *Simulation Block Diagram*

ML4-28-89-8

Appendix C

WIND TURBULENCE MODEL

C.1 Introduction

A number of efforts have been directed toward generating mathematical models of wind turbulence near the surface of the earth. References 3-6 all recommend the use of the Von Karman isotropic power spectra over the Dryden spectra, apparently due to their greater accuracy at high frequency.

The Von Karman spectra provide a complex spacial distribution of wind velocity vectors, which must be converted to a temporal distribution, by aircraft speed and flight path, for use in a flight simulation. The size of the aircraft, in response to the gust velocities, must also be taken into account. Reference 3 proposes to approximate the Von Karman gust distributions by driving shaping filters with white noise. It proposes a second-order filter for the longitudinal direction and a third-order filter for the lateral and vertical directions. Reference 4 also proposes shaping filters, based on the landing conditions of a transport aircraft, for this approximation. It uses a first-order filter for the longitudinal direction and a second-order filter for the lateral and vertical directions. This is the model that has been implemented in our simulation.

C.2 Model Description

The form of the wind turbulence model shaping filters used in the flight simulation is taken from Reference 4. Block diagrams of the continuous froms of the filters, in terms of displacement along the flight path, are shown in figures C-1 and C-2. In the simulation these filters are discretized and the aircraft speed is used to convert time steps to distance steps. The parameters of the filters are determined from the aircraft wing span (b) and the chosen integral scale length (L), which determines the frequency response of the filters. The chosen variance level (sigma) of the wind components, along with the integral scale length, determines the level of the input white noise to drive the gust spectra.

The choice of appropriate integral scale length and turbulence variance is difficult since these vary with altitude and measured data show large variations. Figures C-3 and C-4 from Reference 4 provide an indication of the probabilities and measured variations in these values. Figure C-5 from Reference 6 gives altitude profiles of these values as chosen for use in Space Shuttle simulations.

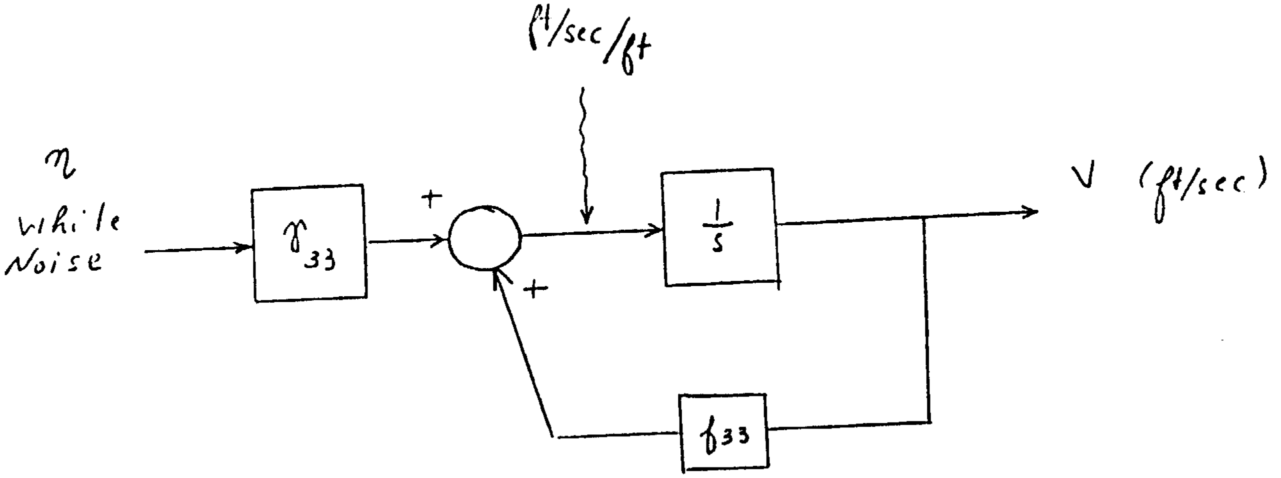

$$f_{33} = -\frac{(1 + 1.5\beta)^{2/3}}{1 + 3\beta} \quad , \quad \beta = \frac{b}{2L}$$

L = Turbulence Integral Scale

b = Wing Span of Aircraft (21 ft)

$$\gamma_{33} = -1.4 \, f_{33}$$

$$E\left\{\eta(x_1)\,\eta^T(x_2)\right\} = \sigma^2 L * \delta(x_1 - x_2)$$

Figure C-1 Turbulence Model for X-Axis

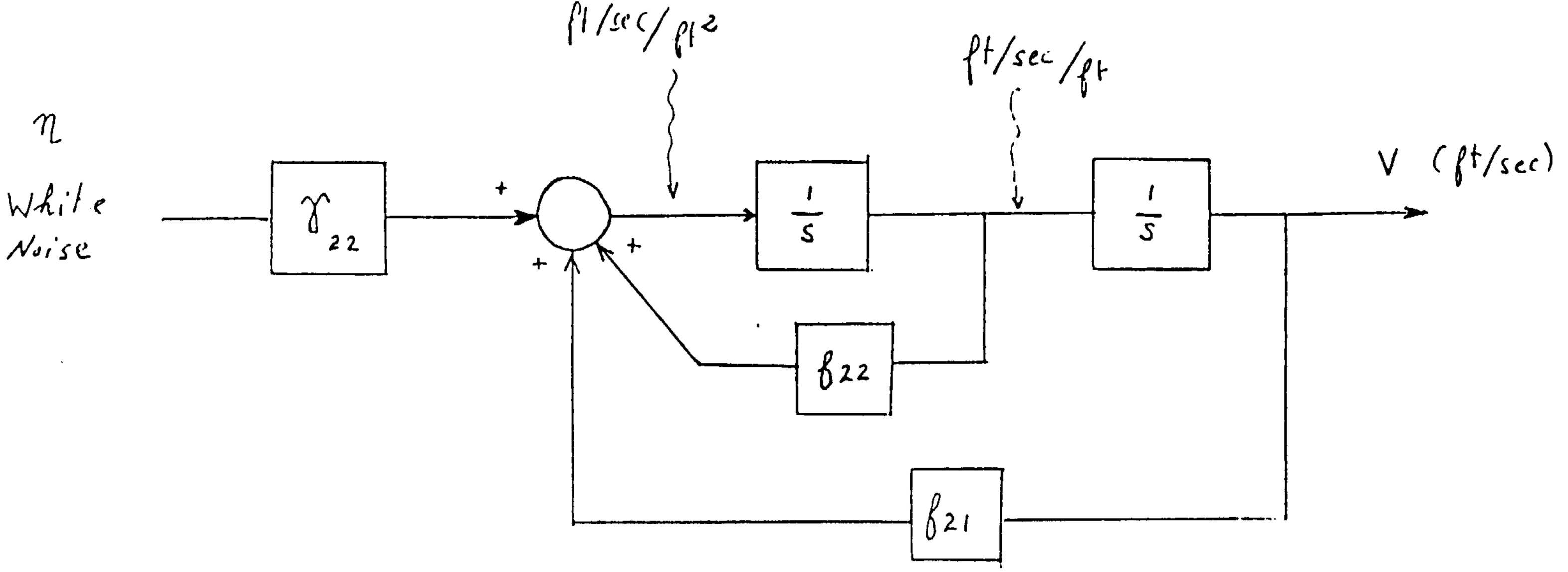

$$\beta_{21} = \frac{-(1+\beta)^{2/3}\,\beta^{-4/3}}{L^2}, \qquad \beta = \frac{b}{2L}$$

$$\beta_{22} = \frac{-0.5\,(1+3\beta)\,\beta^{-4/3}}{L}$$

L = Turbulence Integral Scale

$$\gamma_{22} = -\beta_{21}$$

b = Wing Span of Aircraft (21 ft)

$$E\left\{\eta(x_1)\,\eta^T(x_2)\right\} = \sigma^2 L * \delta(x_1 - x_2)$$

Figure C-2 Turbulence Model for Y and Z-Axis

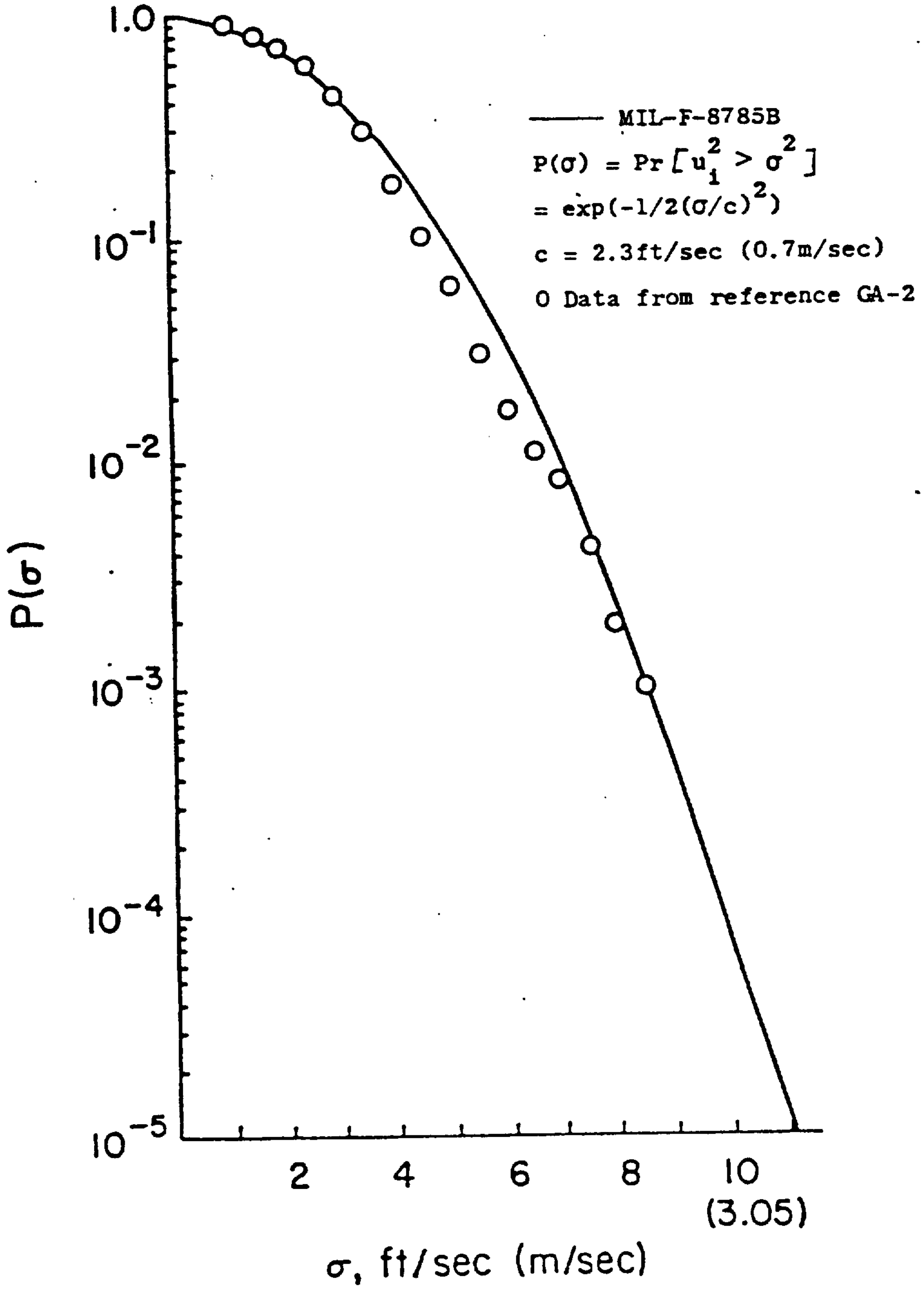

PROBABILITY DISTRIBUTION OF THE
RMS TURBULENT VELOCITY
$P(\sigma) = \Pr\{\bar{v}_i^2 \geq \sigma^2\}$

Figure C-3 Probability Distribution of the RMS Turbulent Velocity

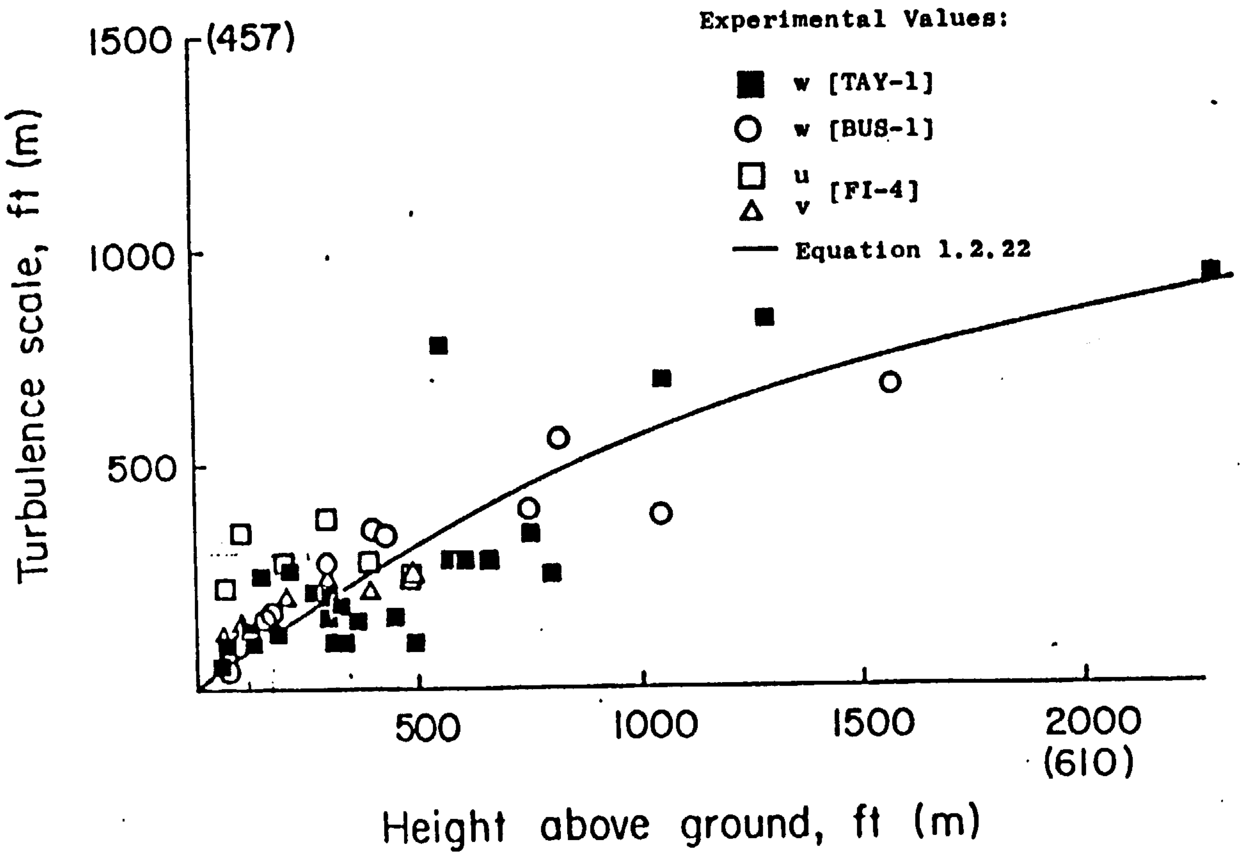

Figure C-4 Variation of the Turbulence Scale with Height

VARIATION OF STANDARD DEVIATION
AND LENGTH SCALE WITH ALTITUDE*

ALTITUDE (m)	STANDARD DEVIATION OF TURBULENCE			INTEGRAL SCALES OF TURBULENCE		
	σ_1(m/sec)	σ_2(m/sec)	σ_3(m/sec)	L_1(m)	L_2(m)	L_3(m)
10	2.31	1.67	1.15	21	11	5
20	2.58	1.98	1.46	33	19	11
30	2.75	2.20	1.71	43	28	17
40	2.88	2.36	1.89	52	35	23
50	2.98	2.49	2.05	61	42	29
60	3.07	2.61	2.19	68	49	35
70	3.15	2.71	2.32	75	56	41
80	3.22	2.81	2.43	82	63	47
90	3.28	2.89	2.54	89	69	53
100	3.33	2.97	2.64	95	75	59
200	3.72	3.53	3.38	149	134	123
304.8	3.95/4.37	3.95/4.37	3.95/4.39	196/300	190/300	192/300
400	4.39	4.39	4.39	300	300	300
500	4.39	4.39	4.39	300	300	300
600	4.39	4.39	4.39	300	300	300
700	4.39	4.39	4.39	300	300	300
762	4.39/5.70	4.39/5.70	4.39/5.70	300/533	300/533	300/533
800	5.70	5.70	5.70	533	533	533
900	5.70	5.70	5.70	533	533	533
1524	5.70/5.79	5.70/5.79	5.70/5.79	533	533	533
2000	5.79	5.79	5.79	533	533	533
3048	5.79/5.52	5.79/5.52	5.79/5.52	533	533	533
4000	5.52	5.52	5.52	533	533	533
5000	5.52	5.52	5.52	533	533	533
6096	5.52/5.27	5.52/5.27	5.52/5.27	533	533	533
7000	5.27	5.27	5.27	533	533	533
8000	5.27	5.27	5.27	533	533	533
9144	5.27/4.22	5.27/4.22	5.27/4.22	533	533	533
10000	4.22	4.22	4.22	533	533	533
20000	6.01	6.01	4.22	6691	6691	955

*Double entries for a tabulated altitude indicate a step change in standard deviation or integral scale at that altitude.

Figure C-5 Variation of Standard Deviation and Length Scale With Altitude

This page was intentionally
left blank

Appendix D

Simulation Results of Approach and Landing Nominal Mission Without Wind

The nominal approach and landing mission was simulated without wind. The conditions of this simulation are defined in section 4.2 .The results are plotted in the following figures. These results show the nominal autoland performance .

PRECEDING PAGE BLANK NOT FILMED

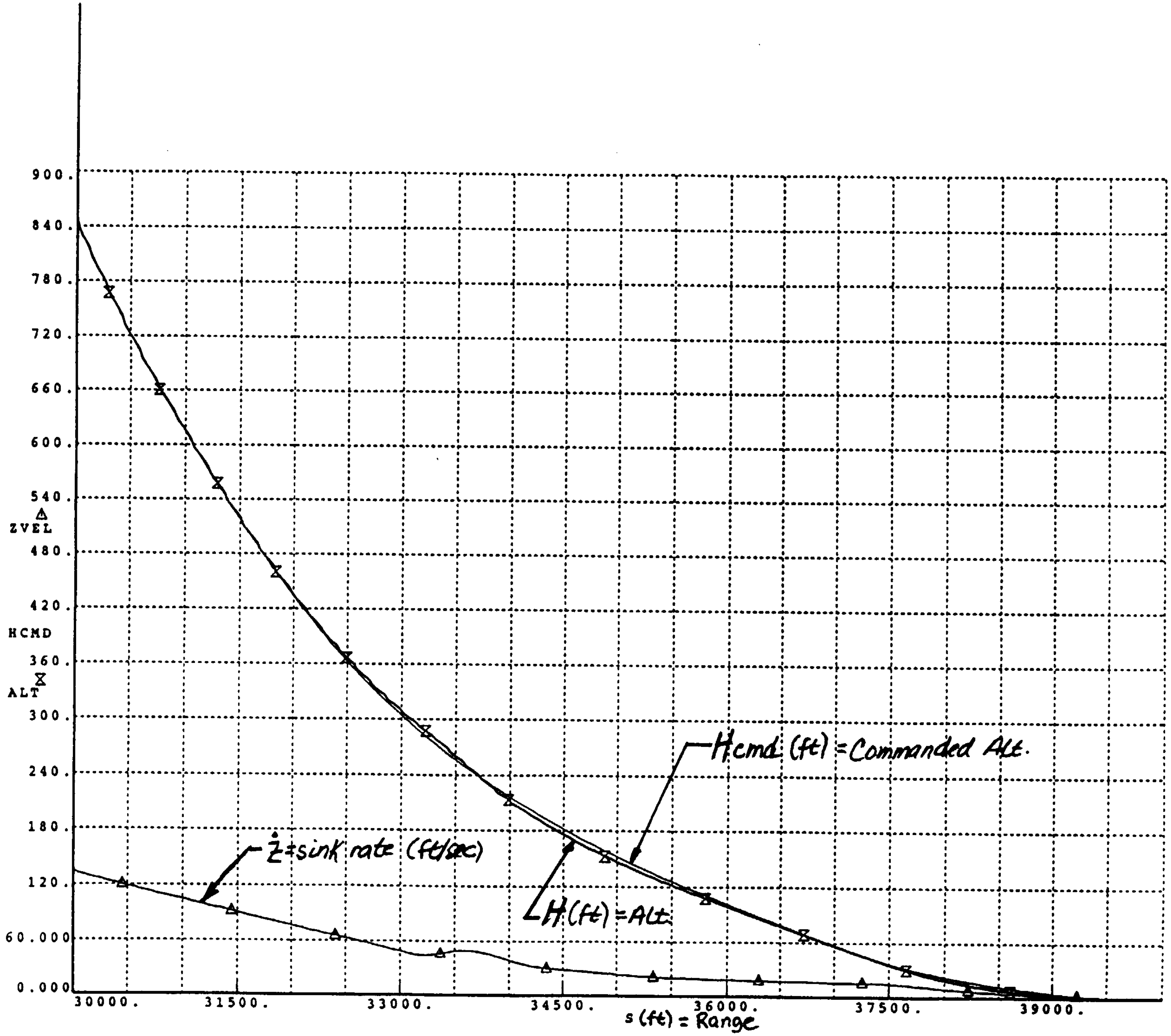
900.
840.
780.
720.
660.
600.
540.
ZVEL
480.
420.
HCMD
360.
ALT
300.
240.
180.
120.
60.000
0.000
30000.
31500.
33000.
34500.
36000.
37500.
39000.
s (ft) = Range
$\dot{Z}$=sink rate (ft/sec)
Hcmd (ft) = Commanded Alt.
H(ft) = Alt.

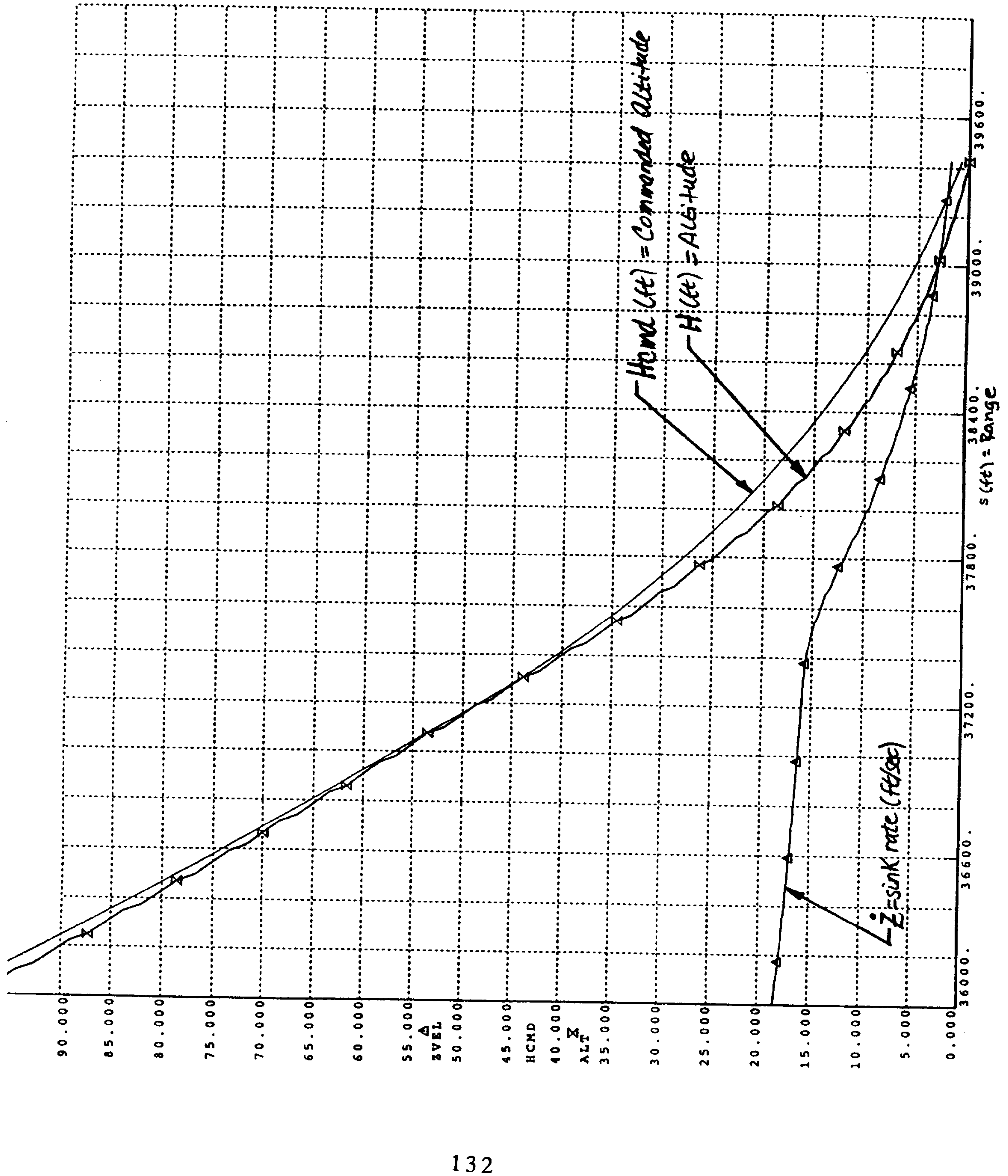
90.000
85.000
80.000
75.000
70.000
65.000
60.000
55.000
ZVEL
50.000
45.000
HCMD
40.000
ALT
35.000
30.000
25.000
20.000
15.000
10.000
5.000
0.000
36000.
36600.
37200.
37800.
38400.
39000.
39600.
s (ft) = Range
Hcmd (ft) = Commanded Altitude
H (ft) = Altitude
Ż = sink rate (ft/sec)

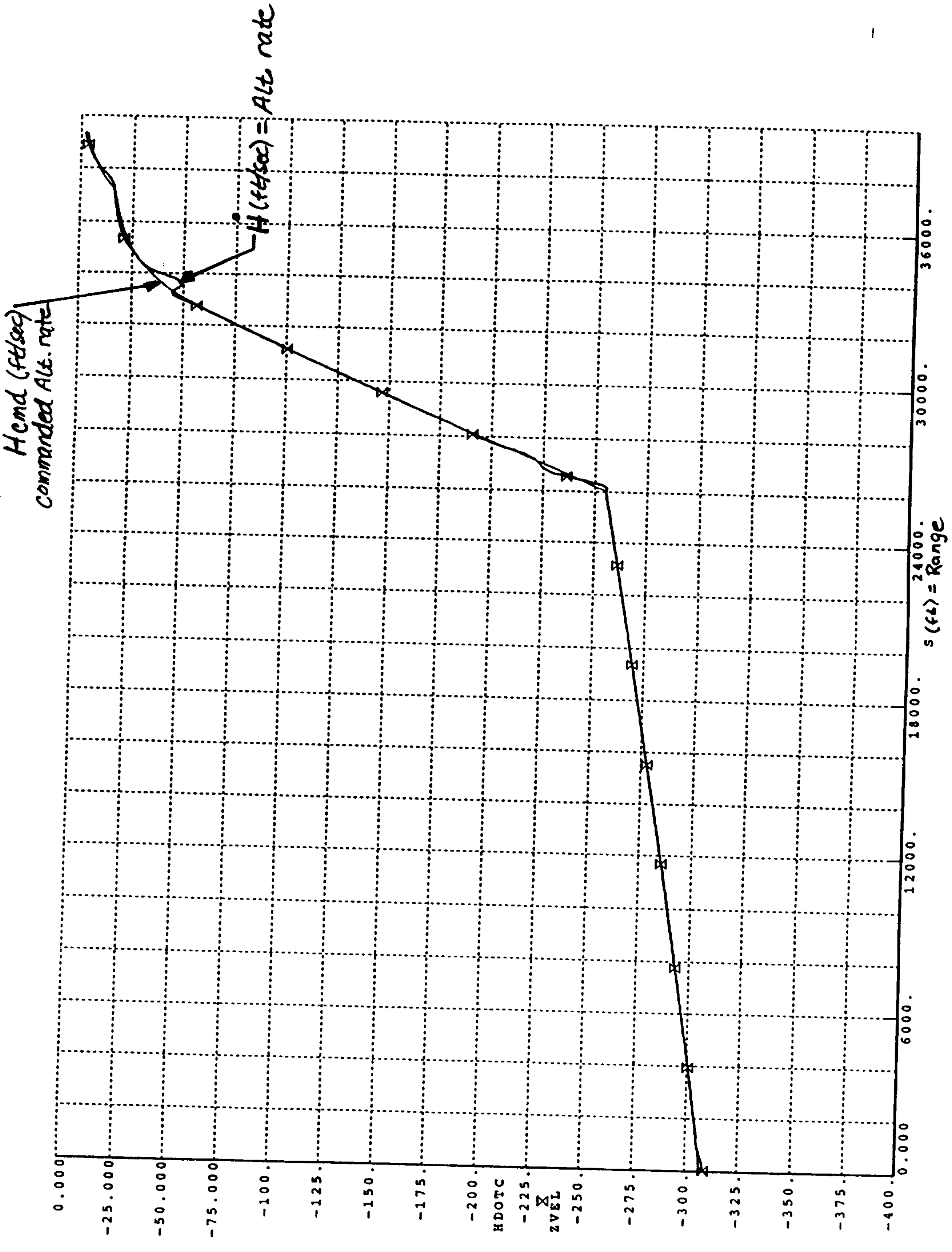
Ḣcmd (ft/sec) commanded Alt. rate
Ḣ (ft/sec) = Alt. rate
0.000
6000.
12000.
18000.
24000.
30000.
36000.
s (ft) = Range
0.000
-25.000
-50.000
-75.000
-100.
-125.
-150.
-175.
-200.
-225.
-250.
-275.
-300.
-325.
-350.
-375.
-400.
HDOTC
X
ZVEL

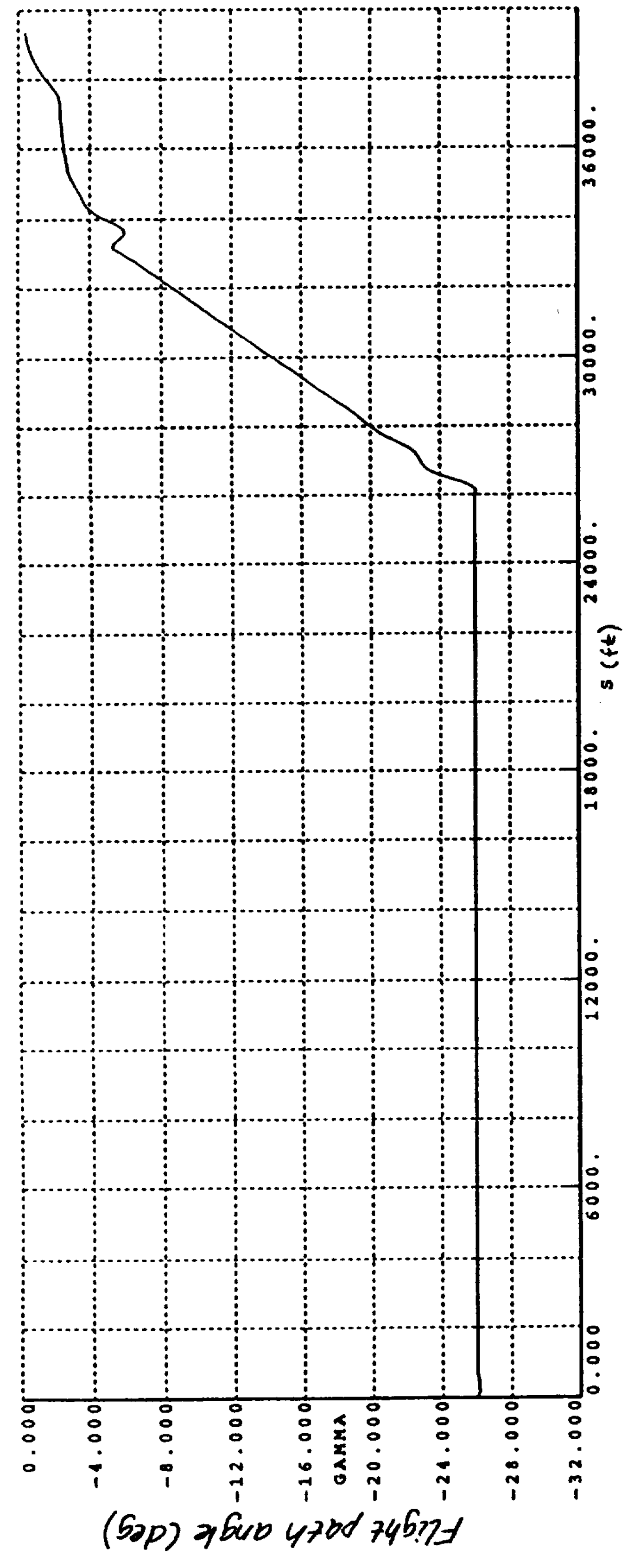
0.000
-4.000
-8.000
-12.000
-16.000
GAMMA
-20.000
-24.000
-28.000
-32.000
Flight path angle (deg)
0.000
6000.
12000.
18000.
24000.
s (ft)
30000.
36000.

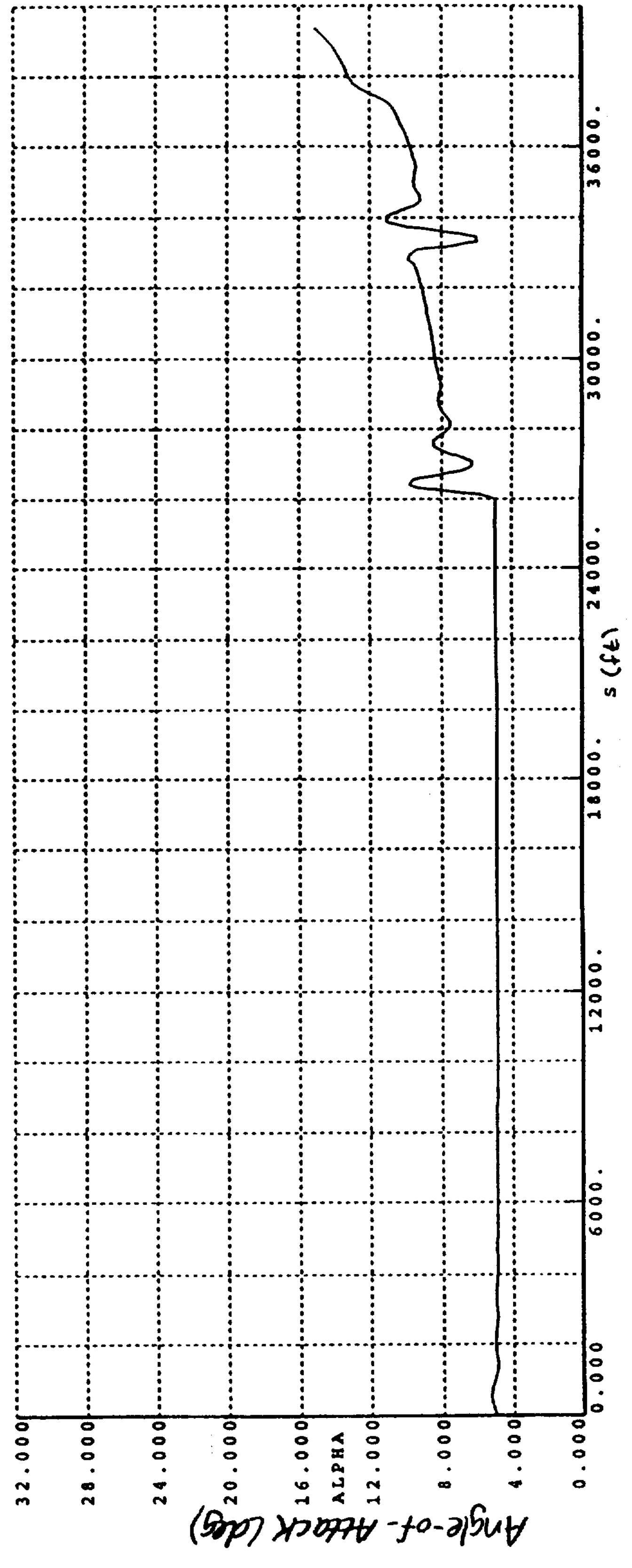
32.000
28.000
24.000
20.000
16.000
ALPHA
12.000
8.000
4.000
0.000
Angle-of-Attack (deg)
0.000
6000.
12000.
18000.
24000.
s (ft)
30000.
36000.

Appendix E

Simulation Results of Approach and Landing Nominal Mission With Wind Turbulence

The nominal approach and landing mission was simulated with wind turbulence. The conditions of this simulation are defined in section 4.3 . The results are plotted in the following figures. These results show excellent touchdown performance.

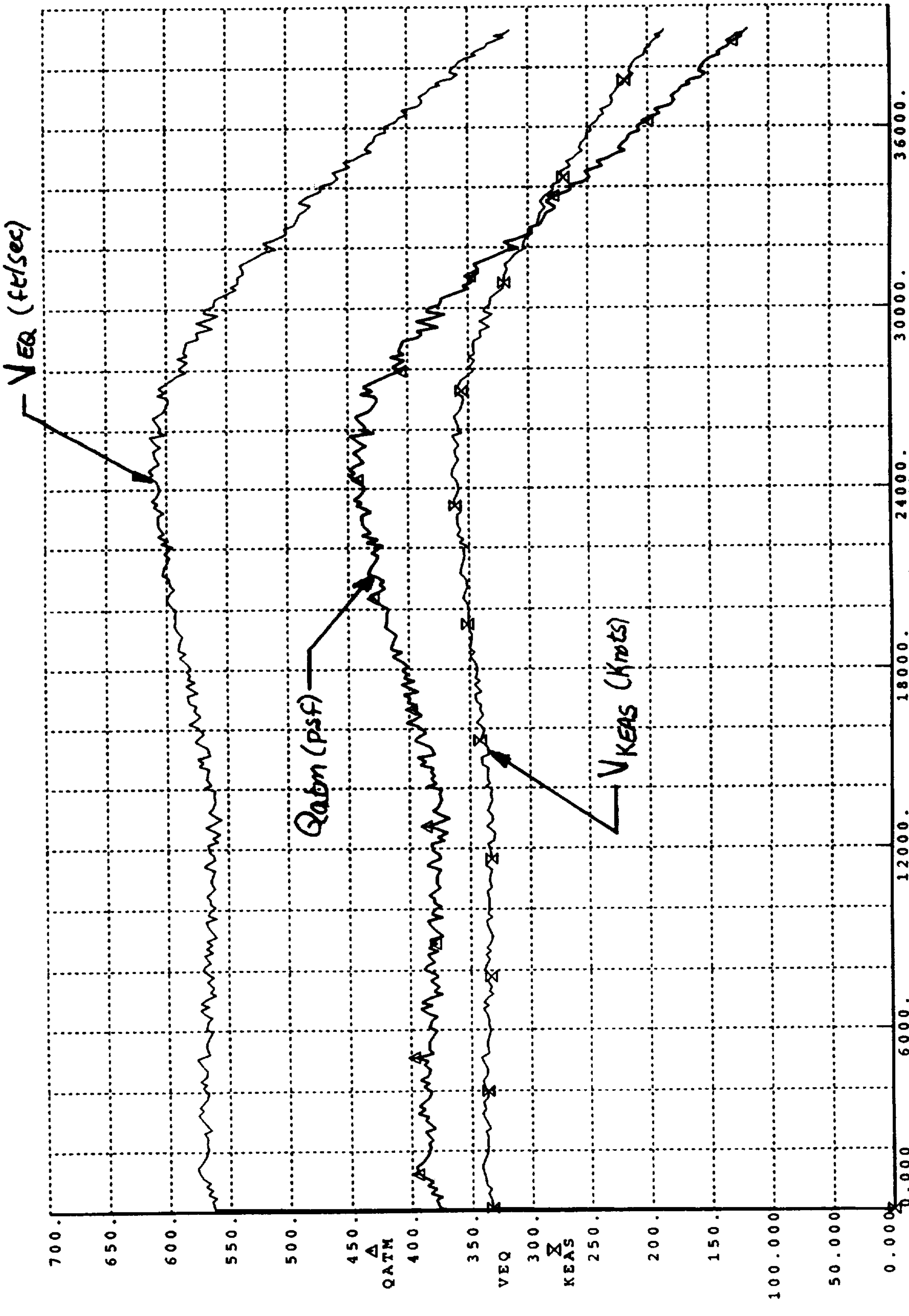

700.
650.
600.
550.
500.
450.
△ QATM
400.
350.
VEQ
300.
⌛ KEAS
250.
200.
150.
100.000
50.000
0.000
0.000
6000.
12000.
18000.
24000.
30000.
36000.
s (range) ft
VEQ (ft/sec)
Qatm (psf)
VKEAS (Knots)

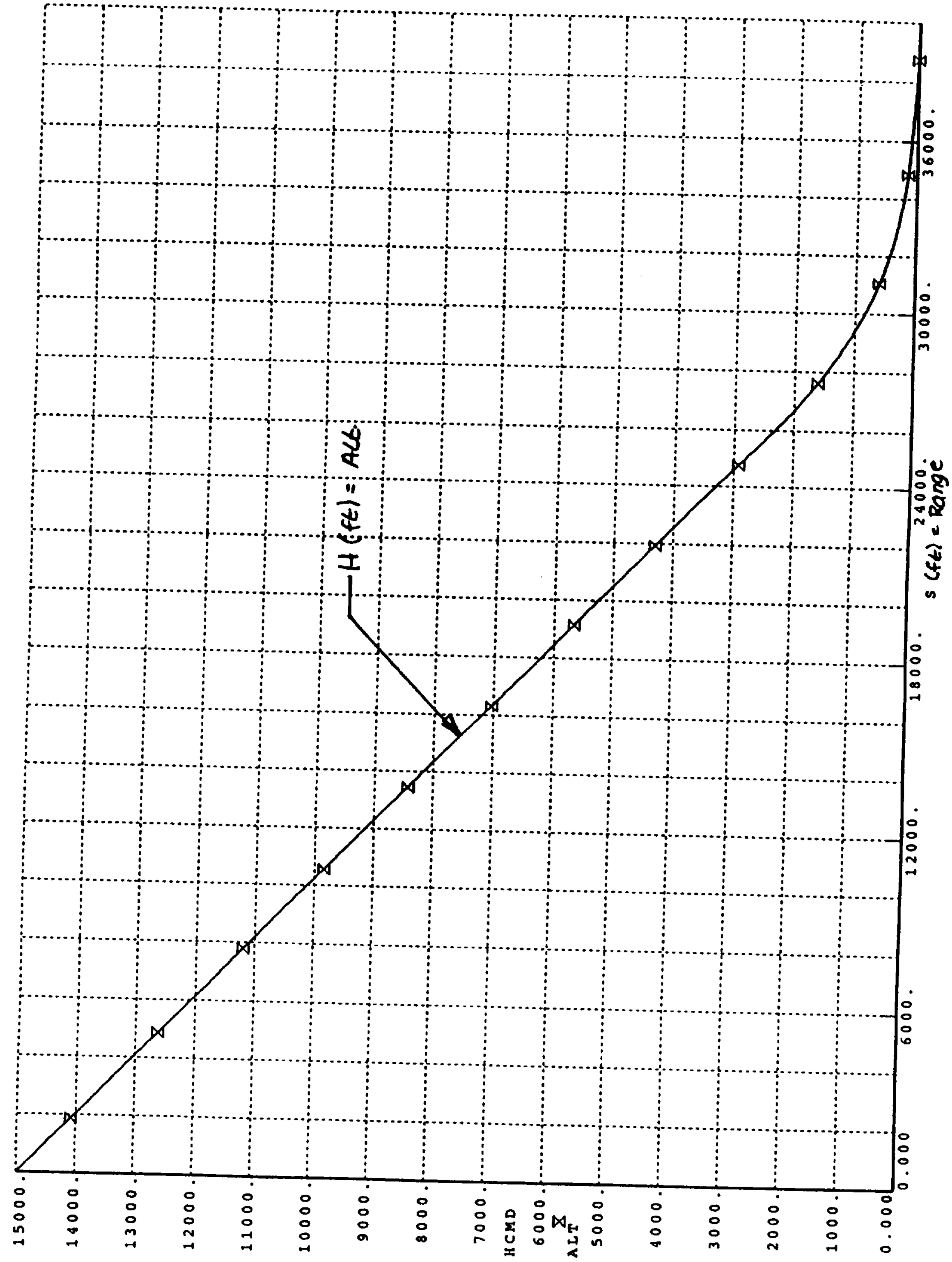
H (ft) = Alt
s (ft) = Range
HCMD
ALT
15000.
14000.
13000.
12000.
11000.
10000.
9000.
8000.
7000.
6000.
5000.
4000.
3000.
2000.
1000.
0.000
0.000
6000.
12000.
18000.
24000.
30000.
36000.

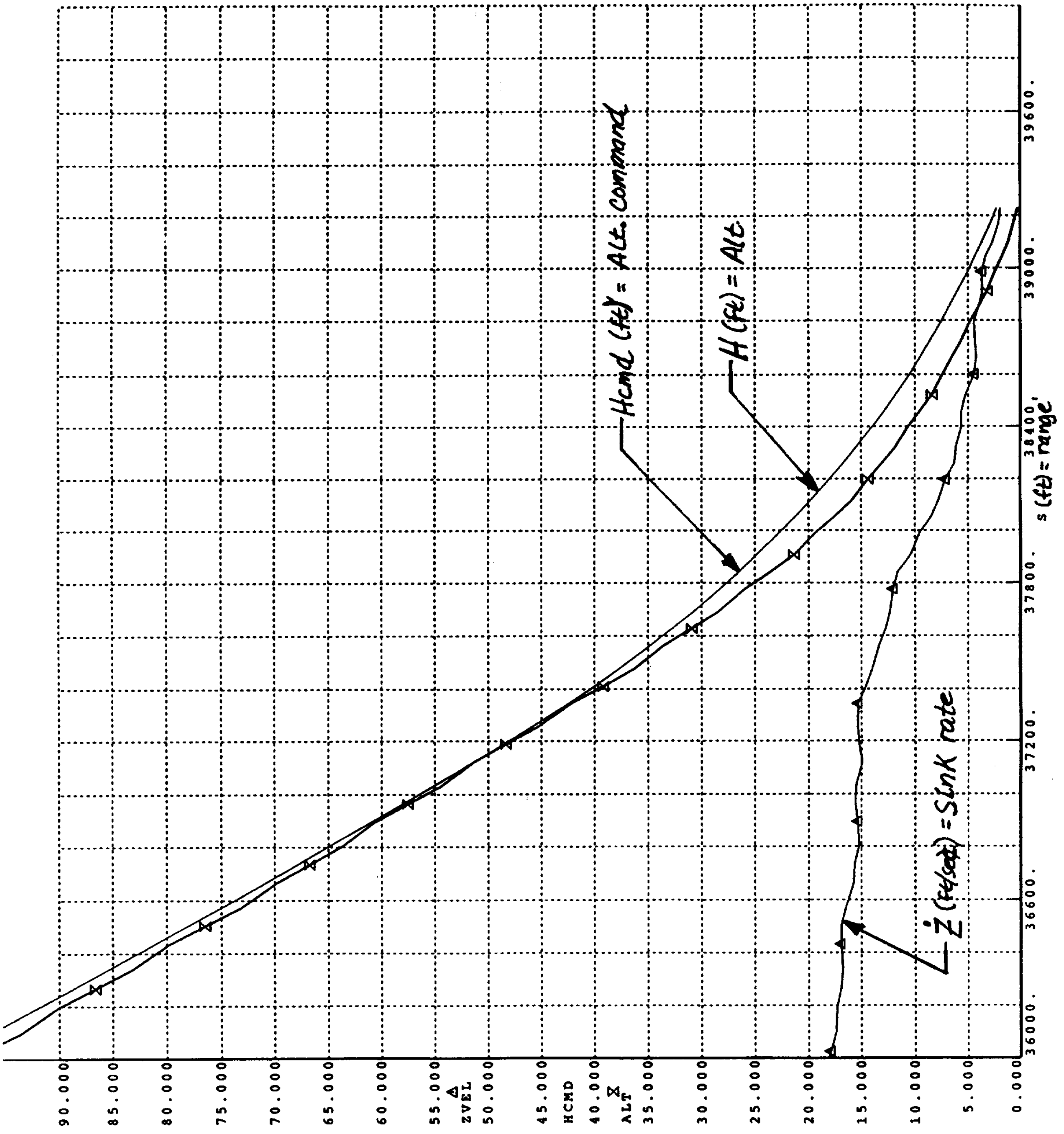
90.000
85.000
80.000
75.000
70.000
65.000
60.000
55.000
ZVEL
50.000
45.000
HCMD
40.000
ALT
35.000
30.000
25.000
20.000
15.000
10.000
5.000
0.000
36000.
36600.
37200.
37800.
38400.
39000.
39600.
s (ft) = range
Hcmd (ft) = Alt. command
H (ft) = Alt
Ż (ft/sec) = Sink rate

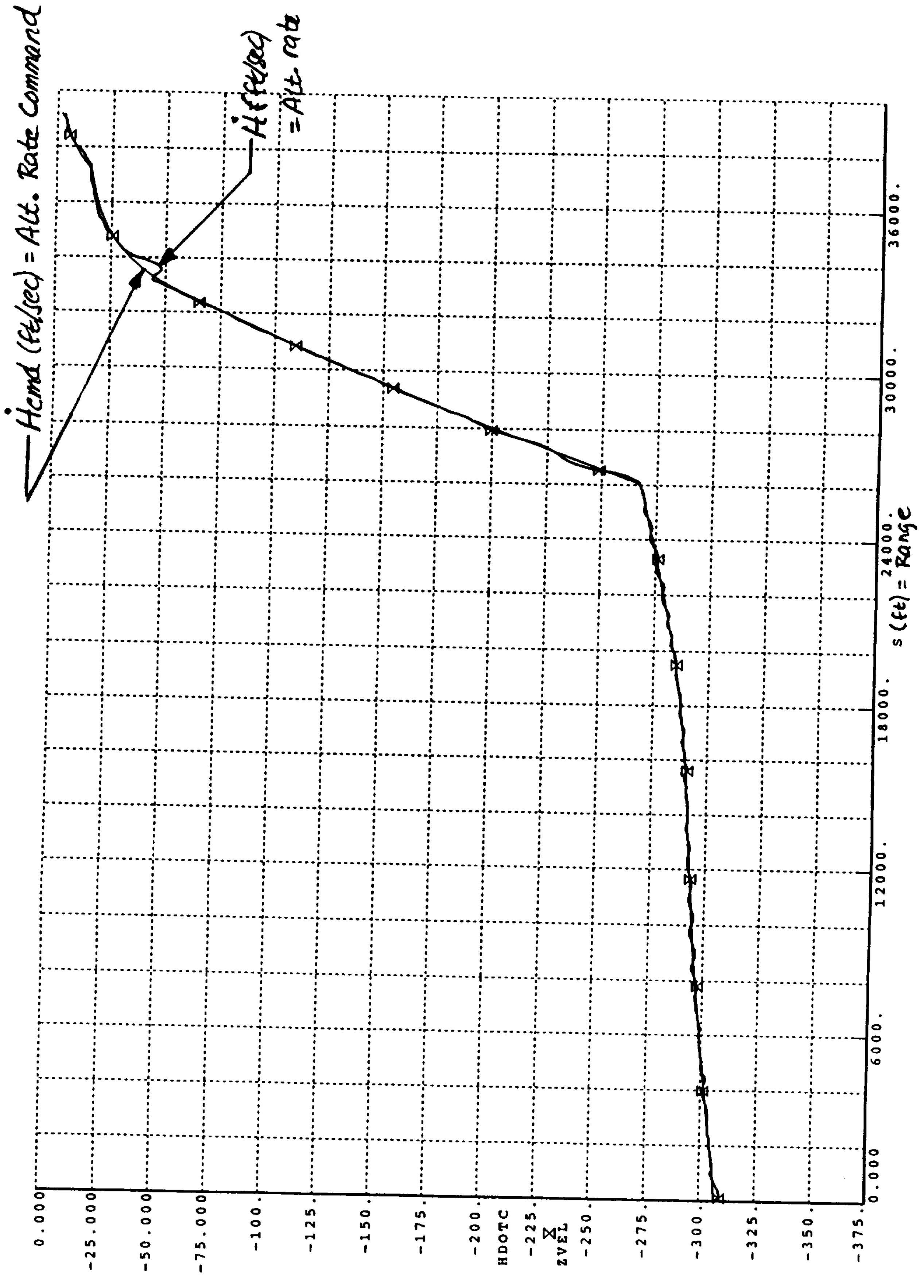

$\dot{H}cmd$ (ft/sec) = Alt. Rate Command
$\dot{H}$ (ft/sec) = Alt. rate
0.000
-25.000
-50.000
-75.000
-100.
-125.
-150.
-175.
-200.
-225.
-250.
-275.
-300.
-325.
-350.
-375.
HDOTC
ZVEL
0.000
6000.
12000.
18000.
24000.
30000.
36000.
s (ft) = Range

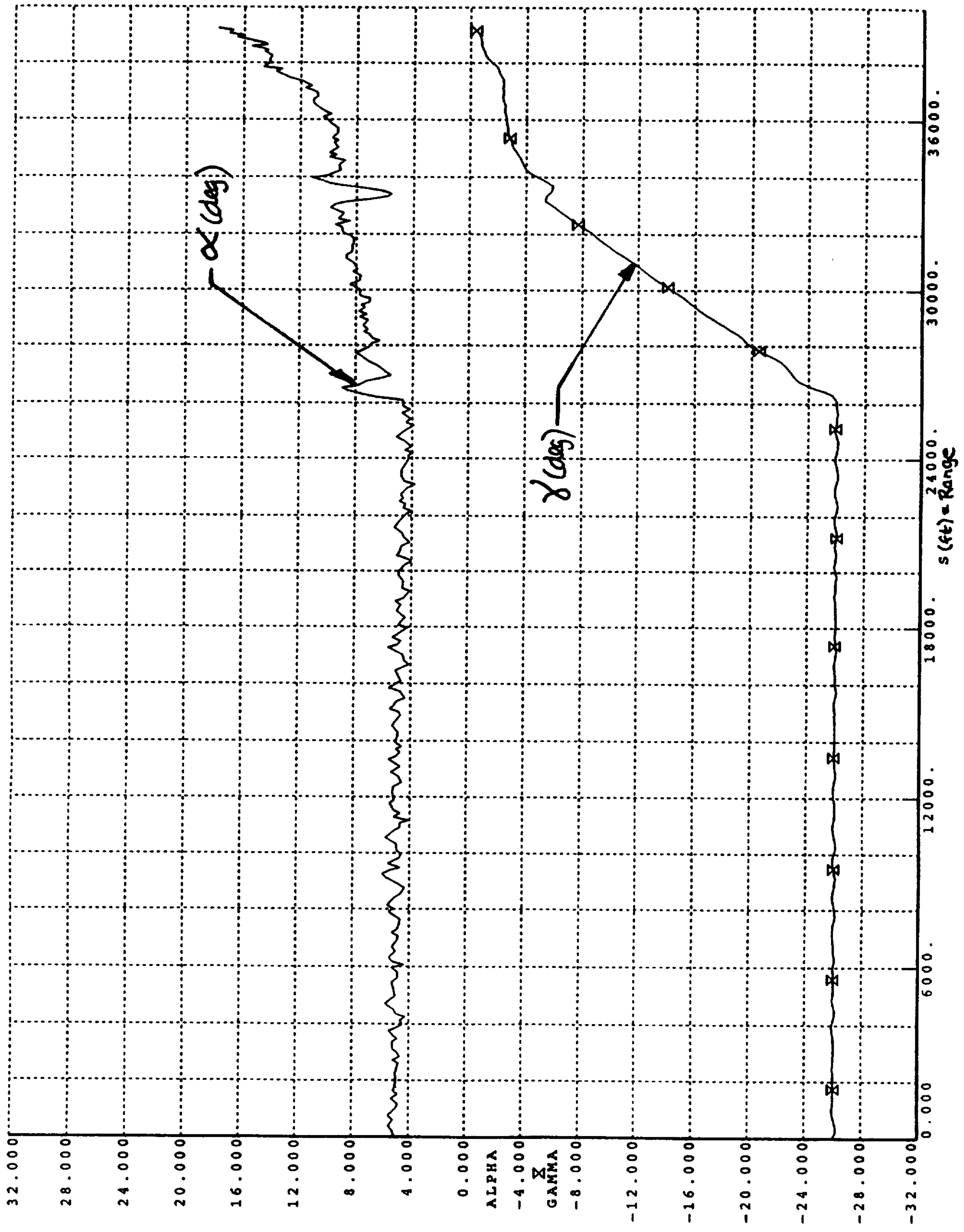

32.000
28.000
24.000
20.000
16.000
12.000
8.000
4.000
0.000
ALPHA
-4.000
GAMMA
-8.000
-12.000
-16.000
-20.000
-24.000
-28.000
-32.000
0.000
6000.
12000.
18000.
24000.
30000.
36000.
s (ft) = Range
α (deg)
γ (deg)

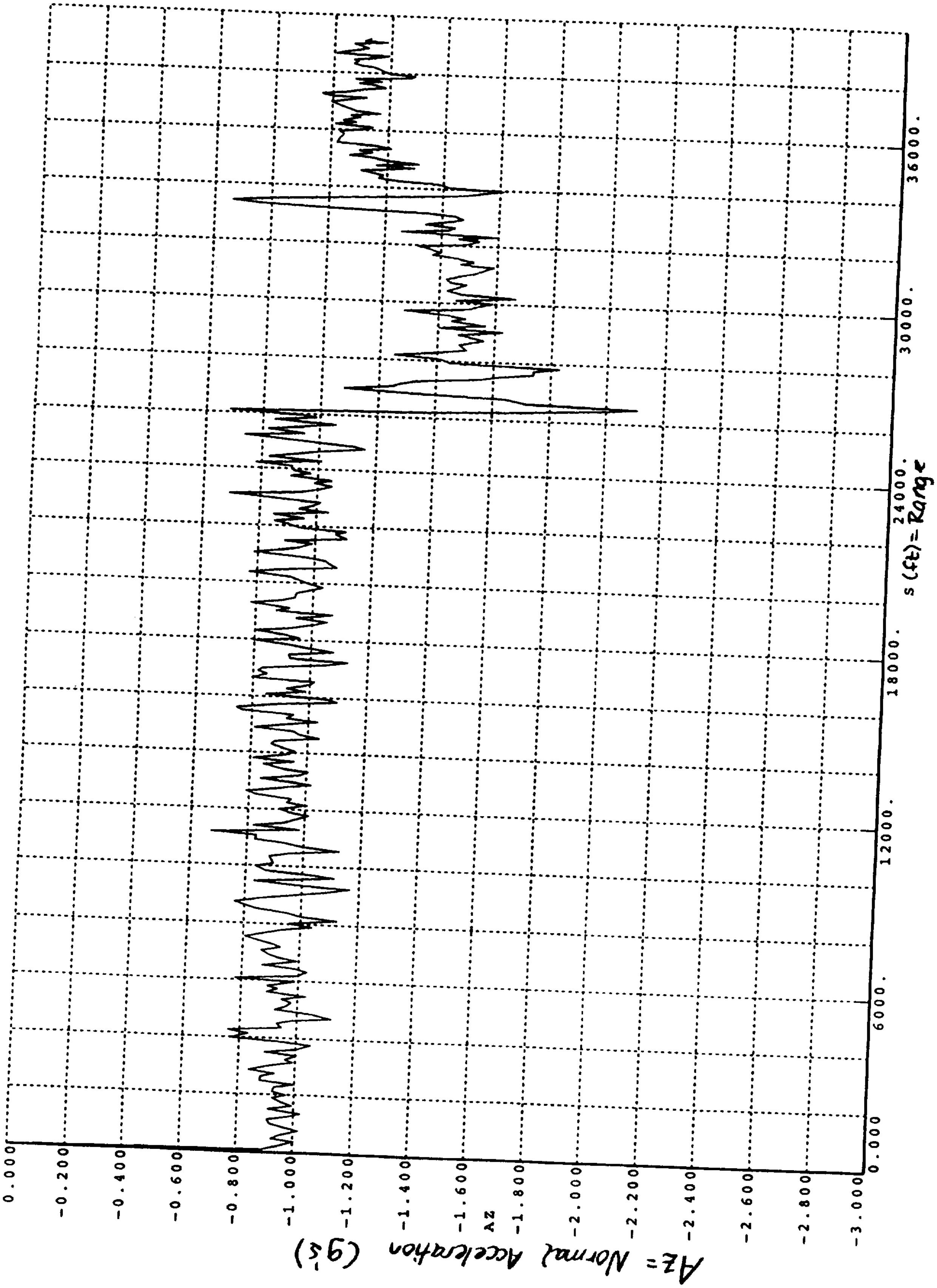

0.000
-0.200
-0.400
-0.600
-0.800
-1.000
-1.200
-1.400
-1.600
-1.800
-2.000
-2.200
-2.400
-2.600
-2.800
-3.000
Az
0.000
6000.
12000.
18000.
24000.
30000.
36000.
s (ft)= Range
Az= Normal Acceleration (g's)

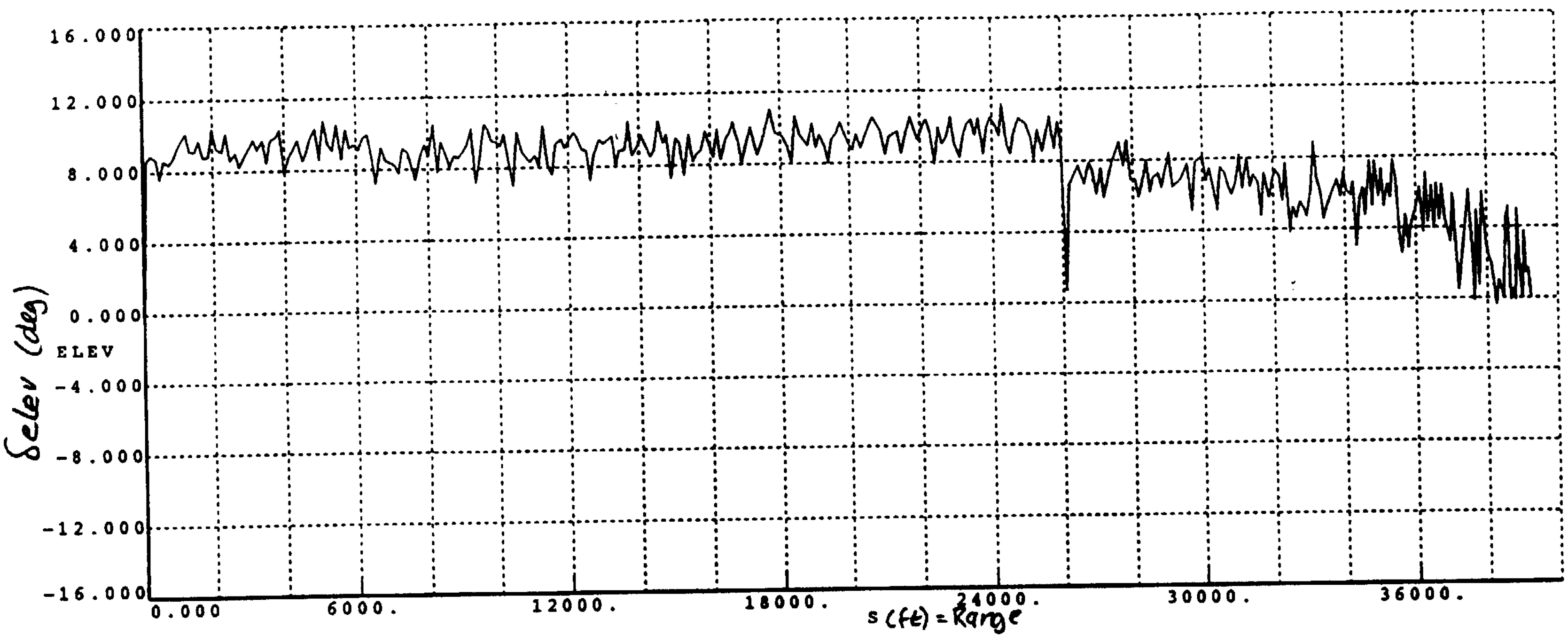

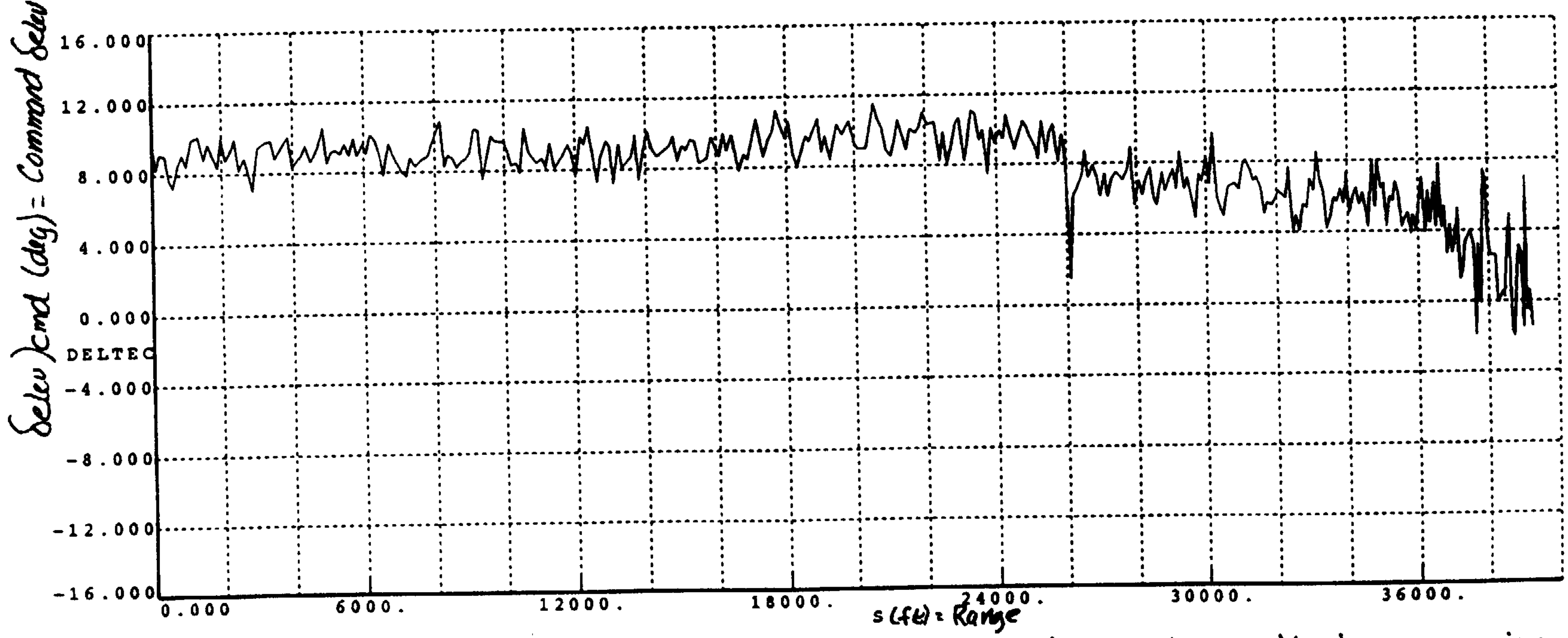

Note: Raw unfiltered α, β, ϕ data is fed into autopilot; this results in excessive surface deflection as shown above.

Appendix F

Simulation Results of a TAEM Nominal Mission With Wind Turbulence

A nominal TAEM mission was simulated with wind turbulence. The conditions of this simulation are defined as follows. The turbulence 1σ gaussian distribution and integral scale length is set according to the data in Appendix C, at an altitude of 9000 meters. These parameters are set at:

- $\sigma_X = \sigma_Y = \sigma_Z =$ 17.3 ft/sec
- $L_X = L_Y = L_Z =$ 1753 ft.

The results are plotted in the following figures.

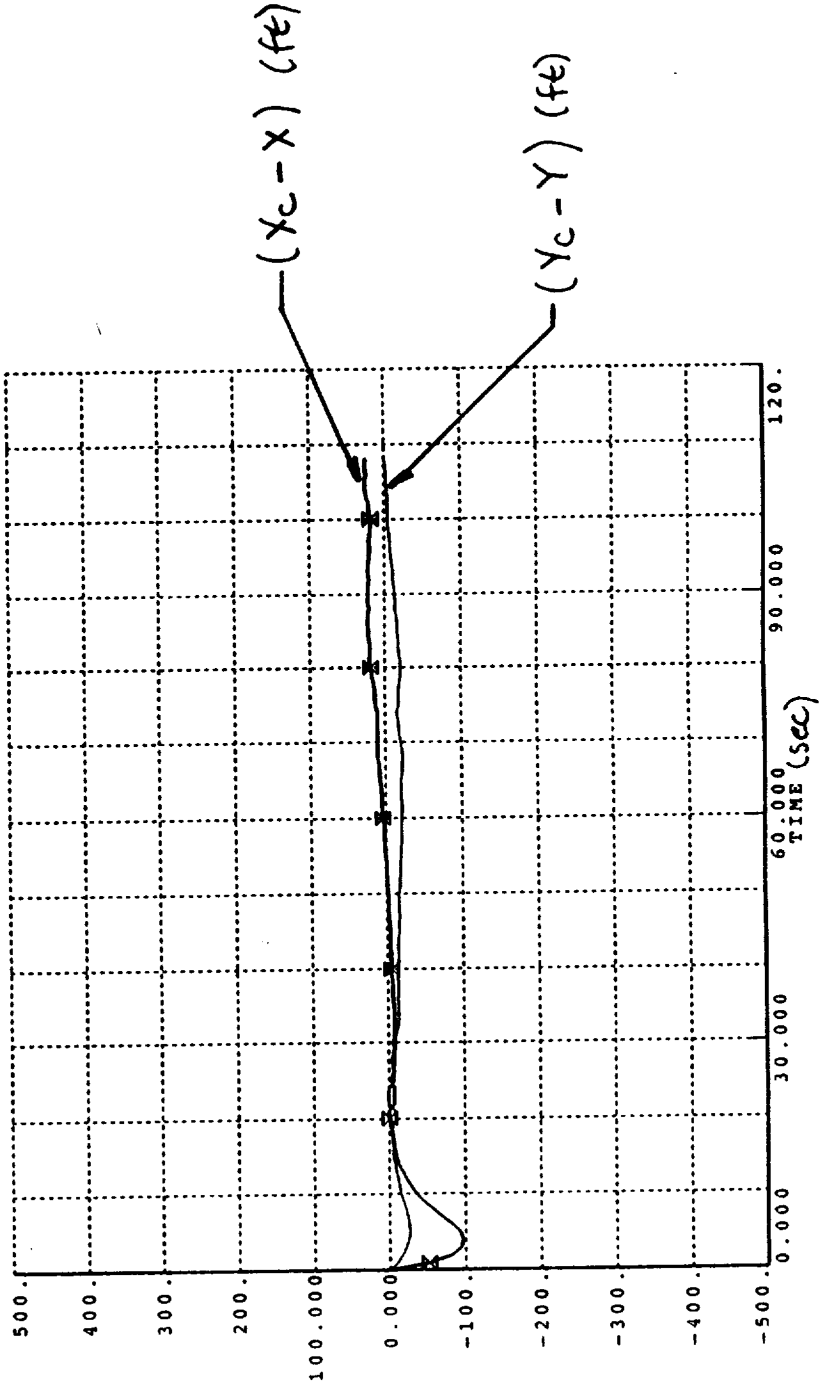
500.
400.
300.
200.
100.000
0.000
-100.
-200.
-300.
-400.
-500.
0.000
30.000
60.000
90.000
120.
TIME (sec)
$(X_c - X)$ (ft)
$(Y_c - Y)$ (ft)

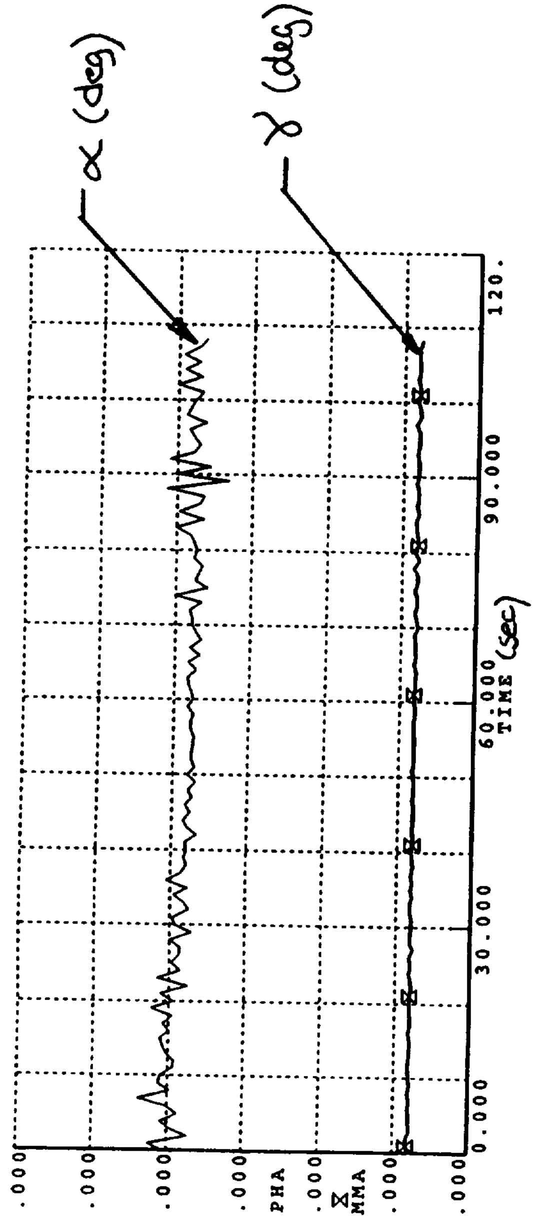
α (deg)
γ (deg)
30.000
20.000
10.000
0.000
ALPHA
-10.000
⊠
GAMMA
-20.000
-30.000
0.000
30.000
60.000
90.000
120.
TIME (sec)

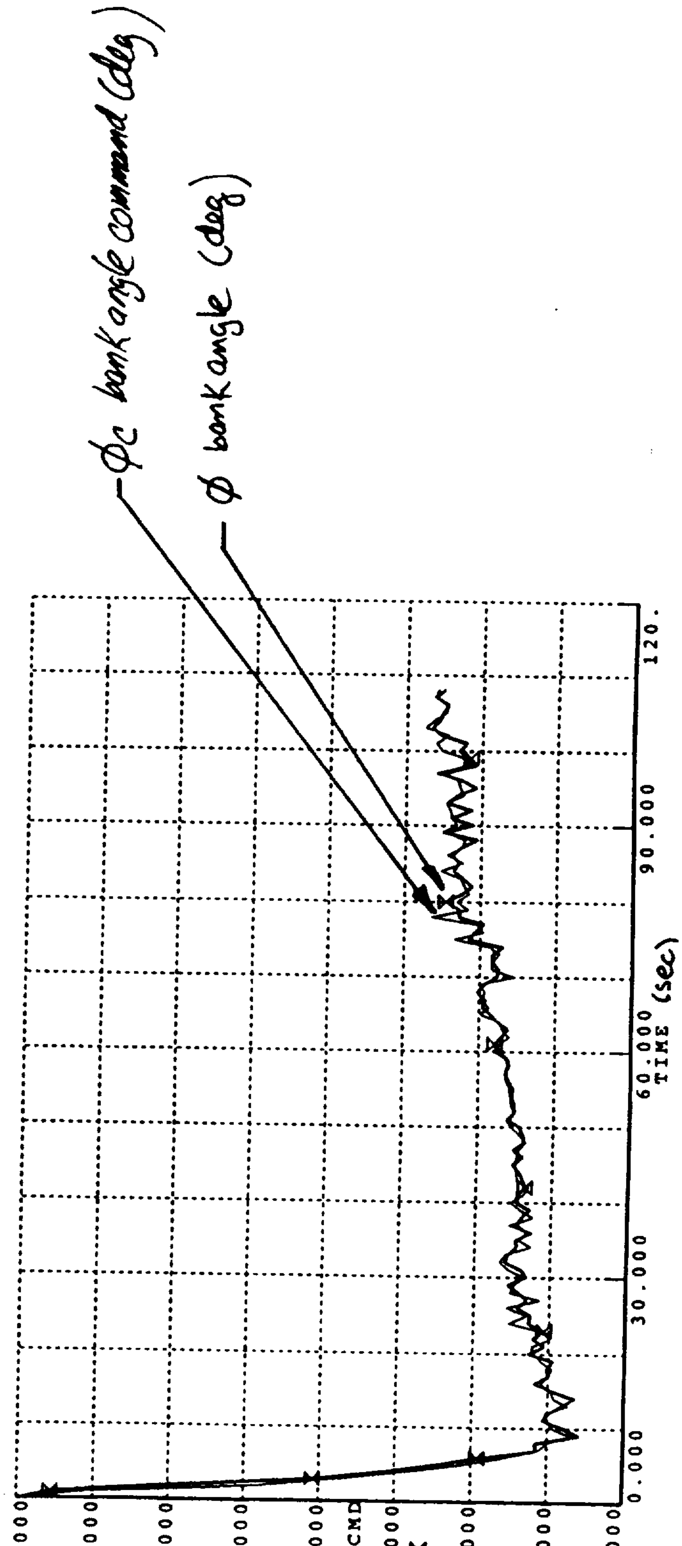
φc bank angle command (deg)
φ bank angle (deg)
0.000
-5.000
-10.000
-15.000
-20.000
PHICMD
-25.000
⊠
PHI
-30.000
-35.000
-40.000
0.000
30.000
60.000
90.000
120.
TIME (sec)

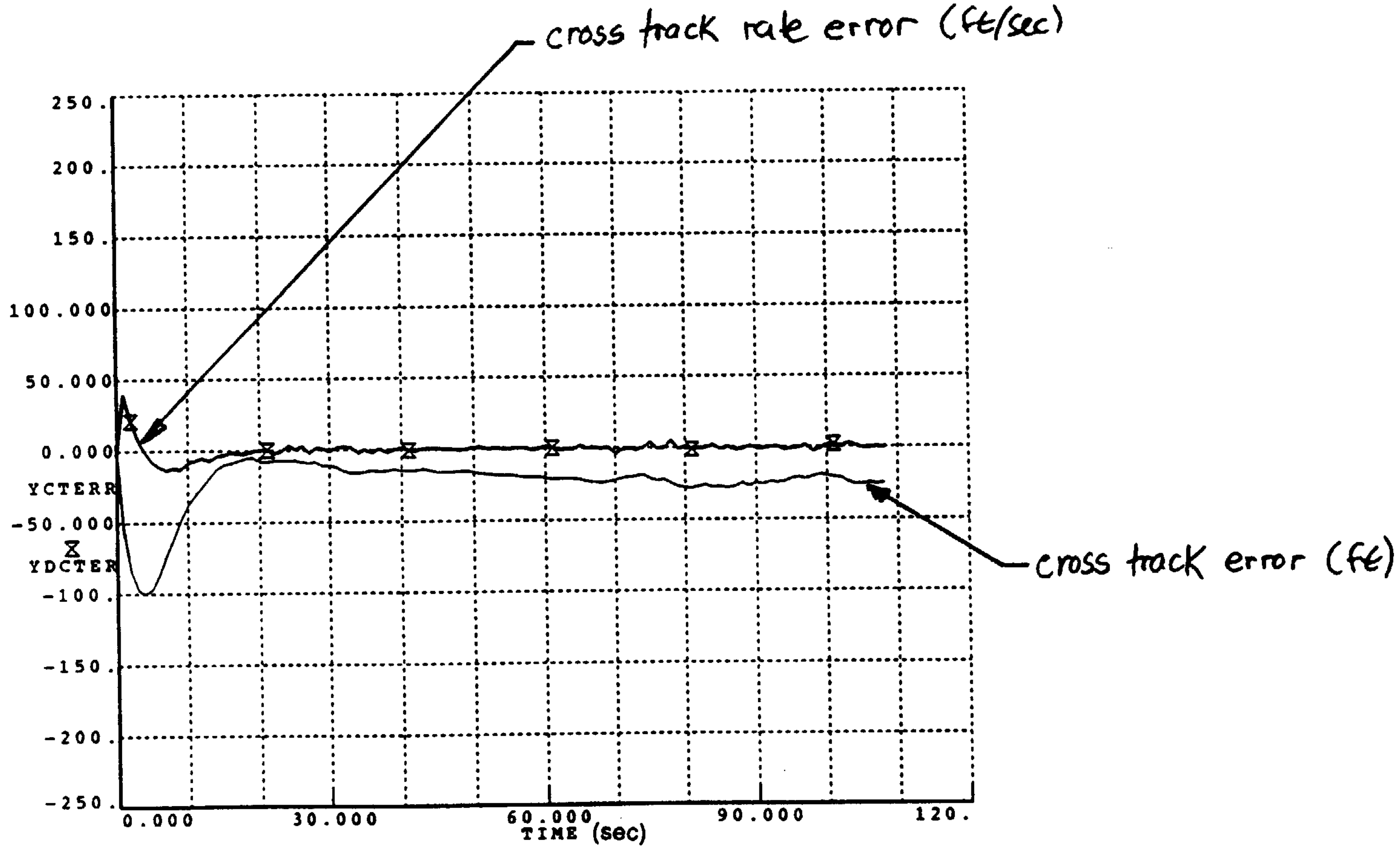

cross track rate error (ft/sec)

cross track error (ft)

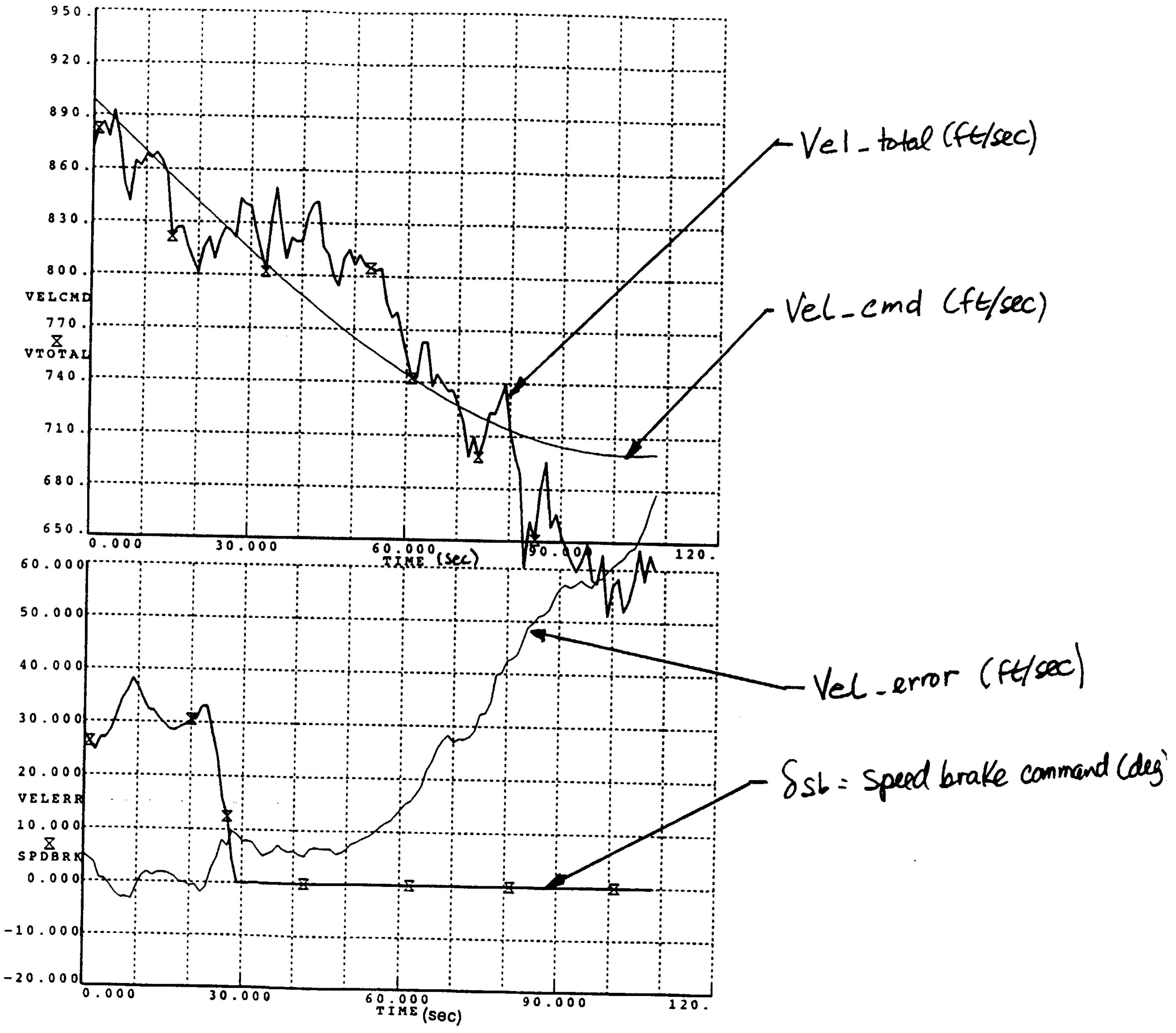
950.
920.
890.
860.
830.
800.
VELCMD
770.
VTOTAL
740.
710.
680.
650.
0.000
30.000
60.000
90.000
120.
TIME (sec)
Vel_total (ft/sec)
Vel_cmd (ft/sec)
60.000
50.000
40.000
30.000
20.000
VELERR
10.000
SPDBRK
0.000
-10.000
-20.000
0.000
30.000
60.000
90.000
120.
TIME (sec)
Vel_error (ft/sec)
δsb = Speed brake command (deg

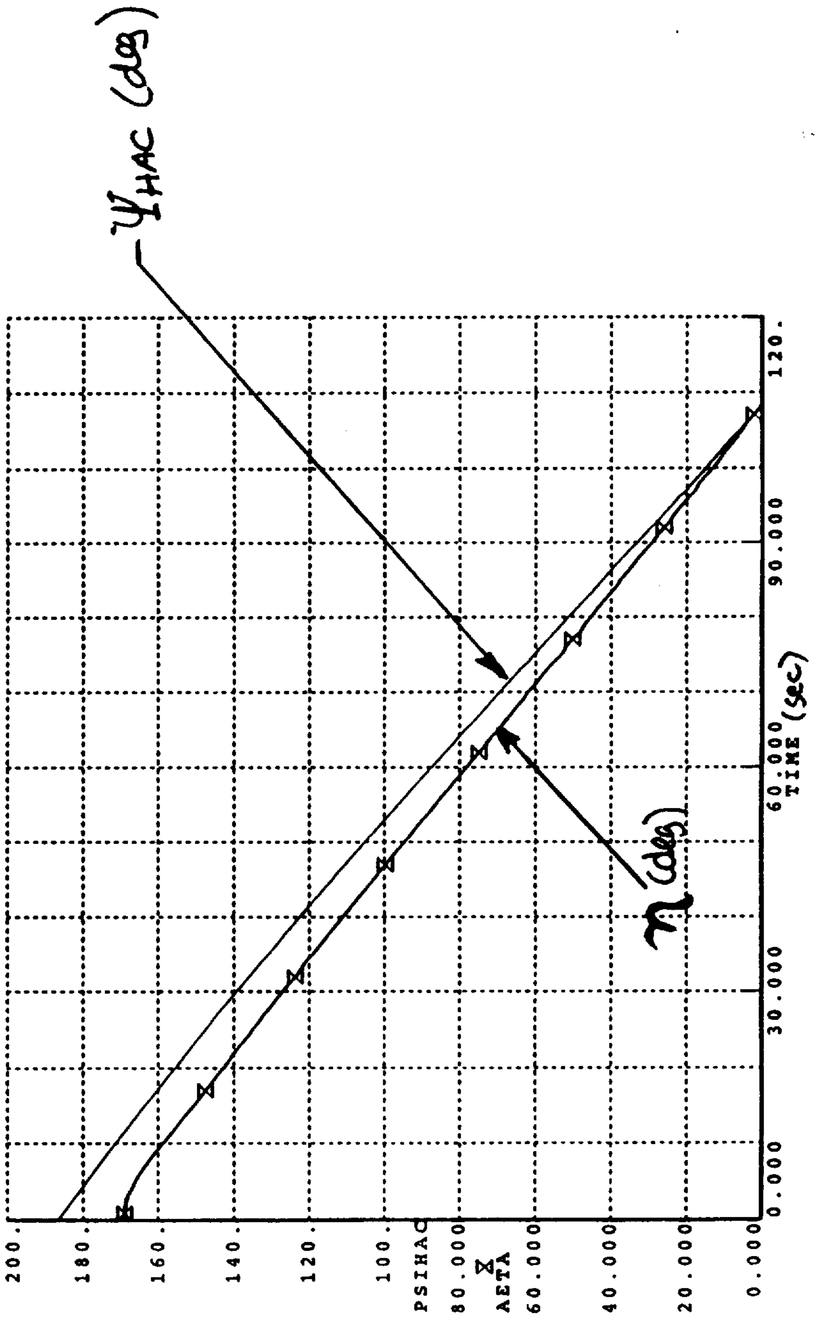
200.
180.
160.
140.
120.
100.
80.000
60.000
40.000
20.000
0.000
PSIHAC
AETA
0.000
30.000
60.000
90.000
120.
TIME (sec)
Ψ HAC (deg)
η (deg)

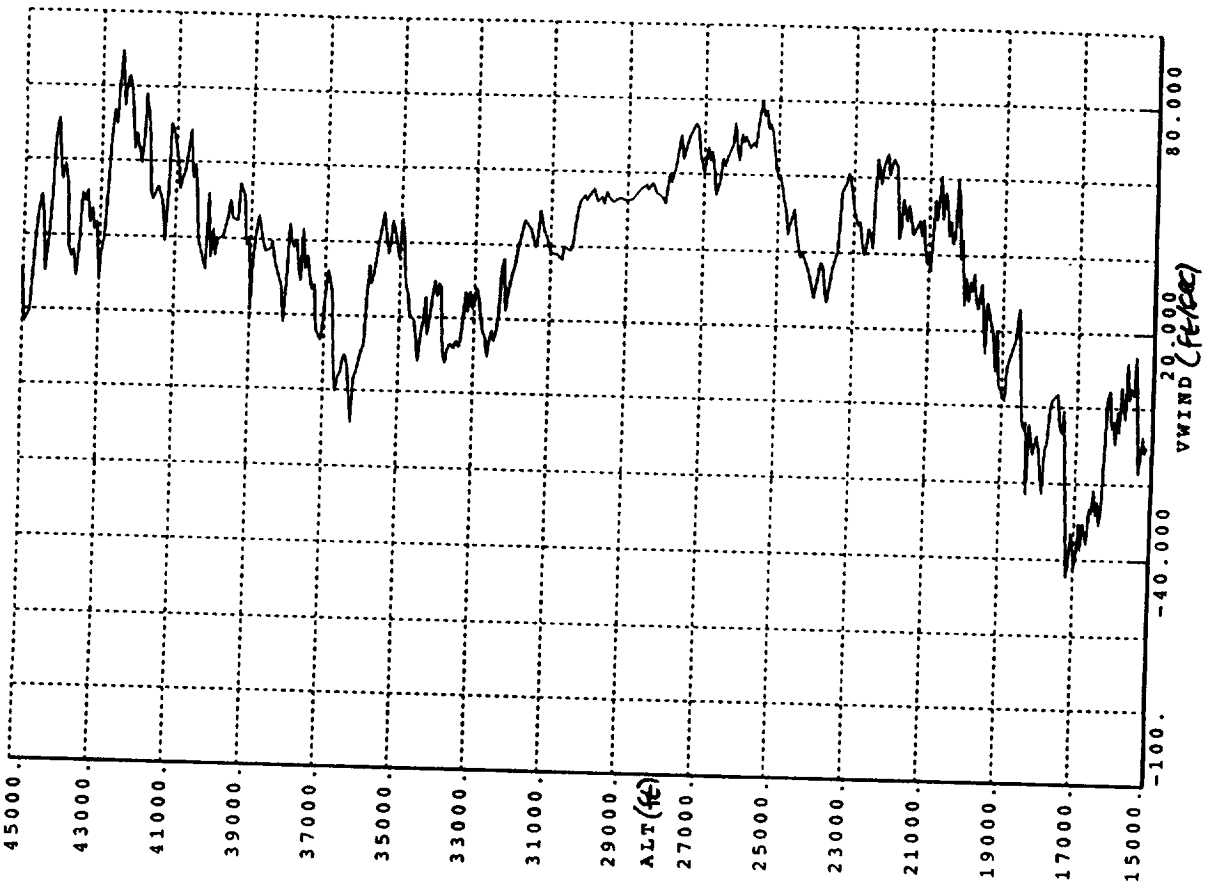
45000.
43000.
41000.
39000.
37000.
35000.
33000.
31000.
29000.
ALT (ft)
27000.
25000.
23000.
21000.
19000.
17000.
15000.
-100.
-40.000
20.000
80.000
VWIND (ft/sec)

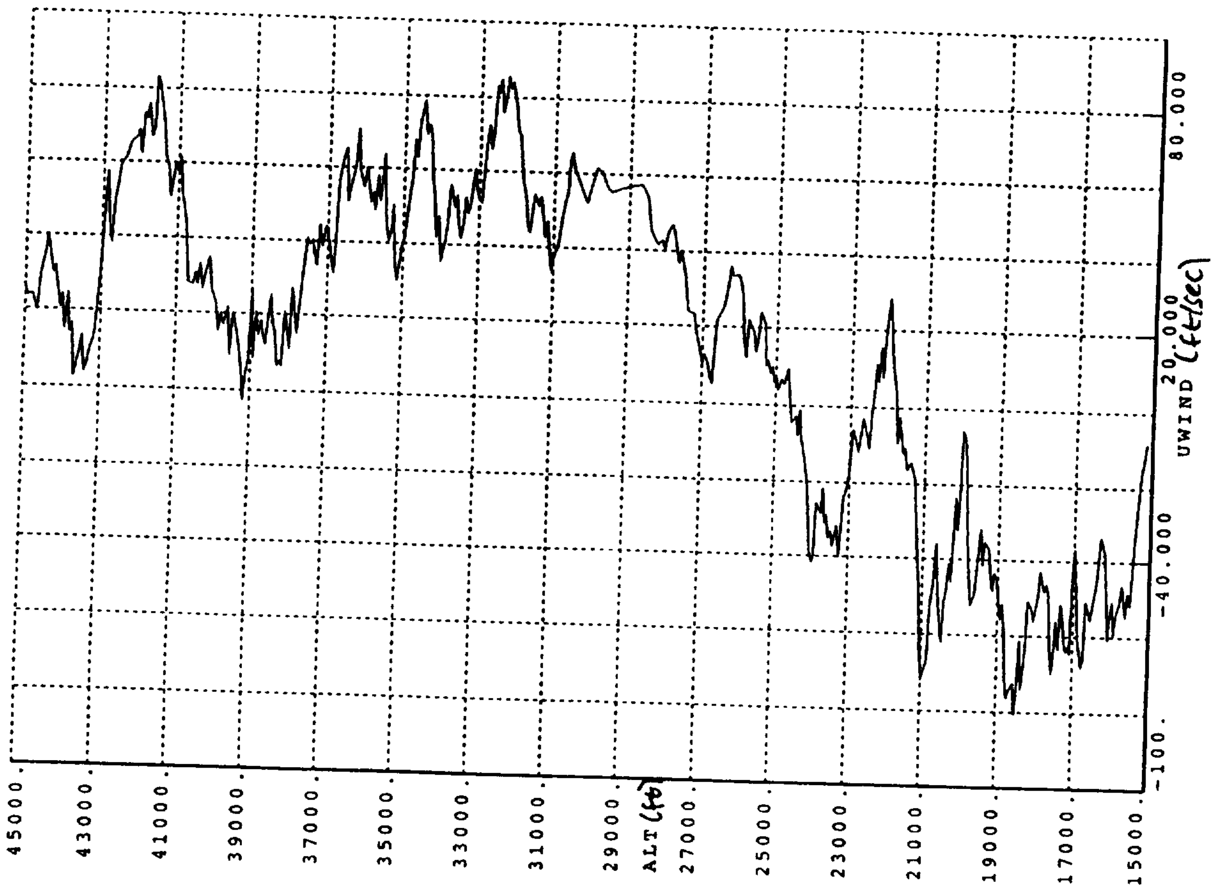
45000.
43000.
41000.
39000.
37000.
35000.
33000.
31000.
29000.
ALT (ft)
27000.
25000.
23000.
21000.
19000.
17000.
15000.
-100.
-40.000
20.000
80.000
UWIND (ft/sec)

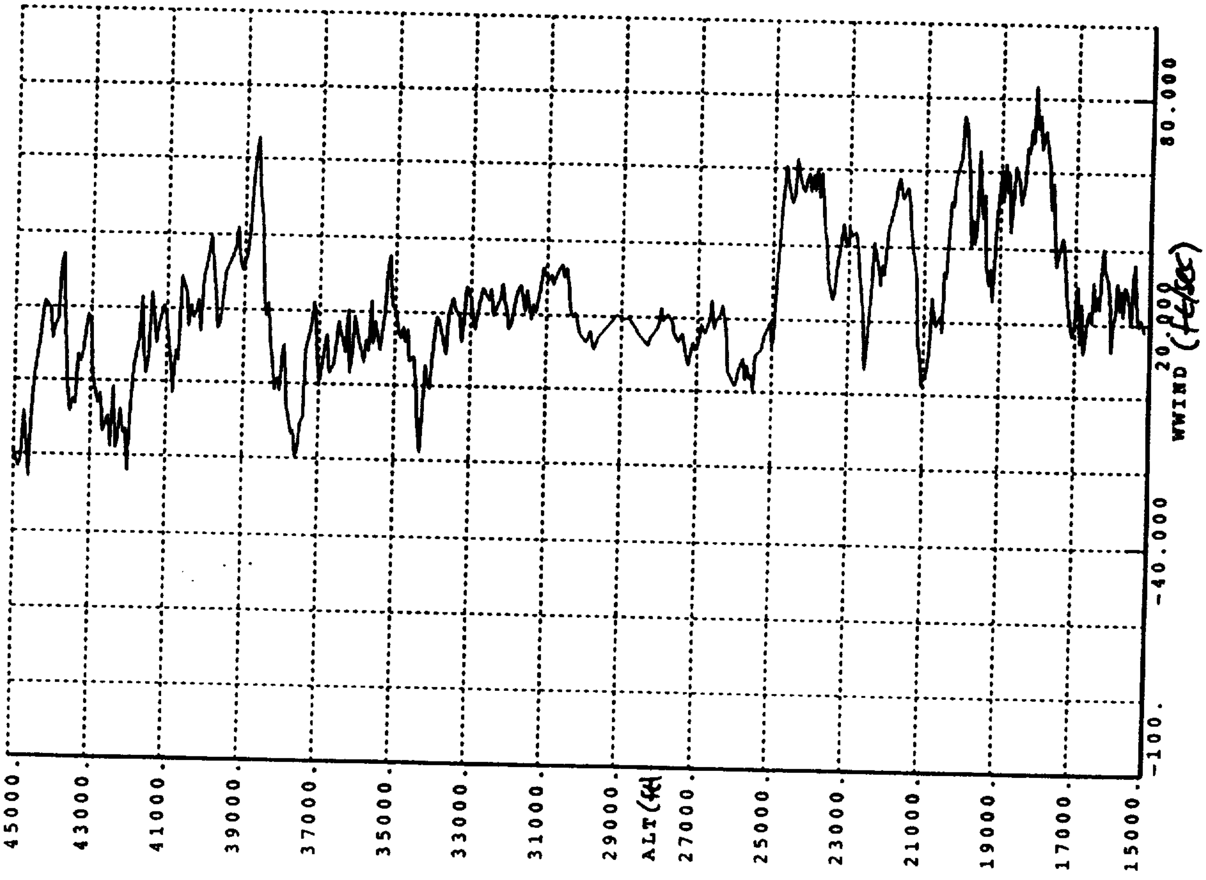

45000.
43000.
41000.
39000.
37000.
35000.
33000.
31000.
29000.
ALT(ft)
27000.
25000.
23000.
21000.
19000.
17000.
15000.
-100.
-40.000
20.000
80.000
WWIND (ft/sec)

Appendix G

Autoland Approach and Landing Trajectory Generation Algorithms

The following section contains a block diagram of the trajectory generator used to generate guidance commands during the autoland A/L phase. These algorithms also define the second order exponential transition equations used in guiding the vehicle from the end of the pre-flare maneuver (from altitude of H2C to H2), and during the final flare (altitude H3 to touchdown).

The definition of the autoland A/L trajectory is covered in section 3.2.1 .

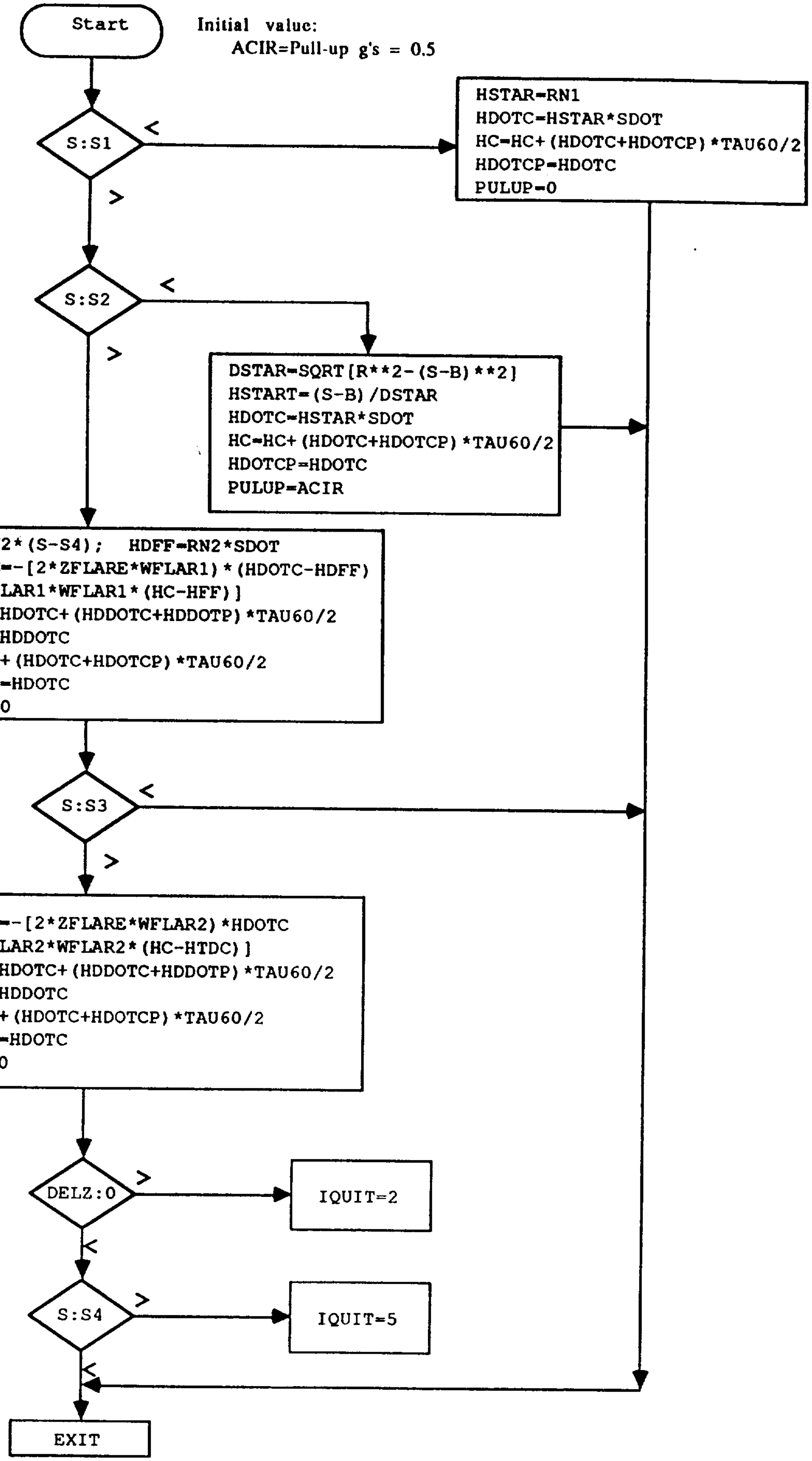

Figure G-1 PLS TRAJECTORY ALGORITHMS BLOCK DIAGRAM

Appendix H

Cross Track Error/ Cross Track Rate Error Generation Algorithms

The following section contains a block diagram (see figure H-1) of the cross track error and cross track rate error generator used to generate bank angle guidance commands during the TAEM phase. These algorithms serve to define the functions given in figure 5-7. A unique feature is the adaptive loop which calculates d(Ψe)dt. This error function serves to adapt the trajectory command such that when, d(Ψe)dt.=0 , then the commanded angular rate [d(Ψc)dt] equals the actual rate [d(Ψ)dt].

A plot of the adaptive loop signal d(Ψe)dt from the nominal TAEM case without wind, is included in figure H-2 . Notice that over time, d(Ψe)dt approaches zero.

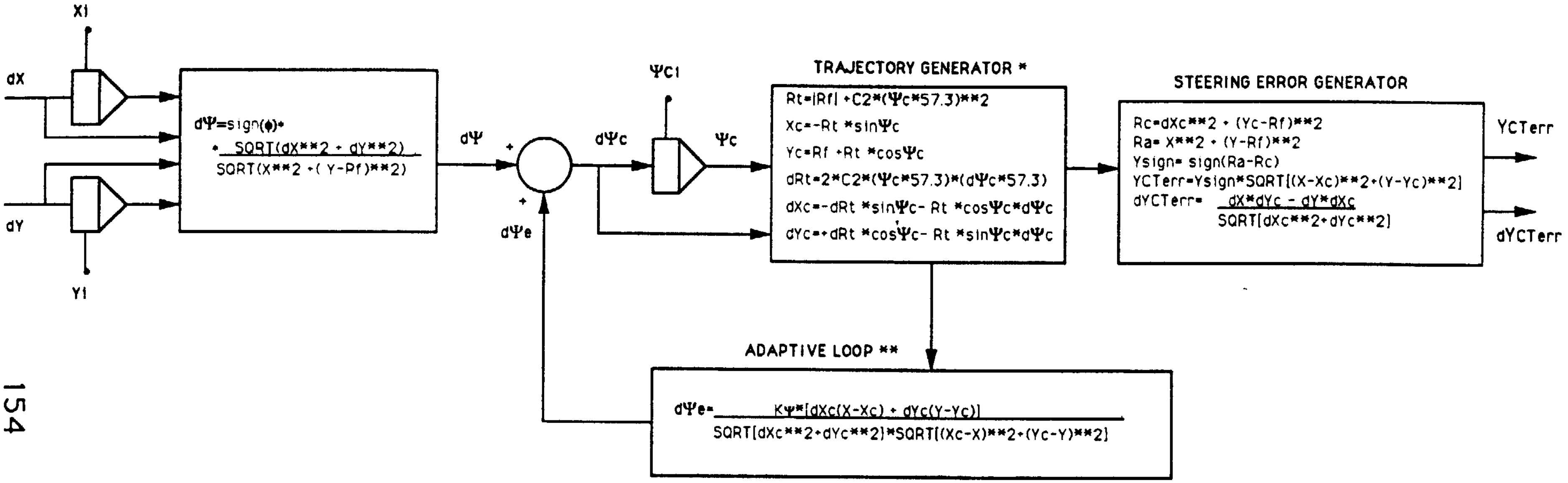

Notes: see sections 5.1 and 5.2 and figure 5-7 and 5-8 for definition of terms

* C2= spiral coefficient R2 from equation (3)

** KΨ= adaptive loop gain ; nominal value= -0.03

Nomenclature:

dX= d(X)/dt; dY=d(Y)/dt; dΨ=d(Ψ)/dt

Figure H-1 Cross Track Error and Rate Error Algorithm Block Diagram

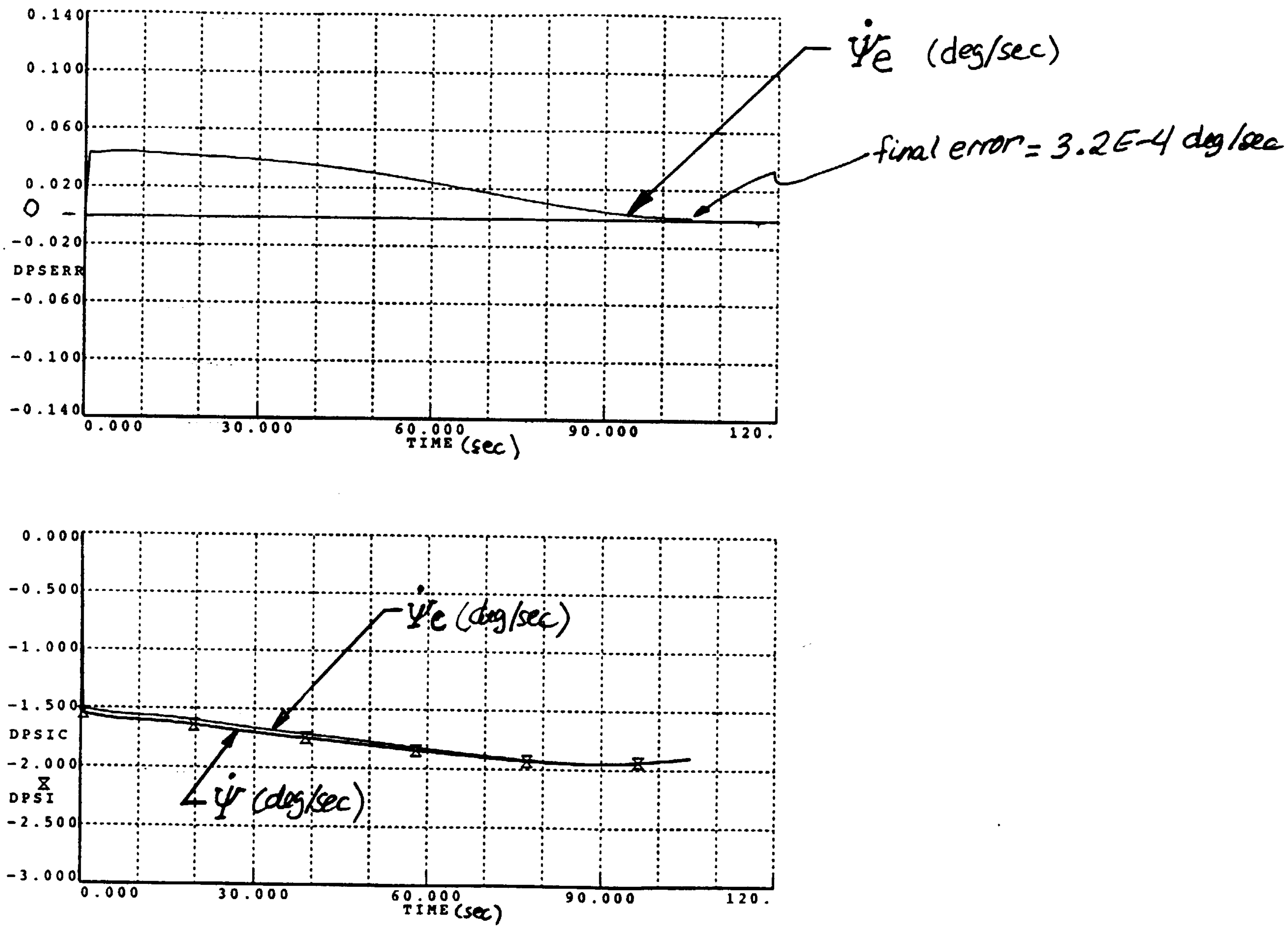

Figure H-2 Adaptive Loop Simulation Results

NASA
National Aeronautics and
Space Administration

Report Documentation Page

1. Report No. NASA CR-187495	2. Government Accession No.	3. Recipient's Catalog No.

4. Title and Subtitle Personnel Launch System Autoland Development Study	5. Report Date January 1991
	6. Performing Organization Code
7. Author(s) J.A. Bossi M.A. Langehough J.C. Tollefson	8. Performing Organization Report No.
	10. Work Unit No. 906-11-01-01
9. Performing Organization Name and Address Boeing Aerospace & Electronics P.O. Box 3999 M/S 82-24 Seattle, WA 98124-2499	11. Contract or Grant No. NAS1-18762
12. Sponsoring Agency Name and Address National Aeronautics and Space Administration Langley Research Center Hampton, VA 23665-5225	13. Type of Report and Period Covered Contractor Report
	14. Sponsoring Agency Code

15. Supplementary Notes

Langley Technical Monitor: Richard M. Hueschen
Final Report - Task 8

16. Abstract

The Personnel Launch System (PLS) Autoland Development Study focused on development of the guidance and control system for the approach and landing (A/L) phase and the Terminal Area Energy Management phase. In the A/L phase a straight-in trajectory profile was developed with a initial high glide slope, a pull-up and flare to lower glide slope and the final flare to touchdown. The TAEM system consisted of using a heading alignment cone spiral profile. The PLS autopilot was developed using integral LQG design techniques. The guidance and control design was verified using a nonlinear 6DOF simulation. Simulation results demonstrated accurate steering during the TAEM phase and adequate autoland performance in the presence of wind turbulence and wind shear.

17. Key Words (Suggested by Author(s)) Autoland Spacecraft Control System Guidance 6DOF Simulation	18. Distribution Statement Unclassified - Unlimited Subject Category 08

19. Security Classif. (of this report) Unclassified	20. Security Classif. (of this page) Unclassified	21. No. of pages 168	22. Price A08

NASA FORM 1626 OCT 86